Repair of Steel Beam/Girder Ends with Ultra High Strength Concrete (Phase I)

Prepared by:
Arash Esmaili Zaghi, PhD, P.E.; Kay Wille, PhD;
Kevin Zmetra, and Kevin McMullen

Department of Civil and Environmental Engineering

University of Connecticut

Report Number CT-2282-F-15-2

Final Report

June 6, 2015

Research Project Number SPR-2282

Prepared for:

Connecticut Department of Transportation

Michael Connors

Transportation Assistant Planning Director

Bureau of Policy and Planning

DISCLAIMER

This report does not constitute a standard, specification or regulation. The contents of this report reflect the views of the authors who are responsible for the facts and the accuracy of the data presented herein. The contents do not necessarily reflect the views of the Connecticut Department of Transportation or the Federal Highway Administration.

TECHNICAL REPORT DOCUMENTATION PAGE

1.Report No. CT-2282-F-15-2	**2. Government Accession No.**	**3. Recipients Catalog No.**
4. **Title and Subtitle** Repair of Steel Beam/Girder Ends with Ultra High Strength Concrete (Phase 1)		**5. Report Date** June 6, 2015 **6. Performing Organization Code** SPR-2282
7. Author(s) Arash Esmaili Zaghi, Kay Wille, Kevin Zmetra, Kevin McMullen		**8. Performing Organization Report No.** CT-2282-F-15-2
9. Performing Organization Name and Address **University of Connecticut** **Dept. of Civil & Environmental Engr.** **261 Glenbrook Road, Unit 2037** **Storrs, CT 06269-2037**		**10. Work Unit No. (TRIS)** **11. Contract or Grant No.** CT Study No. SPR-2282 **13. Type of Report and Period Covered** Final Report 2013-2015
12. Sponsoring Agency Name and Address Connecticut Department of Transportation 2800 Berlin Turnpike Newington, CT 06131-7546		**14. Sponsoring Agency Code** SPR-2282

15. Supplementary Notes
Prepared in cooperation with the U.S. Department of Transportation, Federal Highway Administration.

16. Abstract

The end corrosion in steel girders at the bearings due to joint leakage is a significant problem in many of the old bridges around the nation. This critical damage impairs the shear and bearing capacities of girders. Research has been conducted investigating a novel method for retrofitting the corroded ends of steel bridge girders using ultra-high performance concrete (UHPC) encasings. The repair involves casting thin UHPC panels on each side of the girder web. Shear studs welded to undamaged portions of the web and flange engage the UHPC panels and provide an alternate load path. This repair method is expected to be superior to the current practice of attaching steel cover plates. It can be easier to design and install, reduce obstruction to traffic during the repair, prevent future corrosion to the girder end, and reduce the total cost of repair. To investigate the effectiveness of the repair in recovering the capacity of the corrosion damaged girders, three large-scale experiments were performed on the undamaged, damaged and repaired rolled girders. This report presents results of these experiments, describes the finite element analysis (FEA) model, compares the model results to the tests, and describes the performance of the full-scale FEA.

17. Key Words Ultra-high Performance Concrete (UHPC), Beam/Girder End Repairs, Beam/Girder End Corrosion, Bridge Maintenance Repair Methods, Bridge Repairs, Concrete Encasing Steel Beams/Girders.	**18. Distribution Statement** No restrictions. Hard copy of this document is available through the National Technical Information Service, Springfield, VA 22161. The report is available on-line from the National Transportation Library at http://ntl.bts.gov

19. Security Classif. (Of this report) Unclassified	**20. Security Classif.(Of this page)** Unclassified	**21. No. of Pages** 287	**20. Price**

Form DOT F 1700.7 (8-72) Reproduction of completed page authorized

ACKNOWLEDGEMENTS

The authors would like to thank John Henault, Timothy Fields, Richard Van Allen, James Fallon, Leo Fontaine, Kevin Mahoney, Bao Chuong, Rabih Barakat, and Anne-Marie McDonnell of Connecticut Department of Transportation supporting this research. The significant contribution of Michael Culmo of CME Associates is highly appreciated.

The authors thank Peter Glaude and Jim Onley of the UConn School of Engineering machine shop for their extensive help in preparing the specimens; James Mahoney, Carolyn Ward, and Lori Judd of Connecticut Transportation Institute for managing the grant, John Gasparine of Inframetals for donating the steel for the experiment, David Hunt of Berlin Steel for donating steel for the load frame, Joseph D'Agostino of PB and Kaylene Perras of UConn SoE for their support in the project, Vic Perry, Dominique Corvez, John Ephraim, Gaston Doiron and Andrew Ross of Lafarge for donating the UHPC used.

The student support of Manish Roy, Masoud Mehr, Man Xu, Javier Duluc, Michael Humphreys, Amanda McBride, Christopher Pawlowski, and Andy Dauphinais is also thanked.

SI* (MODERN METRIC) CONVERSION FACTORS

APPROXIMATE CONVERSIONS TO SI UNITS

Symbol	When You Know	Multiply By	To Find	Symbol
		LENGTH		
in	inches	25.4	millimeters	mm
ft	feet	0.305	meters	m
yd	yards	0.914	meters	m
mi	miles	1.61	kilometers	km
		AREA		
in^2	square inches	645.2	square millimeters	mm^2
ft^2	square feet	0.093	square meters	m^2
yd^2	square yard	0.836	square meters	m^2
ac	acres	0.405	hectares	ha
mi^2	square miles	2.59	square kilometers	km^2
		VOLUME		
fl oz	fluid ounces	29.57	milliliters	mL
gal	gallons	3.785	liters	L
ft^3	cubic feet	0.028	cubic meters	m^3
yd^3	cubic yards	0.765	cubic meters	m^3
	NOTE: volumes greater than 1000 L shall be shown in m^3			
		MASS		
oz	ounces	28.35	grams	g
lb	pounds	0.454	kilograms	kg
T	short tons (2000 lb)	0.907	megagrams (or "metric ton")	Mg (or "t")
		TEMPERATURE (exact degrees)		
°F	Fahrenheit	5 (F-32)/9 or (F-32)/1.8	Celsius	°C
		ILLUMINATION		
fc	foot-candles	10.76	lux	lx
fl	foot-Lamberts	3.426	$candela/m^2$	cd/m^2
		FORCE and PRESSURE or STRESS		
lbf	poundforce	4.45	newtons	N
lbf/in^2	poundforce per square inch	6.89	kilopascals	kPa

APPROXIMATE CONVERSIONS FROM SI UNITS

Symbol	When You Know	Multiply By	To Find	Symbol
		LENGTH		
mm	millimeters	0.039	inches	in
m	meters	3.28	feet	ft
m	meters	1.09	yards	yd
km	kilometers	0.621	miles	mi
		AREA		
mm^2	square millimeters	0.0016	square inches	in^2
m^2	square meters	10.764	square feet	ft^2
m^2	square meters	1.195	square yards	yd^2
ha	hectares	2.47	acres	ac
km^2	square kilometers	0.386	square miles	mi^2
		VOLUME		
mL	milliliters	0.034	fluid ounces	fl oz
L	liters	0.264	gallons	gal
m^3	cubic meters	35.314	cubic feet	ft^3
m^3	cubic meters	1.307	cubic yards	yd^3
		MASS		
g	grams	0.035	ounces	oz
kg	kilograms	2.202	pounds	lb
Mg (or "t")	megagrams (or "metric ton")	1.103	short tons (2000 lb)	T
		TEMPERATURE (exact degrees)		
°C	Celsius	1.8C+32	Fahrenheit	°F
		ILLUMINATION		
lx	lux	0.0929	foot-candles	fc
cd/m^2	$candela/m^2$	0.2919	foot-Lamberts	fl
		FORCE and PRESSURE or STRESS		
N	newtons	0.225	poundforce	lbf
kPa	kilopascals	0.145	poundforce per square inch	lbf/in^2

*SI is the symbol for the International System of Units. Appropriate rounding should be made to comply with Section 4 of ASTM E380.
(Revised March 2003)

TABLE OF CONTENTS

LIST OF FIGURES

LIST OF TABLES

LIST OF EQUATIONS

GLOSSARY

ACMC - Advanced Cementitious Materials and Composites

ASCE - American Society of Civil Engineers

CNC - Computer Numeric Control

DOF - Degree of Freedom

FE - Finite Element

FEA - Finite Element Analysis

FEM - Finite Element Model

GISSMO - General Incremental Stress-State dependent damage MOdel

HBM - Hottinger Baldwin Messtechnik

K&C - Karagozian and Case

LSCT - Linear Strain Converting Transducer

LSTC - Livermore Software Technology Company

mil - One thousandth of an inch (0.001 in)

NI - National Instruments

PTFE - Polytetrafluoroethylene

RTD - Resistance Temperature Detector

UConn - University of Connecticut

UHPC - Ultra-High Performance Concrete

UHSC - Ultra-High Strength Concrete

EXECUTIVE SUMMARY

The condition of highway infrastructure in the State of Connecticut and across the United States has been deteriorating for years. Bridges are some of the most critical links in this system and some of the most vulnerable to failure. The American Association of State Highway and Transportation Officials (AASHTO) estimate that it would cost roughly $48 billion to repair the 72,868 structurally deficient bridges in the country [AASHTO, 2008]. Innovative designs for bridge rehabilitation are necessary to lower this cost. Such techniques need to be structurally effective and easy to implement while minimizing interruptions to traffic and increasing work zone safety. The State of Connecticut currently maintains 4,182 bridges, 1,810 of which are simple-span steel bridges. One of the most prevalent deficiencies for steel bridges is the corrosion of the steel girder ends at the bearing, as seen in Fig. 1. This corrosion damage may severely reduce load capacity of these girders at the ends and could potentially lead to structural deficiency, a posted load rating, or ultimately failure.

Figure 1. Typical End Corrosion of Bridge Girders [Photos Courtesy of Michael P. Culmo]

The conventional method of repairing damaged girder using cover plates or adding steel shapes has several drawbacks, among which include:

Removal of existing paint: Steel members of many structures in need of repair are likely coated with lead based paint due to their current age. Therefore, paint removal during preparation for rehabilitation requires extensive abatement protocols to prevent lead contamination to the surrounding environment.

Preparation: Preparation of the girder surface is required when adding steel plates or shapes. This requires either sanding/grinding when welding, or drilling holes for bolted additions. In extreme cases, cutting and removing of the corroded plates may be necessary before application of the repair.

Jacking: In order to achieve nearly stress-free condition required for the repair process, removal of the load from the girder end is necessary. This is performed by jacking the entire superstructure, which can account for as much as 70% of the project cost.

Lane closure: The lanes over the girder being rehabilitated may have to be temporarily closed while the repair work is in progress.

Repair Time: The rehabilitation process may be significantly time consuming.

Service after repair: Conventional repair designs do not necessarily stop future corrosion of the base metal and the repair itself is vulnerable to corrosion.

Custom design process: The rehabilitation design is specific to each project based on the severity and pattern of the corrosion and the geometry of girder ends.

One possible method involves the use of Ultra-High Performance Concrete (UHPC) cast over the sides of the corroded web. UHPC is a low porosity cement based fiber reinforced composite with compressive strengths in excess of 22 ksi and excellent durability properties. The concrete panels are mechanically attached to the member using steel shear studs shot to the undamaged portions of web and flange. This repair method has the potential to address multiple problems associated with traditional techniques for corrosion rehabilitation. The major advantages of this repair concept are:

Minimal surface preparation: Paint removal and surface preparation is not required for this rehabilitation method as high-strength concrete may be cast over the painted surfaces. The shear studs can be welded over existing paint. This significantly reduces the time and cost of preparation by eliminating the need for complex lead abatement. No preparation is needed beyond the removal of loose material.

No jacking required: The rehabilitation can be applied under in-situ stress conditions.

Reduced need of lane closure: Minimal road closure would be required if fast setting concrete is used.

Reduced construction time: The construction process is straightforward and simple. This enables the accelerated application of repairs.

Ease of application: UHPC is self-consolidating and pumpable, making it ideal for application in complex geometries and tight spaces common around bridge bearings and diaphragms.

Superior durability: UHPC is a highly durable material due to particle packing and low matrix porosity, reducing the ingress of ionic aggressors responsible for corrosion. Concrete panels may protect the original steel from further corrosion.

Diversity of use: Standard designs may be developed for typical girder types. This eliminates the need for project specific repair design.

RESEARCH OBJECTIVES

This proof-of-concept project was conducted to demonstrate the effectiveness of UHPC encasement to rehabilitate corrosion damage in steel girder ends. Specifically, the project has been emphasized on investigating the load bearing capacity of a damaged girder to potentially restore its capacity using this repair technique.

In addition, a high fidelity finite element modeling (FEM) method was developed and validated with experimental results. This FE modeling method enables future studies of different girder types, corrosion patterns, and optimization of the repair technique.

RESEARCH METHOD

In order to fulfill the objectives of this research, the following tasks are performed:

1. Development of a Preliminary Finite Element Modeling Method

A reliable finite element model was necessary to study possible repair concepts, design the test specimens, and ensure the adequacy of the test setup for beam experiments. LS-Dyna, a general-purpose finite element program, [LSTC, 2012a] was

selected as the software to perform the analysis. The modeling method utilized shell elements to model the girder plates, beam elements to model the studs, and solid elements to model the concrete panels.

2. Investigation of Potential Repair Designs and Selection of Test Specimen

The finite element models were used to develop potential designs for rolled and plate girders. The designs deemed most viable to restore the capacity of damaged girders were found to be the following. The concrete fill refers to Ultra-High Performance Fiber Reinforced Concrete (UHPC).

Plate Girder/Full Panel Fill. In this method, the entire first panel of a plate girder, between the bearing and first stiffeners, is filled with concrete. The panel is held in place by the flange and stiffener, so no shear studs are necessary. This repair method is shown in Fig 2a.

Plate Girder/Partial Panel Fill. Only a partial height concrete fill is considered in the first panel to clear the bridge diaphragm. Shear studs are required on the web to hold the panel in place and transfer forces. Figure 2b shows this repair.

Rolled Girder/Full Height Fill (for girders with and without stiffeners). Concrete fill covers the entire height of the web. Shear studs are provided on the top and bottom flanges to secure the panel, as stiffeners are not present as in the plate girder. Figure 2c and 2d show this repair with and without bearing stiffeners, respectively.

Rolled Girder/Partial Height Fill (for girders with and without stiffeners). In this method, only partial fill was considered. Shear studs are required on both the web and bottom flange. Figure 2e and 2f show this repair with and without bearing stiffeners, respectively.

Rolled Girder/L-Shaped Fill (for girders with and without stiffeners). This is a hybrid method of the full and partial height methods. A full height is cast at the bearing to provide a concrete column on the end bearing. The panel is only partially filled outside the bearing area. Shear studs are required on the top and bottom flange only. Figure 2g and 2h show this repair with and without bearing stiffeners, respectively.

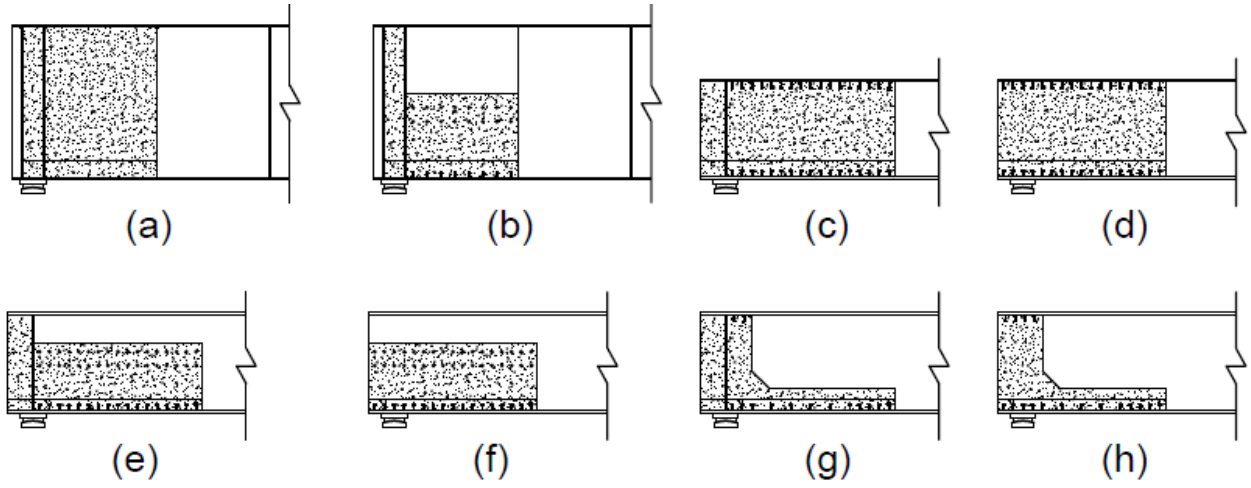

Figure 2. Proposed UHPC Repair Designs

The goal of these analyses was to demonstrate that this repair technique can be adapted to a variety of girder types.

For the large-scale experiment, the rolled girder with a partial height repair was selected. This was done in order to stay within the capacity of the structures lab floor tie downs. The rolled girder with the partial height fill was also found to be the least conservative of the viable methods. Bearing stiffeners were not included for the same reason. Completing a successful trial under these conditions would prove the method's viability to rehabilitate corrosion damage in steel girders.

3. Construction of the Specimens

Undamaged Girder (Benchmark Specimen): An undamaged girder was included in the experimental program to measure the capacity of the intact girder. This capacity was used as the reference load. The girder was a rolled W21x55. This shape was a half scale of a structurally deficient bridge in Waterford, which utilized W36x160 girders (Bridge No. 00352A/B, constructed in 1955). Both the W36x160 and W21x55 have web slenderness ratios (D/t_w) of 55.5. This ratio is critical for proper scale as it directly affects web buckling load at bearing. The shape has a total height of 21 in and flange width of 8.125 in. The web thickness of the undamaged girder was 0.339 in. The bottom flange thickness was 0.558 in.

Damaged Girder: To simulate the section loss due to corrosion, the thickness of lower portions of the web and inside of flange were reduced using machining. A 66% section loss was applied. This specimen was tested to measure the effect of simulated section loss similar to that of corrosion damage on the capacity of the girder. This level of damage was found in the inspection report of a structurally deficient bridge in Hartford, CT (Bridge No. 03399D) [Kristoff, 2011].

Figure 3 shows the section reduction applied to the damaged girders. The average thickness of the undamaged and damaged portion of the web was measured as 0.335 in and 0.113 in, respectively. The undamaged and damaged portion of the bottom flange had average thicknesses of 0.558 in and 0.325 in, respectively.

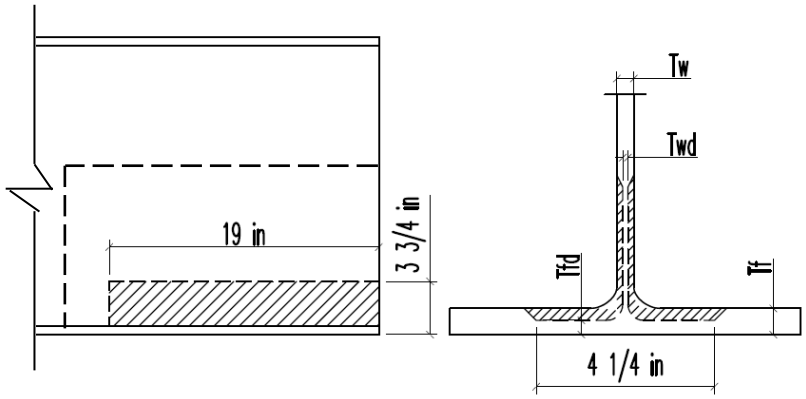

Figure 3. Section Reduction Pattern Utilized in the Damaged and Repaired Girders

Damage was created by cutting out the bottom tee of the girder (shown by the dashed line), and removing the section with a computer numeric controlled milling machine (Fig.

4a). The edges of the damaged section were milled at an angle in an effort to reduce stress concentration at the corners, and to prevent steel from bearing on the concrete. Once finished, the tee (Fig. 4b) was placed back in place using full penetration groove welds (Fig. 4c). The welds were ground flush.

(a) (b) (c)

Figure 4. Section Reduction Process: (a) Milling the Tee, (b) Damaged Section on Tee, and (c) Adding Back the Tee Section

Damaged/Repaired Girder: The third specimen had the same section reduction pattern as the damaged girder. The repaired girder had 10% more web section loss compared to the damaged girder given machining tolerances. The original and reduced web thicknesses measured as 0.383 in and 0.102 in, respectively. The original flange thickness of 0.504 was machined to 0.271 in in the reduced section.

In the repaired specimen, $^{3}/_{8}$-in diameter, $1^{1}/_{4}$-in long headed shear studs were welded in a 2-in grid pattern on both the web and flange. Care was taken so the studs on opposite one another on the web would not be congruent. A staggered pattern would resist possible damage to the web during welding and loading given the small thickness of the web plate. The arrangement of these studs is shown in Fig. 5a. Studs were installed with a stud-welding gun by a professional contractor, as is standard practice, as seen in Fig. 5b. This process involves running a high current (>500 A) through the stud. This causes the base of the stud to liquefy, forming a molten metal pool in the ceramic welding ferrules, which are removed after stud application. This ensures that the studs are consistently attached to the base material.

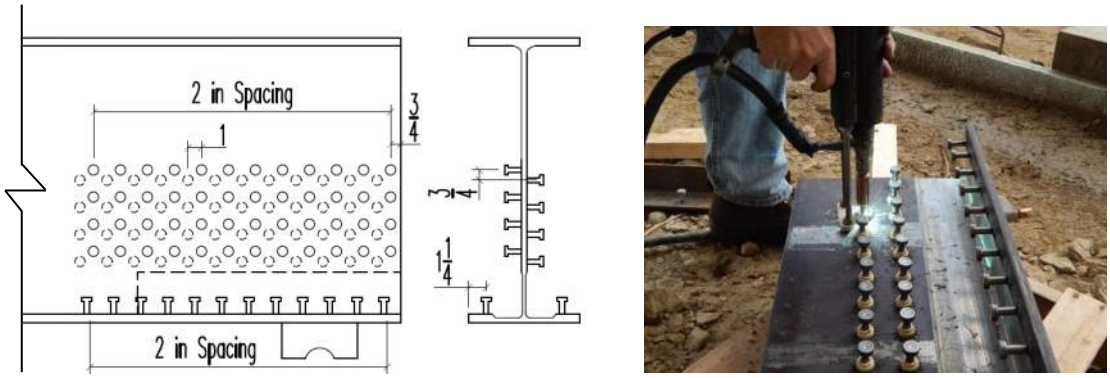

(a) (b)

Figure 5. Design and Installation of Studs for the UHSC Repair

4. Application of Concrete Repair

After welding of the studs, the cut portion of the beam was welded in place similar to the second specimen. Figure 6 shows the dimension of concrete panel used in the third specimen. The panel was 25-in long and 13-in tall. This is sufficient to cover the 19-in long reduced section. The thickness of the panel is 1 3/4 in, providing 1/2 in clearance for studs on the web. A bevel at the bottom of the panel was designed to prevent water from pooling on the bottom flange. This mitigates corrosion and provides cover for flange studs.

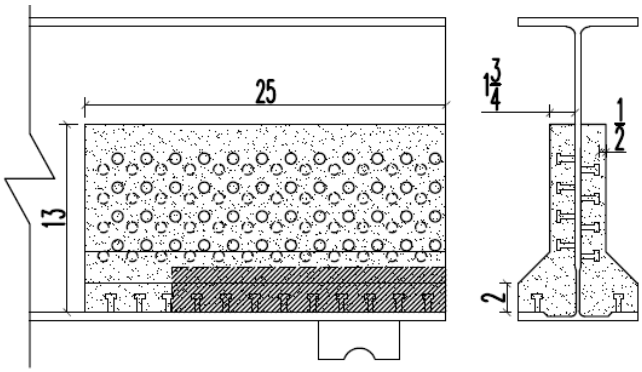

Figure 6 Dimensions of the Concrete Cast

The concrete used in this study was off-the-shelf Ductal® JS-1212, a proprietary mix designed by Lafarge to achieve high early strength. This ultra-high performance concrete formulation contains premix powder, water, Premia 150 (a modified phosphonate plasticizer), Optima 100 (a modified polycarboxylate high-range water-reducing admixture), Turbocast 650A (a non-chloride accelerator), and steel fibers. The fibers included in this mix design were straight, brass coated, high- strength steel fibers with a diameter of 0.008 in and a length of 0.5 in. The steel tensile strength is specified to be greater than 290 ksi. The thin brass 14 coating provides lubrication during the drawing process and mitigates corrosion of the raw fibers [Yuan and Graybeal, 2014]. A constant steel fiber content of two percent by volume was used in this study. A trial mix was performed prior to casting the panel to verify workability and to determine the desired curing time between casting and testing.

The mixing process began by mixing the dry powdered premix to remove agglomerations. Water and the chemicals were then added. After addition of the liquids the mix remained dry for a time as the water and chemicals dispersed. After about 15 min of mixing, the mix began to turn over from a solid into a fluid state. After this ‘turn over’, steel fibers were carefully added to the mix, and the UHPC was ready to cast. Figure 7 shows the turn over and mixing process.

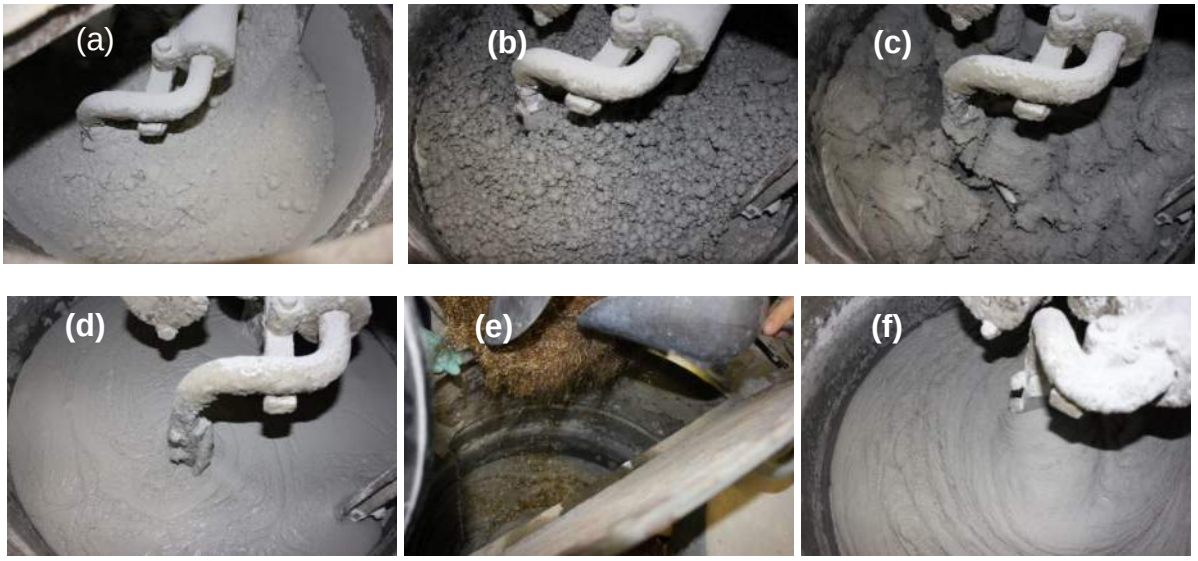

Figure 7. Mixing the UHPC: (a) Mix Just After Addition of Liquids, (b) 15 min After Liquids, (c) 22 min After Liquids, UHPC Turning Over, (d) 25 min After Liquids, UHPC Matrix Ready, (e) Addition of Fibers, (f) 3 min After Fiber Addition, UHPC Ready

A standard spread test for self-consolidating concretes, which is the counterpart to a slump test for non-consolidating concretes, was performed in accordance to ASTM C230 [ASTM, 2014]. The results of the spread test showed a spread of 11.0 in (Figure 8a,b). This level of flowability ensures the concrete to flow sufficiently and allows self-consolidation, negating the need for vibratory compaction. At the same time the concrete was sufficiently viscous to prevent steel fiber segregation. The concrete was transferred into five gallon buckets for casting. Casting forms made from standard foam-board wall insulation and Plexiglas were fixed to the beam using construction adhesive and wooden framework. The rigid foam-board insulation was shaped using a milling machine, and the finished pieces built up using spray adhesive. Plexiglas was used to cover the end of the beam allowing monitoring the height of the cast and its consolidation.

The steel girder and formwork had been treated with mineral oil prior to casting to prevent bonding, as shown in Fig 8c, this was intended to simulate the layer of paint present on the girder. Care was taken not to apply the oil to the shear studs. The concrete was then poured from the buckets into the top of the mold, Fig 8d. During casting one of the foam-boards formwork detached from the steel and began floating on the concrete. This created gaps between the forms and the girder, creating leaks allowing concrete to escape the mold. These leaks were immediately contained by further shoring the formwork and by sealing leaks. Because of the low temperature in the Structures Lab, after casting, the girder end was covered with an insulating concrete curing blanket and a heater installed and left to cure, Fig 8e. The average temperature under the blanket was measured 72° F. After two days the forms were removed, and excess concrete cut away with a grinding wheel. The finished panel can be seen in Fig. 8f.

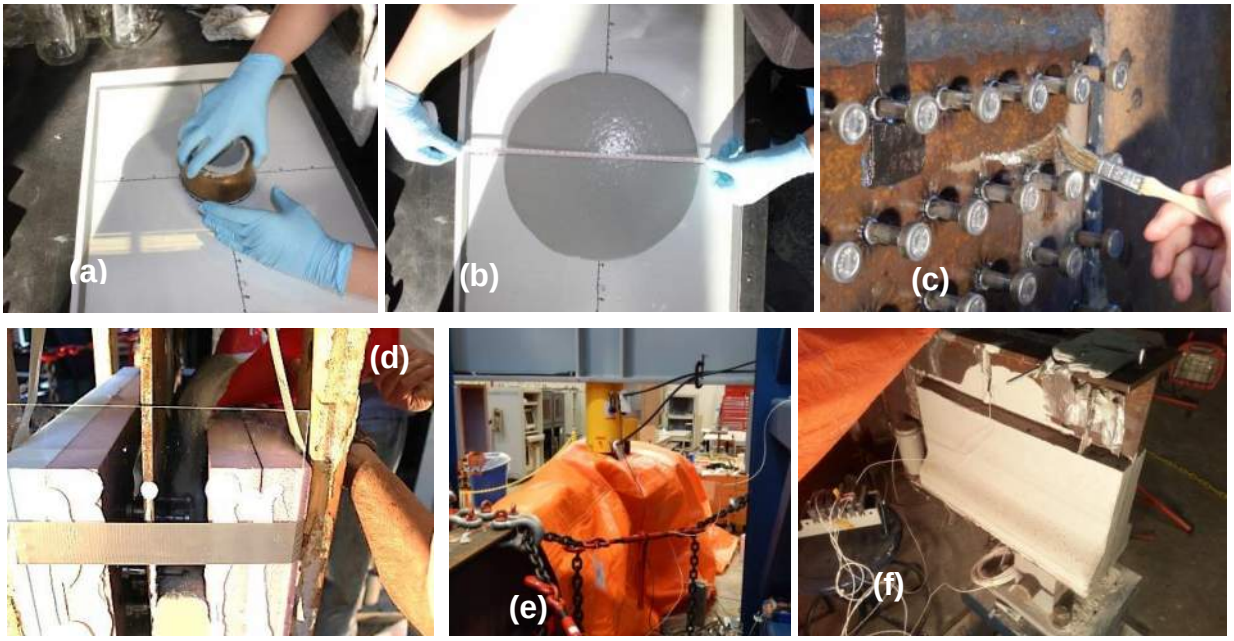

Figure 8. Casting of UHPC: (a) and (b) Spread Test of UHPC, (c) Application of Mineral Oil to Inhibit Bond to Girder, (d) Casting UHPC Panel, (e) Curing Under Insulated Blanket, and (f) Finished Panel

3-in x 6-in concrete test cylinders were cast at the time of casting the panel. Three cylinders were tested at 12 hours, and 1, 2, 3, 4, 7, and 28 days.

Figure 9a shows the time dependent compressive strength development curve. This mix achieved a compressive strength of 4 ksi in 12 hours when cured in laboratory conditions. Testing occurred four days after casting, at which point the concrete had achieved 16 ksi compressive strength. Variations in cylinder strength were noted for the batch of concrete cast with the panels. This potentially results from a temperature gradient under the blanket due to the location of the heater. Figure 9b is a representative stress-strain relation for a cylinder four days after casting. Curing temperatures of the concrete were tracked by probes cast in the concrete panel and cylinder and ambient temperatures were simultaneously read under the tarp and in the lab.

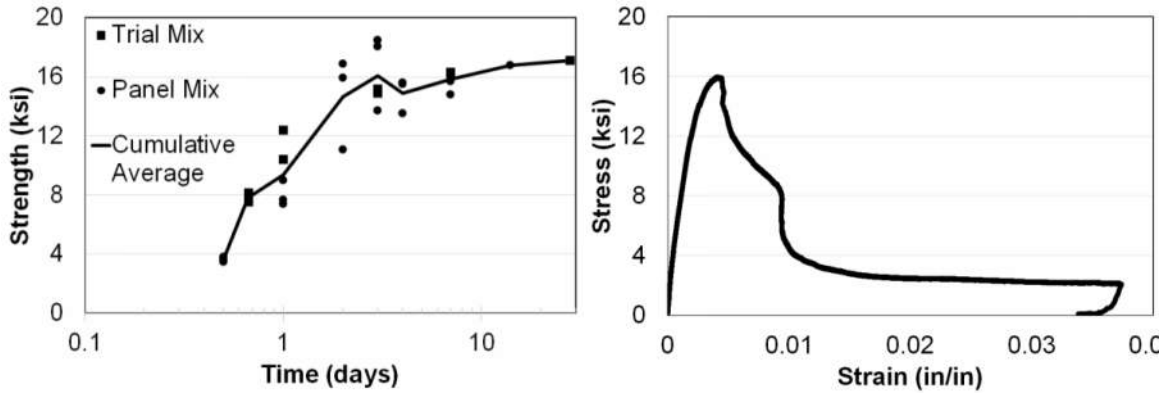

(a) (b)

Figure 9. Ductal JS-1212 (a) Strength Gain, and (b) Four Day Stress-Strain Relationship

5. Design and Construction of the Test Setup

In order to carry out the experiment, a significant investment in the capital equipment of the University of Connecticut structures laboratory was required. Figure 10a shows a schematic of the test setup. Figure 10b and 10c shows the complete test setup and the test beam. Investments were made in the form of high-capacity load cells, a stiff load frame, a high-capacity hydraulic load ram, and expansion of data acquisition capabilities.

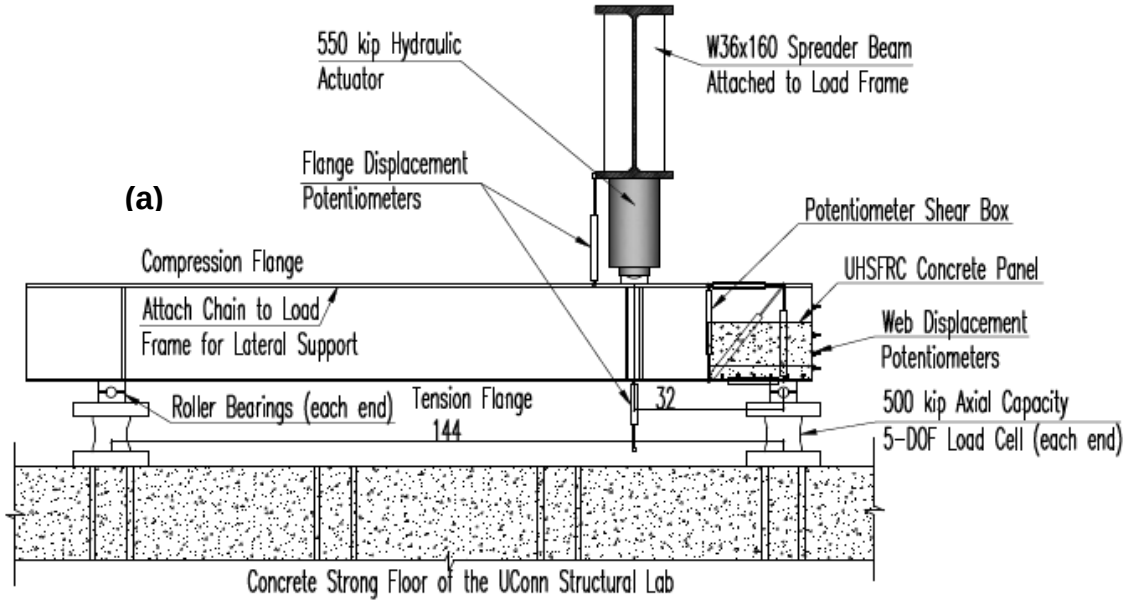

(b)

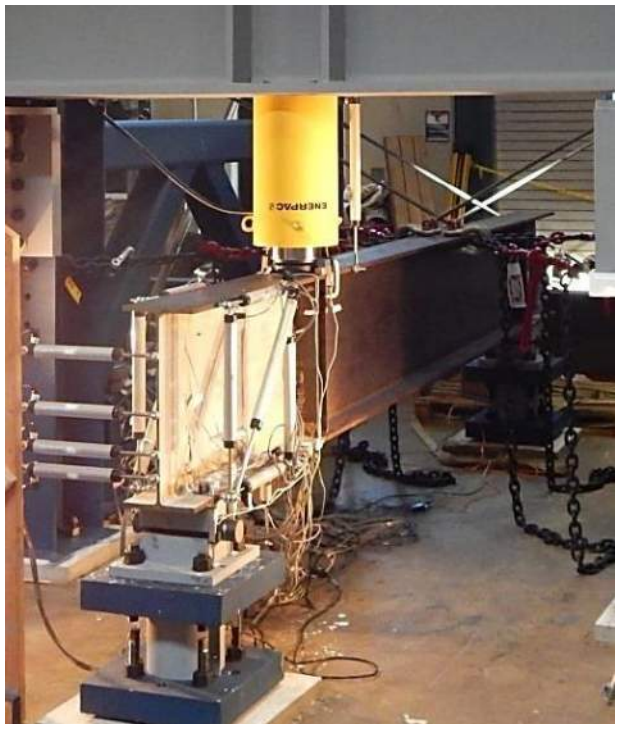

(c)

Figure 10. Test Setup. a) Sketch of the Setup and Specimen, b) Load Frame and Girder Specimen, c) Instrumented Girder

The UConn Structures Lab reaction frame had to be modified for the experiment. K-braces were added to each half of the frame to increase its lateral stiffness. Attachment holes were drilled along the four outside column faces to facilitate bolting various attachments at any height along the frame. In addition, a ten-foot W36x160 was acquired and stiffened with 1-in plate. This was bolted to the load frame with brackets manufactured from HP14x311 and acted as a spreader beam for the hydraulic actuator to be attached. The hydraulic actuator load ram purchased for these experiments was Enerpac's CLRG-25012. It has a maximum capacity of 568 kip, and a stroke of 11.8 in. Four $^{1}/_{2}$-in, Grade 100 chains were used as lateral support for the top flange to prevent lateral torsional buckling. The chain was bolted to the frame through eyebolts, secured to each side of the girder with clevises, and pretensioned with four load binders.

6. Instrumentation and Load Testing

Over 50 channels of data were collected in each test. Data was collected using an existing NI-cDAQ-9178, and two new HBM MX-1615 bridge modules. The strain reading collected through the MX-1615 is 100 times more sensitive than those collected using the NI module, providing noise levels of only ±0.5 με (microstrain). This data would be used to validate the finite element model, and act as a means of comparison to identify load-carrying mechanisms, detect damage, and analyze failure.

The load cells utilized to record bearing forces at each end of the test girder were designed, manufactured, and calibrated in house. The design used was scaled up from a smaller load cell designed from the University of Buffalo [Reinhorn and Bracci, 1992]. The axial, shear, and moment capacities of the load cell manufactured for the structures lab were ±500 kip, ±100 kip, and ±500 kip-in, respectively, to ensure linearity and repeatability. After calibration of the axial circuit, the load cells were found to have a maximum error in the range of 0.3% of full scale. This is within acceptable error toleration with commercially manufactured high-capacity load cells. The load cells on each bearing were set up to measure bearing force, longitudinal shear, and transverse moment. Axial loads were verified with a pressure transducer on the load ram to calculate applied force. The load cell is pictured in Fig. 11a. Figure 11b shows the pressure transducer, circled in red, and one of the load ram displacement potentiometers, circled in blue.

Six pairs of uniaxial strain gauges were positioned vertically along the height of the girder at the bearing, circled in red in Fig. 11c. These gauges were placed on opposite sides of the web in order to find the difference between the axial strains on the web. This difference of readings on each side of the web indicates buckling in the web as the strains began to diverge. These gauges also detected changes in bearing strains between the girders. A strain rosette, circled in blue in Fig. 11c, was included to measure maximum shear on each side of the web on the girder. Eight uniaxial strain gauges were positioned along the bottom flange to measure changes in strain in the flange. The gauges are shown with the edge of bearing as a reference in Fig. 11d.

On the repaired girder, ten additional strain gauges were added. Two were placed on opposite ends of the top row of shear studs to measure axial load indicated with arrows in Fig. 11e. These were placed to measure axial strains in the studs, aimed at

determining load distribution. Four strain gauges were placed on the face of the concrete to measure bearing and shear strains, Fig. 11f.

Four potentiometers were placed on the end of the web of the girder to measure global web displacement, and tracking buckling. These were placed to compare deformed shapes of the web after failure; they are visible in Fig. 11a. Four potentiometers measured the displacements of the top flange, bottom flange and the extension of the cylinder. Shear deformation and displacement field at the end of the beam was measure using a configuration of five potentiometers fixed to the top and bottom flange of the girder (Fig. 11a). When combined with rotation data extracted from two potentiometers on the bearing, shown circled in red in Fig. 11a, the vertical, longitudinal and shear strains of the girder can be calculated.

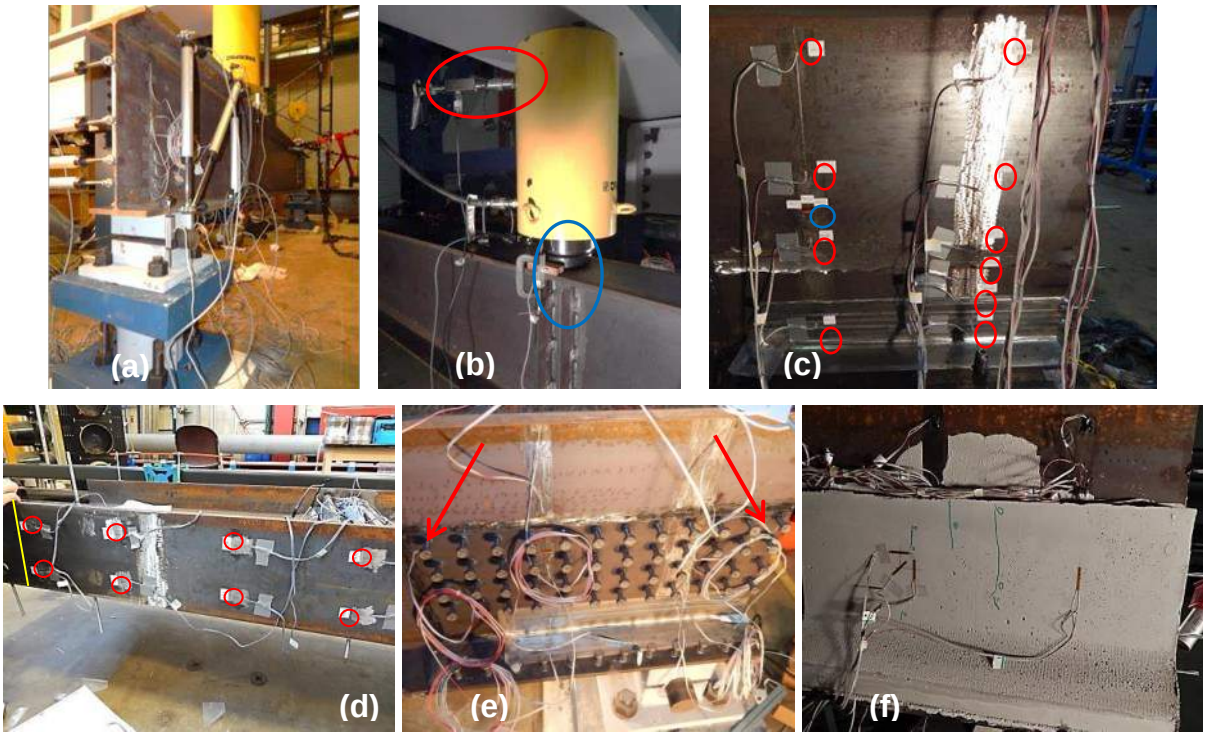

Figure 11. Instrumentation Installed Each of the Girders

7. Validation of Finite Element Models of Test Specimens

The final task of the project was to take the data collected from the experiment and use it to refine and validate the finite element model. Minor changes made to the modeling method were able to change earlier discrepancies between the model and experimental results. With this validated model, it will be able to be used to perform an in depth parametric study of many of the aspects of the repair, including panel geometry, stud number and positioning, as well as size of studs used.

RESULTS

Load-Displacement Relationships

Loading-unloading cycles of increasing magnitude were used for load testing of the three specimens. The initial loading protocol for each test was load controlled using the load ram force. Load steps for the undamaged girder used 25 kip increments, damaged loaded in 10 kip increments and the repaired in 15 kip increments. After the girders experienced failure, loading protocol shifted to displacement controlled - increasing the displacement of the bottom flange approximately 0.25 in/cycle for the undamaged and damaged girders.

Figure 12 shows the superimposed relationship of bearing force and displacement of the bottom flange at the centerline of the load ram. Ultimate bearing capacities were found to be 180 kip for the undamaged girder, 43 kip for the damaged girder, and 225 kip for the repaired girder.

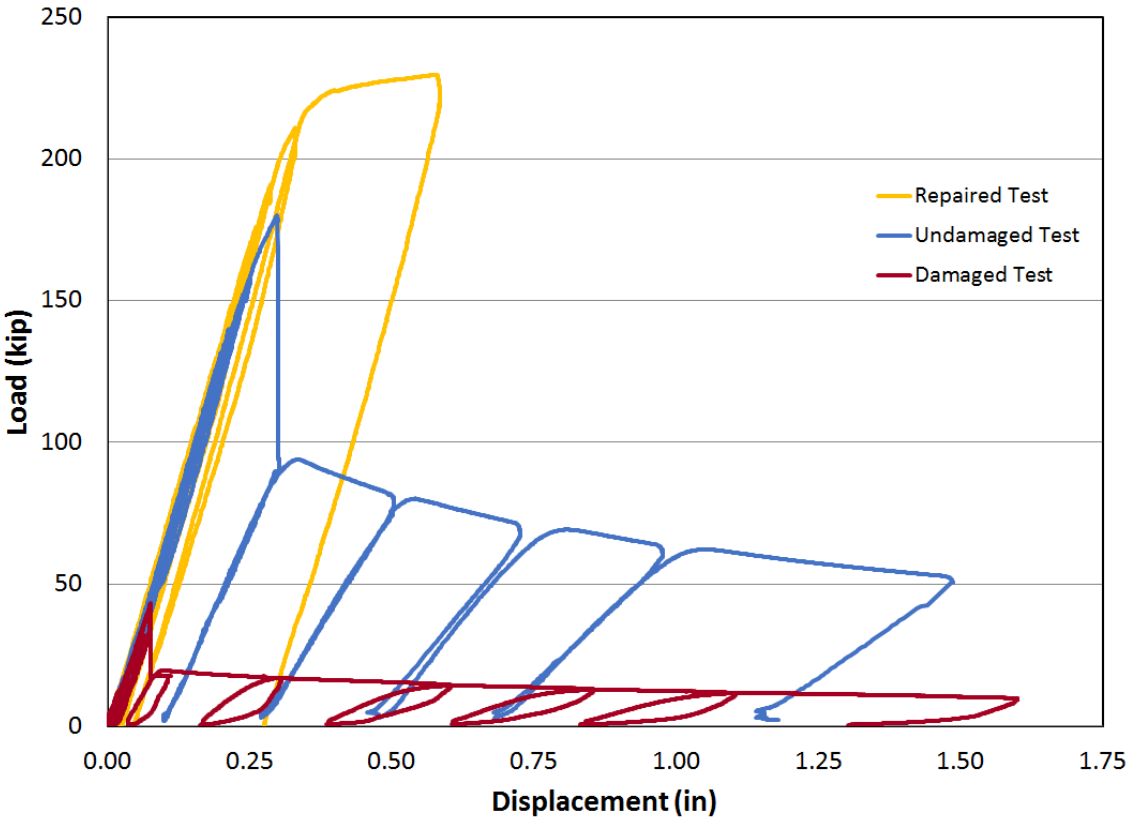

Figure 12. Load Displacement Relations for the Three Tested Girders

The stiffness of the three girders was measured as 567 kip/in. Neither the applied damage nor the UHPC repair had an effect the stiffness of the girder. Due to 66% section loss in the damaged girder, the residual capacity was only 24% of the undamaged girder. The UHPC not only restored the load bearing capacity, but exceeded the capacity of the undamaged girder by 25%. This corresponds with a 424% increase in the capacity compared to the damaged girder.

Figure 13 shows the condition of each specimen at the conclusion of the test. The undamaged girder experienced web buckling. This failure happened suddenly and caused extensive yielding on clearly defined yield lines on the entire height of the web as it deformed out of plane. The damaged girder experienced a failure due to localized web instability. Like the buckling of the undamaged girder, the damaged girder also failed suddenly and deformed out of plane; but the damage was localized in the reduced section. The intact portion of the web experienced only minor yielding at the end of the damaged section, indicated with an arrow. The repaired girder had an ultimate load 25% higher compared with the undamaged girder, and caused flexural yielding. While cracks were clearly visible through the entire test, Fig 13d, the panel remained intact. No significant out of plane movement was noted. This demonstrates the remarkable ability of the UHPC to restore bearing capacity of corroded steel girders.

Figure 13. Appearance of the Failed Girders (a) Undamaged, (b) Damaged, (c) Repaired, (d) UHPC Cracking

Strains and Deformations

Axial strains in the reduced section of the damaged girder showed a 400% increase when compared to axial strains in the undamaged girder at similar loads. Axial strain in the reduced portion of the damaged girder prior to failure was -1670 με, while at similar load, the same gauge in the undamaged girder only read -336 με. The gauges also found bearing strains in the reduced section of the repaired girder to be only 6% of the

strain in the undamaged girder, despite the loss of section. Axial strain at the bottom of the web prior to buckling of the web of the undamaged girder read -3347 με. The same load on the repaired section induced an axial strain of -202 με, despite being on a thinner section of web. Strain gauges on the bottom flange were able to confirm that section loss did not affect the development of flexural strains. Stain rate was seen to increase in the repaired method by an average of 50%. This is due to the concrete and bottom flange acting as a composite member to carry the load. Increase in the bottom flange strain was more severe at the end of the panel, and lessened toward the bearing.

Shear strains were calculated from the displacements read in the box of potentiometers at the girder end. The shear straining rate for the undamaged girder was found to be -20 με/kip. Shear straining rate of the beam end was found to increase 50% in the damaged girder, increasing to -30 με/kip due to section loss. The UHPC repair made the end of the girder stiffer, decreasing the shear strain rate 50% compared to the undamaged girder, only -10 με/kip.

Studs at the bearing were found to have a lower strain rate compared to those away from the bearing. This suggests that the studs away from the bearing have higher utilization. This could prove to be useful if height of corrosion at the bearing is sufficiently large that the majority of studs need to be placed at the end of the panel. Bearing strains in the concrete were found to only increase at a rate around 20% that of steel. It is logical that concrete strain is less as it is not bonded to the steel girder and the outside face of the concrete should be less strained than the concrete nearer the girder due to shear lag.

Finite Element Simulation Results

In the final models steel material for the girder was defined as a piecewise linear plastic material capable to account for damage progression. The concrete material was modeled using the Karagozian and Case Concrete Model - Release III, a rigorous model capable of capturing concrete failure in compression and tension. Stud connection was modeled by node sharing between the stud and mate material. This assumes a perfect bond to the concrete or a weld to the steel. Further investigation of the stud – concrete interaction has been studied separately using the finite element code Abaqus. The interested reader is referred to the technical report by Roy et al., 2015 for detailed information. No bond was assumed between the steel girder and the concrete; instead a basic contact algorithm was used. Loading applied was displacement based, to ensure the model was able to capture post-failure ductility.

The finite element model was found to predict all critical aspects of the large scale tests. Failure loads, and displacements as well as post-failure loads and ductility were found to be extremely accurate. Figure 14 shows the finite element load displacement relations superimposed on the large scale test data. Load carrying mechanisms were also found to be correctly predicted, from level of bearing strain in the web of the girder, to the increase of flange strains under the UHPC panel due to composite action. Failure mechanisms and failed shapes were also well predicted. Figure 15 shows the deformed shapes for each of the specimens. Magenta on the concrete panel in Fig. 15c

indicates predicted cracking, all of which were observed in the large scale test seen in Fig. 13d.

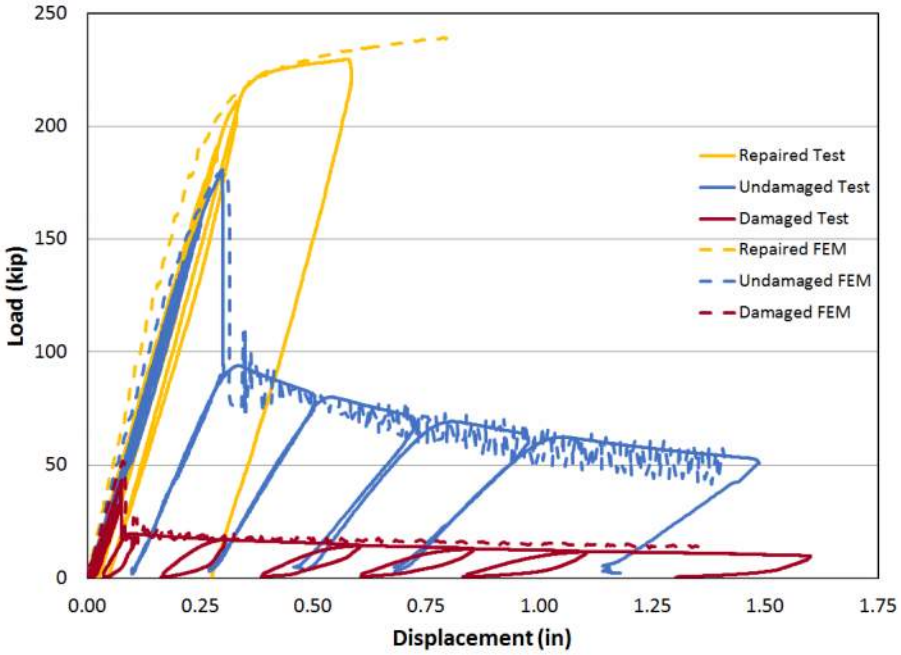

Figure 14. Load Displacement Relations of FEA Compared with Large Scale Experiment

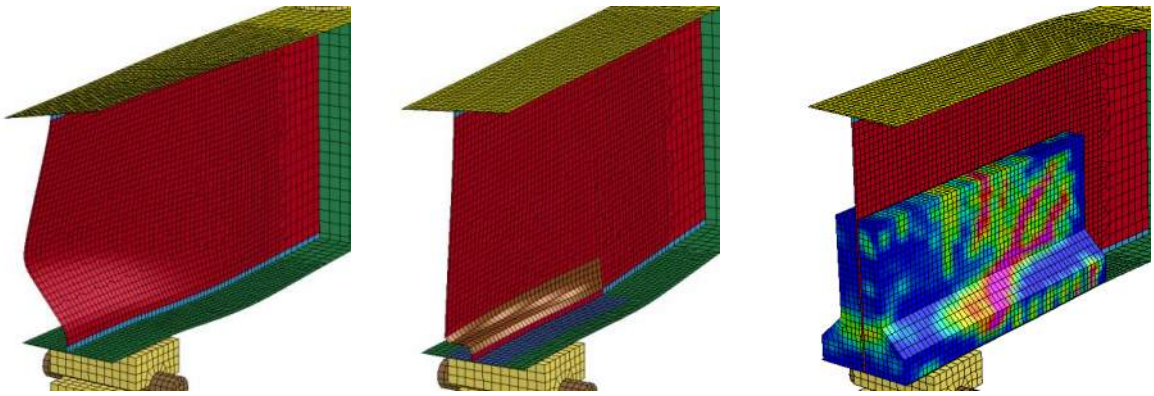

(a) (b) (c)

Figure 15. Deformation of the FEA Girders, (a) Undamaged, (b) Damaged, (c) Repaired

OBSERVATIONS AND CONCLUSIONS

1. Section loss attributed to corrosion damage at bridge bearing can severely impact the bearing capacity of the girder. Section loss of 66% was found to decrease the bearing capacity 76%.
2. The repair was successful in restoring the bearing capacity of damaged girder. *The capacity of the repaired girder exceeded the capacity of undamaged girder by approximately 25%.* This proved the effectiveness of the repair method using UHPC.

3. The repair method prevented the failure of the girder at the bearing. Only very fine cracks formed on the UHPC panels. Instead, the beam began experiencing extensive flexural yielding converting the sudden failure into a ductile failure mode.
4. The UHPC mix was highly flowable and self-consolidating. It made it easy to cast in the form. It fully incased embossed studs without any disaggregation.
5. When cured at an average temperature of 72° F, compressive strengths of 4 ksi in 12 hours, and 16 ksi in four days were achieved.
6. Stiffness of the system was unaffected between the three tests.
7. A high level of axial strain was noted to concentrate in the reduced section of the damaged girder. The addition of the concrete drastically lowered this strain demonstrating the successful transfer of loads from the steel web to the UHPC panels.
8. The addition of the concrete panels increased the longitudinal strains in the bottom flange. This demonstrates that the concrete panels and the bottom flange formed a composite section.
9. The shear studs located far from the bearing had larger axial strains compared to the ones placed at the proximity of the bearing. This suggests that having fewer studs at the bearing, due to corrosion further up the height, may not be overly detrimental.
10. Finite element model provided reliable predictions of load-deformation relationship and strains. The model also displayed correct failure modes, deformed shapes, and cracking pattern.
11. Finite element model has the ability to serve as a powerful tool in development of design standards for UHPC repair of corrosion damaged girders.

1 Introduction

1.1 INTRODUCTION

In his State of the Union address given February 12, 2013, President Obama articulated the need to repair the aging American infrastructure, particularly our bridges. The President urged,

"America's energy sector is just one part of an aging infrastructure badly in need of repair. Ask any CEO where they'd rather locate and hire, a country with deteriorating roads and bridges or one with high-speed rail and Internet, high-tech schools, self-healing power grids. The CEO of Siemens America -- a company that brought hundreds of new jobs to North Carolina -- has said that if we upgrade our infrastructure, they'll bring even more jobs. And that's the attitude of a lot of companies all around the world. And I know you want these job-creating projects in your district; I've seen all those ribbon- cuttings. So, tonight, I propose a ``Fix-It-First'' program to put people to work as soon as possible on our most urgent repairs, like the nearly 70,000 structurally deficient bridges across the country." (NPR, 2013)

The condition of highway infrastructure in the State of Connecticut and across the United States has been deteriorating for years. The average age of bridges in the US is approximately 42 years (ASCE, 2014). The design life of most bridges is only 50 years. The American Society of Civil Engineers (ASCE) estimates that it would cost roughly $76 billion to repair the 66,749 structurally deficient bridges in the country (ASCE, 2014). The State of Connecticut currently maintains 4,218 bridges. 2,221 of these bridges utilize girder super structures (FHWA, 2014). A total of 406 of the State's bridges are structurally deficient (Davis & Goldberg, 2013). Figure 1.1 shows the percentage of structurally deficient bridges in the state from 1992-2012 (Kauffman, 2013). Immediate attention is needed to devise repair strategies that will help reduce the cost to repair these bridges to make future repairs more viable.

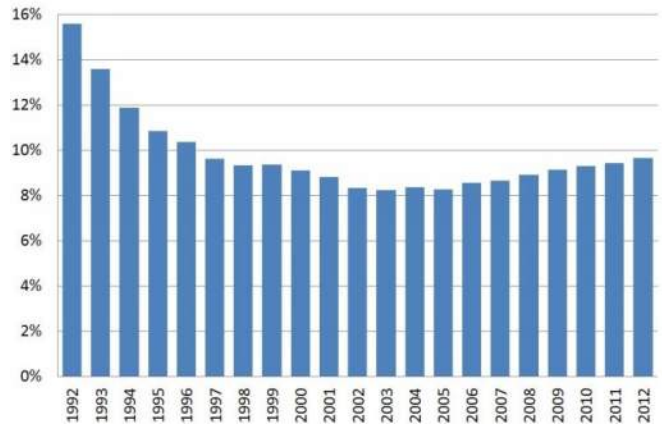

Figure 1.1 Percentage of Structurally Deficient Bridges in the State of Connecticut

1.2 CORROSION PROBLEM AND CONVENTIONAL REPAIR METHODS

Figure 1.2 Typical End Corrosion in Steel Girder Ends (Photos: Michael P. Culmo)

Bridges are some of the most critical links in the national highway system and some of the most vulnerable to failure. Corrosion at bearing ends is a prevalent problem in steel girders, as seen in Figure 1.2. This is caused when water, which carries chemicals and chlorides from the roadway, leaks through deck joints and causes section loss at the bearing. This corrosion damage may severely reduce load carrying capacity of girder ends and could lead to structural deficiency, a posted load rating, or ultimately failure.

The conventional method of restoring the original capacity of corrosion damaged girders involves cleaning of damaged area and adding steel cover plates or other shapes. This method has several drawbacks, among which include:

Lead Paint: Due to the age of many structures needing repair, the paint is likely lead based. Therefore, paint removal during preparation for rehabilitation requires

extensive abatement protocols to prevent lead contamination to the surrounding environment.

Preparation: Preparation of the girder surface is required for the addition of steel plates or shapes. This requires sanding or grinding when welding, or drilling holes for bolted additions. In extreme cases, cutting and removing of the corroded plates may be necessary prior to the application of the repair.

Jacking: To achieve the nearly stress-free condition required for the process of repairing with steel, removal of the load from the girder end is required. This is performed by jacking the entire superstructure. This can account for up to 70% of the project cost.

Lane Closure: Lanes over the girder being rehabilitated may have to be temporarily closed while the repair work is in progress.

Repair Time: The rehabilitation process may be significantly time consuming.

Service after Repair: Conventional repair designs do not inhibit future corrosion of the base metal. The repair itself is also vulnerable to corrosion and might need to be reinstated after several years of use.

Custom Design Process: The rehabilitation design is specific to each project and is based on the severity and pattern of the corrosion as well as the geometry of girder ends.

(a) (b)

Figure 1.3 Traditional Rehabilitation with Steel Shapes

(a) Repair with Angle Shapes, (b) Repair with Steel Plate

1.3 PROPOSED REPAIR TECHNIQUE

Innovative designs for bridge rehabilitation are necessary to lower the cost of corrosion damage rehabilitation. Such techniques need to be structurally effective, durable, and easy to implement while minimizing interruptions to traffic and increasing work zone safety.

One possible method involves the use of Ultra-High Performance Concrete (UHPC) encasing the sides of the corroded web. UHPC is a low porosity cement-based fiber reinforced composite with compressive strengths in excess of 22 ksi and excellent durability properties. UHPC differs from Ultra-High Strength Concrete (UHSC) by the addition of steel fibers that provide required ductility, toughness, and energy dissipation through micro-crack bridging.

The UHPC panels are mechanically attached to the member using steel shear studs shot to the undamaged portions of web and flange. This repair method has the potential to address multiple problems associated with traditional rehabilitation techniques for corrosion. The major advantages of this repair concept are as follows:

Minimal Surface Preparation: Paint removal and surface preparation are not required for this rehabilitation method as high-strength concrete may be cast over the painted surfaces. The shear studs can be welded over existing paint. This significantly reduces the time and cost of preparation by eliminating the need for complex lead abatement procedures. No preparation is needed beyond the removal of loose material with hand tools.

No Jacking Required: The rehabilitation can be applied under in-situ stress conditions.

Reduced Need of Lane Closure: Minimal road closure would be required if fast setting concrete is used.

Reduced Construction Time: The construction process is straightforward and simple. This enables the accelerated application of repairs.

Ease of Application: UHPC is self-consolidating and pumpable, making it ideal for application in complex geometries and tight spaces common around bridge bearings and diaphragms.

Superior Durability: UHPC is a highly durable material due to particle packing and low matrix porosity, reducing the ingress of ionic aggressors responsible for corrosion. UHPC panels may protect the original steel from further corrosion.

Diversity of Use: Standard designs may be developed for typical girder types. This eliminates the need for project specific repair design.

1.4 REVIEW OF RELATED RESEARCH

Little research has been performed on this type of composite girder system. The concept of concrete-encased steel beams was originally proposed by Elnashai, et al. as a novel beam-column for use in buildings (Elnashai, et al., 1991). Because the application was intended for building columns, standard wide flange sections were used. A small cage of rebar was included between the flanges and was welded to the wide flange section, seen in Figure 1.4a. Nakamura extended this idea to bridge plate girders and led much of the research on the performance in shear and bending (Nakamura, et al., 2002) (Nakamura, & Narita, 2003). This research was focused on developing a two-span continuous composite steel-concrete plate girder which maintained a constant height, seen in Figure 1.4b. Reinforcement was welded between flanges and stiffeners in panels near the middle bearing to resist the increased shear and hogging moments. This would typically require adding haunches to the plate girder. They noted that this method could also be used to rehabilitate steel girders which have experienced buckling deformation in their flanges (Hyashi, et al., 2003). Research done by He has focused on a similar design that utilizes a steel girder with an offset, corrugated web encased with concrete on only one side of the web (He, et al., 2012a) (He, et al., 2012b). This concept is shown in Figure 1.4c. Shear performance was increased due to the concrete and the corrugation of the steel web. Concrete was held to the girder with a combination of rebar and steel shear studs.

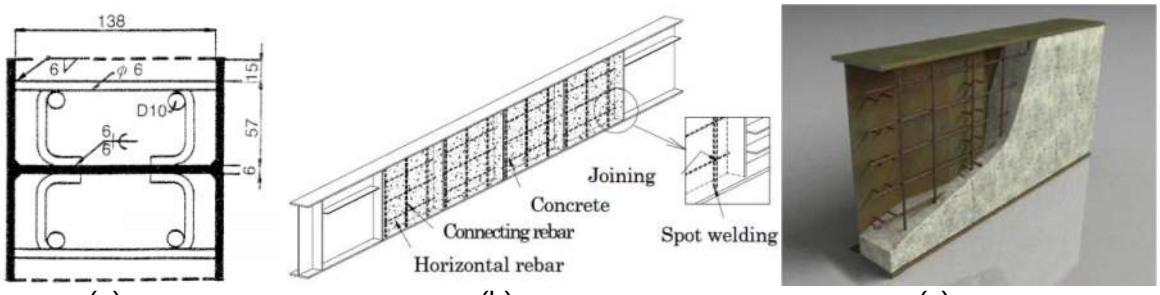

(a) (b) (c)

Figure 1.4 Progression of Concrete Encasement of Steel Beam/Girders

(a) (Elnashai, et al., 1991), (b) (Nakamura, et al., 2002), (c) (He, et al., 2012a)

1.5 OBJECTIVE AND SCOPE

This project was divided into two sections, an experimental phase, and an analytical phase.

1.5.1 Experimental Study

A series of three tests were run in the University of Connecticut's (UCONN) Structures Laboratory on half-scale rolled girders to act as a proof of concept of a repair method utilizing UHPC. One girder was undamaged, to determine baseline bearing capacity. A second girder had section loss at the bearing to simulate severe corrosion damage. This isolated the effect of corrosion on bearing capacity. A third girder had the same level and pattern of simulated corrosion damage, but included a repair with UHPC. This determined the capacity restored by the repair technique. Each of these tests was meticulously instrumented to record data on force, strain, and displacement distributions on the girders while they were tested. This data was used to create a finite element model for use in an analytical study.

1.5.2 Analytical Study

The finite element model created from the experimental study was used to run full-scale simulations of rolled and plate girders. This was done to verify the performance of eight different repair methods on three configurations of bridge girders. All of the girders had extreme levels of corrosion damage which would be realistic for bridge girders rated as structurally deficient.

1.6 LAYOUT OF DOCUMENT

This report will first detail the design and setup of the experiment in Chapter Two. Chapter Three provides a full description of all the instrumentation utilized in the course of the experiment. Chapter Four details material testing performed. Chapter Five presents the results and observations from the three large-scale tests. Chapter Six describes the construction of the finite element model, comparison of the model results to the large-scale tests, and the performance of the full-scale FEA. The report is summarized and concluded in Chapter Seven.

2 Design and Construction of Large-Scale Test

2.1 INTRODUCTION

This chapter describes the design and setup of the large-scale experiments performed in the UCONN Structures Lab. First, the objective and design of the test will be explained, followed by the discussion about the construction of the test frame for the experiment. Then, the design of the girder specimens will be presented. This will include the manufacturing performed to the girders to introduce the corrosion damage, as well as the steps performed in the application of the repair. Afterwards, secondary components needed for the test will be discussed, including bracing and bearings used. The section will conclude with loading protocols.

2.2 OBJECTIVE

The objectives of the large-scale test are to: 1) determine the loss in bearing capacity associated with severe corrosion at the ends of the steel bridge girders; 2) perform a proof of concept on a novel repair technique utilizing UHPC to restore the intact capacity; and 3) investigate the constructability of this repair technique. To do this, three bridge girder specimens were investigated: 1) an undamaged girder to determine baseline capacity; 2) a girder with a realistic level of section loss associated with corrosion damage; and 3) a girder with the same level of damage as the second girder that is retrofitted using the proposed technique. This will enable the determination of the capacity lost due to corrosion damage and the ability of the repair technique to restore capacity.

2.3 TEST SETUP DESIGN

To stay within the force limitations of the Structures Lab, the test was designed to be half-scale. Figure 2.1 shows a schematic of the test setup. The three girders used are W21x55 rolled girders. The girder being tested sits on a pair of roller bearings with 12-ft spacing. The 12-ft span allows each end of the span to be secured to the floor of the Structures Lab. The Structures Lab floor utilizes a cluster of four $1^1/_8$-in diameter threaded anchor holes in an 8-in square pattern. These anchor points thread into steel beams under the 4-ft thick strong floor. These clusters provide a way to secure large structural members to the floor and uplift resistance. These clusters are arranged in a 4-ft square pattern throughout the lab.

Loading is applied via a single point load positioned at approximately $^2/_9$ span. This method of loading is used because bearing and shear failures are caused by wheel loads from trucks close to the bearing. Purely uniform loads result in yielding in bending rather than crippling at the bearing. The end of the girder on the bearing nearer the applied load is referred to as the studied end. A large hydraulic load ram attached to a stiff load frame applies the loading. Web stiffeners are provided under the hydraulic load ram and at the non-studied bearing to reduce the probability of web buckling. With the positioning of the load and the locations of the stiffeners, failure occurs at the studied end of the girder.

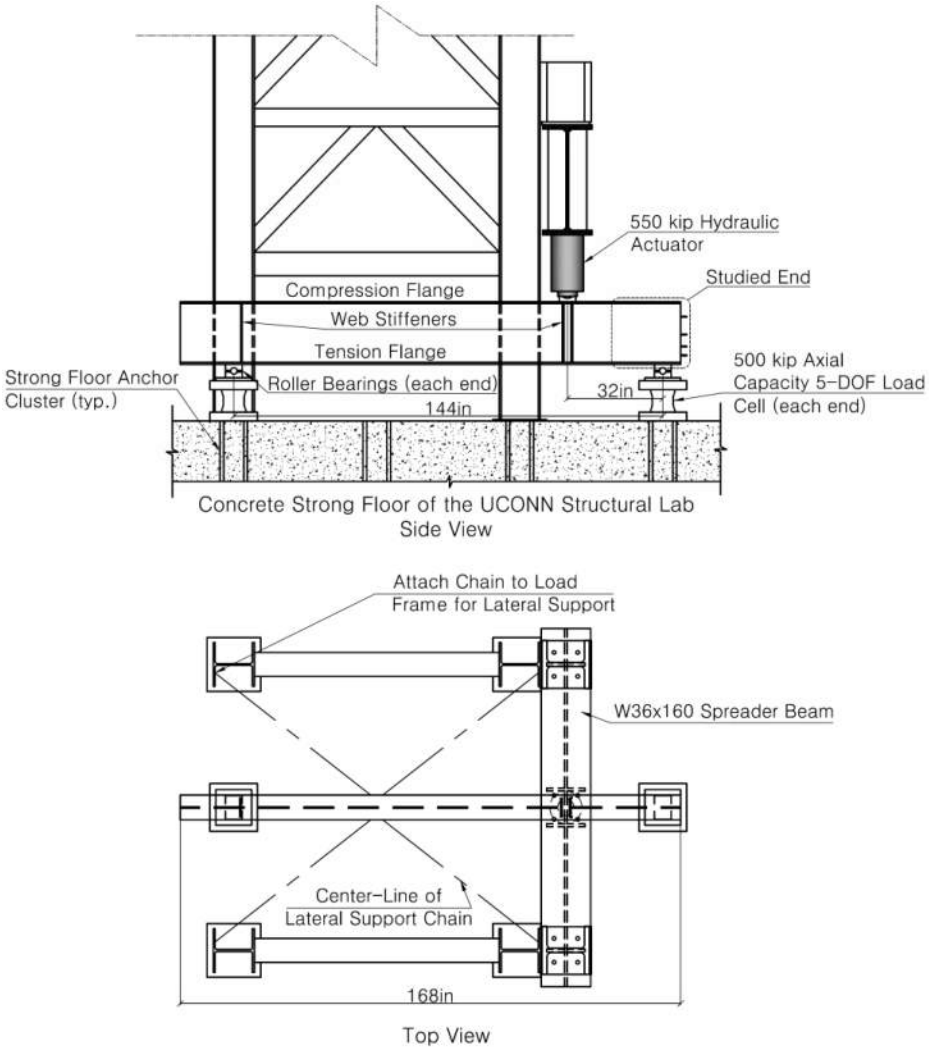

Figure 2.1 Sketch of the Setup of the Large-Scale Experiment

The total length of the rolled girders is 14 ft to allow the girder to extend past each bearing. The size, rotational point, and termination of the girder past the studied end are designed to scale of an in-service bridge. Each bearing is seated on a high-capacity, multi-degree of freedom load cell. The load cells are seated on a level steel seat plate which was grouted to provide a level and firm base.

The leveling and grouting of the seat plate for the load cells is shown in Figure 2.2. The plates were raised about 1 in above the structures lab floor, balanced on a structural nut. This allowed the seat plate to be leveled by adjusting the tension in the four anchor rods. Foam pipe insulation was included around the anchor holes to prevent grout from filling the anchor points. The surface of the Structures Lab floor was coated in oil to inhibit bonding of the grout to the floor. The gap present allowed grout to flow beneath the plate and ensured a solid and level base for the load cells to sit on.

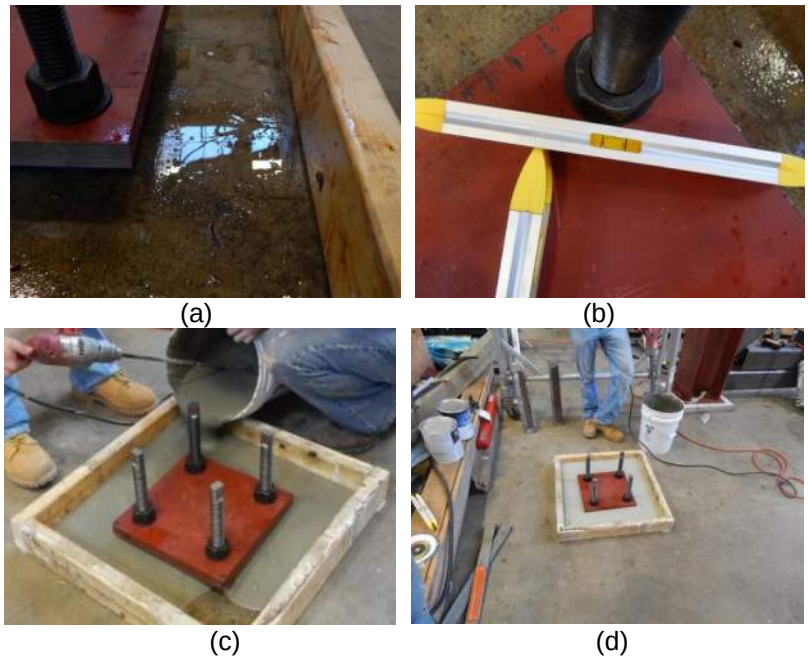

(a) (b)

(c) (d)

Figure 2.2 Leveling and Grouting the Base Plate for Load Cells

(a) Gap Present Between the Leveling Plate and Structures Lab Floor, (b) Leveling the Plate by Tensioning the Floor Bolts, (c) Casting the Grout, and (d) the Finished Pour

To carry out the experiment, significant investments were needed in the capital equipment of the UConn Structures Laboratory. Major investments to the lab were required for a stiff load frame, a high-capacity hydraulic load ram, a flexible expansion of data acquisition capabilities, and high-capacity multi-degree-of-freedom (DOF) load cells.

2.4 CONSTRUCTION OF THE LOAD FRAME

The UCONN Structures Lab reaction frame had to be modified for the experiment. The existing frame was constructed from four 20-ft tall HP14×89 columns. The load frame before any modification can be seen in Figure 2.3a. The frame was originally intended to apply small axial loads on tall specimens. Lateral stiffness of the frame needed to be increased to ensure distribution of load to the anchor clusters. K-braces were added to each half of the frame. These K-braces were constructed from lateral HSS8×8×$^1/_2$ and inclined HSS7$^1/_2$×7$^1/_2$×$^1/_2$. K-braces were welded to the existing flanges of the columns. The frame after the installation of the braces can be seen in Figure 2.3b.

To plumb the frame and guarantee a solid base, the frame was grouted in place. This was done in a similar method to the load cell seat plates. To do this, the frame

was elevated, and seated on three structural bolts under each column. Foam pipe insulation was included around the anchor holes to prevent grout from filling the anchor points. Columns were leveled through varying the tension in the anchor rods. The vertical alignment of each column was assured using a total station, Figure 2.3c. This verified that the lateral variance of the column along its height was less than 5 seconds, or 0.0014°. Oil was sprayed on the Structures Lab floor and frame base to minimize bonding between the grout and facilitate future removal. With the frame leveled and the surfaces oiled, the grout was poured. The grout established a firm base for the frame to bear on.

Holes were drilled in the outer flanges of the four columns to facilitate bolting various attachments to the frame. The load frame had $^{7}/_{8}$-in bolt holes in an existing 5 $^{3}/_{4}$ in × 4 in pattern on the flanges at the top of the columns. This pattern was extended down the exterior flange of each column until they reached the bottom 2 ft of the column. The total station was first used to mark the top and bottom hole location for each line of bolts. A chalk line was then snapped to mark the line of holes. A marker was then used to mark 4-in increments along the chalk line to mark the centers of the holes. A random selection of these marks was sited using the total station to assure they were properly located. Figure 2.3d shows the chalk line and two center marks for the holes indicated with arrows. The red laser point, which is visible in the figure, is the light from the total station used to verify the point location. No hole measured had a variance of greater than $^{3}/_{32}$ in vertically or horizontally. A center punch was then used on the center marks. Because the holes needed to be drilled on a vertical surface, a magnetic drill was used. This allowed the drill to be secured to the column flange after being positioned using the Structures Lab's bridge crane, Figure 2.3e. Two drill bits were used to drill the holes. First, a center drill bit was used to align the drill and enlarge the center punch mark. This ensured the larger drill bit would not jump off the center of the hole. After the center drill bit, the finished $^{15}/_{16}$ in hole was drilled with a larger bit. The two drill bits used to make the holes are visible in Figure 2.3f.

With all holes drilled on the columns, patchwork on the frame could begin. Figure 2.3g shows some of the holes and excess plate which had to be repaired. The holes were patched by welding in plates of steel. The excess steel was removed using a cutting wheel. After patching of these holes, the frame was primed with a rust inhibiting primer and painted. Figure 2.3h shows the frame after it has been primed and while it was in the process of being painted.

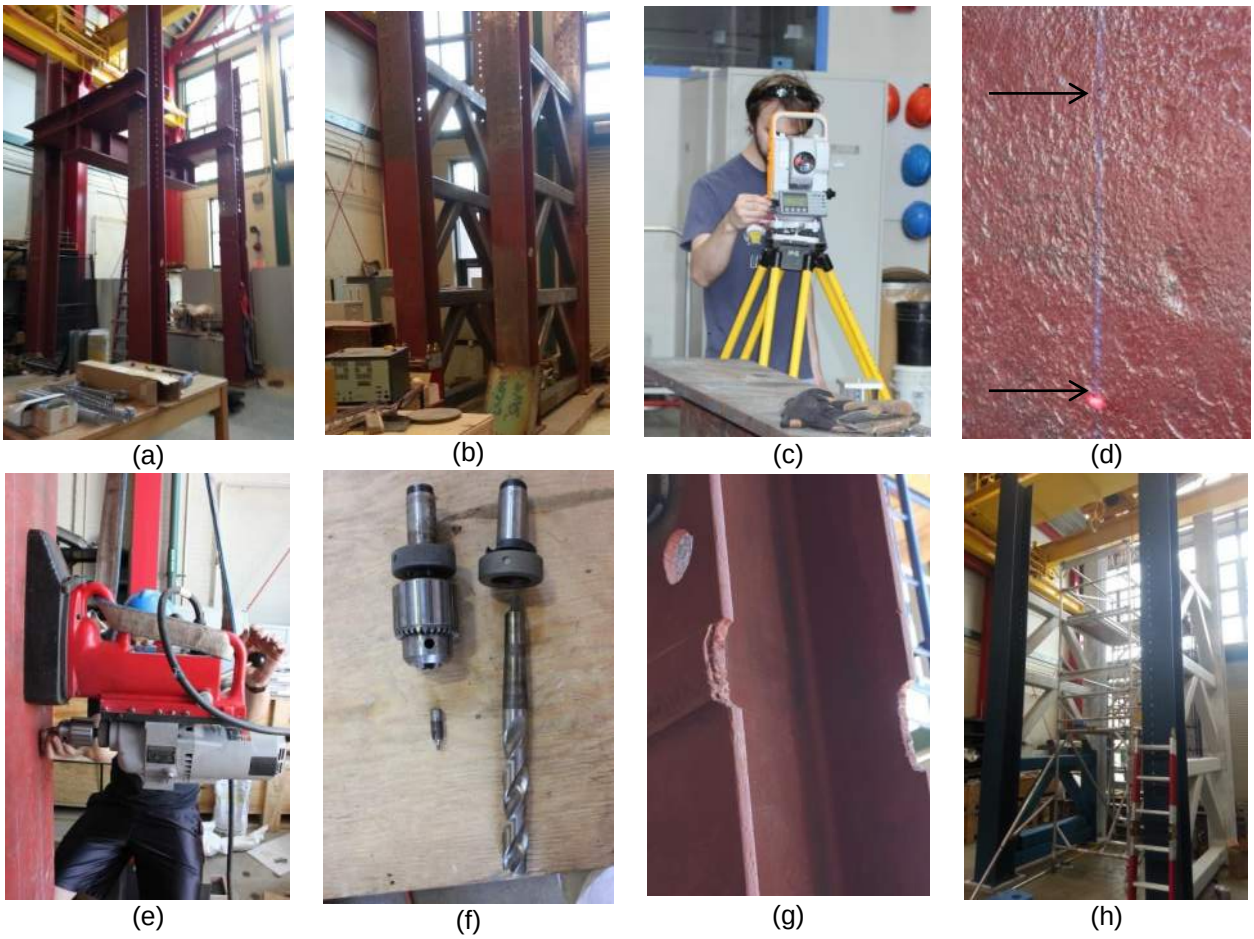

Figure 2.3 Modification of the Structures Lab Load Frame

(a) Unmodified Original Load Frame, (b) Load Frame with Added K-Brace Stiffeners, (c) Total Station Used for Vertical Alignment and Hole Alignment, (d) Chalk Line with Two Points Marked for Drilling, (e) Positioning and Fixing the Magnetic Drill, (f) Center Drill Bit and $^{15}/_{16}$ in Hole Drill Bit, (g) Holes Needing Patching and Excess Steel Needed to be Removed, (h) Primed Load Frame Being Painted

A ten-foot W36×160 was acquired for use as a spreader beam between the two halves of the frame, Figure 2.4a. The top and bottom flanges of the spreader beam were drilled to maintain the same anchor cluster pattern and spacing. This allowed for the beam to be aligned with the anchor points between the frame halves. An additional series of holes were drilled in the center of the spreader beam's bottom flange to allow the attachment of the hydraulic load ram. Figure 2.4b shows the finished holes in the spreader beam. Threaded holes were drilled into the tops of the connection brackets so that eye bolts could be fastened, allowing the bridge crane to be used to position the spreader beam on the frame. A 1-in plate was welded to the web and flanges to stiffen the web in both the center of the beam and at attachment points to the frame. Once completed, the spreader beam was primed with a rust inhibiting primer and painted. The finished spreader beam can be seen in Figure 2.4c.

The spreader beam was bolted to the load frame with brackets manufactured from a W14×311 shape. This W-shape was 20 in long, and had a 1 in plate welded to one end. The anchor cluster pattern was drilled into the end plate and the frame flange pattern was drilled into one of the flanges. Attachment holes to the frame were $^{3}/_{16}$ in oversize to facilitate bolting to the frame. This would allow the brackets to be attached to the spreader beam, and the spreader beam to subsequently be located at any height along the frame. Figure 2.4d shows the bracket. To assemble the frame, the load ram was first secured to the spreader beam, while the spreader beam was held by the bridge crane, Figure 2.4e. The spreader beam and load ram were then placed on the bottom brackets and loosely bolted in place. These were kept loose to facilitate bolting to the frame. The top brackets were then added and firmly bolted. $1^{1}/_{8}$-7 threaded rod was used to bolt the spreader beam to the brackets. Figure 2.4f shows the assembly. The spreader beam assembly was then positioned with the bridge crane and the bottom brackets were bolted to the frame. With the bottom brackets bolted, the holes in the top bracket were aligned and the top bracket secured, Figure 2.4g. Standard $^{7}/_{8}$ in structural bolts were used. Lock washers were used to ensure no loosening of the nut would occur during the test. Oversize washers were used to span the oversize holes. Figure 2.4h shows the bolt assembly used. Figure 2.4i shows the completed load frame.

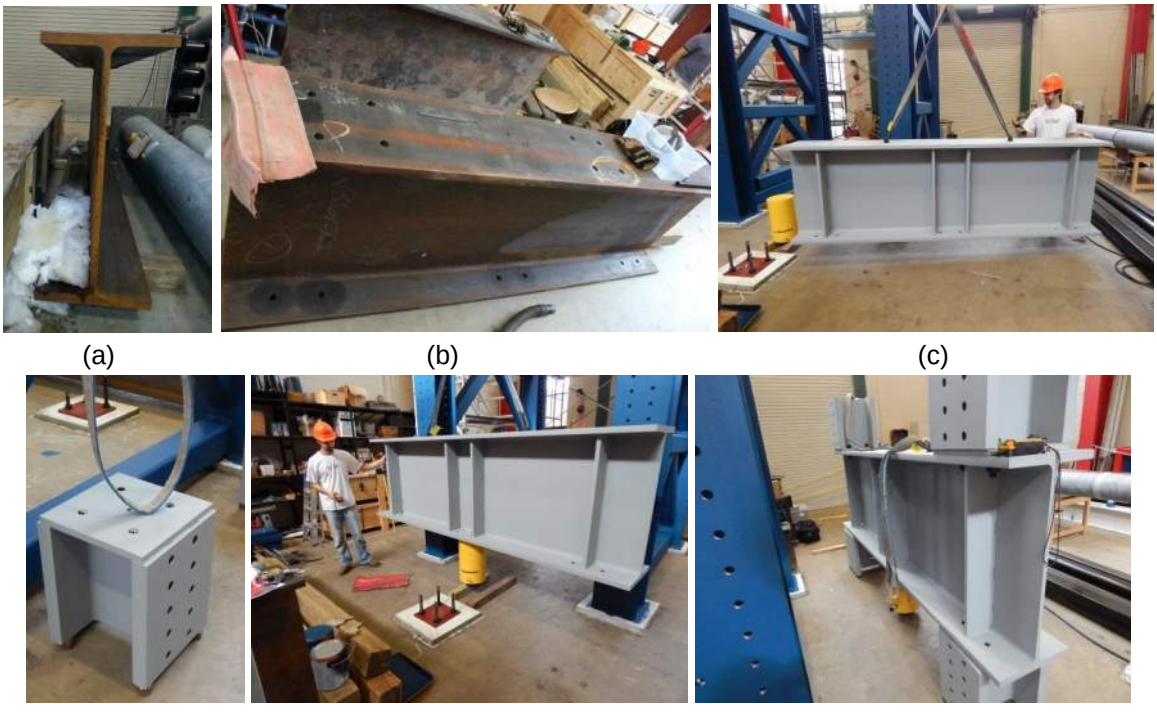

(a) (b) (c)

(d) (e) (f)

(g) (h) (i)

Figure 2.4 Spreader Beam and Bracket and Final Load Frame

(a) Unmodified 10-ft W36×160 Spreader Beam, (b) Spreader Beam after Holes Drilled, (c) Stiffened and Painted Spreader Beam, (d) Spreader Beam Bracket, (e) Spreader Beam with Load Ram Mounted, (f) Spreader Beam and Bracket Assembly, (g) Securing the Spreader Beam to the Frame, (h) Nut, Bolt and Washers Used to Secure the Brackets to the Frame, (i) Completed Load Frame

2.5 GIRDER SPECIMENS

To stay within the capacity of the UCONN Structures Lab, it was decided to run the proof of concept test at half-scale. Specimens are rolled girders without bearing stiffeners. Virtually all bridge girders have bearing stiffeners at their ends. However, preliminary analysis showed that even without the bearing stiffeners, the proposed repair method was able to rehabilitate corrosion damage.

The girder selected is a rolled W21×55. This shape is half-scale of a structurally deficient bridge in Waterford, which utilizes W36x160 girders (Bridge No. 00352, 1955). Both the W36×160 and W21×55 have web slenderness ratios (D/t_w) of 55.5. This ratio is critical for proper scale as it directly affects web buckling load. Studs are not detailed on the flanges of the design bridge to create a composite structure with the deck. This justifies the exclusion of a concrete deck in the proof of concept.

A preliminary finite element analysis (FEA) estimated that the bearing capacity of the W21×55 to be 225 kip. Given the setup in Figure 2.1, the load frame must resist a 300 kip force. Spreading this 300 kip reaction between two of the anchor clusters results in 150 kip reactions in each cluster. The capacity of the anchor clusters was unknown. Each anchor cluster uses four $1^1/_8$ in threaded rods. A capacity of 200 kip per cluster is conservatively calculated based on 50 ksi yield strength for the anchor rods. The W21×55 is therefore considered an ideal member to test.

Modifications were made to all three girders. To assure buckling failure at the studied end, web stiffeners were added to the girder. Multiple ½-in thick stiffeners were

added at the loading point and at the bearing not being tested. The non-studied end had a single stiffener welded at the inside edge of the bearing. The center loading point had a pair of stiffeners spaced 3 in apart. Figure 2.5a shows the location of the stiffeners.

Holes for attaching the specimen to the bearings and to the lateral restraint system were also added. 1-in diameter holes were drilled in the bottom flange at the center of each bearing. These holes were centered on the web, spaced $4^{7}/_{8}$ in. Four $1^{3}/_{8}$ in holes were drilled in the top flange centered 4 ft from the non-studied end. This placed the pattern in the center of the load frame and was used to attach the clevises in the lateral restraint system. Holes drilled in all girders are shown in Figure 2.5a.

Ten lengths of $^{1}/_{4}$-20 threaded rod were welded to the top and bottom flange to attach potentiometers. Four lengths of the same size rod were added along the height of the web. Rods were long enough to accept the potentiometers as well as the nuts and lock washers needed to secure the potentiometers. The position of the rods is shown in Figure 2.5b.

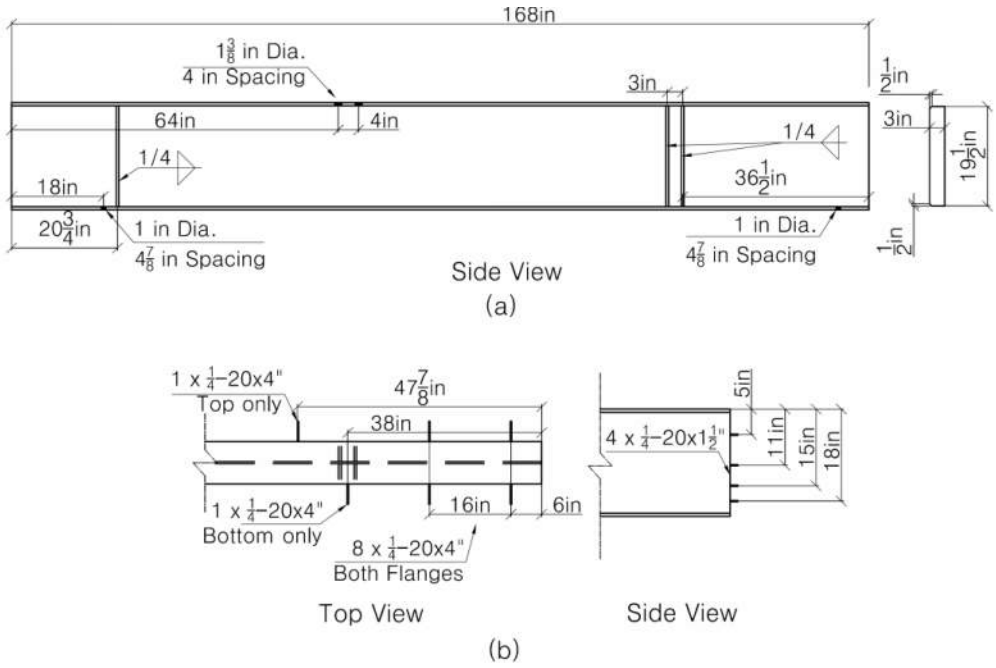

Figure 2.5 Layout of Stiffeners and Potentiometer Rods in Girder Specimens

(a) Stiffener and Drilled Hole Locations in All Girder Specimens, (b) Placement of Threaded Rod for Potentiometer Attachment

Prior to testing, the exposed webs of the girders were treated with a mixture of limestone and water. As the water evaporated, a thin white film of limestone remained

on the surface of the girder. This film would flake and fall off as damage occurred to the steel below. The pattern exposed in the limestone would be indicative of the type of damage to the steel as it formed lines perpendicular to the principal compressive force. Figure 2.6 shows the whitewashed area of the undamaged girder.

Figure 2.6 Whitewashed Area of the Undamaged Girder

2.5.1 Undamaged Girder

No modifications aside from the stiffeners, potentiometer attachment rods, and drilled holes were applied to the undamaged girder. This girder represented the undamaged baseline bearing capacity of the girder being studied.

2.5.2 Damaged Girders

Corrosion damage was simulated by a reduction in the cross-sectional area of the bottom of the web and the inside portion of the bottom flange. The extent of corrosion damage had to be in agreement with corrosion loss observed in structurally deficient bridge structures. This would ensure that the loss of capacity would be realistic. The damage used was based on an inspection report of a structurally deficient bridge in Hartford, CT (Bridge No. 03399D, 1962) (Kristoff, 2011).

Corrosion loss in the girders in Bridge No. 03399D varies from girder to girder. Figure 2.7 shows examples of some of the more severe cases of corrosion in terms of length and depth. In the most extreme case in terms of length, corrosion extends over 6 ft (1.5D), rusting through the first intermediate stiffener and into the second panel, Figure 2.7a. The most severe depth of web corrosion reported on Bridge No. 03399D

can be seen in Figure 2.7b. In this girder, the entire thickness of the web is lost at the bearing 4 in high (0.08D). Halfway between the bearing stiffeners $^{1}/_{4}$-in of rust penetration is noted on the $^{3}/_{8}$-in thick web, a section loss of 67%.

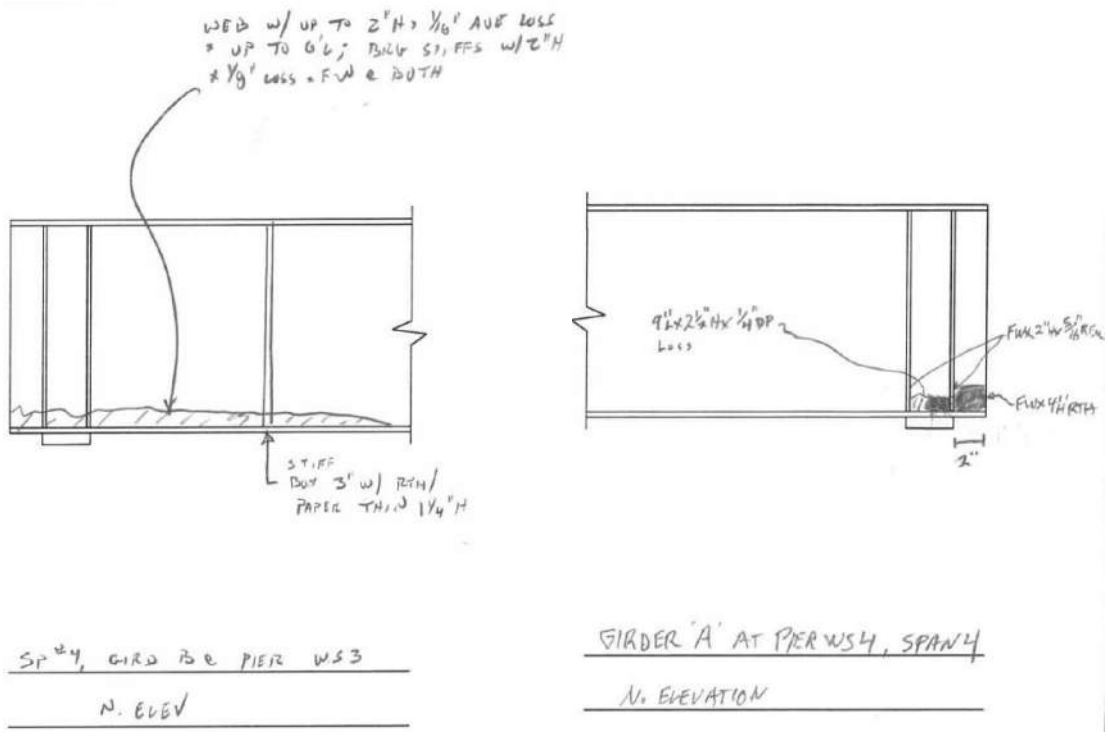

(a) (b)

Figure 2.7 Examples of Corrosion in Bridge No. 03399D (Kristoff, 2011)

(a) Extreme Length of Corrosion Damage in Bridge No. 03399D: 33% section loss 0.05D High, 1.5D Long, (b) Extreme Depth of Corrosion Damage in Bridge No. 03399D: 100% section loss 0.08D High, 0.16D Long

Figure 2.8 shows the pattern of section reduction applied to the damaged and repaired girders in the large-scale experiment. The reduced area extends 19-in (0.90D) from the end of the girder and approximately $3^{1}/_{4}$ in up the height of the web or 0.14D. The section reduction extends for half the width of the flange, or $4^{1}/_{4}$ in. Due to variations in the rolling process of the girder, the thickness of the web (T_w) and the thickness of the flange (T_f) are not identical between the three girders. The average web section reduction ($1-^{Twd}/_{Tw}$) for the two girders is 70%, equivalent to some of the more severe damage noted in the inspection report (Kristoff, 2011). The average flange section reduction ($1-^{Tfd}/_{Tf}$) is 44%. This results from an equivalent loss of thickness in the flange as in the web. Dimensions of the damaged and undamaged thicknesses of all three girders can be found in Table 2.1.

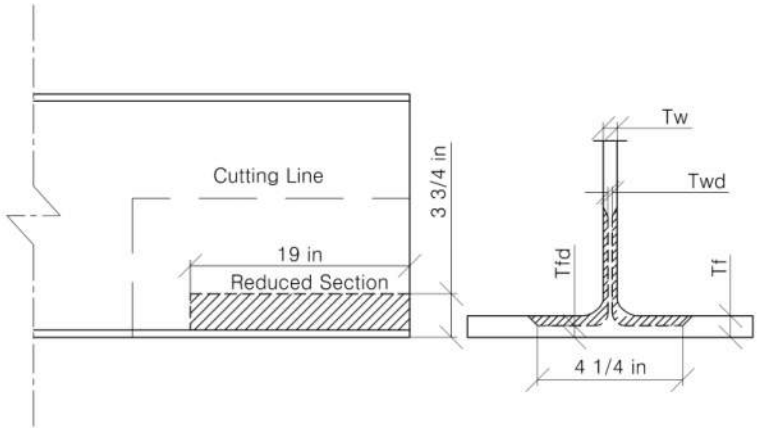

Figure 2.8 Section Reduction Patterns in the Damaged and Repaired Girders

To reduce the thickness of the web and flange of the girders, the lower tee was removed and machined using a computer numeric controlled (CNC) milling machine. The tee was removed by cutting along the dashed line in Figure 2.8 using a plasma cutter, as seen in Figure 2.9a. Plasma cutting works by cutting through the steel with an electric arc combined with a mix of flammable and inert gasses, usually oxygen and argon, respectively. Then, the tee was clamped into a CNC milling machine, Figure 2.9b. Coolant was used during the cutting process to reduce the heat of cutting and prevent warping. Milling progressed on each side of the web and flange leaving the finished depth on each side, Figure 2.9c. Multiple passes were done to minimize the chance of damaging the machine.

Table 2.1 Thickness of the Girders in the Study

Girder	Web Thickness (T_w) (in)	Bottom Flange Thickness (T_{fb}) (in)	Top Flange Thickness (T_{ft}) (in)	Reduced Web Thickness (T_{wd}) (in)	Reduced Flange Thickness (T_{fd}) (in)
Undamaged	0.339	0.558	0.568	N/A	N/A
Damaged	0.335	0.558	0.569	0.113	0.325
Repaired	0.383	0.504	0.504	0.102	0.271

(a) (b) (c)

Figure 2.9 Removal of the Tee and Rough Milling of the Damage

(a) Removal of the Tee from the Girder Using a Plasma Cutter, (b) CNC Machine Cutting Damage into the Tee, (c) Close View of the Cutting Progression of the Damage on the Flange

After removal from the CNC machine, the bulk of the damage is complete. Steps are clearly visible along the edges of the damage and on the fillet in Figure 2.10a. These steps had to be removed to reduce stress concentrations from the change in geometry and to prevent the non-damaged portion of the girder from bearing on the concrete. The edges of the damage were therefore milled at an angle. The fillet at the base of the web was also smoothed in this step. This was performed by securing the tee in a second CNC machine, Figure 2.10b. Once the end milling was finished, the tee had all the rough edges smoothed and the fillet rounded, Figure 2.10c. With this milling completed, the machining of the damage was complete.

(a) (b) (c)

Figure 2.10 Finish Milling Required to Complete the Damage

(a) Steps at the Edges of the Damage Left by the Rough Milling, (b) Angled Milling of the Stepped Edges, (c) Finished Rounded Edges of the Damage

The finished damaged tee is shown in Figure 2.11a. The edges of the tee and girder were ground down at an angle on each side. This allowed full penetration groove welds to be made on each side of the girder. Figure 2.11b shows the ground edges and the

level of penetration of the groove weld. The girder was stood upright and the lower tee positioned. Short line welds were used to hold the tee in place. Short groove welds from each side were used to hold the bottom tee in place, Figure 2.11c. The short welds were extended so that the entire boundary of the tee was welded. Figure 2.11d shows full penetration of one side of the weld throughout the length of the cut. Once the welding was completed, all welds were ground flush with the surface of the girder. This ensured that the concrete would not bear on the weld, Figure 2.11e. Figure 2.11f shows the completed damaged girder after the tee had been welded back in.

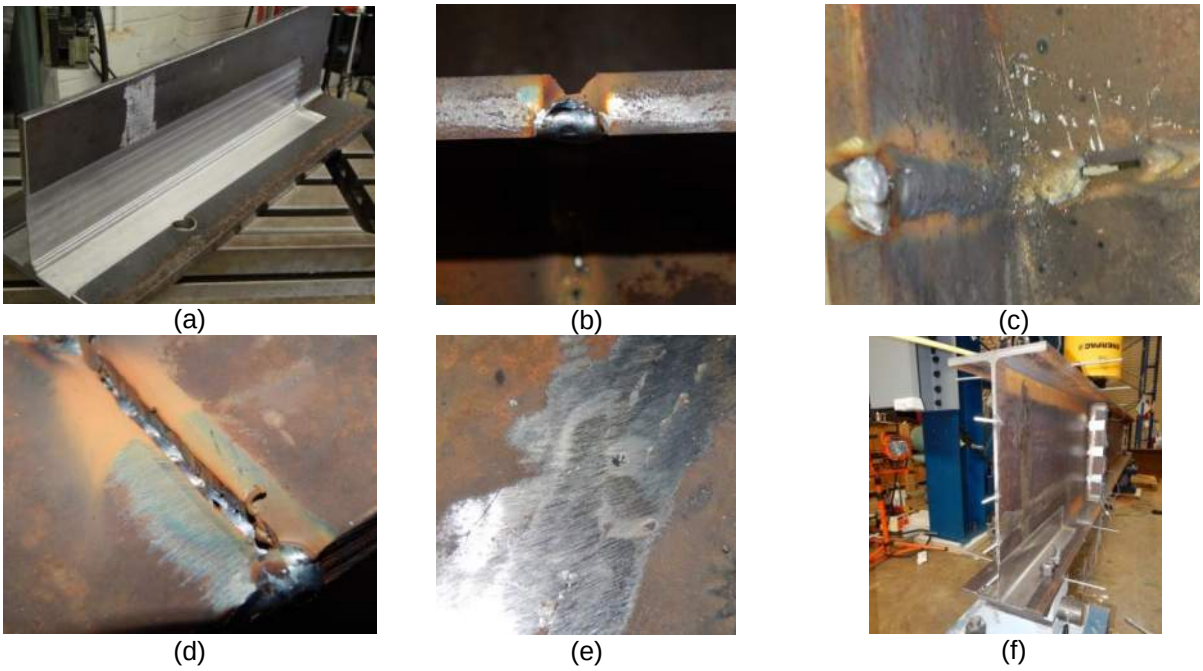

Figure 2.11 Finished Damaged Tee and Reinstallation into Girder

(a) Damage Imposed on the Tee, (b) Beveled Edge and Depth of Groove Weld, (c) Initial Short Groove Welds, (d) Penetration of the Grove Weld through the Length of the Cut, (e) Finished Ground Weld, (f) Bottom Tee Installed on the Girder

2.5.3 Repaired Girder

The repair method selected for the large-scale experiment utilizes UHPC encasing only a portion of the full height of the girder. This was done to stay within the capacity of the Structures Lab floor tie downs. Preliminary analysis found this repair to have the lowest rehabilitated capacity in rolled girders. The rolled girder with a partial height fill was the only method for which the repair itself failed. All others shifted failure to another part of the girder. Completing a successful trial under these conditions would prove the method's ability to rehabilitate corrosion damage in steel girders.

This section is divided into four parts: 1) designing the repair; 2) welding the studs; 3) creating the molds; and 4) casting the concrete.

2.5.3.1 Designing the Repair

In order to maintain consistency with the half-scale girders used in the tests, the repaired specimen utilizes $^{3}/_{8}$-in diameter, $1^{1}/_{4}$-in long, headed shear studs. These are scaled-down equivalents of $^{3}/_{4}$-in diameter 2 $^{1}/_{2}$-in long shear studs. $^{3}/_{4}$-in diameter shear studs are a more typical size used in bridges. Stud length is chosen to provide 1 in of cover. The studs are welded in a 2-in grid pattern on both the web and flange to replicate the spacing of flange studs to create composite beam. Care was taken so the studs on opposite sides of the web were not opposite one another. This reasoning is twofold, each stemming from the limited thickness of the base material. First the staggered pattern resists possible heat damage to the web from the welding process. Second, it helps to resist possible tearing of the web during loading. The proposed arrangement of these studs is shown in Figure 2.12.

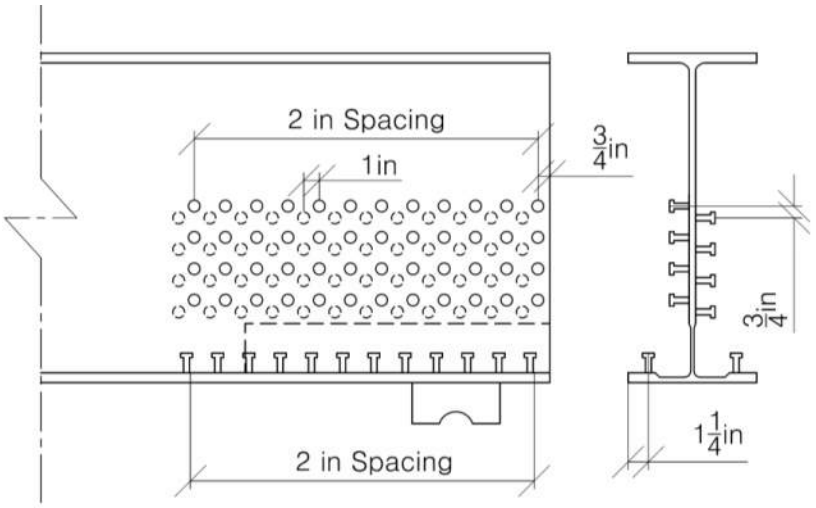

Figure 2.12 Stud Arrangement of the UHPC Repair for the Large-Scale Test

Figure 2.13 shows the dimension of the concrete panel used in the repaired specimen. The panel is 25 in long and 13 in tall. This is sufficient to cover the 19-in long reduced section, and provides enough height to include multiple rows of studs above the reduced section. The thickness of the panel is a minimum of 1 $^{3}/_{4}$ in, which provides $^{1}/_{2}$ in of cover for the web studs. There is a bevel at the bottom of the panel which is 2 in tall and extends to the edge of the flange. This is designed to inhibit corrosion by preventing water from pooling on the bottom flange, and to provide cover

for studs installed on the flange. The edges of the bevel are rounded to reduce stress concentrations at these changes in geometry.

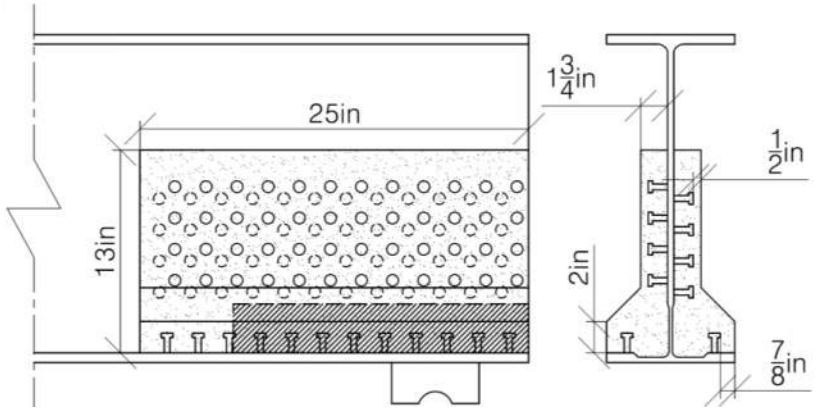

Figure 2.13 Dimensions of the UHPC Panel for the Large-Scale Repair

2.5.3.2 Stud Welding

(a) (b) (c)

Figure 2.14 Installation of Studs for the UHSC Repair

(a) Shear Stud with and without the Ceramic Ferrule, (b) Generator Used in Stud Welding, (c) Welding of the Shear Studs

After the damage was machined on the girder which would have the UHPC repair, the studs used in the repair had to be welded to the web and flange. Studs used were Nelson Stud Welding H4L Headed Concrete Anchors, $^{3}/_{8}$-in diameter, 1 $^{1}/_{4}$-in long. The studs were made of grade C-1015 steel. This steel has yield strength of 84.1 ksi and ultimate strength of 84.7 ksi at 30% elongation. The studs utilized a standard ceramic welding ferrule. The ferrules were broken off after the welding was complete. Figure 2.14a shows the studs before and after removal of the ferrule. Studs were installed with a stud-welding gun by a professional contractor, as is standard practice. This process required a diesel generator, shown in Figure 2.14b, to generate a high current (>500 A) to pass through the stud. This current caused the base of the stud to

liquefy, forming a molten metal pool in the ceramic welding ferrules. This consistently attaches the studs to the base material. Figure 2.14c shows the welding process.

Figure 2.15a shows the pool of metal contained by the ferrule after the weld has solidified and the ferrule removed. All studs were installed on a horizontal surface as was required by the type of ferrule used. There are ferrules which may be used to install studs on vertical surfaces. Figure 2.15b shows the completed tee of the girder with studs installed. After installation of the studs, the tee was welded back onto the girder in the same manner as the tee without the studs. Figure 2.15c shows the girder completed stud installation.

(a) (b) (c)

Figure 2.15 Completed Stud installation

(a) Detail of the Weld at the Base of the Stud after Removal of the Ferrule, (b) Stud Installation on the Tee, (c) Stud Installation on the Finished Girder

2.5.3.3 Preparing the Molds and Girder

Casting forms were made from standard 2-in thick R-10 foam-board wall insulation. The forms needed to be built up from three layers of shaped foam board to create the shape required for one side of the repair. The foam-board was shaped using a CNC machine, shown in Figure 2.16a. The three shaped foam board pieces required for one side are shown in Figure 2.16b. Once the form board pieces were properly shaped, they were glued together. This was done using a spray adhesive safe for use on foam board. The foam board pieces were then weighted with a steel plate to ensure bonding. The finished forms are shown in Figure 2.16c. Spacing between the studs and the formwork are visible in Figure 2.16d. The steel girder and formwork had been treated with mineral oil prior to casting to inhibit bonding, as shown in Figure 2.16e. This was intended to simulate the lack of bond to the steel due to the girder paint, and to facilitate removal of the forms. Care was taken not to apply the oil to the shear studs. These forms were fixed to the girder using construction adhesive and wooden framework, Figure 2.16f. The end of the girder and forms were sealed with Plexiglas. The

Plexiglas was used to cover the end of the girder and monitor the height of the cast and consolidation.

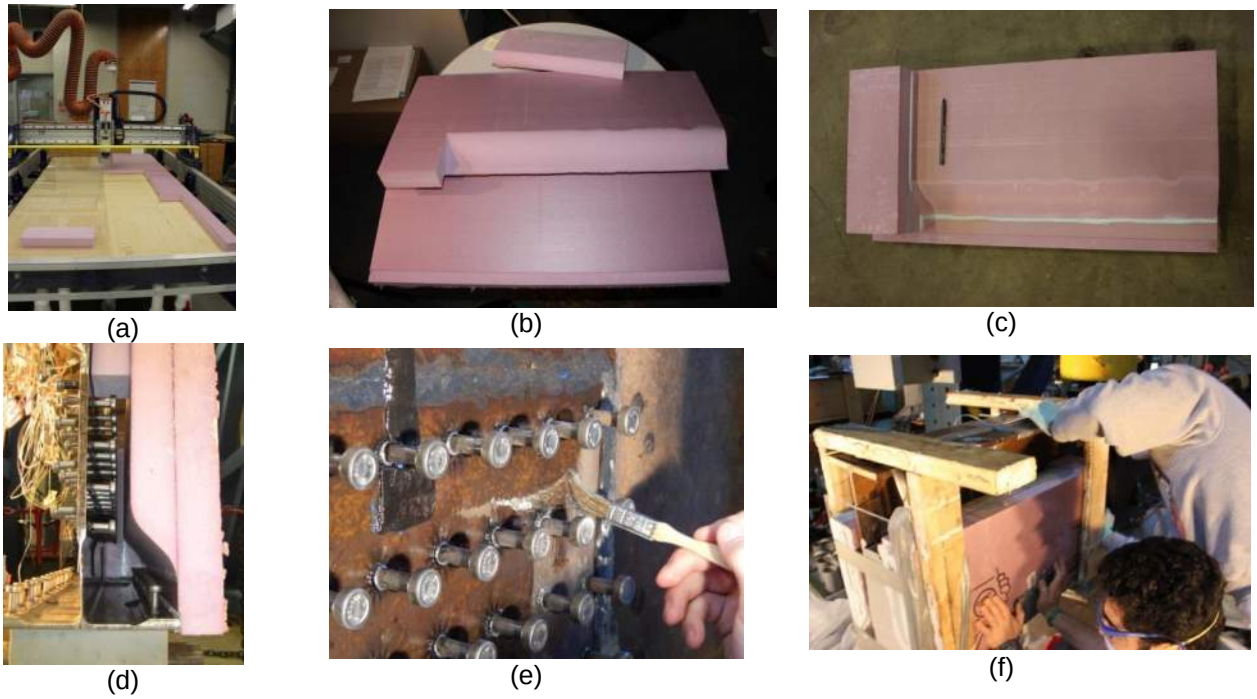

(a) (b) (c) (d) (e) (f)

Figure 2.16 Creating the Molds for the UHPC

(a) CNC Machine Used to Cut the Foam Board Molds, (b) Three Pieces Used to Build Up One Side of the UHPC Molds, (c) Completed Mold, (d) Spacing between the Studs and the Mold, (e) Applying Mineral Oil to the Girder to Simulate Paint, (f) Securing the Mold to the Girder with Wooden Framework

2.5.3.4 Concrete Casting

The concrete used in this study is the commercially available product Ductal® JS-1212, a proprietary mix designed by Lafarge to achieve high early strength. This mix is capable of achieving 12 ksi compressive strength in 12 hours when cured at 120°F and 90% RH. This ultra-high performance concrete formulation contains premix powder, water, Premia 150 (a modified phosphonate plasticizer), Optima 100 (a modified polycarboxylate high-range water-reducing admixture), Turbocast 650A (a non-chloride accelerator), and steel fibers. The steel fibers included in this mix design are straight, brass-coated, high strength steel with a diameter of 0.008 in and a length of 0.5 in. The tensile strength of the steel fibers is specified to be greater than 290 ksi. The thin brass-14 coating provides lubrication during the drawing process and mitigates corrosion of the raw fibers (Yuan & Graybeal, 2014). A constant steel fiber content of two percent by volume is used in this study. A trial mix was performed prior to casting

the panel to verify workability and to determine the desired curing time between casting and testing.

The mixes for the panels were performed in a 100 quart horizontal pan mixer, Figure 2.17a. Two mixes of $27^{1}/_{2}$ quarts were made. Each mix was used to fill one of the panels as well as perform a spread test and cast approximately one dozen 3 in × 6 in cylinders for compressive strength testing. Two mixes were performed to reduce the shear demand on the mixer and to ensure suitable mix quality.

The UHPC mixing process began by preparing a mix of UHSC. To do this, the dry powdered premix was mixed to remove agglomerations, Figure 2.17b. Figure 2.17c shows the powdered mix before the addition of the liquids. The water added included 50% ice by weight, Figure 2.17d. The ice was added to prevent increase of temperature during UHSC mixing, which could cause premature setting and thus adversely affect the material's workability. Immediately after adding the water/ice mixture, the chemicals were added. Figure 2.17e shows the mix after the addition of the liquids.

After adding the liquids, the mix remained dry for a time as the water dispersed. After approximately 10 min from adding the liquids, a noticeable shift in the color of the mix became apparent, as it shifted to a slightly darker grey, Figure 2.17f. 15 min after adding the liquids, the mix began to show signs of clumping., Figure 2.17g. This process continued over the next five minutes, as the clumps grew larger due to increased adhesion. The growing of the clumps can be seen in Figure 2.17h-i. After 22 min from adding the liquids to the powder, the UHSC began turning over as the clumps conjoined, Figure 2.17j. As the mixing continues, the UHSC became more workable and fluid as the turn over continues, Figure 2.17k. Finally after 25 min from liquid addition, the particles and water were sufficiently dispersed to liquefy the UHSC, Figure 2.17l. After this 'turn over', steel fibers were carefully added to the mix, Figure 2.17m. The fibers were added slowly, over the course of a minute, to minimize fibers from balling. The UHPC mixed for a few minutes to evenly disperse all fibers, Figure 2.17n. After 3 min of mixing with the fibers, the UHPC was ready to cast, Figure 2.17o.

Figure 2.17 Mixing the UHPC

(a) Pan mixer, (b) Adding premix, (c) Mix before addition of water, (d) Water/ice mixture, (e) Mix after addition of all liquids, (f) 10 min after liquids, UHSC darkens, (g) 15 min after liquids, (h) 17 min after liquids, clumps begin to form (i) 20 min after liquids, UHSC clumps growing, (j) 22 min after liquids, UHSC begins turning over, (k) 24 min after liquids, UHSC turns over, (l) 25 min after liquids, UHSC ready, (m) Addition of fibers, (n) Immediately after fiber addition, fibers begin to disperse, (o) 3 min after fiber addition, UHPC ready

The concrete was transferred from the pan mixer into five gallon buckets for casting, Figure 2.18a. Some of the concrete was reserved for flow table and strength tests; this is outlined in Chapter 0. The concrete was then poured from the buckets into the top of the mold, as shown in Figure 2.18b. Figure 2.18c shows the casting visible through the Plexiglas. In the figure, it is clear that the UHPC is able to consolidate around the studs, leaving no air pockets which could reduce capacity. Due to the high density and self-consolidating nature of the concrete the foam-board formwork began floating on the concrete during casting. This created gaps between the forms and the girder, causing leaks allowing concrete to escape the mold, Figure 2.18d. It also caused the Plexiglas to bulge, allowing some UHPC to flow into the other panel. It was quickly contained by further shoring of the formwork and sealing of the leaks, and thus, casting was able to be finished, Figure 2.18e.

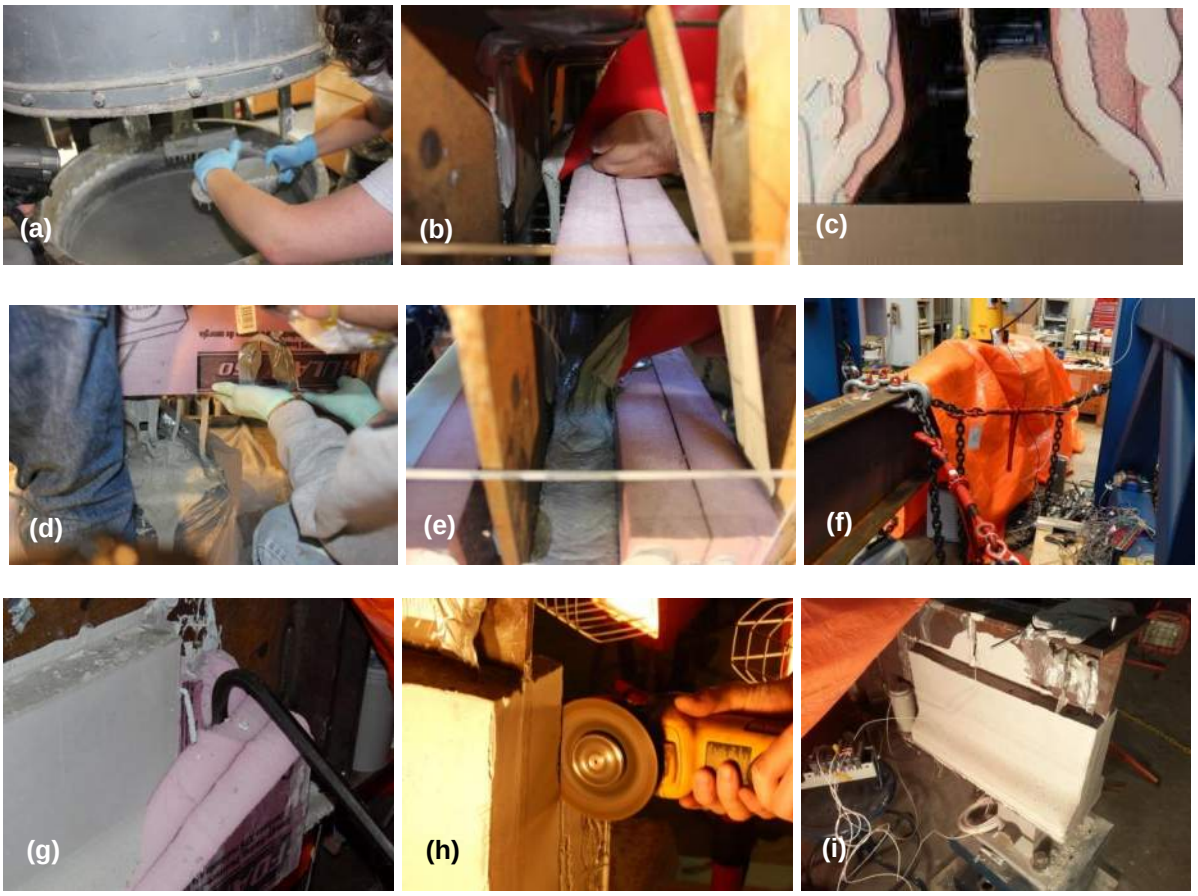

Figure 2.18 Casting and Curing the UHPC Panels

(a) Transferring the UHPC to buckets, (b) Casting the UHPC panels, (c) UHPC consolidation around shear studs, (d) Leaking of the forms, (e) Completion of casting the first form, (f) Curing blanket and heater, (g) Removal of the forms, (h) Removing excess concrete, (i) Finished panels

Because of the low temperature in the Structures Lab, after casting, the panel was covered with an insulated concrete curing blanket. A heater was installed under the blanket and the concrete was left to cure, Figure 2.18f. The average temperature under the blanket was measured as 72° F. After two days, the forms were removed, as shown in Figure 2.18g. There was an excess thickness of UHPC adjacent to the first cast panel and the Plexiglas, due to the bulging of the Plexiglas. This excess concrete was cut away with a grinding wheel, Figure 2.18h. The finished panel can be seen in Figure 2.18i.

2.6 SECONDARY COMPONENTS

The test setup required the fabrication of various secondary components for the test. The first of which that needed to be fabricated was the bearings. Bearings would rest on the load cell and allow the girder to rotate. Bracing was utilized to stabilize the span of the girder between the loading point and the non-studied end. Ultimately, the loading ram and a loading protocol needed to be selected and developed. This section will outline the design of these features of the test.

2.6.1 Bearing

This test utilizes a rocker bearing at each end of the girder. The base of the bearing is a 12-in square 1-in thick plate. This base plate includes the same $1^{1}/_{8}$-in diameter anchor cluster pattern. This maintains the flexibility of the entire system being built. As a point of rotation, a $2^{1}/_{4}$-in round Grade 4140 Chromoloy steel rod is used. This is a high-strength, hard steel which resists deformations caused by the high bearing forces and maintains its shape and ability for the setup to rotate. The point of rotation is set to be 3 in below the bottom flange; this is approximately proportional to the center of rotation of some bearing types found in bridges.

The bearing blocks were cut from a single 6-in plate which was 8 in x 5 $^{5}/_{8}$ in. The plate was cut in half and machined with a CNC milling machine to accept the steel rod. For attachment to the bottom flange, two threaded bolt holes were included on the top of the bearing. These utilized $^{7}/_{8}$-9 threading and were spaced $4^{7}/_{8}$ in. This is the same bolt hole and spacing included on the bottom flange of all the girders. Figure 2.19 shows the bearing design and the finished bearing attached to the load cell. Note the loss of paint along the center of the bearing where the web of the girder was centered.

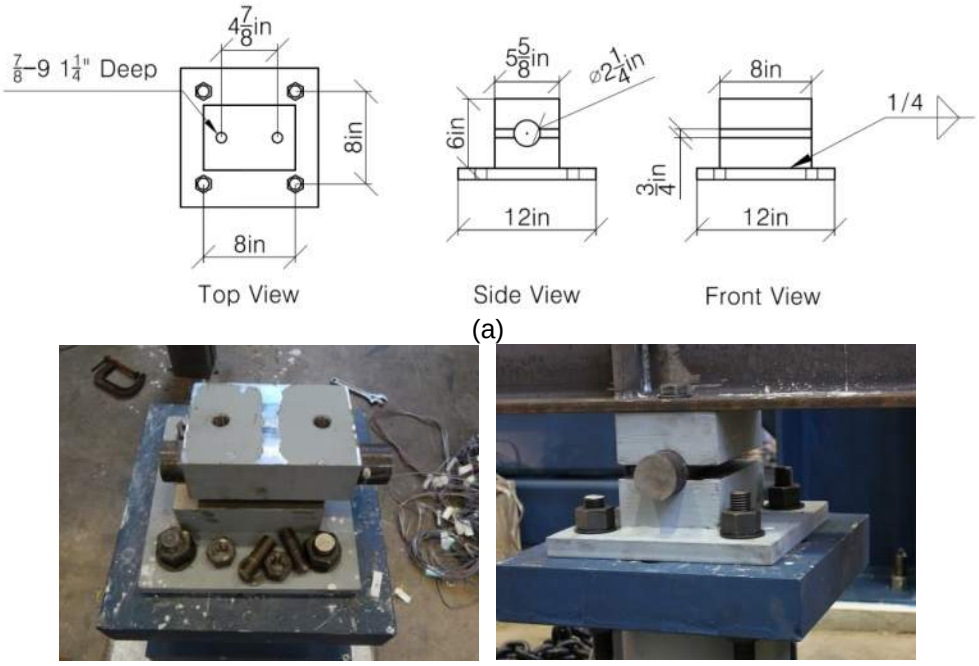

(a)

(b) (c)

Figure 2.19 Bearing Design and Finished Bearing

(a) Bearing Design, (b) Bearing without Girder Seated, (c) Bearing with Girder Seated

The end of the bearing that was being tested was not bolted firmly to the bearing. This was done to provide uniformity between the three tests. The repaired girder could not be bolted down, as the concrete would not allow for the removal of the bearing. Instead, the bolts were cut down to the height of the flange. This allowed shear transfer to be maintained. Gaps around the bolt were then sealed with mastic tape. As a consequence, every other test was run with loose bearing bolts. Because the failure of the damaged girder was expected at the base of the web, nuts were not included to facilitate removal of the girder after the test. Figure 2.20 shows the gaps in the bolts and the mastic tape seal before UHPC casting.

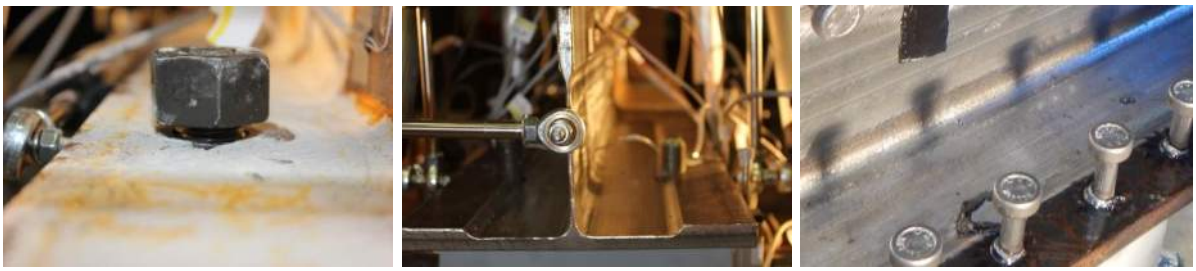

Figure 2.20 Gap in the Bolts and Mastic Tape Sealed Repaired Girder

(a) Undamaged Girder Bolt Gap, (b) Damaged Girder Bolt, (c) Mastic Tape Seal around Trimmed Bolt in Repaired Girder

2.6.2 Bracing

To maintain the vertical orientation of the tested girder, the top flange of the girder is braced. This prevents lateral torsional buckling which could occur if the load was not perfectly centered. Bracing is done with a heavy chain which is tensioned using a load binder. The chain is $^{1}/_{2}$-in, grade 100 chain. This chain has a working load limit of 15 kip. One chain is used on each side of the girder, and grab hooks were added to the end for securing the chain. The ends of the chain are looped through heavy duty hoist rings attached to the holes drilled in each column. Hoist rings are placed below the level of the top flange so that additional tension was not developed during the test. Four clevises are attached on the top flange of each side of the girder. The chain is then run through the clevises on the flange, and two load binders are attached to each chain. The load binders are then tightened uniformly on each side until the chain was sufficiently taught, and the girder is centered under the hydraulic load ram. The chains were simultaneously tightened on each side of the girder. This was done with two people so that tension was similar. A degree of slack was maintained in the chain so that working load of the chain was not reached. Figure 2.21 shows views of the lateral bracing system, including a global view, attachment to girder and frame, and the load binder and grab hooks.

(a) (b) (c) (d)

Figure 2.21 Lateral Brace System

(a) Global View of Lateral Braces, (b) The Clevises on the Girder at the Center of the Frame, (c) Attachment of the Lateral Brace System to the Frame, (d) Grab Hook and Load Binder

2.6.3 Hydraulic Load Ram

In order to perform the large scale test, a high-capacity hydraulic load ram capable of being attached to the spreader beam is required. The Enerpac CLRG-25012 hydraulic cylinder was chosen as the load ram. This cylinder utilizes 10,000 psi hydraulic lines and is double-acting, meaning it has hydraulic ports to apply force in both

directions. It is capable of applying 568 kip on an extending stroke and 236 kip on a retracting stroke. The cylinder has a stroke length of 11.81 in. The cylinder is attached to the bottom of the spreader beam via three M12 threaded bolt holes drilled in the base of the cylinder. The cylinder is equipped with a tilt saddle which allows for up to 5° of rotation in any direction. This allows the top flange of the beam to rotate and maintain a pure axial load on the beam. Figure 2.22a shows the hydraulic cylinder attached to the spreader beam with the test beam in place.

The hydraulic pump used in the test is an OTC Power Team PE17 Series, a 10,000 psi hydraulic pump with two-way valve so that the pump can both advance and retract the hydraulic cylinder. The pump is shown in Figure 2.22b. The return valve is connected directly to the return port on the cylinder, the lower port in Figure 2.22a. The advance valve runs through a needle valve, followed by a load holding valve, shown in Figure 2.22c. The needle valve controls the loading and unloading rates, while the load holding valve maintains pressure at peak load.

Loading was performed by activating the pump through the advance valve. Unloading was performed by switching the valve to unload, and adjusting the load holding and needle valves.

(a) (b) (c)

Figure 2.22 The Hydraulic System

(a) Load Ram Installed on the Spreader Beam, (b) 10,000 PSI Hydraulic Pump, (c) Needle Valve (silver) and Load Holding Valve (black) for Flow Control

2.7 LOADING PROTOCOL

Loading-unloading cycles of increasing magnitude were used for load testing of the three specimens. The initial loading protocol for each test was load controlled, based on the force applied by the load ram. Following the failure of a specimen, loading protocol changed to displacement controlled - increasing the displacement of the bottom flange. The tests utilized different loading protocols due to different levels of anticipated failure. The following loading protocols were followed for each test:

- **Undamaged Girder:** The first cycle of the undamaged specimen progressed to a cylinder force of 50 kip, and increased in 25 kip increments until failure of the specimen. Following failure, three cycles increasing previous peak displacement 0.25 in were conducted followed by a final cycle increasing the previous peak displacement 0.50 in.
- **Damaged Girder:** Due to lower predicted failure load, first cycle went to 10 kip and cylinder force increments of 10 kip were used. Following failure, four cycles increasing peak displacement 0.25 in were used, followed by one cycle of 0.50 in.
- **Repaired Girder:** Cylinder force increments of 15 kip were used up to a cylinder force of 150 kip. After a load of 150 kip, loading protocol increased to 25 kip per increment to a load of 300 kip. No displacement based protocol was followed for the repaired specimen.

3 Instrumentation

3.1 INTRODUCTION

This chapter will describe the data acquisition systems used, as well as the data collected in each test, rationale behind the data collected, and data processing required. Force, displacement, strain, and temperature data were collected. Force measurements included force, shear, and moment at each bearing, and force applied by the load ram. Displacement measurements included displacement of the girder around the hydraulic load ram, lateral displacements of the end of the web, global shear deformation of the girder at the bearing, and the rotation of the bearing. Strain measurements included vertical strain distribution at the bearing, longitudinal strain distribution on the bottom flange, shear strain in the web of the girder, vertical and shear strains in the concrete, and axial strains in the shear studs. Furthermore, crack development in the UHPC panels were marked and visually tracked. Interior temperatures of the concrete panel and cylinder, as well as ambient temperatures of the room and under the curing blankets were recorded during initial curing. This data was used to validate the finite element model, identify load-carrying mechanisms, detect damage, and analyze failure.

3.2 DATA ACQUISITION SYSTEMS

Over 50 channels of data were collected in each test. This required a significant expansion of the data collecting capabilities of the Structures Lab. It was decided that the HBM QuantumX MX1615 was the best candidate. Data was collected using an existing National Instruments (NI) cDAQ-9178, and two new Hottinger Baldwin Messtechnik (HBM) MX-1615 bridge modules.

The existing data acquisition system used in the Structures Lab is the NI cDAQ-9178. This is an eight slot, cartridge based data acquisition system. Each cartridge

used has only one type of data which it is able to record. Cartridges used in this experiment were the NI-9235, an eight channel 120Ω quarter-bridge strain gauge module; the NI-9236, an eight channel 350Ω quarter-bridge strain gauge module; the NI-9205, a 32 channel ±10V analog voltage input module; the NI-9269, a four channel ±10V isolated analog voltage output module; and a NI-9217, a four channel PT100 RTD (Resistance Temperature Detector) analog input module. The NI cDAQ-9178 is shown in Figure 3.1a. A fallback to the cartridge system of the NI cDAQ series is limited data sampling ranges between modules. For instance, the NI-9217 RTD module has no minimum sampling rate, but has a maximum rate of 400 Hz. The NI-9235/6 strain gauges module has a range of 794 Hz to 10,000 Hz. This is problematic as the NI-9235/6 modules were unable to record below 794 HZ, producing data files 40 times larger.

The MX 1615 is a multi-purpose strain gauge bridge amplifier. It is capable of reading full-, half-, and quarter-bridge configurations of any resistance. This would require multiple NI cartridges for each configuration and voltage combination. The MX 1615 is also capable of reading voltage and RTD temperature readings, making it even more flexible. The accuracy of the data collected is also far superior to the current NI system. Noise levels for quarter bridge strain gauges using the NI-9235/6 were typically around 50 με. The new HBM module is 100 times more sensitive, capable of noise of only 0.5 με. This level of noise is equivalent to $^{1}/_{32}$ in over a mile, compared to about 4.25 ft with the NI over the same length. Up to three simultaneous sampling frequencies can be set to each of the channels, from 0.1 Hz up to 19,200 Hz. The sampling rate for all channels was set to 20 Hz to balance file size and resolution. The pair of MX 1615 is shown in Figure 3.1b.

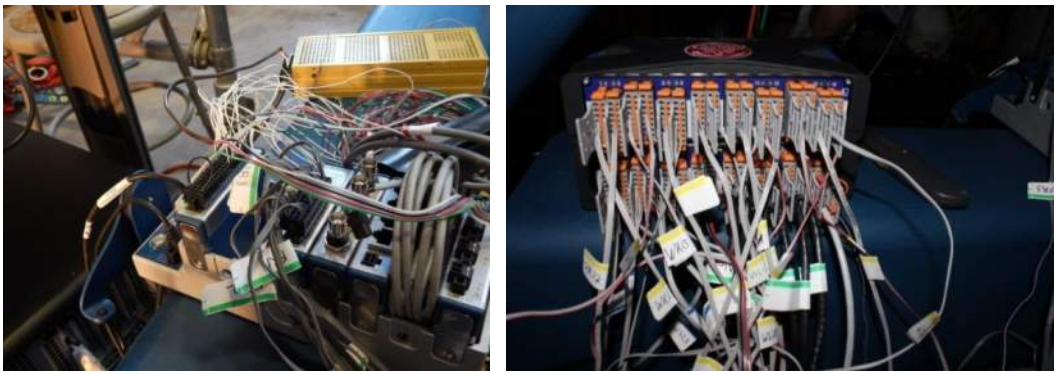

(a) (b)

Figure 3.1The Two Data Acquisition Systems Used

(a) NI cDAQ-9178 with Cartridges NI-9205 Voltage Input (leftmost), NI-9235 120Ω Quarter Bridge (second from left), and NI-9269 Voltage Output (rightmost), (b) The Pair of HBM Quantum-X MX-1615 Multi-Purpose Bridge Modules

The computer used to collect the data is a Dell Precision T3600 with an Intel Xenon CPU #5-1620 0 3.60 GHz processor and 8.00 GB of RAM. The pair of MX1615 are coupled via FireWire connection, and connected to the computer via an Ethernet connection. The NI cDAQ-9178 is connected to the computer via USB 2.0. Software used to interface with the MX 1615 was HBM's CatmanEasy. This is the standard software which interfaces with the MX-1615 and allows for storage of individual sensor parameters for recall, easy sensor calibration, unlimited computational channels, and simple real-time data visualization tools. The computational channels allow for real-time calculations using data read from the physical channels. The software used to interface with the NI cDAQ-9178 was NI's LabView Signal Express. This is the simplified version of LabView which allows for the creation of quick data acquisitions solutions using the NI modules.

In order to synchronize the readings between the two modules, the NI-9269 is used to generate a saw tooth voltage wave with a 15 second period. This voltage was sent to both the NI-9205 and the MX-1615. Because the modules are started within 5 seconds, the 15 second period is able to synchronize the data between the two modules.

Voltage supply for the potentiometers was generated with an Acopian A10TN110M. This is the yellow box visible in Figure 3.1a. This is a sensitive voltage generator capable of generating between 9.5 and 10.5 V up to 1 A. The total amperage demand for the twenty potentiometers was 365 mA. The voltage generated was monitored using the NI-9205.

3.3 SENSOR NAMING CONVENTION

Due to the large number of sensors used, an alpha-numeric identification system was developed for naming displacement potentiometers and strain gauges. This system utilized a one to three letter prefix and a one or two number suffix. The letters denoted the category of the measurement. The number related the relative location on the girder. For this metric, a left and right side of the girder was defined as shown in Figure 3.2. Numbering included one or two digits, each digit began incrementing from one. In instances of two digits, the first digit denoted longitudinal positon. This began at '1' at the studied end and would increase toward the load ram. The second digit would denote height on the web, and increase from bottom flange to top. Figure 3.2 shows how these digits increase on the girder.

When the letter referring to the side of the girder is excluded, it refers to sensors on both sides of the girder.

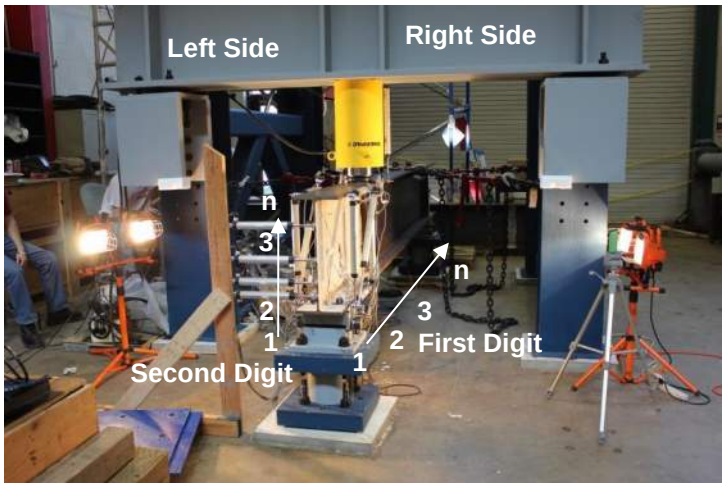

Figure 3.2 Definition of Girder Sides in Naming Convention

3.4 FORCE SENSORS

Seven force sensors are used in the large scale experiment.

3.4.1 Load Cells

The load cells utilized to record bearing reactions at each end of test girder were designed, manufactured, and calibrated in-house. The design used was a larger version of a 40-kip load cell designed at the University of Buffalo (Reinhorn & Bracci, 1992). The axial, shear, and moment capacities of the load cell manufactured for the Structures Lab to ensure linearity and repeatability were ±500 kip, ±100 kip, and ±500 kip-in, respectively. All circuits utilize a full-bridge arrangement of 350 Ω, transducer quality strain gauges manufactured by Omega Engineering. Calibration of the axial circuit found the load cells had a maximum error of 0.3% of full-scale. This is within acceptable error toleration of commercially manufactured high-capacity load cells. Figure 3.3 shows the internal wiring of the load cell, as well as the load cell after installation of the protective cover. Strain gauges are circled in blue. Input and output is handled with RJ-45 jacks for each of the five circuits, normal (N), moment in two directions (Mx, My), and shear in two directions (Sx, Sy). Load cell directions are indicated both on the internal cylinder and external sheath, and are aligned with the bolt holes on the end plates, and are circled in red in the figure. A complete description of the design, manufacture, and calibration procedure for the load cells is given in Appendix A.

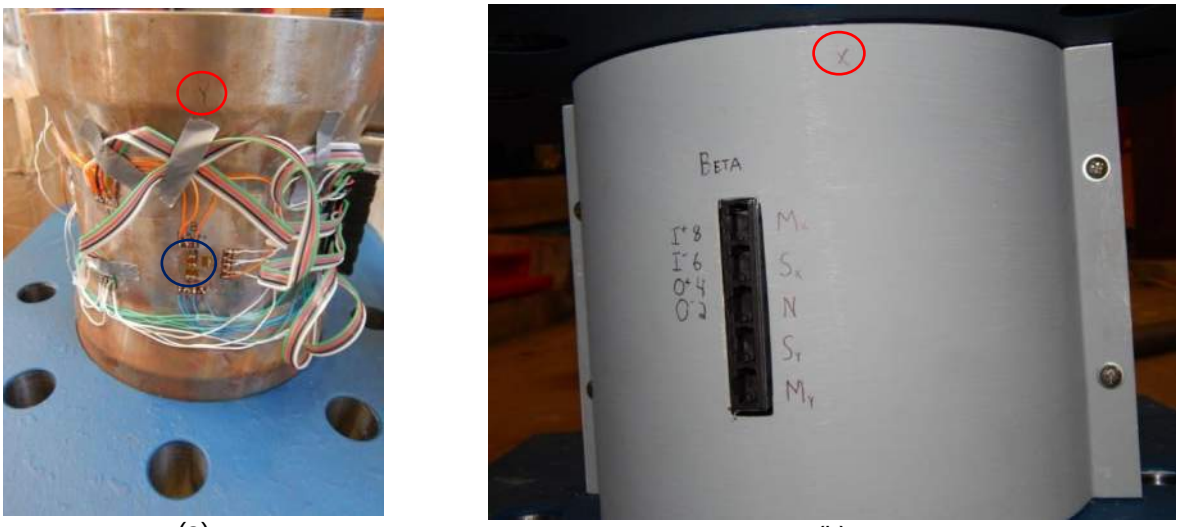

(a) (b)

Figure 3.3 UConn 500 kip Load Cell

(a) Internal Wiring of One Quarter of the Load Cell Core, (b) External Sheath and Plugs of Load Cell

Readings for the load cell were recorded using the MX-1615 at a rate of 20 Hz. The load cells on each bearing were set up to measure bearing force, longitudinal shear, and transverse moment. Bearings were differentiated in naming as the 'test' bearing for the studied end, and 'end' bearing for the non-studied end. Bearing force was denoted as 'axial', longitudinal shear as 'shear', and transverse moment as 'moment'. This resulted in six channels: Test_Axial, Test_Shear, Test_Moment, End_Axial, End_Shear, and End_Moment. The axial calibration factor allowed for axial load to be recorded in kip. Positive values denoted increasing bearing load. Because the circuits for the shear and moment had not been calibrated, readings for these channels were recorded in $^{mV}/_{V}$. This would allow scale factors to be applied once they are known. Axial force was the bearing force and was the critical piece of information needed in the study. Longitudinal shear and transverse moment were included because the bearing used was capable of transmitting theses forces. Transverse shear and longitudinal moment were excluded as these forces were not transferred.

3.4.2 Hydraulic Pressure Transducer

Pressure in the hydraulic load ram was monitored using a pressure transducer installed directly on the advancing port of the hydraulic load ram, as shown in Figure 3.4. The transducer was located directly on the cylinder to obtain the most accurate reading possible. If a hose was included between the transducer and the

cylinder, expansion of this hose would result in a drop in the pressure read by the transducer.

The pressure transducer chosen is the PX309-10KGV manufactured by Omega Engineering. It is a 10,000 psi gauge-pressure transducer. It is a full-bridge type sensor, utilizing a silicon sensor mounted on a stainless steel diaphragm. Accuracy of the gauge is 0.25% (25 psi), and its signal is output as 0-100 $^{mV}/_{V}$. A scaling factor is applied to record values in psi.

Figure 3.4 Hydraulic Load Ram Pressure Transducer

The data from this pressure transducer was recorded in the MX-1615 at a rate of 20 Hz, and named 10,000psiPressure. In addition to recording the internal pressure of the cylinder, five computational channels were included which used data gathered by the pressure transducer. The EasyCat software from HBM calculated these channels in real time. One of the channels converted the pressure to force exerted on the girder; this was used as the benchmark for the loading steps. The force exerted by the cylinder was proportionally divided to create predicted reaction forces at each bearing. These were used to verify loads read by the load cell. The last two channels calculated the load difference between the predicted reaction force and the load recorded by the load cells.

3.5 DISPLACEMENT POTENTIOMETERS

Twenty displacement potentiometers are used in the large scale test. All the potentiometers are recorded with the NI-9205 at a rate of 20 Hz. Displacement potentiometers require a supply voltage, and return a portion of that voltage based on

the position of the actuator. When fully retracted they return 0 V, and when fully extended, they return the full supply voltage. Scale factors are applied based on the stroke length of the potentiometer, and the voltage supplied.

3.5.1 Cylinder/Girder Vertical Displacement

Four potentiometers were used to measure the displacements of the girder around the load ram. Individual measurements of the top flange, bottom flange and the extension of the hydraulic cylinder were taken. The naming convention for these photometers included a two letter prefix. The first letter, 'C', denoted the sensor was at the center of girder, the second letter denoted the side of the girder the sensor was on. Sensors also had a two digit suffix. The first digit denoted if it measured displacement at the loading point, '1', or past the loading point, '2'. The second number denoted which flange the gauge was mounted on, '1' for bottom, '2' for top. For instance, CL11 was the center potentiometer on the left bottom flange at the point of loading. Figure 3.5 shows the vertical potentiometers used. These four potentiometers were intended to obtain various vertical displacements of the girder around the point of loading.

Figure 3.5a shows a Novotechnik LGW-300 linear potentiometric position transducer. The LGW-300 is a linear rod type potentiometric transducer with an 11.8-in displacement range. The resolution of the measurements is 0.00039 in, and the linear accuracy for the transducers is ±0.07% of the sensors full length (8.26 mil). It utilizes a 10 V supply voltage. The scale factor used is 1.18 $^{in}/_{V}$, based on stroke length and supply voltage. The LGW series of potentiometers are not spring loaded; they are able to move freely in both directions. The potentiometer is secured on a $^{1}/_{4}$-20 threaded rod, with a pair of nuts and lock washers.

This potentiometer measured the relative displacement between the top flange of the girder and the bottom flange of the spreader beam, and was given the designation CR22. This displacement reading was not directly at the point of loading, it was located $9^{3}/_{4}$ in past the loading point away from the studied end. This allowed the sensor to be attached vertically to the spreader beam. The sensor would include any displacement from the upward deflection of the spreader beam.

Figure 3.5b is a Novotechnik LGW-150 linear potentiometric position transducer. This transducer has the same general properties as the LGW-300. It has a stroke of 5.9-in, with the same level of resolution and similar linear accuracy (4.13 mil). The

smaller stroke results in a scale factor of 0.59 $^{in}/_{V}$. The same method of attachment is used.

This potentiometer was located between the two web stiffeners on the bottom flange and measures absolute displacement of the bottom flange below the point of loading. It was given the designation CL11. The measurement was absolute as it was measured with respect to the floor. Because the girder was stiffened at the point of loading, this displacement can be considered as the total displacement of the girder at the loading point.

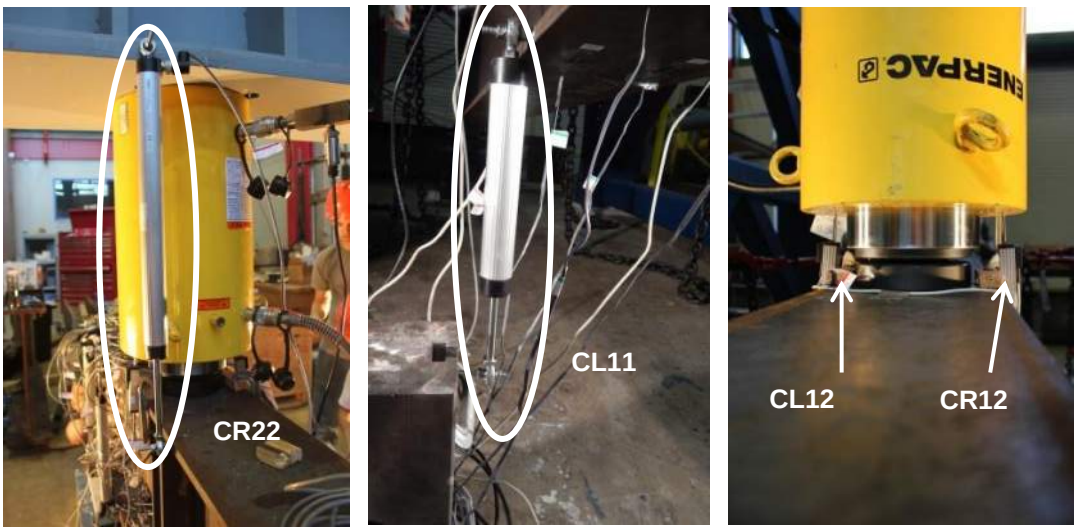

(a) (b) (c)

Figure 3.5 Vertical Girder Displacement Potentiometers

(a) Sensor CR22: A LGW-300 Linear Rod Potentiometer, (b) Sensor CL11: A LGW-150 Linear Rod Potentiometer, (c) Sensors CL12 and CR12: Two LS-50 Linear Spring Potentiometers

The last two potentiometers are Novotechnik LS-50, a non-contracting spring return position potentiometric transducer with 2.0 in displacement. The spring return extends the rod. The sensors were installed such that the rod was nearly entirely compressed to obtain a full stroke. The resolution of the potentiometer is 0.002 in and has a linear accuracy of 0.003 in. The LS-50 utilizes the same 10 V supply, and therefore it uses a 0.20 $^{in}/_{V}$ scale factor.

These potentiometers measured the displacement of the load ram cylinder. There are two potentiometers mounted to the top flange on each side of the girder, as seen in Figure 3.5c. They were given the designations CL12 and CR 12. The measurement includes the upward displacement of the spreader beam as the load ram is attached to the spreader beam. Combining the values of the potentiometers, the rotation of the girder at the point of loading could be calculated.

3.5.2 Web Displacement

Four potentiometers were placed on the web of the girder to measure global out-of-plane deformations of the web. They were given the prefix 'W', for web. The numerical suffix ranged from '1', for the sensor nearest the bottom flange, to '4' for the one nearest the top flange. The potentiometers were positioned in an attempt to best show the deformed shape of the girder webs.

The potentiometers used to measure web displacement are Novotechnik LGW-150, the same as CL11. Because the direction in which the web would buckle was unknown, the potentiometers were initially placed at mid stroke. This allowed 3 in of displacement in either direction.

The locations were chosen based off the predicted deformed shape from a preliminary finite element model of the undamaged girder. The upper most potentiometer, W4, was 5 in from the top of the girder. The other three were located at distances of 11 in, 15 in, and 18 in below the top flange for sensors W3, W2, and W1, respectively. Figure 3.6 shows the web displacement potentiometer locations on both the damaged and undamaged specimens. Note that sensor W1 is located on the reduced section of the girder.

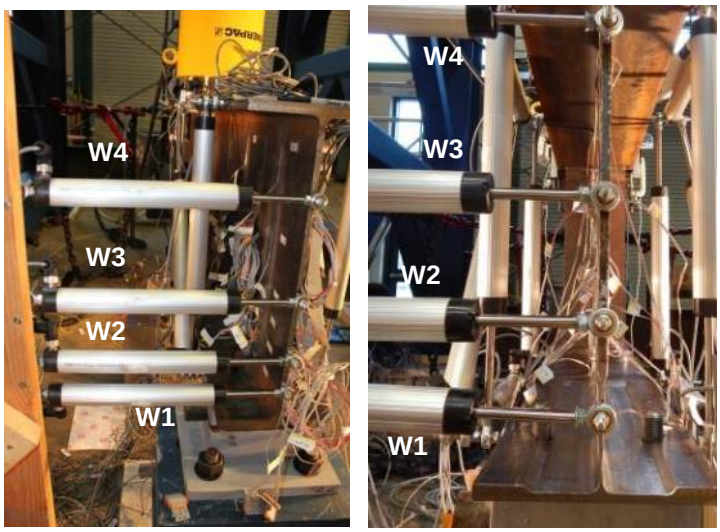

(a) (b)

Figure 3.6 Web Displacement Potentiometers in Undamaged and Damaged Specimens

(a) Web Displacement Potentiometers on the Undamaged Girder, (b) Detail of the Web Displacement Potentiometers on the Damaged Girder

3.5.3 Shear Box/Bearing Rotation

The shear deformation and displacement field at the end of the girder was measured using a configuration of five potentiometers. These potentiometers were fixed to the top and bottom flange on each side of the girder. The configuration of these five potentiometers is referred to as a 'shear box'. Two spring potentiometers were mounted to the bearing to calculate rotation. Figure 3.7 shows one of the shear boxes and the pair of spring potentiometers on the bearing. All ten shear box potentiometers had a three letter prefix and one number suffix. The first letter was always 'S' for shear box, the second letter denoted the side, and the last described the orientation: 'H' for horizontal, 'V' for vertical, and 'D' for diagonal. Numbering followed the predefined numbering mentioned in Section 3.3. This resulted in the ten potentiometers being named SRH1, SRH2, SRV1 SRV2, SRD1, SLH1, SLH2, SLV1, SLV2, and SLD1. The bearing potentiometers were named 'BR' for bearing, and were numbered BR1 and BR2 for the potentiometers on the outside and inside of the bearing, respectively.

The spring potentiometers on the bearing are the same Novotechnik LS-50 used for CL12 and CR12. The potentiometers in each shear box include two horizontal Novotechnik LGW-150s, two vertical Novotechnik LGW-225s, and a diagonal Novotechnik LGW-300. The diagonal runs from the bottom flange of the bearing. The LGW-150 and -300 are identical to those mentioned before. The LGW-225 has identical characteristics for resolution and supply voltage, and a similar accuracy (6.23 mil). The stroke for the LGW-225 is 8.9 in, resulting in a scale factor of 0.89 $^{in}/_{V}$. All potentiometers are placed such that readings can be made in both extension and retraction.

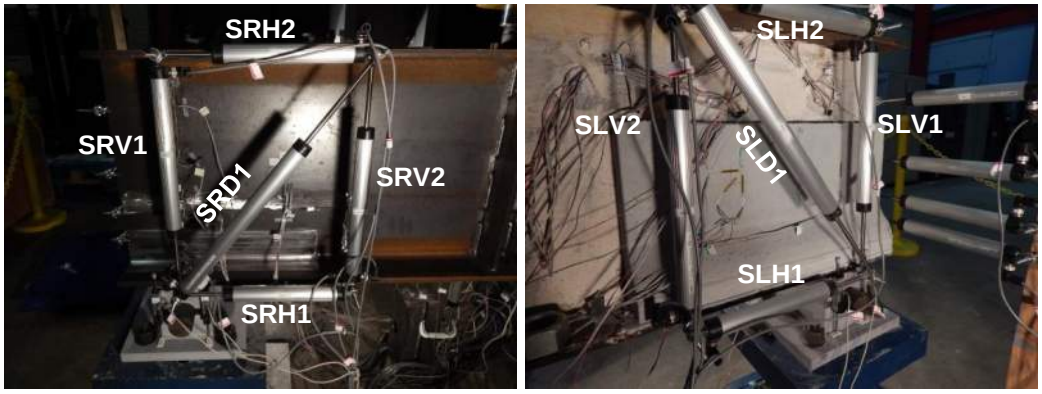

(a) (b)

Figure 3.7 Shear Box Potentiometers

(a) Right Side Shear Box on the Damaged Girder, (b) Left Side Shear Box on the Repaired Girder

Four attachment points for the shear box were situated on both the top and bottom flanges. The first set was placed on the flanges at the center line of the bearing. The second pair was positioned 16 in past the bearing towards the loading point. The 16-in spacing allowed the shear box to extend past the damaged section, but not past the end of the repair. This would include deformations of the entire damage section. Deformations with the repair could be over-estimated if the second set extended past the repair. This would be due to difference of stiffness between the two locations. Figure 3.7 shows the labeling for each shear box.

The potentiometers were fixed to the top bearing using double-sided tape. The spring potentiometers were positioned with their edges on the bearing edge. This provided the largest spacing from the rotation point. This results in larger displacement readings. The spacing between the sensors measured $4^{7}/_{8}$ in. A $^{1}/_{8}$-in Polytetrafluoroethylene (PTFE) plate was glued to the base of the bearing. This provided a smooth surface for the potentiometers to read from. Figure 3.8 shows the bearing potentiometers

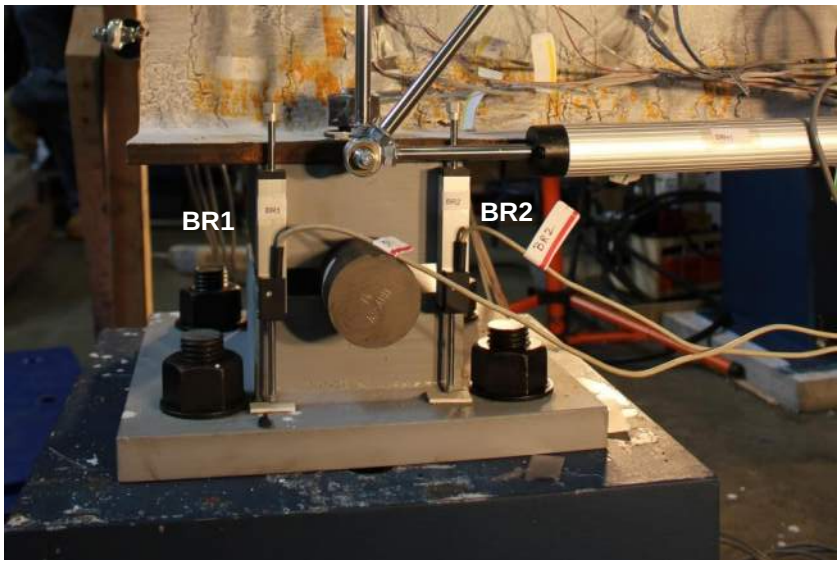

Figure 3.8 Bearing Potentiometers

Displacement data from the shear box is combined with the bearing rotation data to calculate the displacements of the flange at the four attachment points. These displacements are used to calculate the shear, longitudinal, and vertical strains of the shear box. The methodology used in these calculations is explained.

Figure 3.9 shows the numbering for the four attachment points for the shear box, definition of the coordinate axis, and the three critical angles used in calculations. Two

initial assumptions are made: 1) point 1 was fixed, and defined as the origin (x_1=y_1=0); and 2) θ_0, the initial bearing rotation, was 0. These assumptions left six unknowns: x_2, y_2, x_3, y_3, x_4, and y_4. These unknowns were balanced by six variables: H_1, H_2, V_1, V_2, D_1, and θ denoting the length of each potentiometer and the rotation of the bearing. The first and second prefix letter denoting shear box and side are excluded for brevity. Initial lengths of each potentiometer are known from measurements. The displacement measurements are combined with these values to acquire the length of each potentiometer.

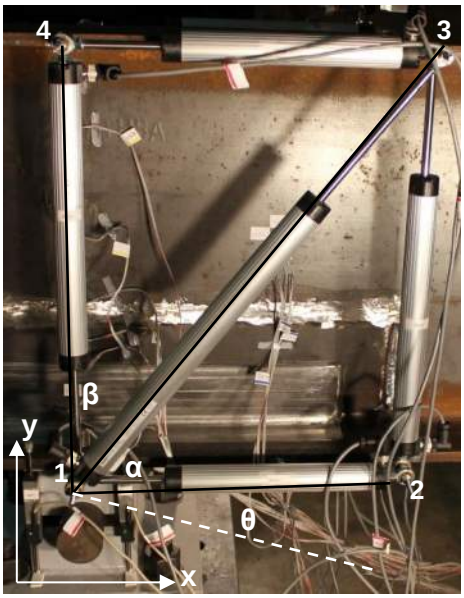

Figure 3.9 Definition of Nodal Locations and Angles in the Shear Box

Definitions of θ, α, and β are given in Equation 3.1. Displacements of the two bearing, *BR1* and *BR2*, and the distance between them, L_B are to calculate θ. Orientation values for positive θ are shown in Figure 3.9. The lengths of the five potentiometers can be used to calculate the angles α and β. This is done using the law of cosines.

$$\theta = \tan^{-1}\left(\frac{BR2 - BR1}{L_B}\right)$$
$$\alpha = \cos^{-1}\left(\frac{D_1^2 + H_1^2 - V_2^2}{2D_1H_1}\right)$$
$$\beta = \cos^{-1}\left(\frac{D_1^2 + V_1^2 - H_2^2}{2D_1V_1}\right)$$

Equation 3.1 Definition of Critical Angles within the Shear Box

With the critical angles calculated, they can be used in Equation 3.2 to calculate the positions of the attachment points 2, 3, and 4.

$$x_2 = H_1 \cos(\theta)$$
$$y_2 = -H_1 \sin(\theta)$$
$$x_3 = D_1 \cos(90 + \theta - \alpha)$$
$$y_3 = D_1 \sin(90 + \theta - \alpha)$$
$$x_4 = V_1 \sin(90 + \theta - \alpha - \beta)$$
$$y_4 = V_1 \cos(90 + \theta - \alpha - \beta)$$

Equation 3.2 Calculation of the Positions of Attachment Points in the Shear Box

This provides the longitudinal (*x*) and vertical (*y*) positions of the attachment points through the entire test. Longitudinal and vertical displacements, *u* and *v*, respectively, are calculated from these positions. The assumption is made that these points represent a Q4 element: a two-dimensional, four-node plate element. A sample Q4 element is shown in Figure 3.10. The displacement field describes the displacements of all points within the element. The generalized displacement field for a Q4 element is given in Equation 3.3.

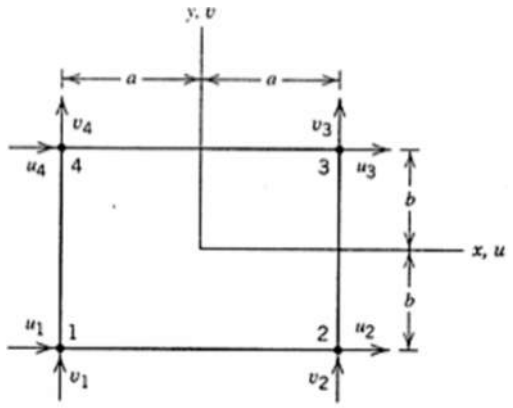

Figure 3.10 Basic Q4 Finite Element

$$u = \varphi_1 + \varphi_2 x + \varphi_3 y + \varphi_4 xy$$
$$v = \varphi_5 + \varphi_6 x + \varphi_7 y + \varphi_8 xy$$

Equation 3.3 Displacement Field for the Q4 Element

The displacement field can be rewritten such that φ_i in the equation can be replaced with four shape function for the Q4 element. A shape function is a Lagrangian interpolation with a value of one at a single coordinate node, and values of zero at all other nodes (Fung & Tong, 2010). The shape functions of the Q4 element are shown in Equation 3.4.

$$N_4 = \frac{(a-x)(b+y)}{4ab} \quad N_3 = \frac{(a+x)(b+y)}{4ab}$$
$$N_1 = \frac{(a-x)(b-y)}{4ab} \quad N_2 = \frac{(a+x)(b-y)}{4ab}$$

Equation 3.4 Shape Functions of the Q4 Element

Using Equation 3.4, the displacement field in Equation 3.3 can be rewritten in terms of the shape functions, as is done in Equation 3.5. This replaces the φ_i with N_i, and x and y with u_i and v_i.

$$\begin{Bmatrix} u \\ v \end{Bmatrix} = \begin{bmatrix} N_1 & 0 & N_2 & 0 & N_3 & 0 & N_4 & 0 \\ 0 & N_1 & 0 & N_2 & 0 & N_3 & 0 & N_4 \end{bmatrix} \begin{Bmatrix} u_1 \\ v_1 \\ u_2 \\ v_2 \\ u_3 \\ v_3 \\ u_4 \\ v_4 \end{Bmatrix}$$

Equation 3.5 Shape Function Based Displacement Field of a Q4 Element

From classical solid mechanics, strain is the derivative of displacement. The displacement field for the Q4 element can therefore be transformed into a strain field by taking the spatial derivatives, as defined in Equation 3.6. This is used to calculate the strain at the center of each element.

$$\begin{Bmatrix} \varepsilon_x \\ \varepsilon_y \\ \gamma_{xy} \end{Bmatrix} = \begin{Bmatrix} \frac{du}{dx} \\ \frac{dv}{dy} \\ \frac{dv}{dx} + \frac{du}{dy} \end{Bmatrix} = \frac{1}{4ab} \begin{bmatrix} -(b-y) & 0 & (b-y) & 0 & (b+y) & 0 & -(b+y) & 0 \\ 0 & -(a-x) & 0 & -(a+x) & 0 & (a+x) & 0 & (a-x) \\ -(a-x) & -(b-y) & -(a+x) & (b-y) & (a+x) & (b+y) & (a-x) & -(b+y) \end{bmatrix} \begin{Bmatrix} u_1 \\ v_1 \\ u_2 \\ v_2 \\ u_3 \\ v_3 \\ u_4 \\ v_4 \end{Bmatrix}$$

Equation 3.6 Strain Field of a Q4 Element

In the formulation, *2a* was taken to be the average of H_1 and H_2, and *2b* was the average of V_1 and V_2. A MatLab code was developed to perform the steps given in this section. A sample of the code is available in Appendix E.

3.6 STRAIN GAUGES

Thirty channels of strain data on the steel girder are collected in each test. An additional ten channels are added in the repaired girder: eight to read strains on the concrete, and two on shear studs.

Strain gauges utilize a small linear grid resistor mounted to a non-conductive backing material. This linear grid is visible in Figure 3.11a. The gauge is firmly fixed to the surface of the material. The gauge has a known resistance. Strain in the material can be determined from the change in voltage as the gauge deforms with the material.

To attach the gauge, the surface of the steel must be prepared. This is done by first grinding the steel to remove the patina. The surface of the steel is rubbed with a 120-grit sandpaper to remove surface rust and optimize the surface for adhesion of the gauges, Figure 3.11b. Positions of the gauges are measured and marked on the edge of the girder. Lines are scribed into the steel with a T-square and scribe, Figure 3.11c. This line acts as one of the alignment marks for the gauge. Gauge alignment marks are visible on the gauge in Figure 3.11a. Marker lines are placed on each side of the scribed line to align a perpendicular scribe line for the second alignment mark. The intersection of these perpendicular marks is shown with an arrow in Figure 3.11d. The surface of the ground and scribed steel is cleaned with a rag and acetone until no more residue is present, Figure 3.11e. With the surface prepared, the gauge is ready to be applied.

To position the gauge, it is adhered to a piece of clear tape, and the alignment marks on the gauge carefully positioned over the scribe lines, Figure 3.11f. With proper positioning of the gauge, the tape is pulled back to expose the back of the gauge. The tape is not fully removed to maintain alignment. All strain gauges used are attached using a cyanoacrylate adhesive, Figure 3.11g. With the adhesive applied, the tape is replaced, and the gauge held down for approximately one minute. A thin piece of PTFE is used as a nonstick barrier to prevent the adhesive from bonding to skin. Once the gauge is adhered, the clear tape is removed and the gauge labeled. Figure 3.11h shows the finished and labeled gauge. Before the concrete was cast, the gauges and wiring were protected by mastic tape, Figure 3.11i. Mastic tape is rubber-based soft and non-conducting tape which will protect the gauges against abrasion from the concrete.

Mounting the gauge on concrete follows the same procedure, except does not include grinding and sanding. The surface is prepared by cleaning with acetone, and

marked with pencil. The porous surface of the concrete removes the need for sanding. The gauge is aligned and glued with the same clear tape and cyanoacrylate adhesive.

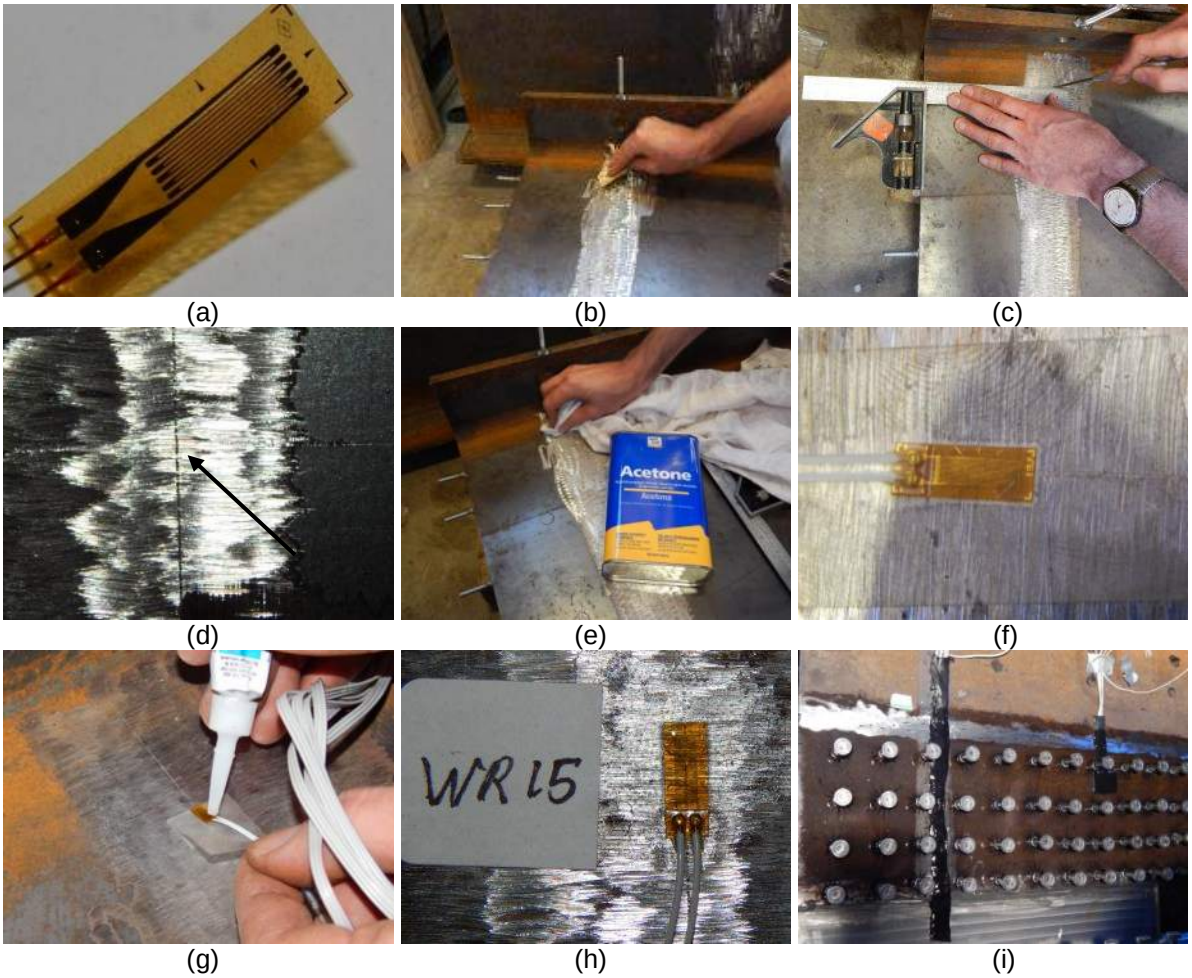

(a) (b) (c)

(d) (e) (f)

(g) (h) (i)

Figure 3.11 Bonding the Strain Gauges to the Steel

(a) Linear Grid Pattern on Strain Gauge, (b) Sanding the Ground Steel Surface, (c) Scribing Alignment Marks, (d) Pair of Perpendicular Marks, (e) Washing Surface with Acetone, (f) Strain Gauge Positioned with Clear Tape, (g) Applying Cyanoacrylate Adhesive to Gauge Back, (h) Adhered and Labeled Strain Gauge, (i) Black Mastic Tape Protection for Gauges and Wires in Concrete Application

3.6.1 Axial Strain Gauges

Six uniaxial strain gauges are positioned vertically along the height of the girder at the centerline of the bearing on each side of the web. Four additional gauges are positioned a distance of 10 in from the centerline of the bearing. The gauge identification uses a two letter prefix and two letter suffix. The first letter of the prefix is 'W' for web, and a second denotes the side. The first digit of the suffix is '1' at the bearing and '2' away from the bearing. The second digit ranges from 1-6 for the

position on the height. The gauges at the bearing were placed on opposite sides of the web at the same height. The difference between the axial strains on the surface of the web can predict buckling in the web. This is because strains diverge due to bending stresses developing. Gauges located away from the bearing detect differences in the vertical strain caused by alteration of the load path with the addition of the concrete panel.

The axial gauges used in the experiment are gauge type KFH-6-350-C1-11L3M3R manufactured by Omega Engineering. These gauges are pre-wired, 3 wire strain gauges with a resistance of 351.2Ω and a gauge factor of 2.04. These gauges utilize a 0.24 in x 0.079 in constantan foil grid on a 0.41 in x 0.15 in polyimide carrier. The axial strain gauges were recorded on the MX1615 at a rate of 20 Hz. The gauge can be seen in Figure 3.12a.

(a) (b)

Figure 3.12 Omega Strain Gauge and Axial Web Gauge Arrangment

(a) Omega KFH-6-350-C1-11L3M3R Uniaxial Strain Gauge, (b) Positioning of the First and Second Rows of Axial Strain Gauges on the Damaged Girder

Sixteen axial gauges were used on the web of the girder. The right side of the girder only had a column of gauges located at the center of bearing. The left side of the girder had two columns of gauges. The first line was at the centerline of the bearing, and the second was 10 in from the centerline of bearing toward the loading point. The gauges were distributed along the height of the web to capture the distribution along the height of the girder. The vertical positioning of the gauges was determined from strain distribution in the preliminary finite element analysis. The locations of the strain gauges

can be seen in Figure 3.12b. Table 3.1 gives the labels and measurements to each of the gauge centers.

Table 3.1 Positioning of Axial Gauges on the Web

Gauge Label	Longitudinal Measurement from Girder End (in)	Vertical Measurement from Bottom of Girder (in)
WL11/WR11	6.0	2.5
WL12/WR12	6.0	4.5
WL13/WR13	6.0	6.5
WL14/WR14	6.0	8.5
WL15/WR15	6.0	12.5
WL16/WR16	6.0	18.5
WL21	16.0	2.5
WL22	16.0	8.5
WL23	16.0	12.5
WL23	16.0	18.5

3.6.2 Rosette Strain Gauges

A strain gauge rosette is included on each side of the web on the girder. A rosette is an arrangement of multiple strain gauges in a defined orientation. The naming convention for the rosettes had a three letter prefix and one letter suffix. The prefix 'WS' for web shear followed by either 'R' or 'L' denoting the side of the girder. The numerical suffix was 1-3 following the numbering convention outlined in Section 3.3. The three strains from this rosette can be used to calculate the maximum shear at the placement of the girder.

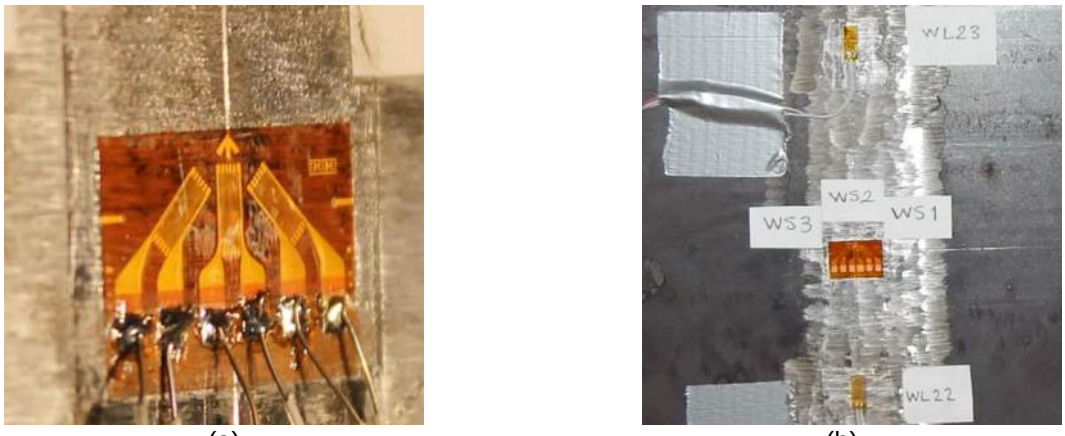

(a) (b)

Figure 3.13 Micro-Measurements Rosette Strain Gauge

(a) Micro-Measurements CEA-06-125UR-120 Strain Gauge Rosette, (b) Position of Left Side Rosette with Respect to WL22 and WL23

The rosettes used are manufactured by Micro-Measurements, gauge type CEA-06-125UR-120. This is a 0-45-90° non-stacked 120.2 Ω rosette. It has a gauge factor of 2.075. The rosette has three 0.25 in x 0.12 in constantan foil grids mounted on a 0.75 in x 0.50 in polyimide carrier. The gauge can be seen in Figure 3.13a. The rosette gauges are recorded on the MX 1615 at a rate of 20 Hz. In addition to the six channels associated with the two rosettes, two computational channels were used in the MX-1615 to calculate maximum shear in real time while recording. CatmanEasy would take the values from the three gauges and calculate the maximum strain based on Equation 3.7.

$$2\gamma_{max} = |\epsilon_1 - \epsilon_2| = \sqrt{2[(WS_1 - WS_2)^2 + (WS_2 - WS_3)^2]}$$

Equation 3.7 Maximum Shear Strain Equation

The gauges were positioned so they would lie in a line running from the bearing to the point of loading. This was where the finite element analysis predicted highest shear strain. The gauges were placed longitudinally 10 in from the bearing and 9.5 in from the bottom flange. This positioned it between WL22 and WL23, as seen in Figure 3.13b.

3.6.3 Flange Strain Gauges

Eight uniaxial strain gauges are positioned along the bottom flange to measure changes in flexural strain in the flange. The naming convention utilizes a two letter prefix: ‘F’ for flange and ‘R’ or ‘L’ denoting side. A one number suffix is used: 1-4 following the numbering convention. This resulted in eight gauges: FR1, FR2, FR3, FR4, FL1, FL2, FL3, and FL4.

Uniaxial strain gauges used on the flange are manufactured by Tokyo Sokki Kenkyujo Co., gauge type FLA-5-11-3L, Figure 3.14a. These gauges utilize a pre-wired 0.20 in x 0.06 in constantan foil gird with 119.5Ω resistance and 2.1 gauge factor. The gauge is mounted on a 0.39 in x 0.12 in epoxy carrier. Flange gauges are recorded using the NI-9235.

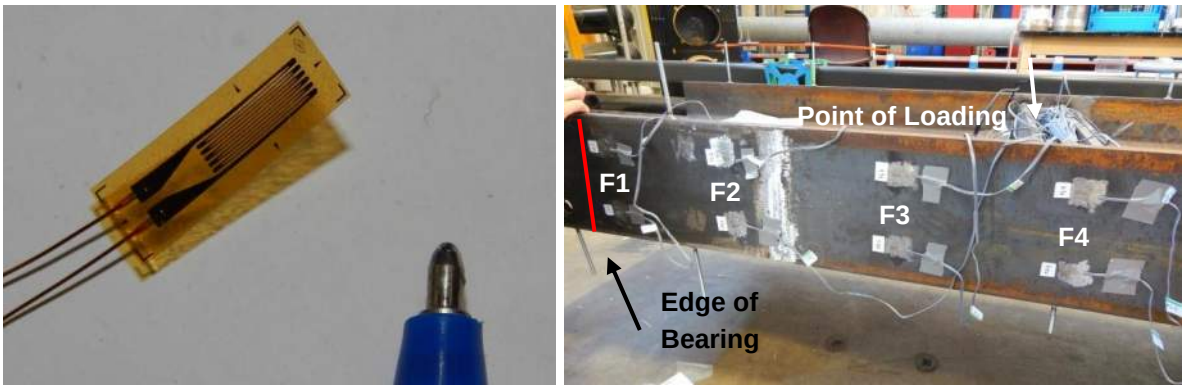

(a) (b)

Figure 3.14 TSK Uniaxial Gauge and Flange Gauge Positioning.

(a) TSK FLA-5-11-3L Uniaxial Strain Gauge, (b) Bottom Flange Gauge Positioning

Gauges were placed in pairs on both the left and right flange of the girder. These pairs were distributed along the bottom flange to record the distribution of flexural strains. They were placed at distances of 10.5 in, 19.5 in, 29.5 in, and 38.5 in from the end of the girder for F1-F4 gauges, respectively. These distances were chosen such that the first two would be positioned under the UHPC panel. This was to detect increased strain development from the composite action in the flange from the concrete panel. The furthest gauge was positioned under the load ram, where flexural yielding would first occur. Gauges were placed 2 in from the edge of the flange. This enabled F1 and F2 gauges to be on the reduced portion of the flange. This would detect if loss of thickness caused an increase in flexural strain. The gauge positions are visible in Figure 3.14b. The line indicates the edge of the bearing.

Because the NI-9235 had a minimum sampling frequency of 794 Hz, samples were recorded at 800 Hz sampled down to 20 Hz. A MatLab code was developed to process the data. All the data recorded by the cDAQ-9178 had a consistent timestamp. A vector was made of the timestamp values recorded in the 20 Hz file. The code searched for these timestamps in the 800 Hz file and extracted the corresponding strain values. If the 20 Hz timestamp fell between 800 Hz timestamps, linear interpolation was used to calculate the strain. An example file of this code is available in Appendix E.

3.6.4 Shear Stud Strain Gauges

Two strain gauges were placed on shear studs to measure axial strain in the studs. The gauges were named SS1 and SS2 for shear stud. The gauges used were the Omega Engineering KFH-6-350-C1-11L3M3R, and were recorded using the MX-1615

at a rate of 20 Hz. The axial strains in the studs help to determine load distribution between the studs.

The gauges are positioned on the top row of shear studs at opposite ends of the repair. The studs with installed gauges are circled in Figure 3.15a. The gauges were placed on the vertical portion of the shaft to negate vertical bending strains the gauge may experience. This would isolate the axial strain as the stud elongates. Strain gauge positioning on the stud nearest the end of the girder is shown in Figure 3.15b.

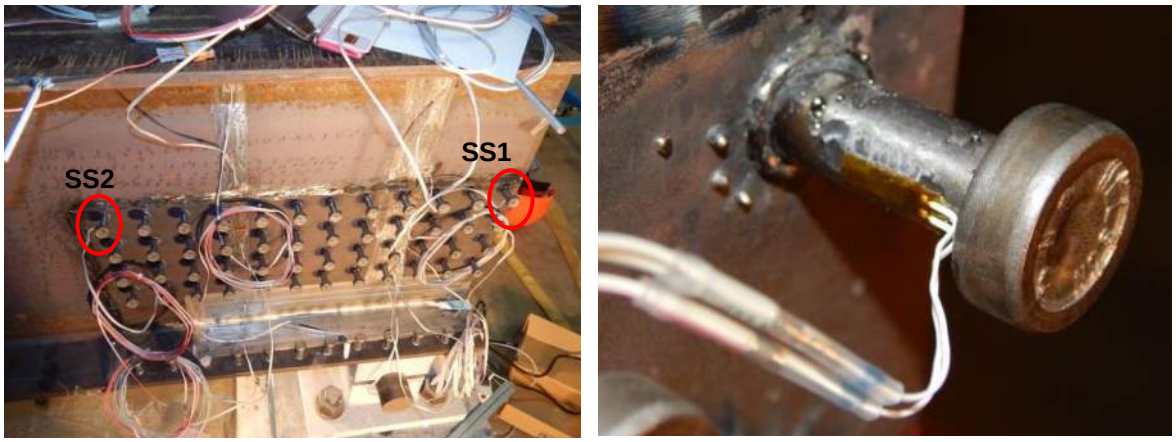

(a) (b)

Figure 3.15 Strain Gauge Installation on Shear Studs

(a) Studs with Installed Strain Gauges, (b) Detail of Strain Gauge Orientation on Stud

3.6.5 Concrete Strain Gauges

Four strain gauges are placed on each of the concrete panels to measure bearing and shear strains. Concrete gauges utilize a three letter prefix for each gauge, and no numerical suffix. The first letter 'C', indicates it was mounted on concrete, the second indicates side, and the third indicates location: 'B' for bearing, 'H' for horizontal, 'V' for vertical, and 'D' for diagonal. This resulted in eight gauges: CRB, CRH, CRV, CRD, CLB, CLH, CLV, and CLD.

The strain gauges used for the concrete are Omega Engineering gauge type SGD-30/350-LY40. This is a 350.1 Ω 1.18 in x 0.12 in constantan foil grid on a 1.42 in x 0.20 in polyimide carrier, and has a gauge factor of 2.05 (see Figure 3.16a). The increased length of this gauge accounts for inhomogeneity of the base material. Strains are recorded using the NI-9236 at a rate of 800 Hz. The same MatLab code is used to extract the data as was used for the flange strains.

The gauges on the left panel are shown in Figure 3.16b. The bearing gauges were in line with the centerline of bearing, 4 in from the top of the panel. This gauge measured axial bearing strains in the concrete to compare to the W1x series of strain gauges. The other three gauges were centered 16 in from the end of the girder and 4 in from the top. The diagonal gauge was oriented at 45° and positioned at the marked center, perpendicular to predicted shear cracks. The horizontal and vertical gauges were positioned one inch from the marked center point. The arrangement of the horizontal, vertical, and diagonal gauges created a rosette pattern to find maximum shear in the panel using Equation 3.7. The gauges *CH*, *CD*, and *CV* would replace WS_1, WS_2, and WS_3, respectively.

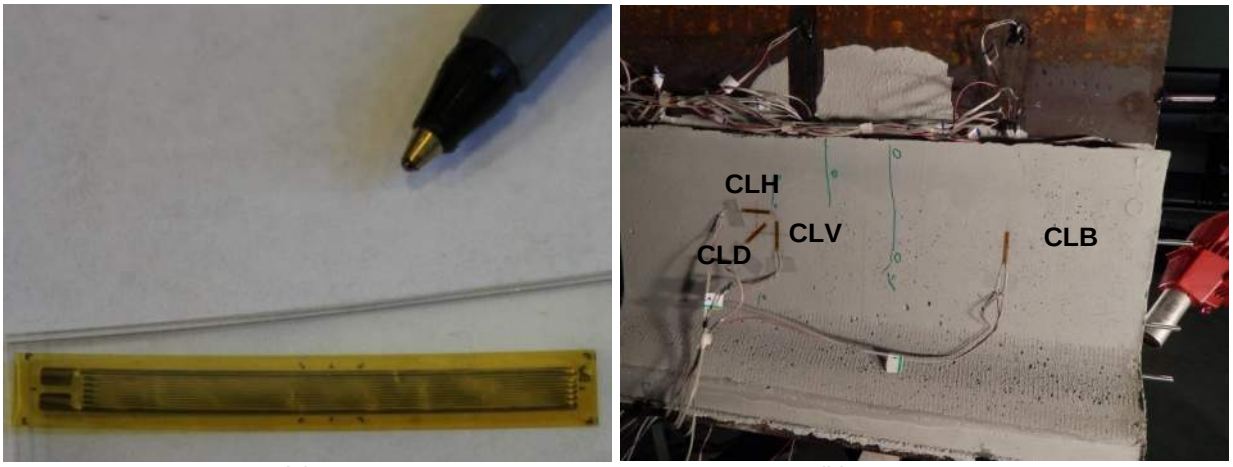

(a) (b)

Figure 3.16 Concrete Strain Gauges and Positioning

(a) Omega Engineering SGD-30/350-LY40 Uniaxial Strain Gauge, (b) Locations of Strain Gauges on Left Concrete Panel

3.7 TEMPERATURE PROBES

In order to monitor the temperature in and around the concrete during curing, four temperature probes were used. All of the probes were RTDs with a class-A 100 Ω platinum element. These probes measure changes in resistance as temperature changes. This class of probe had a scale factor of α=0.00385 Ω/Ω/°C. The probes inserted in the concrete were Omega Engineering PR-20-2-100-1/8-2-E-T RTD probes. These are 2-in long, $^1/_8$-in diameter RTD probes intended for small spaces. No information was available for probes used for air temperature other than class.

Two small temperature probes were inserted in the concrete panel and in one of the concrete cylinders to monitor the internal temperature in each. Figure 3.17a shows the

location of the PR-20-2-100-1/8-2-E-T RTD probe used in the left concrete panel. The probe was $1^{3}/_{4}$ in from the web. The arrow in Figure 3.17b shows the location of the cylinder which had the RTD sensor. Two additional temperature probes were used to record the ambient temperature under the curing blanket and in the Structures Lab. The probe under the blanket is visible on the bearing in Figure 3.17b. Figure 3.17c shows the location of the ambient temperature probe for the Structures Lab.

(a) (b) (c)

Figure 3.17 RTD Temperature Probe Locations

(a) Probe Installed Inside Left Concrete Panel, (b) Probe Locations Under the Curing Blanket, (c) Location of Structures Lab Probe

4 Material Testing

4.1 INTRODUCTION

To fully characterize the materials used in this research, a series of tests were performed on steel and concrete to determine their physical characteristics. This chapter will outline the sample preparation and tests performed on the UHPC used in the panel and the steel from the girder specimens.

4.2 CONCRETE

Fresh and hardened UHPC properties were characterized to determine the suitability of material performance. The flow table test was performed immediately after the mixing process finished. The test determines the ability of the concrete to spread and self-consolidate as well as homogeneously distribute the steel fibers without segregation. If the concrete can self-consolidate, vibratory compaction is not necessary during casting. A series of uniaxial compressive strength tests were performed. These tests were carried out at various times after casting to determine the time-dependent strength development of the concrete. This section will discuss preparation of the samples, detail the tests performed, and present the results from the tests.

4.2.1 Flow Table Test

A spread test for self-consolidating concretes was performed based on ASTM C230: Standard Specification for Flow Table for Use in Tests of Hydraulic Cement (ASTM, 2014a). This test is the counterpart to a slump test for non-consolidating concretes. The test utilizes a conical bronze mold. The mold is 2 in tall and has upper and lower diameters of $2^3/_4$ in and 4 in, respectively. Due to the high consolidation of the UHPC, the standard 10.0 in diameter bronze flow table was not used. Instead, a glass panel

laid over paper marked with the same gradation as the standard flow table was used. As a consequence, rotation and drops as standardized in ASTM C230 were not performed. The mold and flow table can be seen in Figure 4.1a. The mold was centered on the flow table and filled with UHPC, Figure 4.1b. The filled mold was lifted while rotating the cone to allow the concrete to flow, Figure 4.1c. The concrete remaining in the mold was removed to so that the full volume of concrete was spread, Figure 4.1d.

Figure 4.1e shows the UHPC as it spreads on the flow table. The spread of the concrete was measured after no further movement could be visibly observed, and compared to manufacturer's standards for the material based, Figure 4.1f. The results of the flow table test gave spreads of 11.0 in and 10.8 in for the right and left panel batch, respectively. These are within the manufacturer's standards for the mix. This level of spread demonstrates the concrete is able to flow and self-consolidate.

The concrete was sufficiently viscous to prevent steel fiber segregation. This was checked by investigating the edge of the spread as well as the top layer of the UHPC in the mixer and in the buckets. In these critical areas sufficient steel fibers were noticed indicating the suitable viscosity of the UHPC matrix. If the concrete would have been less viscous, and thus significantly more flowable, fiber segregation might have occurred leading to a separation of the fiber reinforcement from the matrix. The fibers would have sunk to the bottom of the cast and detrimentally affected the performance.

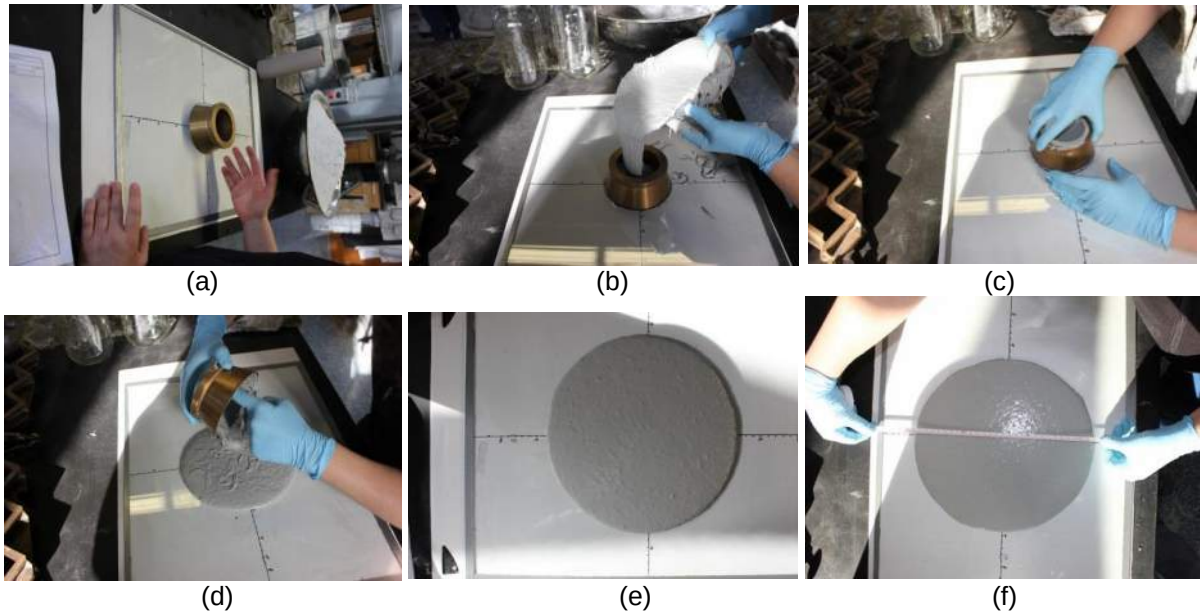

Figure 4.1 Flow Table Test Setup and Execution

(a) Flow Table and Conical Mold, (b) Filling the Conical Mold with UHPC, (c) Lifting the Filled Conical Mold, (d) Removing Excess UHPC from the Mold, (e) UHPC Spreading on Flow Table, (f) Measuring Spread

4.2.2 Compressive Strength Test

A series of compression tests were performed based on specifications given in ASTM C39: Compressive Strength of Cylindrical Concrete Specimens (ASTM, 2014b). Specimens were nominally 6 in × 3 in, per the 2:1 H:D requirement specified by C39. Specimens were cast in three batches. The first was the test batch; the casts for the right and left panel were second and third, respectively. This would give a representative sample of strength from each panel. Specimens were cast in plastic molds and placed under the insulated blanket to have similar curing conditions to the panel (see Figure 4.2a). The cylinders were demoled, cut, ground and tested at pre-determined times after casting to determine time-dependent strength development of the concrete. The tests performed at each interval followed the same procedure outlined in this section.

Figure 4.2 Concrete Cylinder Preparation

(a) Concrete Specimens Under the Curing Blanket, (b) Cylinders After Removal from the Plastic Molds, (c) Cylinder Secured in the Wet Saw, (d) Cylinder After Wet Saw Cutting, (e) Diamond End Grinder, (f) Measuring Cylinder Diameter

Specimens were prepared for testing in UCONN's Advanced Cementituous Materials and Composites (ACMC) Lab. Three plastic specimen containers were chosen at the time of testing. The cylinders were removed from the plastic containers

using a box cutter. These cylinders were then labeled in accordance to cast number, time since casting, and number of cylinder of same test series. As an example, the cylinder designated 2D3C2 was tested two days after casting, was from the right panel cast, and was the second cylinder tested in that series. These cylinders had uneven tops from the casting process. The unevenness and the labeling can be seen in Figure 4.2b. The uneven tops of the cylinders were cut using a wet concrete saw, Figure 4.2c. Figure 4.2d shows the cylinder after cutting. To guaranteed planeness of load faced surfaces within 0.5° specified in ASTM C39, the cylinders were loaded in to a diamond end grinder, Figure 4.2e. Both ends of the cylinders were ground within the specifications of ASTM C39 checked by a dilatometer. The finished dimensions of the cylinders were recorded using a digital caliper, as shown in Figure 4.2f. Two measurements of diameter were taken at third-points, and one measurement of length was taken. Mass of each of the cylinders was recorded using a digital scale.

The prepared samples were taken back into the Structures Lab. Compression tests were performed using the Structures Lab SATEC 400 kip load frame, with MTS FlexTest-40 controller. This controller is capable of extremely fine control on the hydraulics of the load frame. The load frame and controller are visible in Figure 4.3a. The specimen would sit on a pivot table which allowed for rotation while the top platen was fixed.

Each specimen was fitted with an axial-circumferential compression device and loaded into the load frame, Figure 4.3b. This devise has a pair of Linear Strain Converting Transducers (LSCT). LSCTs are highly accurate linear displacement measurement devises uses a different principal than potentiometric transducers to measure displacement. An LSCT causes small cantilever beams within the devise to bend as it displaces. These beams are instrumented with strain gauges, and the change in strain can then be converted to displacement. The LSTCs used in the compression devise were Humboldt model HM-2310.04. These LSCT had 0.4 in stroke and accuracy to 0.00004 in. LSCTs were used to measure axial and circumferential displacements of the concrete during the duration of the test. This enabled the calculation of both axial strain and circumferential strain required for calculation of stress strain curves and determination of the Poisson’s ratio.

Loading protocol was displacement controlled, at a rate of 0.02 in/min. This allowed stress development around the standard 35 psi/s defined in ASTM C39. Displacement controlled was used to show the ductility of the specimens after failure occurred. Had force control been used, as peak strength was reached the actuator would have accelerated. This could have damaged the axial-circumferential compression device.

Displacement control enabled the measurement of material softening as well as assured the instrument would remain undamaged.

Figure 4.3c shows the ability of the steel fibers to bridge cracks. The specimens tested exhibited five basic failure modes, shown in Figure 4.3d-h. Of the 33 specimens tested, four exhibited cone-cone failure (Figure 4.3d), six had cone-split failure (Figure 4.3e), four displayed cone-shear failure (Figure 4.3f), nine failed with a shear failure (Figure 4.3g) and ten had columnar failure (Figure 4.3h).

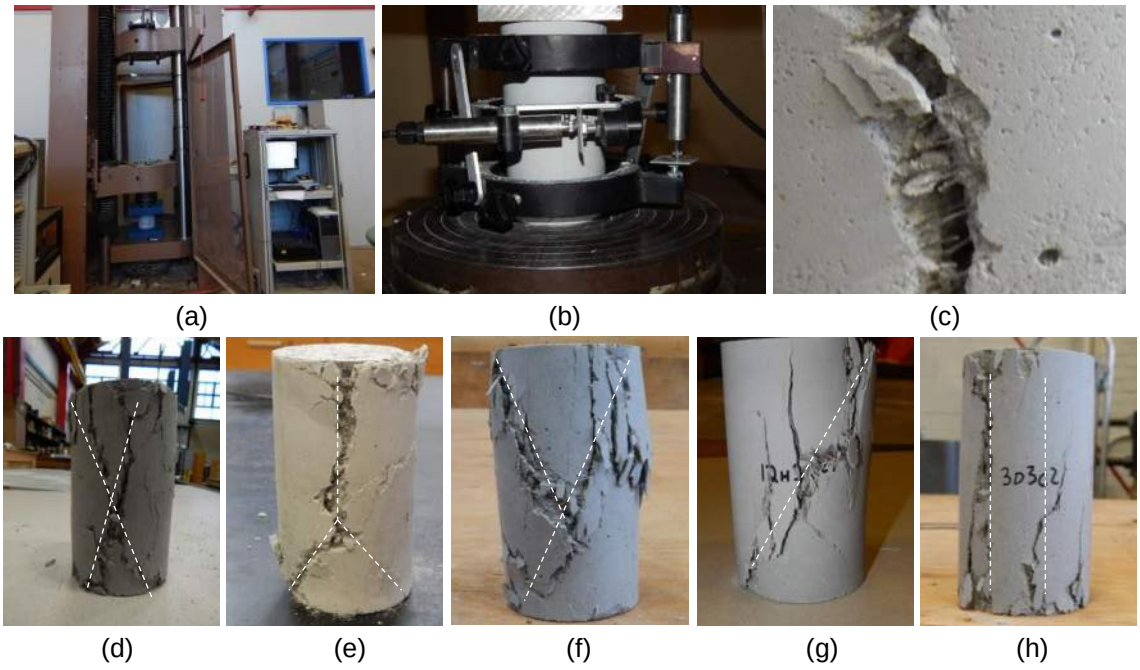

Figure 4.3 Concrete Compressive Test Setup and Failure Modes

(a) SATEC 400 kip Load Frame with MTS FlexTest-20 Controler, (b) Cylinder in Load Frame with Axial-Circumferential Compression Devise, (c) Fibers Bridging a Large Crack in UHPC, (d) Cone-Cone Cylinder Failure, (e) Cone-Split Cylinder Failure, (f) Cone-Shear Cylinder Failure, (g) Shear Cylinder Failure, (h) Columnar Cylinder Failure

4.2.3 Concrete Curing and Strength Development

Three batches of concrete were mixed and cylinders cast, one for the trial mix, and one from each of the concrete panel batches. Cylinders were tested from these various mixes at 12 hours, 16 hours, 1 day, 2 days, 3 days, 4 days, 7days, 14 days, 28 days and 38 days. The trial mix was cured in the concrete lab, which maintained a constant temperature around 73°F. The two mixes cast with the panels were cured in the Structures Lab under the insulated blanket with an installed heater, see Figure 4.2a.

Temperature readings from the RTD probes are graphed in Figure 4.4. The temperature in the concrete panel remained higher than the concrete test cylinder. The initial peak temperature occurred after 12 hours leading to 102°F in the panel and 76°F in the cylinder. The drop in tarp temperature seen after 1 day occurred from repositioning the tarp. The spike at two days occurred from repositioning the heater. Average temperature for the concrete was 84°F in the panel and 76°F in the cylinder. Average temperature under the tarp was 72°F.

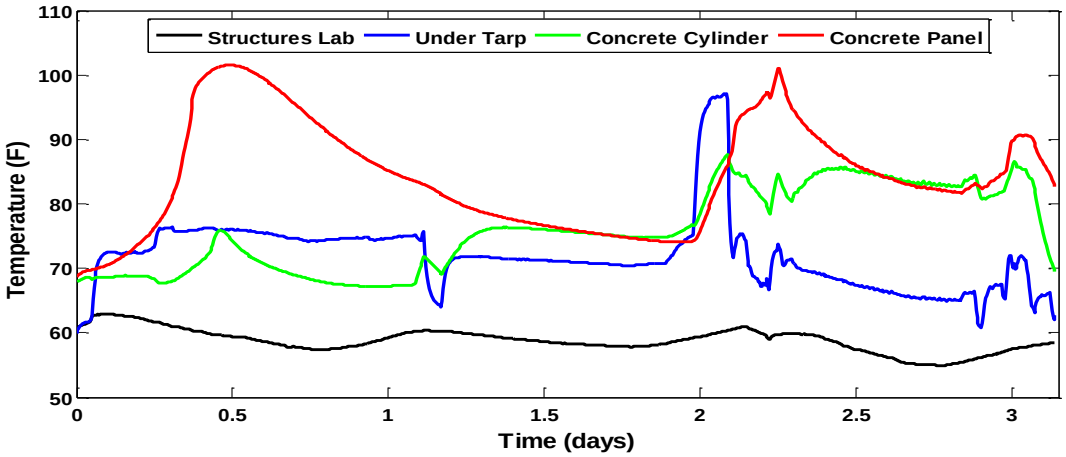

Figure 4.4 Readings from the RTD Probes during Initial Concrete Cure

Figure 4.5a shows the time dependent compressive strength development curve. This mix achieved a compressive strength of 4 ksi in 12 hours when cured in laboratory conditions. Testing occurred four days after casting. The compressive strength was 16 ksi at the time of testing. Variations in strength were noted in cylinders for the batch of concrete cast with the panels. This is potentially due to a temperature gradient under the blanket caused by the location of the heater. The actual strength of the panel was likely higher than the cylinders at the time of testing. This can be inferred from the higher internal temperature of the panel. Figure 4.5b is a representative stress-strain relation for a cylinder four days after casting.

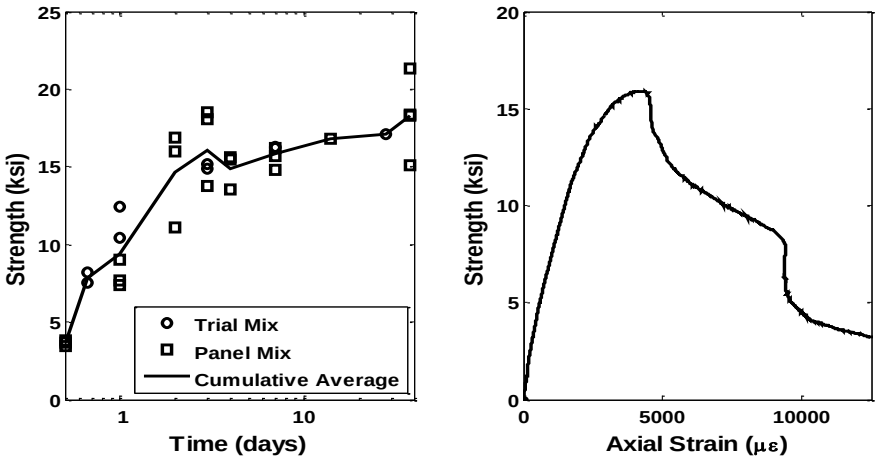

(a) (b)

Figure 4.5 Strength Characteristics of Ductal JS-1212

(a) Time-Dependent Strength Development, (b) Cylinder Stress-Strain Relationship at Four Days

4.3 STEEL

In order to determine the performance of the steel in the girder, a series of coupons were fabricated from the web steel of the girder. These coupons were tested in a standard tensile test using the same 400 kip SATEC load frame. There are three horizontal platens in the load frame, Figure 4.3a. The center platen remains stationary, while the top and bottom platen displace upwards to load. Specimens loaded between the middle and bottom platen are tested in compression. Specimens loaded between the middle and top platens experience tension. This section will cover the fabrication, test setup, and results of the steel tensile tests.

4.3.1 Coupon Fabrication

Specimens were cut from the web of the girders after testing had finished. The coupons were cut from the non-studied end of the girder so damage was minimal. Coupon dimensions were selected in accordance to ASTM E8: Standard Test Methods for Tension Testing of Metallic Materials (ASTM, 2013). Because the webs of the girders were nominally $^{3}/_{8}$-in thick, dimensions were used for a standard plate-type specimen. These dimensions can be seen in Figure 4.6. Coupons oriented vertically along the height of the web. This was chosen because the loading at the bearing was considered the critical to the failure mechanism in this experiment. Therefore, the critical stress-strain relationship in the FEM should be from this orientation.

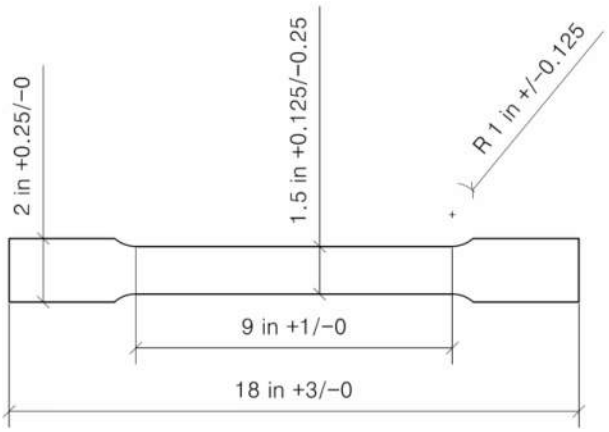

Figure 4.6 Dimensions of ASTM Standard Plate-Type Specimen

The portions of the webs removed for coupons are shown in Figure 4.7a-b. Two coupons were fabricated from each plate removed. The plates were cut in half using a band saw to create the individual specimens. The blanks were then placed into a CNC milling machine and the central portion of the coupon reduced to its finished width. The fillets between the gauge length and the grips were subsequently added. The finished specimens can be seen in Figure 4.7c.

(a) (b) (c)

Figure 4.7 Fabricated Steel Coupons

(a) Sections Removed from the Damaged and Undamaged Girders, (b) The Removed Web Blanks, (c) The Finished Coupons

4.3.2 Tensile Test

The specimens were held in the load frame with standard wedge grips. A specimen was loaded into the center of the wedge grips to minimize eccentricity, Figure 4.8a. The grips were in contact with as large a portion of the coupon as possible to avoid slippage. The specimen was first secured in the top grip. The coupon was then plumbed with a bubble level, Figure 4.8b. The middle platen was raised until the bottom wedge grip could tighten onto the specimen, Figure 4.8c. Due to the weight of the bottom wedge grips, the handle was weighted to maintain a solid grasp onto the specimen. This weight also prevented the bottom wedges from falling after failure of the specimen.

(a) (b) (c) (d)

Figure 4.8 Installation of the Steel Coupons

(a) Centering the Coupon in the Top Chuck, (b) Leveling the Specimen, (c) Securing the Coupon in the Bottom Chuck, (d) Attaching the Extensometer

With the specimen installed in the load frame, an extensometer was placed onto the specimen, Figure 4.8d. The extensometer used in this experiment was an Epsilon model 3543-0400-400T-ST. It has a 4 in gauge length and 4 in extension and utilizes a full-bridge strain gauge configuration to measure displacement. Its linearity accuracy is 0.006 in. The extensometer was placed on the specimen centered on the testing length at an approximate initial length of 6 in. This is less than the 8 in specified by ASTM E8, but long enough to record up to 33% strain. The initial length of the extensometer was recorded as the baseline length for strain calculation.

(a) (b) (c) (d)

Figure 4.9 Testing of the Steel Coupon

(a) Striations Forming in the Steel at the Onset of Yielding, (b) Striations Spreading Through the Length of the Coupon, (c) Necking in the Coupon during Softening, (d) The Four Failed Coupons

Specimens were tested displacement controlled until failure at a strain rate of 0.015 in/in/min as is specified by ASTM E8. Damage first became visible as striations in the patina of the steel occurring at 45°, Figure 4.9a. This became visible as yielding of the steel began. This spread through the length of the specimen through the yielding plateau, Figure 4.9b. As strain hardening began, the striations began widening. After peak stress developed, softening began. As softening continued, necking became visible in the specimen, Figure 4.9c. The specimen would ultimately fail by rupturing at the neck, Figure 4.9d. The test was considered valid if the failure occurred within the grips of the extensometer, that way full plasticity could be determined. All of the coupons tested were valid tests.

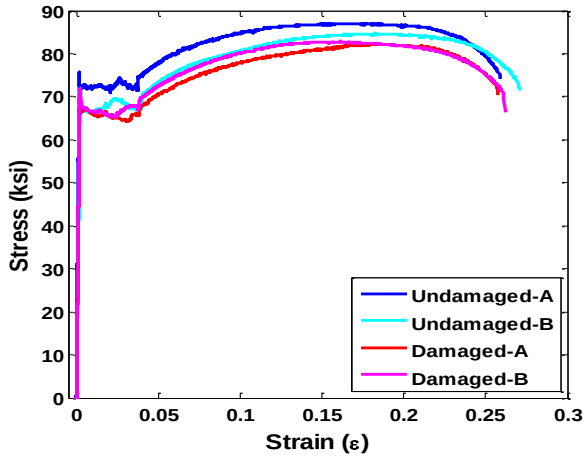

Figure 4.10 Example Stress Strain Curve of the Web Steel

Results of the tensile tests are shown in Table 4.1. Figure 4.10 shows an example stress-strain relation of the steel. The elastic modulus was found to be 33,000 ksi, with upper and lower yield strengths of 72.4 ksi and 66.8 ksi, respectively. Ultimate strength was found to be 84.2 ksi with a total elongation of 26.3%.

Table 4.1 Results of the Tensile Tests

Specimen	Elastic Modulus (ksi)	Yield Strength (ksi)		Ultimate Strength (ksi)	Ultimate Elongation (%)
		Upper Point	Lower Point		
Undamaged-A	34,300	75.8	71.4	87.0	25.9
Undamaged-B	33,000	71.9	66.2	84.7	27.1
Damaged-A	31,800	70.0	64.2	82.1	25.8
Damaged-B	32,900	72.0	65.2	82.8	26.3
AVERAGE	33,000	72.4	66.8	84.2	26.3

5 Experimental Results and Observations

5.1 INTRODUCTION

This chapter presents the data collected from each test. First, observations of the damage progression, failure mechanism, and deformed shape are presented. Critical data collected from the instrumentation is then presented. Data is segregated into load-displacement relationships and load-strain relationships. A comparison of all three tests is made after presentation of the individual test data. This comparison discusses the effects of corrosion damage and the UHPC repair.

5.1.1 Terminology and Damage Identification

A loading and unloading cycle is referred to as a run. Loading protocol outlined in Section 2.7 was given in terms of load ram force. Loads reported in this section refer to studied end bearing load. Consequently, loads for each run will be only about 80% of the increment defined in the loading protocol. Displacements less than 1 in are given in terms of mil. 1 mil = 0.001 in.

The type of damage can be inferred by the orientation of the lines formed in the limestone whitewash. The whitewash forms lines orthogonal to principal compression. Compression causes the whitewash to flake under small strains. Lines are not noticeable under principal tension because tension does not cause the whitewash to flake. This lack of flaking makes the lines not visible. Lines indicating bending damage are perfectly vertical. Shear lines appear inclined. The orientation of shear lines would form perpendicular to shear cracks in concrete. This is because concrete cracking is orthogonal to principal tension.

Conversion of potentiometer displacements to strain can be performed if both ends of the potentiometer are fixed to the girder. This is calculated using the displacement and the initial length of the potentiometer.

5.2 UNDAMAGED GIRDER

5.2.1 General Observations

No damage was visible in the girder in the first five runs up to a load of 120 kip. The first signs of visible damage occurred during run 6, at a bearing load of 140 kip. The damage lines in the whitewash are visible in Figure 5.1. Damage caused by bending stresses occurred on the top of the web by the loading ram, circled in Figure 5.1a. Damage caused by shear stresses occurred at the bottom of the web by the bearing, circled in Figure 5.1b. Damage was present on both sides of the girder. No damage lines were noted at the bottom of the web near the load ram.

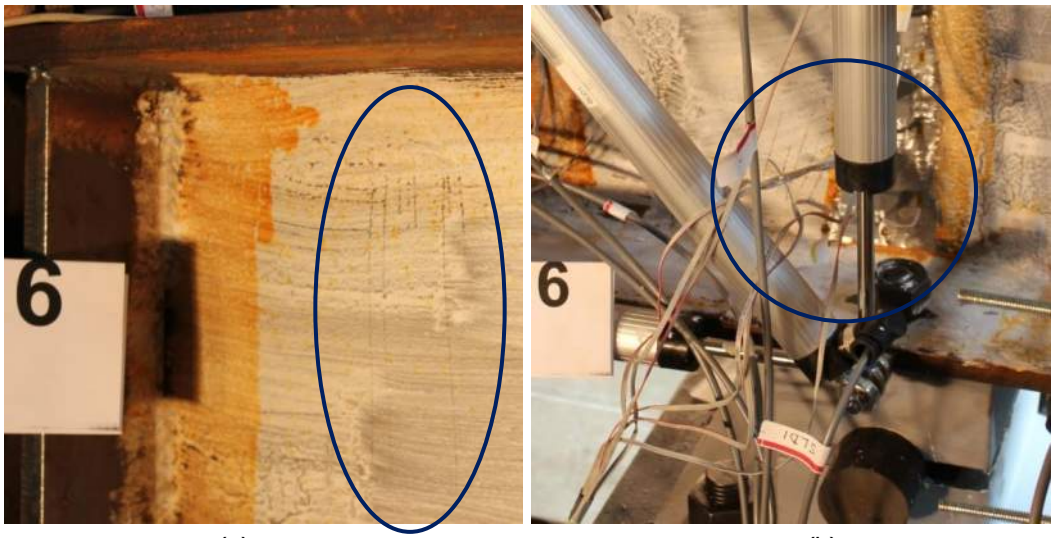

(a) (b)

Figure 5.1 First Signs of Damage in the Undamaged Girder

(a) Flexural Damage Visible to the Upper Web at Load Ram, (b) Shear Damage Visible to the Lower Web at Bearing

Loading continued to 160 kip in run 7, and the damage extended on each side of the girder. Additional damage became visible around these lines. A vertical compression field became visible around the double stiffener at the loading point indicated with the arrow in Figure 5.2a. This can be seen as horizontal lines. A similar vertical compression filed formed around the bearings, shown by the arrow in the Figure 5.2b.

(a) (b)

Figure 5.2 Damage Progression in the Undamaged Girder

(a) Flexural Damage Extension and Additional Vertical Compression Field at Loading Ram, (b) Shear Damage Extension and Additional Vertical Compression Field at Bearing

Failure occurred during run 8, at a load of 180 kip. Failure occurred as web buckling caused the web to deform out of plane. The failure occurred suddenly and took place over the entire height of the bearing. Figure 5.3 shows photos of the failure. This buckling caused the top flange to become tilted.

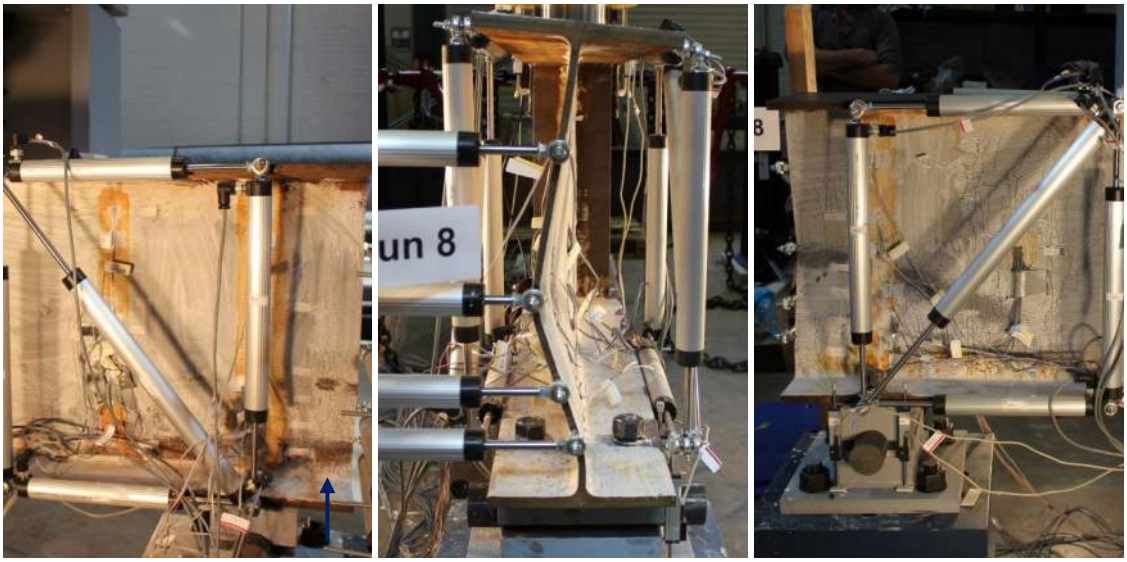

(a) (b) (c)

Figure 5.3 Failure of the Undamaged Girder

(a) Left View, (b) Longitudinal View, (c) Right View

The buckling of the web caused much of the whitewash to flake. Figure 5.4 the flaking caused by the buckling. The whitewash was removed along the entire length of the buckle, from mid-height of the web at the girder end to the base of the web approximately 20 in from the end of the girder. Closer inspections of the orientation of the lines showed they are parallel with the line of buckling. This put them orthogonal to the principal compression. The whitewash on the web opposite these lines was still intact. Only the whitewash at the base of the flange has fallen off, see the arrow in Figure 5.3a.

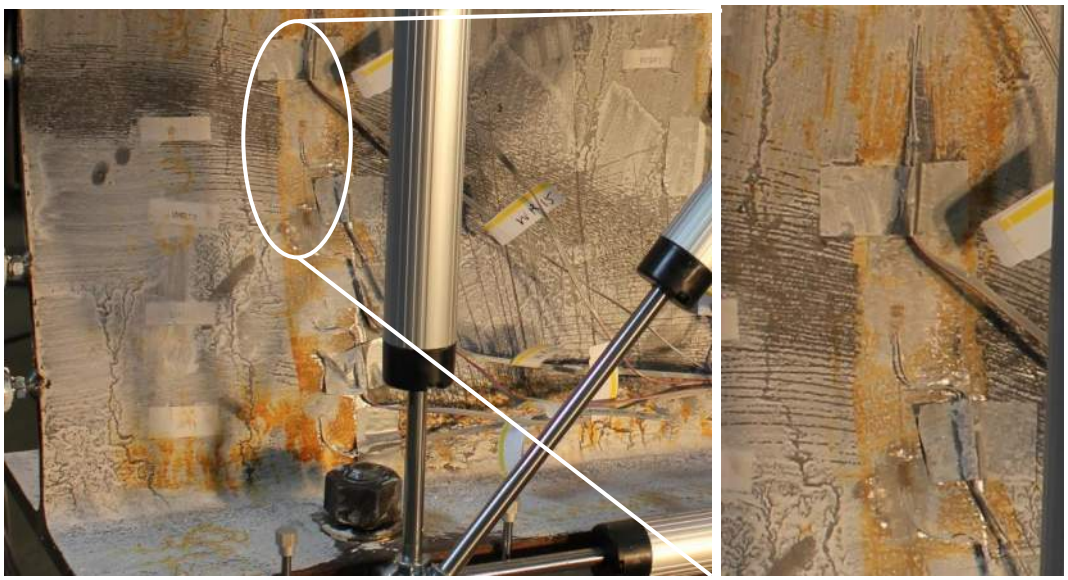

(a) (b)

Figure 5.4 Flaking of the Whitewash after Buckling

(a) Right Side Whitewash Loss from Buckling, (b) Orientation of Lines of Whitewash on Right Side

As loading progressed for the remainder of the test, out-of-plane displacements of the web increased. This occurred due to the buckling of the web. This buckling can be seen in Figure 5.5. The buckle in the web imposed a torque on the top flange. This torque caused a tilt in the top flange. The rotation in the flange was visible at the loading point. The tilt saddle is shown before the test, and after failure in Figure 5.6. The torque on the top flange also caused the bearing to slide. The top half of the bearing began to translate laterally, first becoming visible at a post failure displacement of 0.5 in in run 10, Figure 5.5c. This sliding increased with loading. The rotation of the bearing was also seen to increase. After failure, little to no rotation was visible in the bearing. Bearing rotation remained minimal throughout the remainder of the test. This was due to a pair of plastic hinges in the bottom flange at the point which allowed for

little rotation in the bearing. Bottom flange deformation progression is shown in Figure 5.7. The arrows show the locations of the plastic hinges.

(a) (b) (c) (d) (e)

Figure 5.5 Web Crippling and Bearing Displacement in the Undamaged Girder

(a) Failure Displacement, (b) Displacement +0.25 in, (c) Displacement + 0.50 in, (d) Displacement +0.75 in, (e) Displacement +1.25 in

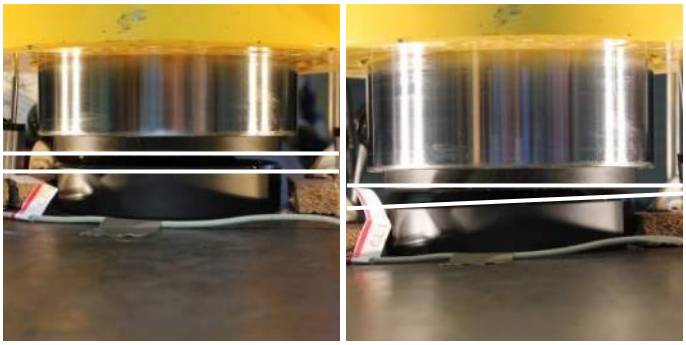

(a) (b)

Figure 5.6 Rotation of the Load Ram Tilt Saddle

(a) Before Testing, (b) After Unloading from Displacement +0.50 in

After the test, clearly defined yield lines were visible on both sides of the web of the girder. These can be seen in Figure 5.8. The dashed lines in the figure show the yield lines from the opposite side. The web in between these yield lines remained mostly plane. There were a few additional yield lines on the top of the web on the left side above the bearing were caused by the torque on the top flange. These yield lines are circled in Figure 5.8c.

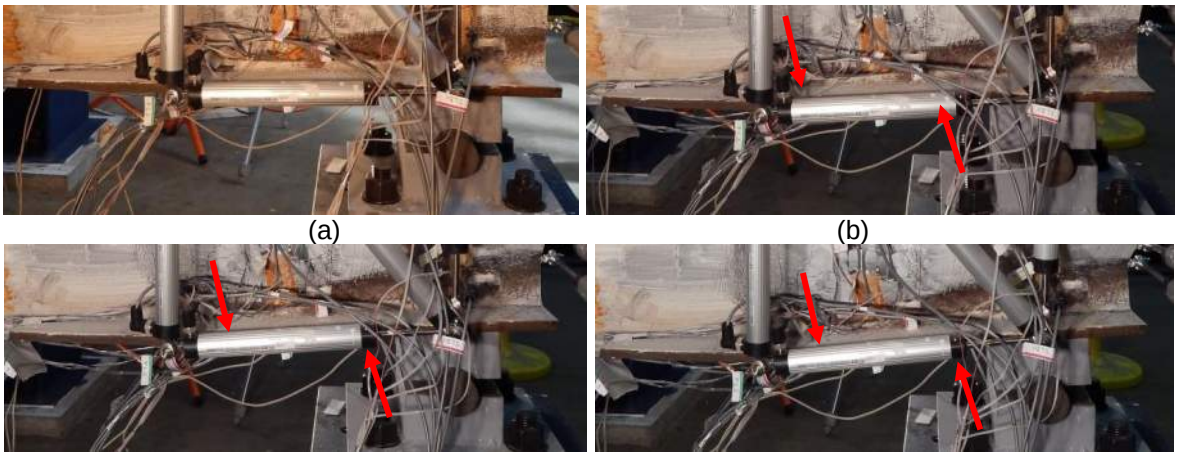

(a) (b)

(c) (d)

Figure 5.7 Two Plastic Hinges Forming in the Bottom Flange of the Undamaged Girder

(a) Failure Displacement, (b) Displacement +0.50 in, (c) Displacement +0.75 in, (d) Displacement +1.25 in

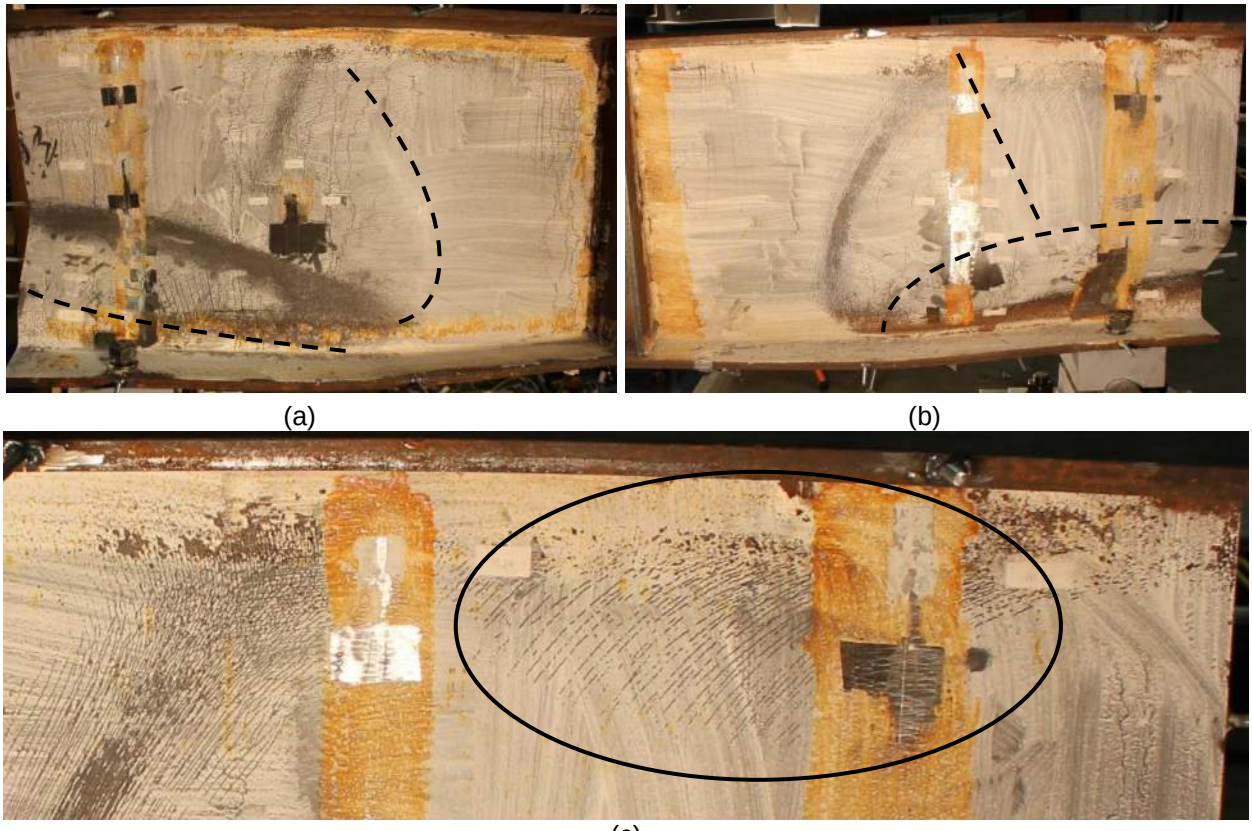

(a) (b)

(c)

Figure 5.8 Yield Lines in the Undamaged Girder

(a) Right Side, (b) Left Side, (c) Detail of Left Side Yield Lines near Top Flange

5.2.2 Load-Displacement Relationships

The undamaged specimen failed at a bearing load of 180 kip. The relationship of the load vs. vertical flange displacement at the hydraulic cylinder is given in Figure 5.9. The potentiometers CL12 and CR12 were not included due to errors caused by incorrect wiring. The response of CR22 is softer than the response of CL11, with average initial stiffness of 362 $^{kip}/_{in}$ and 640 $^{kip}/_{in}$, respectively. This is because CR22 includes the elasticity of the spreader beam and load frame. CR22 also has larger hysteresis loops after failure.

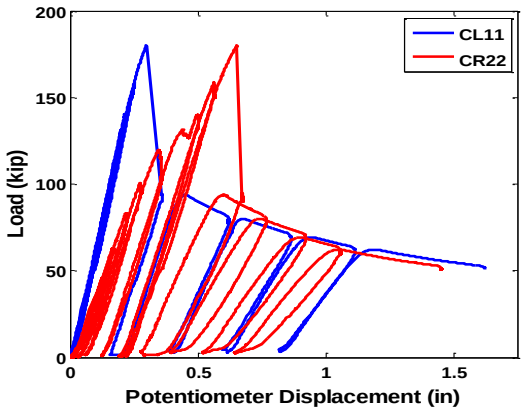

Figure 5.9 Load vs. Center Potentiometer Displacements for Undamaged Girder

The extension of the bottom flange at the bearing was measured with the SH1 shear box potentiometers. Figure 5.10 shows the load displacement relationship of the SH1 potentiometers on the right and left sides of the girder. At early stages of loading, these potentiometers extend at the same rate, an average of 50,600 $^{kip}/_{in}$. The displacements of the potentiometers were very small: 1.55 mil and 2.72 mil, for right and left. Around a load of 140 kip, displacement of SRH1 did not increase with rising load. Displacement of SLH1 slowed, but still increased. Upon failure, the effects of the twisting in the girder become apparent. The right side potentiometer showed a contraction of 1.16 mil, while the left side extended 3.88 mil. As loading continues, the bottom flange potentiometers show differential movements.

Relative vertical displacement between the flanges at the can be seen using the SV1 potentiometers. Figure 5.11 shows the load displacement relationship of the SV1 potentiometers of the right and left sides of the girder. The pre failure displacements of the SV1 sensors were similar to those of the SH1 sensors. Both sensors showed similar initial compression rates on the right and left sides, -3,250 $^{kip}/_{in}$ and -3,470 $^{kip}/_{in}$, respectively. Rates began to diverge around 100 kip, as slight rotations of the top

flange began. Like the sensors on the bottom flange, vertical bearing potentiometers had behaved differently during failure. The right side showed a large compression of 739 mil, and the left side extended 31.1 mil. With larger displacements, both potentiometers began showing compression as the girder end collapsed.

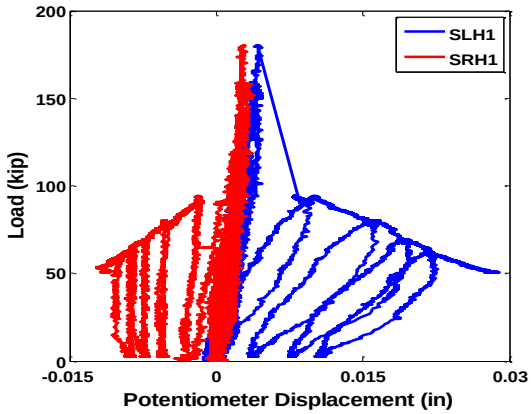

Figure 5.10 Load vs. SH1 Potentiometer Displacements for Undamaged Girder

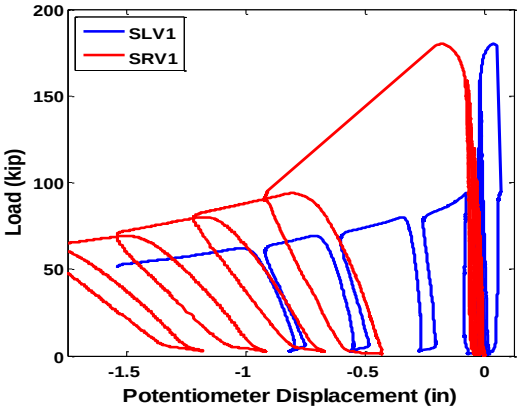

Figure 5.11 Load vs. SV1 Potentiometer Displacements for Undamaged Girder

Shear deformation measured by the shear boxes are compared as shear strain calculated from Equation 3.6. Figure 5.12 shows the load shear strain relation calculated for each side of the member. The straining rate was initially uniformly, increasing on the right side at -22.7 $^{\mu\varepsilon}/_{kip}$ and on the left side at -15.4 $^{\mu\varepsilon}/_{kip}$. As the load rose above 160 kip, magnitude of shear strain began increasing more rapidly on the left side as the buckling began. The magnitude of shear strain on the right began decreasing. Buckling dramatically decreased the shear strain -1,830 με on the right side and -14,600 με on the left side. The magnitude of shear strain continued increasing

with load. The peak shear strain calculated was -31,900 με and -60,400 με on the right and left sides, respectively.

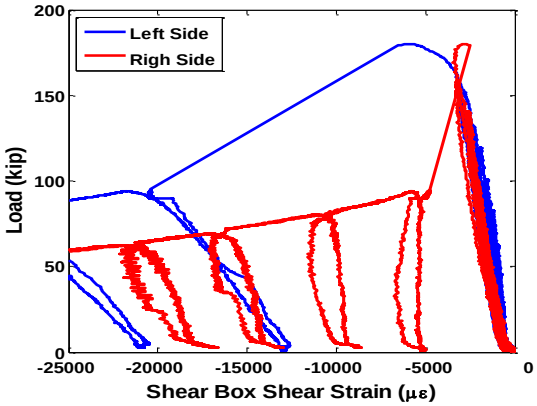

Figure 5.12 Shear Deformation vs Load in Shear Boxes for Undamaged Girder

The progression of out of plane deformations of the web is shown in Figure 5.13. Very little out of plane deformation took place in the web prior to failure. At a load of 135 kip, 75% max load, the web was still nearly vertical. At the peak load, out of plane deformations become noticeable, as W3 displaces 173 mil. The buckling which took place caused all potentiometer to translate to the left side of the girder. The largest of these was seen in W3, with a magnitude of 1.78 in. As displacement progressed past the failure displacement, the W2 potentiometer remained rather stationary. The two upper potentiometers, W3 and W4 continued displacing to the left side of the girder. Displacement W3 occurred at around twice the rate of W4. Potentiometer W1 began displacing right. This is evidence of the bearing sliding in Figure 5.5.

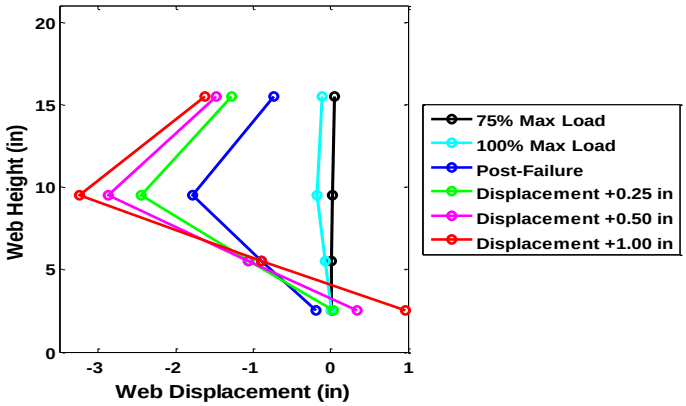

Figure 5.13 Out of Plane Displacement on the Web of the Undamaged Girder

5.2.3 Strain Data

Loading of the girder caused axial compressive strains in the web at the bearing. Figure 5.14a and Figure 5.14c show bearing strain distribution in the height of the web during various stages of loading for the left and right sides, respectively. Figure 5.14b shows the difference between the right and left side strains. Axial strain can be seen concentrated at the base of the girder, evenly distributed on each side. Concentration at the base is expected. This is because the compressive strut that forms at the bearing does not extend to the higher portions of the web. The uniformity can be seen as only minor variations in strain difference at low loads. At a load of 135 kip, axial strains at the base of the girder are nearly at yield strains, -1,860 με on WR11 and -1,770 με on WL11. Yield strain for this steel is 2,000 με. As buckling initiates, strains begin to diverge as bending strains develop through the thickness of the web. Note that at peak load, the strain in WL15 becomes tensile (245 με). Comparing the vertical position of this gauge to the deformation confirms it is at the point of maximum deflection. The variance in strain difference at peak load is 5,060 με, between the W14 and W11 strain differences.

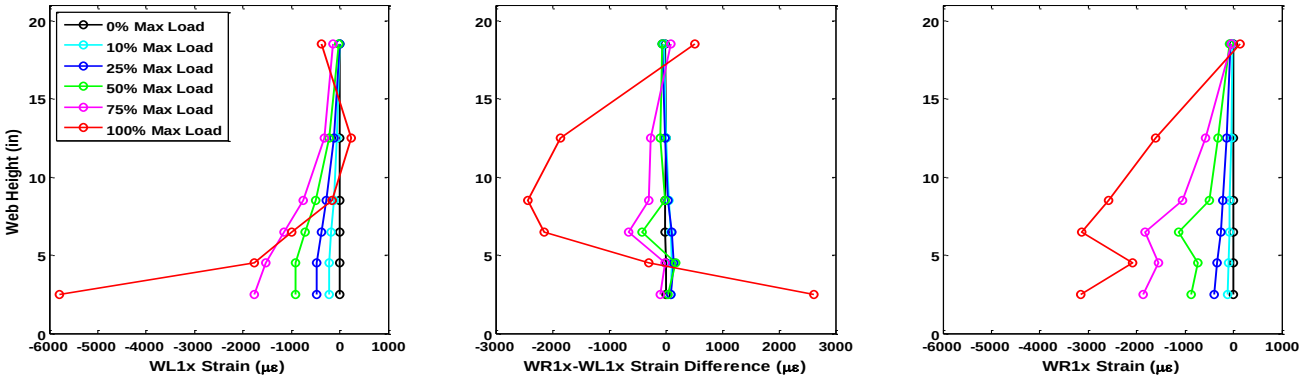

(a) (b) (c)

Figure 5.14 Axial Bearing Strain Distribution in the Web of the Undamaged Girder

(a) Left Side Axial Bearing Strains, (b) Axial Strain Difference, (c) Right Side Axial Bearing Strains

Maximum shear strains from the rosette gauges were calculated using Equation 3.7. Figure 5.15 shows the response of these gauges with loading. The shear on the right side of the web was seen to increase 10% faster than the left, 14.9 $^{\mu\varepsilon}/_{kip}$ compared with 13.5 $^{\mu\varepsilon}/_{kip}$. These shear strain rates match well with the shear strain calculated from the shear box. Maximum shear strain was at yield at the time of failure, 2,830 με on the right side and 2,260 με on the left side.

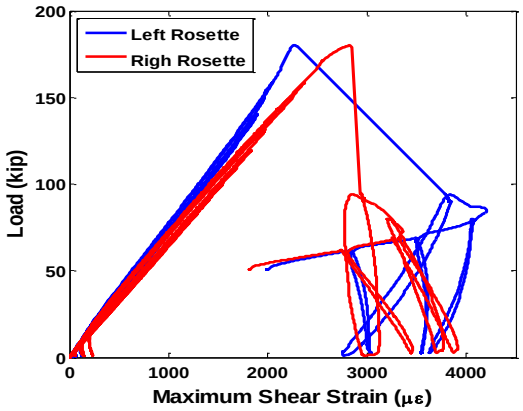

Figure 5.15 Maximum Shear Strain from Rosette Gauges on Undamaged Girder

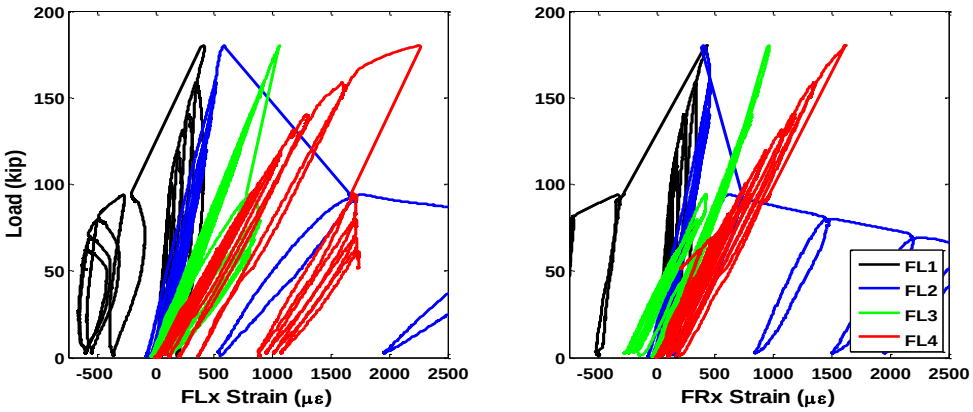

(a) (b)

Figure 5.16 Flexural Strain Development in Bottom Flange of Undamaged Girder

(a) Left Flange Strains, (b) Right Flange Strains

Distribution of bottom flange strains in the undamaged girder is shown in Figure 5.16. Flange strains are similar between left and right sides. Flange strains are larger at relative loads the further from the bearing that they are. This is due to the linear variation in the distribution of the moment. Buckling of the web caused a change in the load carrying mechanism of the girder. This caused a redistribution of strains in the bottom flange. As a result, the strains at F1 become compressive, straining rate at the F2 outpaces all gauges, and F3 and F4 strains remain largely unchanged. This is caused by the pair of plastic hinges in the bottom flange. Figure 5.17 shows the double curve in the girder which results from the two plastic hinges. The arrows indicate the position of the flange strain gauges in colors corresponding with those used in the plots.

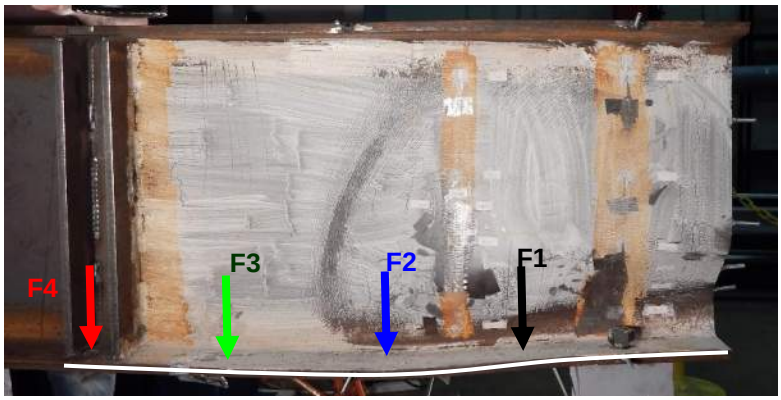

Figure 5.17 Double Curve in Bottom Flange of Undamaged Girder

5.3 DAMAGED GIRDER

5.3.1 General Observations

The failure of the damaged girder occurred suddenly during run 6 at a load of 43.4 kip. Unlike with the undamaged girder, no damage was visible in the whitewash prior to or at the time of failure. The failure of the girder occurred as an instability in the web at the top of the section reduction. The remainder of the web remained relatively intact. Figure 5.18a shows a global photo of the failure which occurred in the member. Figure 5.18b-c show views of the left and right sides of the girder, respectively. Flexural or compressive field damage would not be expected at the load ram as those were not seen to develop in the undamaged girder until loads of 140 kip and 160 kip, respectively. Whitewash damage could appear as shear damage at the bearing, and compressive zone damage around the buckle. Damage at the bearing was possible due to the reduced thickness of the section. No shear damage was visible at the time of buckling. Area where shear damage would appear is circled in Figure 5.18c. No compressive zone damage was noted at the base of the web on the left side as appeared in the undamaged girder. This area is shown with the arrow in Figure 5.18b. Compressive zone damage around the buckle was only visible on the right side at the top of the reduced section, shown at the arrow in Figure 5.18c. This was due to the shock of the failure and did not progress as the test continued.

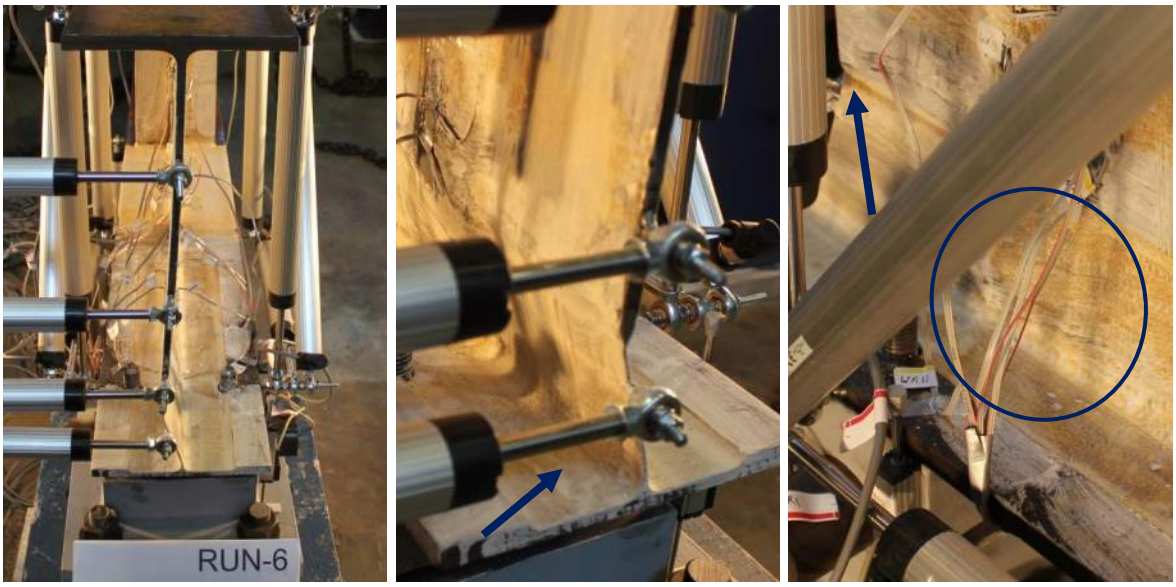

(a) (b) (c)

Figure 5.18 Failure of the Damaged Girder

(a) Longitudinal View, (b) Left View, (c) Right View

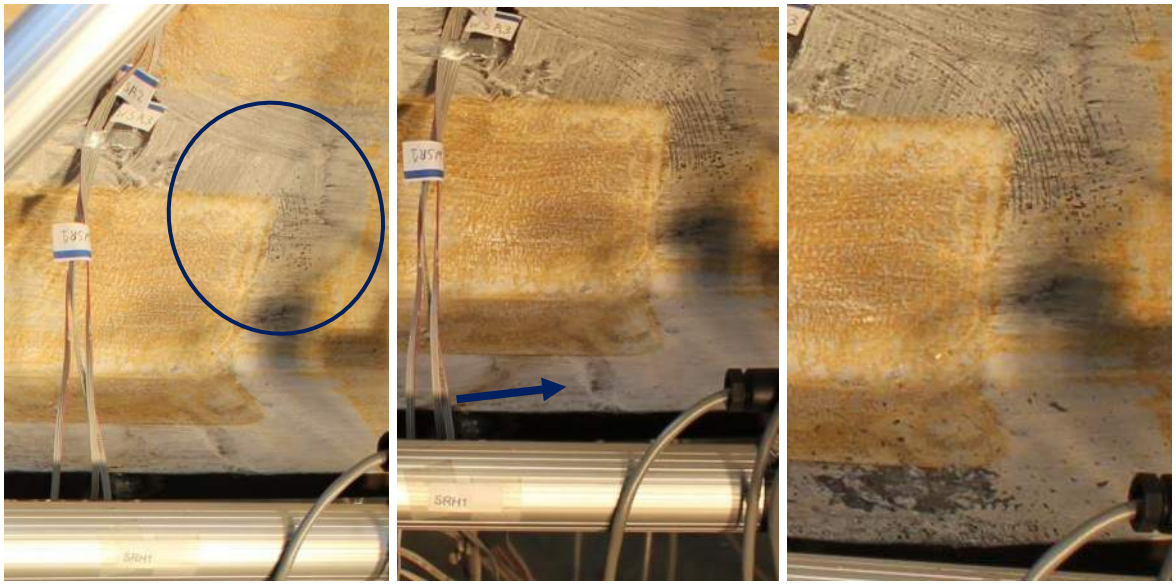

Figure 5.19 Whitewash Damage Progression in the Damaged Girder

(a) Failure Displacement +0.25 in, (b) Failure Displacement +0.50 in, (c) Failure Displacement +1.50 in

Whitewash damage did become visible in two locations as post failure displacement continued. Both of these locations were on the undamaged portions of the girder. After 0.25 in of displacement, shear damage lines became visible on the undamaged portion of the web around the end of the reduced section. This damage is circled in

Figure 5.19a. This damage continued as displacement increased. After a post-failure displacement of 0.75 in, flexural compressive damage appeared on the bottom flange, Figure 5.19b. This was the formation of a plastic hinge. This occurred due to the bottom flange carrying the load through plate bending due to the failure of the reduced web. Both of these damages are shown in Figure 5.19c at the final displacement of 1.50 in past failure displacement.

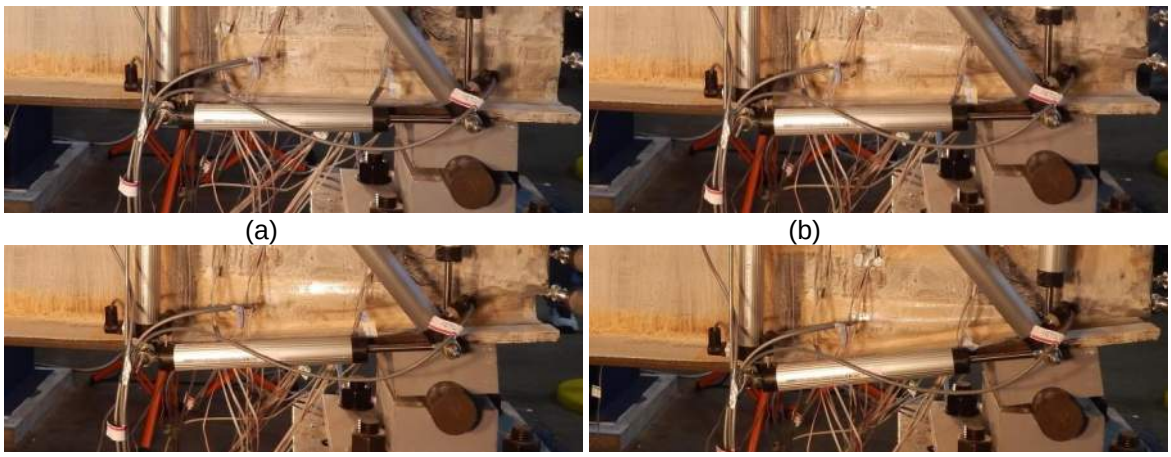

(a) (b)

(c) (d)

Figure 5.20 Bearing Rotation in the Damaged Girder

(a) Failure Displacement, (b) Displacement +0.50 in, (c) Displacement +0.75 in, (d) Displacement +1.50 in

Because only one plastic hinge formed in the bottom flange, rather than two, significant bearing rotation was observed. Figure 5.20 shows the progression of the rotation. After failure and to a displacement of 0.50 in little rotation is noted. This is from the displacement being concentrated in the reduced portion of the web. Once the bearing began showing notable signs of rotation after 0.75 in of displacement past failure. This occurred as the damage in the plastic hinge in the bottom flange grew.

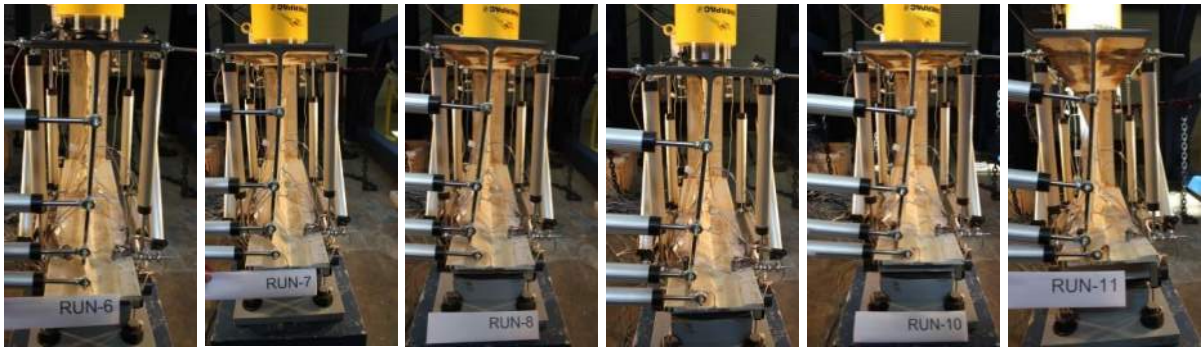

(a) (b) (c) (d) (e) (f)

Figure 5.21 Progression of Web Deformation in the Damaged Girder

(a) Failure Displacement, (b) Displacement +0.25 in, (c) Displacement +0.50 in, (d) Displacement +0.75 in, (e) Displacement +1.00 in, (f) Displacement +1.50 in

The progression of the deformation of the web is shown in Figure 5.21. All of the deformation was contained within the reduced portion of the web. The intact portion of the web remained virtually plane, and rotation in the top flange was minor. The failure was so concentrated that it caused the web to fold over on itself. This folding over ultimately caused the web to rupture at the point where the transition between damaged and undamaged web. Figure 5.22 shows detailed photos of the buckled web after the test was concluded.

(a) (b) (c)

Figure 5.22 Details of the Failed Web after Testing

(a) View of Buckling from the Right Side, (b) View of the Buckled Shape and Bending Over, (c) Rupture of the Web at the Transition

5.3.2 Load-Displacement Relationships

The damaged specimen failed at a load of 43 kip. The relationship of load vs. vertical displacement at the hydraulic cylinder is plotted in Figure 5.23. Initial stiffness of CL11 was stiffer than CR22, as it was in the undamaged girder. The stiffness of

these potentiometers was 573 $^{kip}/_{in}$ for CL11 and 352 $^{kip}/_{in}$ for CR22. The average displacement of CR12 and CL12 is also shown in the figure. The initial stiffness matches with CR22, as all three include the elasticity of the frame. However, during post-failure displacement, the average begins matching with CL11. This corresponds to the formation of the plastic hinge in the bottom flange.

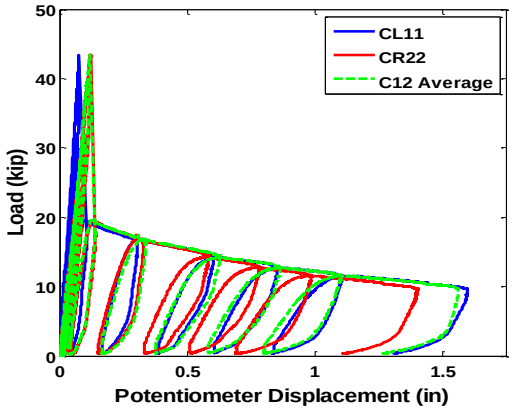

Figure 5.23 Load vs. Center Potentiometer Displacement for Damaged Girder

The deformation of the bottom flange potentiometers are shown in Figure 5.24. They show a trend on loading to extend at an average rate of 41,600 $^{kip}/_{in}$. The average displacement at the time of failure was 1.2 mil. Upon failure, both gauges show extension, but begin contracting as loading progresses. This occurs because of a change in load carrying mechanism and the resulting plastic hinge being within the potentiometer.

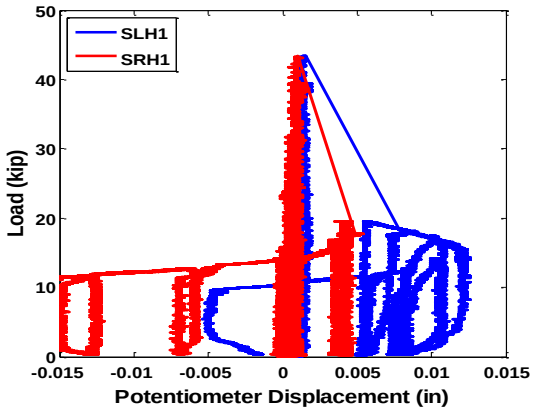

Figure 5.24 Load vs. Bottom Flange Potentiometer Displacement for Damaged Girder

The load displacement relation of the vertical potentiometers at the bearing is shown in Figure 5.25. They show a uniform stiffness of -1,740 $^{kip}/_{in}$ up to failure. Upon failure,

the right potentiometer collapses 203 mil, while the left potentiometer extends 12.8 mil. This is from the kink at the bottom of the web. The remainder of the web remained largely intact, causing the differential displacements. After application of 1.50 in of additional displacement, the average vertical collapse at the bearing was 2.17 in.

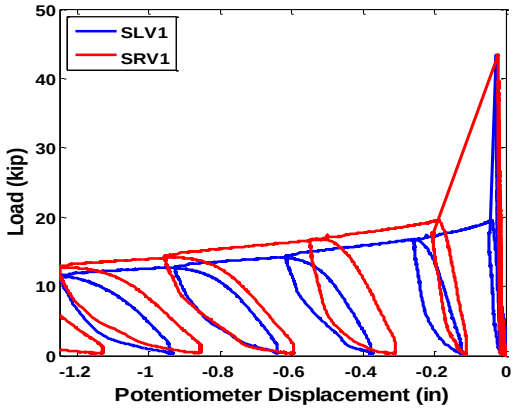

Figure 5.25 Load vs. Vertical Bearing Potentiometer Displacement for Damaged Girder

Figure 5.26 shows the shear strains from the potentiometer box arrangement. The strain development between the two sides was nearly uniform, developing at -35.3 $^{\mu\varepsilon}/_{kip}$ on the right and -25.0 $^{\mu\varepsilon}/_{kip}$ on the left. Failure caused a larger deformation on the left shear box, increasing strain 2,680 με compared to 1,720 με. Strain developed uniformly through the remainder of the test, to a minimum shear strain of -53,500 με and -55,100 με for the right and left sides, respectively.

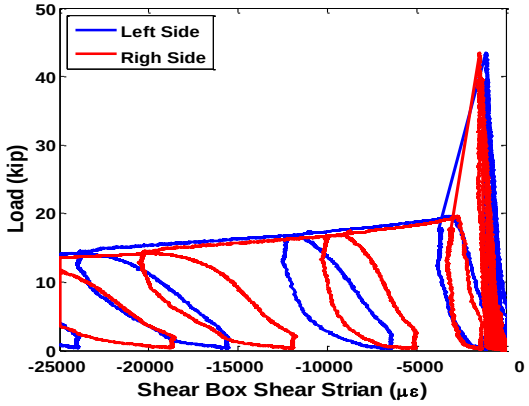

Figure 5.26 Load vs. Shear Box Shear Deformation in Damaged Girder

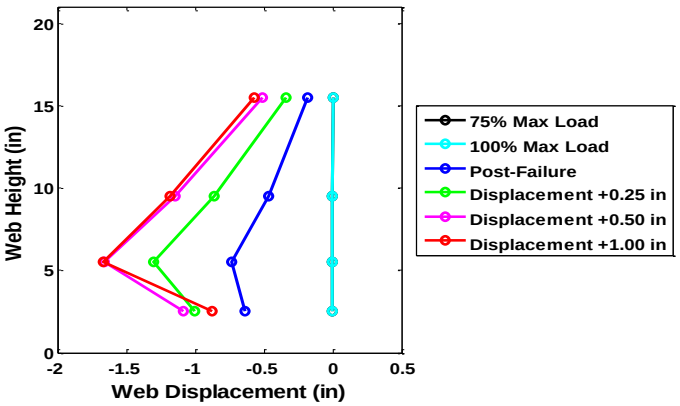

Figure 5.27 Distribution of Out of Plane Deformations on the Web of the Damaged Girder

The out of plane displacement of the damaged girder is given in Figure 5.27. For all loads up to peak load, including the maximum load, the web remained perfectly vertical. Upon buckling, the undamaged segment of the web (W2-W4) remained linear, showing only minor bending. All potentiometers showed increasing displacements as loading progressed. The retracting of W1 from displacements of 0.50 to 1.00 past failure is due to the folding over of the web, see Figure 5.22.

5.3.3 Strain Data

The distribution of axial strains can be seen in Figure 5.28. The reduced thickness of the web concentrates the axial strain. This can be seen as the sharp increase for the W11 strains. Strains at W11 are over three times larger than the W12 strains. All strains were compressive at peak load. Strain difference between the two sides is present at the peak load, but are negligible, only 397 με. This suggests that the level of bending stresses required to fail the girder are much less than the axial strains being experienced.

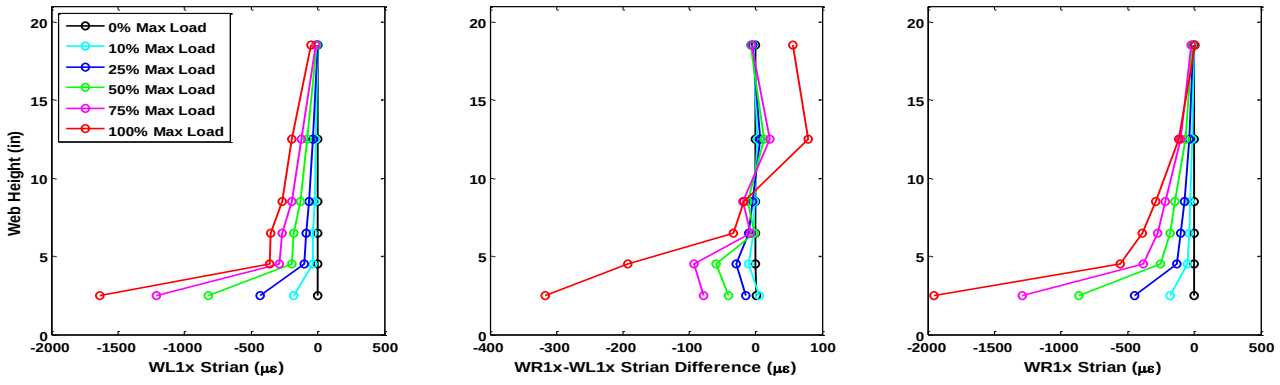

(a) (b) (c)

Figure 5.28 Distribution of Axial Web Strains in the Damaged Girder

(a) Left Side Axial Strains, (b) Axial Strain Difference, (b) Right Side Axial Strain

Maximum shear strains from the rosette gauges are plotted in Figure 5.29. The shear development rate was identical on each side, 15.4 $^{\mu\varepsilon}/_{kip}$ and 15.1 $^{\mu\varepsilon}/_{kip}$ on the right and left sides. This is less than the shear strain estimated by the shear box. This is logical as the shear box included deformation in the reduced section, while the rosettes were on undamaged steel. Maximum shear strain at the time of failure was 618 με on the right side and 702 με on the left side.

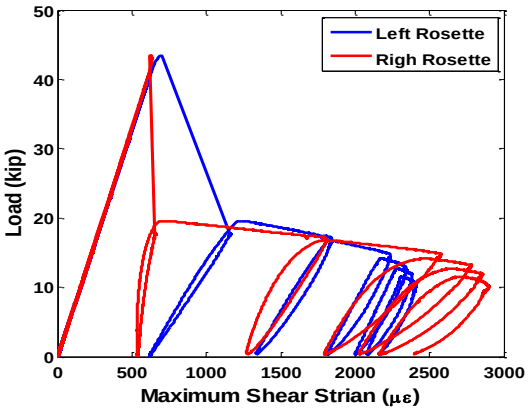

Figure 5.29 Maximum Shear Strains Calculated from the Rosettes in the Damaged Girder

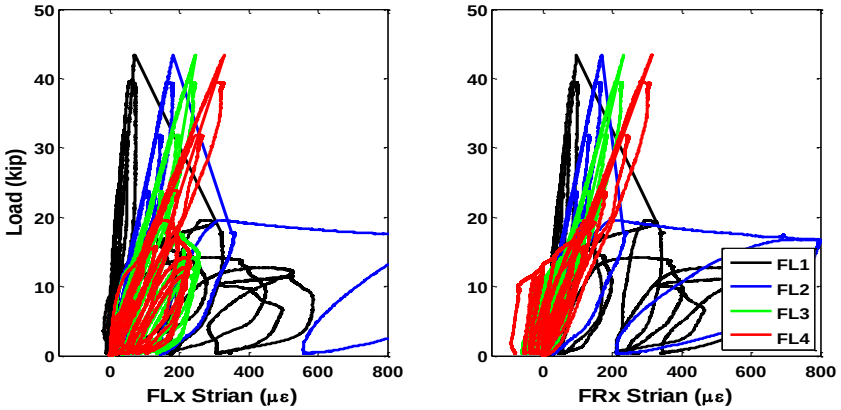

(a) (b)

Figure 5.30 Development of Flexural Strains in the Damaged Girder

(a) Left Side Flexural Strains, (b) Right Side Flexural Strains

Distribution of strains in the flange is shown in Figure 5.30. The same proportionality between strain rate and the applied moment along the flange is present. This shows that the damage to the girder did not affect the flexural strain development in the web.

Virtually no strain was present in any of the gauges aside the F2 gauges after failure. Strains in the F2 gauge were a result of the plastic hinge. At the time of plastic hinge development during run 8, the strains in the F2 gauges were 1,790 με and 2,050 με for FR2 and FL2, respectively. This confirms the yielding of the steel, and the formation of a plastic hinge.

5.4 REPAIRED GIRDER

5.4.1 General Observations

As loading progressed on the repaired girder, cracks which formed in the concrete were marked with markers to make them visible. The crack was then labeled with the step of loading which the crack formed. The color of the marker was indicative of the loading stage. Green was used for runs 0-4 (0-45 kip), blue for runs 5-8 (57-91 kip), red for runs 9-12 (103-148 kip), and black for runs 13-16 (176 kip-230 kip).

Figure 5.31 shows the panels after the molds were removed. Shrinkage cracks are shown with green marker in Figure 5.31b. No shrinkage cracks were noted on the face of the right panel.

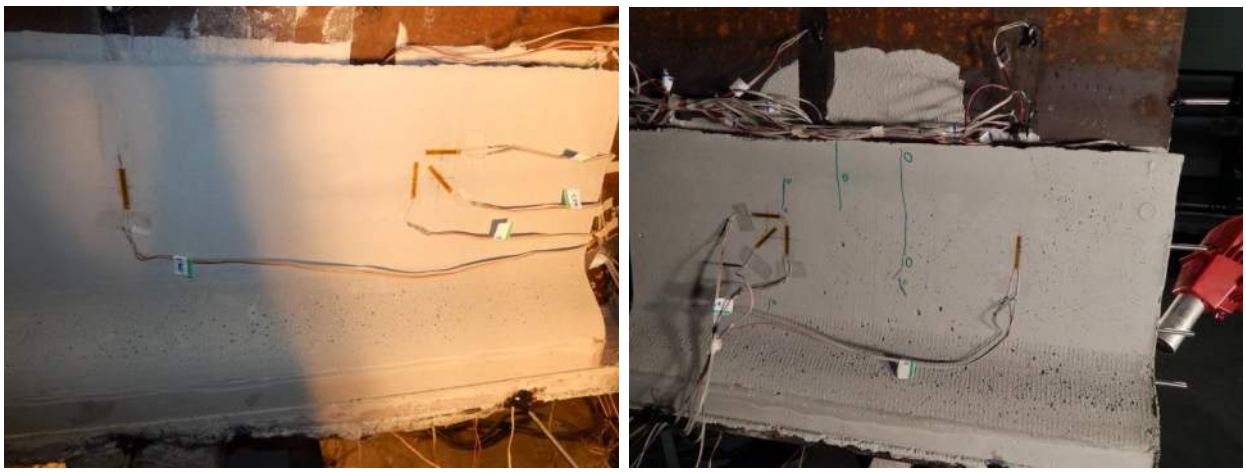

(a) (b)

Figure 5.31 UHPC Panels after Removal of the Molds

(a) Right Panel with Strain Gauges, (b) Left Panel with Strain Gauges, Shrinkage Cracks Marked

The first cracks became visible during run 3, at a load of 35 kip. These appeared as vertical cracks in the top of each panel, and vertical cracks at the bearing. The cracks at the top of the panel formed as initial small displacements of the girder caused the panel to want to rotate about the bearing, inducing tension at the top of the panel.

Vertical cracks at the bearing formed from the bearing stress. Figure 5.32 shows the initial load induced cracking formed in run 3.

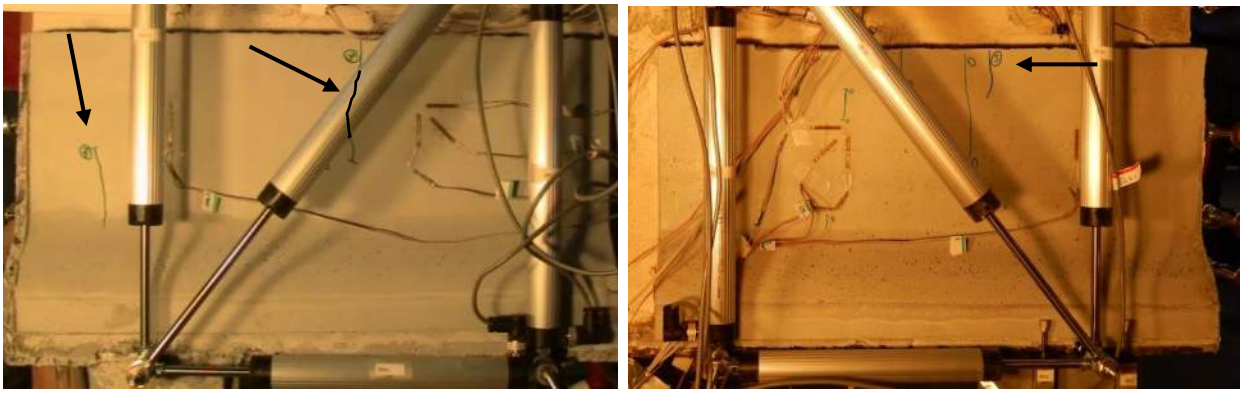

(a) (b)

Figure 5.32 Initial Crack Formation in the Concrete Panels

(a) Right Panel Cracks from Run 3 (Cracking Behind Potentiometer Visualized), (b) Left Panel Cracks from Run 3

The next types of cracks to form were a set of vertical cracks at the top of the panel by the bearing edge, and a set of shear cracks at the bottom of the panel by the bearing. The vertical cracks became visible during run 5 (57 kip) on the right panel. The shear cracks were first visible in the left panel during run 6, at a load of 69 kip. Shear cracks were not seen to extend into the curved section of the repair. Detecting cracks on the bevel was difficult because of the highly textured surface. Figure 5.33 shows these cracks in the right and left panels.

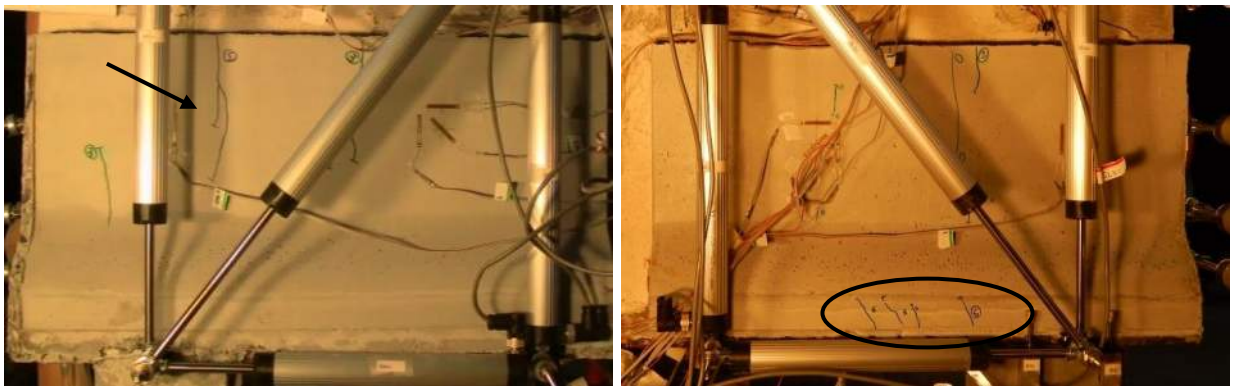

(a) (b)

Figure 5.33 Second Phase of Crack Formation in the UHPC Panels

(a) Vertical Crack Formation at the Top of the Right Panel Aligned with the Edge of the Bearing at 57 kip, (b) Shear Crack Formation at the Bottom of the Left Panel at 69 kip

The last two types of crack which formed were shear cracks on the main height of the panel and a cold joint crack in the left panel. The shear cracks seemed to be extensions of the shear cracks seen in the bottom of the panel. The cracks first became visible on the right panel in run 6, at a load of 69 kip, Figure 5.34a. All four types of cracks continued as loading progressed. A cold joint crack formed from the shear cracks at the bottom of the left along the joint which formed when concrete from the right panel leaked into the left panel during casting. This crack was first visible at 176 kip. The cold joint crack and the shear cracking in the left panel are shown in Figure 5.34b. The final cracking at the end of the test is visible in Figure 5.35.

The UHPC repair was able to prevent the failure at the bearing. Instead, the girder began yielding in flexure at the point of loading. Figure 5.36 shows the progression of the flexural yielding. The first signs of damage to the steel were observed at a load of 176 kip, Figure 5.36a. Both bending damage and vertical compression fields became visible at this point. Unlike the undamaged girder which the bending damage was more prominent, as the damage developed in the repaired girder, Figure 5.36b, the compressive field became more prominent. As the girder began to experience flexural yielding, the width of the whitewash flaking became large, Figure 5.36c.

(a) (b)

Figure 5.34 Shear Cracking in the Main Panel of the UHPC

(a) Initial Cracking Seen in the Right Panel at 69 kip, (b) Progression of the Shear Cracking and Cold Joint Crack at 176 kip

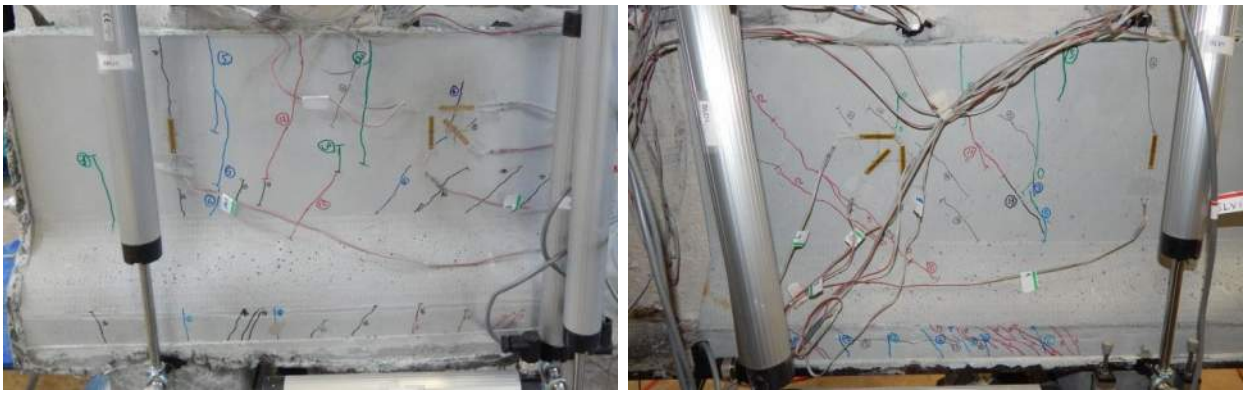

(a) (b)

Figure 5.35 Final Cracking of the UHPC Panels

(a) Right Panel, (b) Left Panel

(a) (b) (c)

Figure 5.36 Flexural Yielding of the Repaired Girder

(a) First Visible Whitewash Damage, 176 kip, Extension of the Whitewash Damage, 211 kip,
(c) Expansion of the Width of the Whitewash Damage, 230 kip

Because failure did not occur at the bearing, the test was not continued. This type of loading would not cause this type of damage in bridge structures due to load redistribution to adjacent girders.

5.4.2 Load-Displacement Relationships

Due to an error with the NI data recording in LabView, data from runs 6, 10, and 14 were lost.

The rehabilitated specimen experienced a maximum load of 230 kip while yielding in flexure. A plot of the load vs. central vertical displacement of the girder is plotted in Figure 5.37. The potentiometers show the same general trends. CR22 is the softest, 398 $^{kip}/_{in}$, and CL11 the stiffest, 674 $^{kip}/_{in}$. The two C12 potentiometers are slightly stiffer than CR22, 429 $^{kip}/_{in.}$

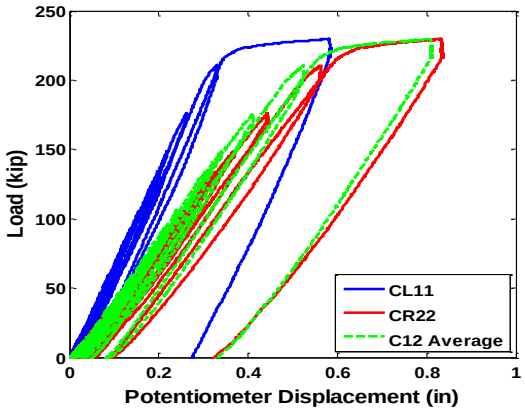

Figure 5.37 Load vs. Central Potentiometer Displacement for Repaired Girder

The addition of the concrete caused no visible extension during yielding in the bottom flange potentiometer. Figure 5.38 shows the relation of load vs. extension of the bottom flange of the repaired girder. Note that up to peak load, no deviation from the initial stiffness of 80,000 $^{kip}/_{in}$ is noticeable. Width of the lines is due to the accuracy of the potentiometer.

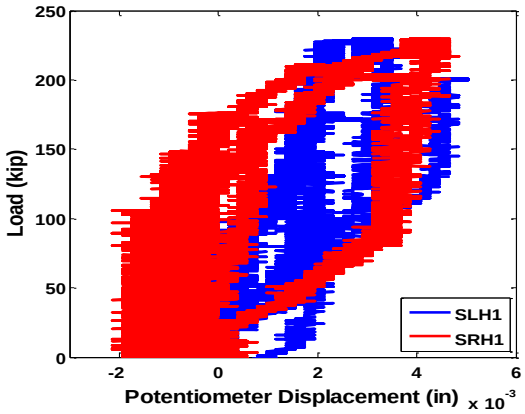

Figure 5.38 Load vs. Bottom Flange Extension in Repaired Girder

The displacement of the four vertical potentiometers is given in Figure 5.39. The plot shows that the girder experienced torsion of the top flange throughout the test. This is evident by potentiometers on the right side of the girder showing compression, while potentiometers on the right showed little change or extension. Relative rotation of the girder was more severe away from the bearing than at the bearing. This can be seen as variances in differential displacement between the right and left side at 115 kip. Displacement difference for the bearing potentiometers was 17.7 mil, while difference for SV2 potentiometers was 25.6 mil. As the girder began yielding, displacements increased at the SV2 potentiometers more than at SV1.

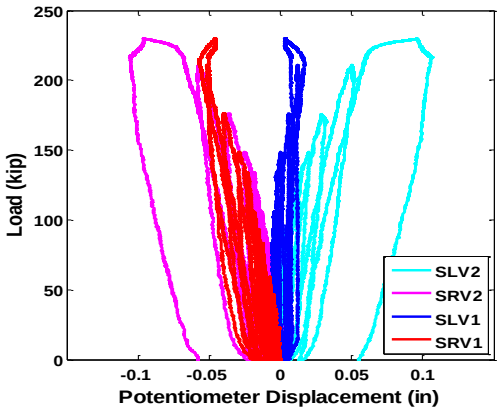

Figure 5.39 Load vs. Vertical Shear Box Potentiometer Displacement

The effects of the growing torsion of the top flange is visible in the shear box shear strain, Figure 5.40. The right side strained 90% faster at a rate of -9.3 $^{\mu\varepsilon}/_{kip}$ compared to -4.9 $^{\mu\varepsilon}/_{kip}$ on the left. But as flexural yielding begins around 179 kip, strain on the right side is seen to decrease, while the shear strain incrases on the left side. This is a cause of the increasing SLV2 potentiometer.

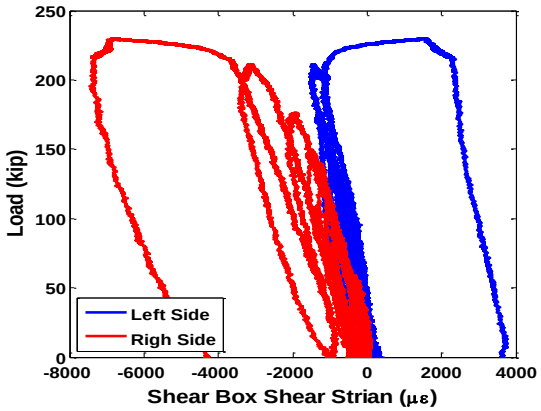

Figure 5.40 Load vs. Shear Box Shear Strain for the Repaired Girder

Displacement of the web is shown in Figure 5.41. Because no failure occurred, plots are given versus levels of maximum load. The repair was able to maintain the verticality of the web extremely well. Maximum translation was only measured to be 24.4 mil. The translation of the W4 potentiometer at max load confirms the translation of the top flange measured by the SV potentiometers.

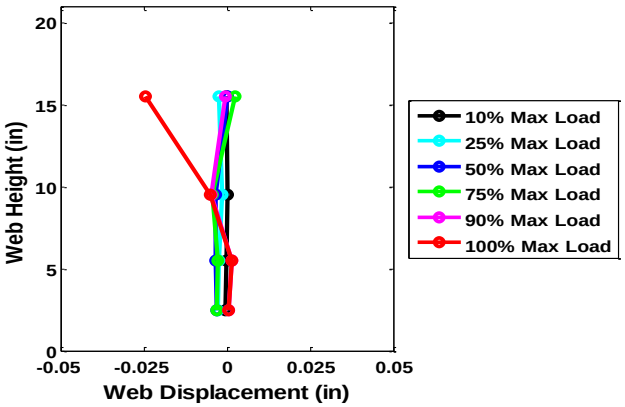

Figure 5.41 Progression of Web Displacement in the Repaired Girder

5.4.3 Strain Data

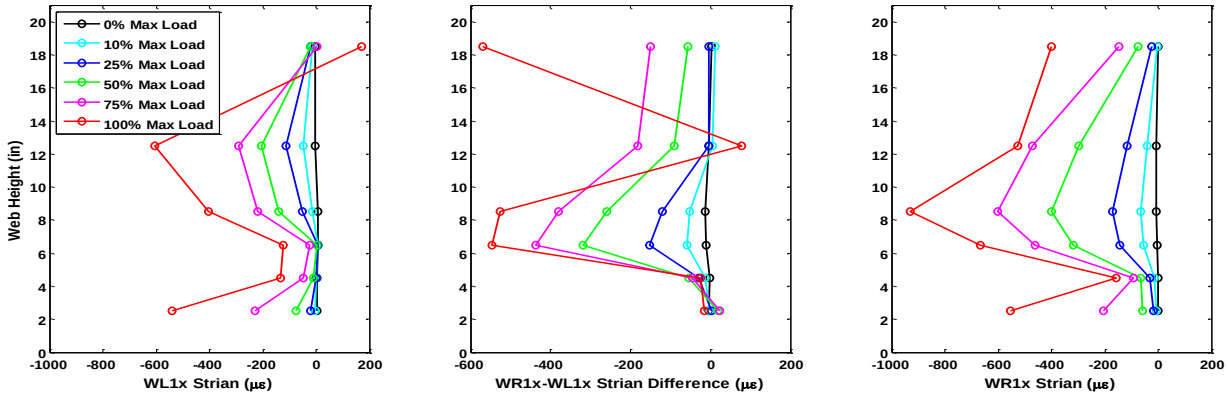

(a) (b) (c)

Figure 5.42 Distribution of Axial Bearing Strains in the Repaired Girder

(a) Left Side Axial Strains, (b) Axial Strain Difference, (c) Right Side Axial Strains

Distribution of axial strains at the bearing is shown in Figure 5.42. This shows the remarkable ability of the UHPC to reduce the strain that the steel is experiencing. No portion of the web at the bearing experiences yielding strains, even as the girder is experiencing flexural yielding. The strain in the reduced section of the web, W11, has a lower level of strain compared to other parts of the web. The peak observable at 8.5 in is likely due to the proximity to a shear stud. The top two gauges, W15 and W16 are not encased in concrete. The strain at WL16 becomes tensile, which helps to confirm the tilting of the top flange.

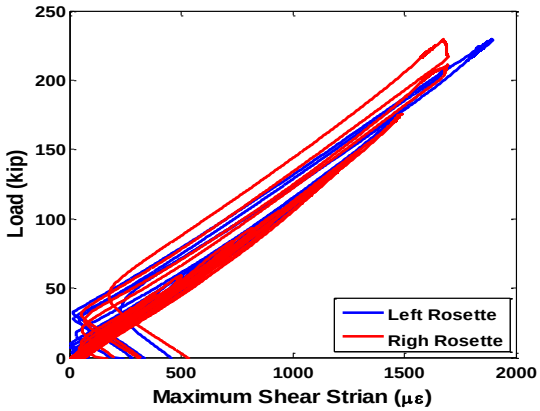

Figure 5.43 Maximum Shear Strain in the Steel

The concrete panel helped to keep shear strains uniform on opposite sides of the steel. Both the right and left side increased uniformly, never reaching yield strain. The rate of straining on the right and left side were 9.1 $^{\mu\varepsilon}/_{kip}$ and 8.9 $^{\mu\varepsilon}/_{kip}$, respectively. This is in agreement with the -9.3 $^{\mu\varepsilon}/_{kip}$ shear strain development calculated from the right side shear box. Maximum shear strains at the rosettes were below yield at 1,700 με and 1,900 με on the right and left sides, respectively. Figure 5.43 shows the load vs. maximum shear strain relation.

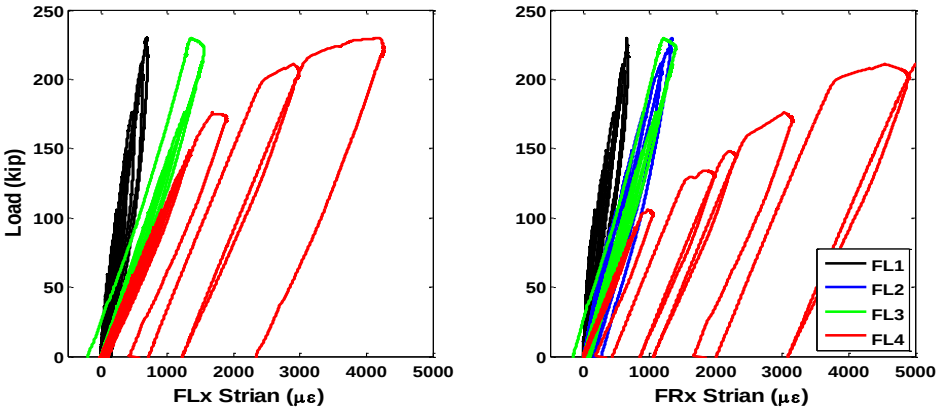

Figure 5.44 Bottom Flange Flexural Strains in the Repaired Girder

(a) Left Flange Strains, (b) Right Flange Strains

Flange strains for the repaired girder are shown in Figure 5.44. Readings for FL2 were lost due to a damaged gauge. Proportionality of the flexural strains differed in the repaired girder. The F1 and F4 strains still maintained the lowest and highest rates, respectively. However, the F2 and F3 strains developed at the nearly the same rate, 5.0 $^{\mu\varepsilon}/_{kip}$ for FR2 strains and 6.0 $^{\mu\varepsilon}/_{kip}$ for FR3 strains. This is likely due to composite

action between the concrete and bottom flange. F4 strains under the hydraulic cylinder saw extensive yielding. Straining in FR4 was larger than in FL4. This increased flexural strain helps to confirm larger displacements seen on the right side.

5.4.3.1 Concrete Related Strains

The strain development in the studs is shown in Figure 5.45. The stud at the bearing, SS1, is shown to develop tension at a rate of about 1.1 $^{\mu\varepsilon}/_{kip}$. The stud away from the bearing actually developed compressive strains at a rate of -3.5 $^{\mu\varepsilon}/_{kip}$. Studs at the bearing were found to have a lower strain rate compared to those away from the bearing. This suggests that the studs away from the bearing have higher utilization. This could prove useful if height of corrosion at the bearing is sufficiently large that the majority of studs need to be placed at the end of the panel. The compression in the SS2 stud is possibly from the early twisting of the top flange, this would initially cause compression in the stud, until it began engaging to hold the panel on. This can be seen as loading increased above 150 kip.

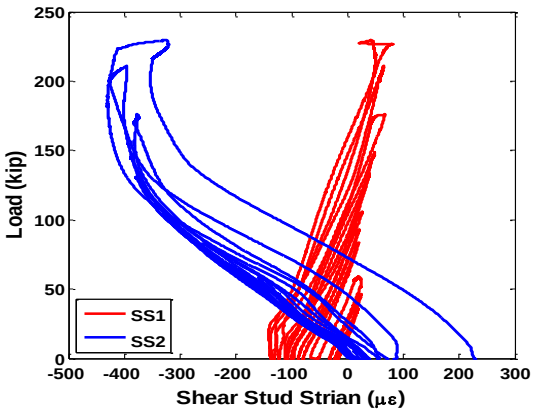

Figure 5.45 Strain Development in Shear Studs

Various strains recorded from the strain gauges on the concrete are plotted in Figure 5.46. Bearing strains in the concrete were found to only increase at a rate around 20% that of steel. It is logical that concrete strain is less as it is not bonded to the steel girder and the outside face of the concrete should be less strained than the concrete nearer the girder due to shear lag. The plateaus of strain seen on the right side at 179 kip and at 230 kip on the left side were due to cracks forming through the strain gauge. Maximum shear strain calculated from the rosette arrangement is plotted in Figure 5.46b. Up to a load of 57 kip, the right and left side develop shear strain at similar rates, 2.1 $^{\mu\varepsilon}/_{kip}$ on the right and 2.6 $^{\mu\varepsilon}/_{kip}$ on the left. On loading to 69 kip, a crack developed on through one of the right side gauges, causing the increased loading seen.

Another crack can be seen to form through a gauge at a load of 148 kip. Figure 5.46c plots longitudinal strains from the rosettes. These both show compression at a rate of -9.6 $^{\mu\varepsilon}/_{kip}$ and -8.6 $^{\mu\varepsilon}/_{kip}$ for the right and left side, until the crack forms in the gauge at 69 kip. This compressive loading confirms the composite action which increased the F2 flexural strains. Cracks formed are visible in Figure 5.35.

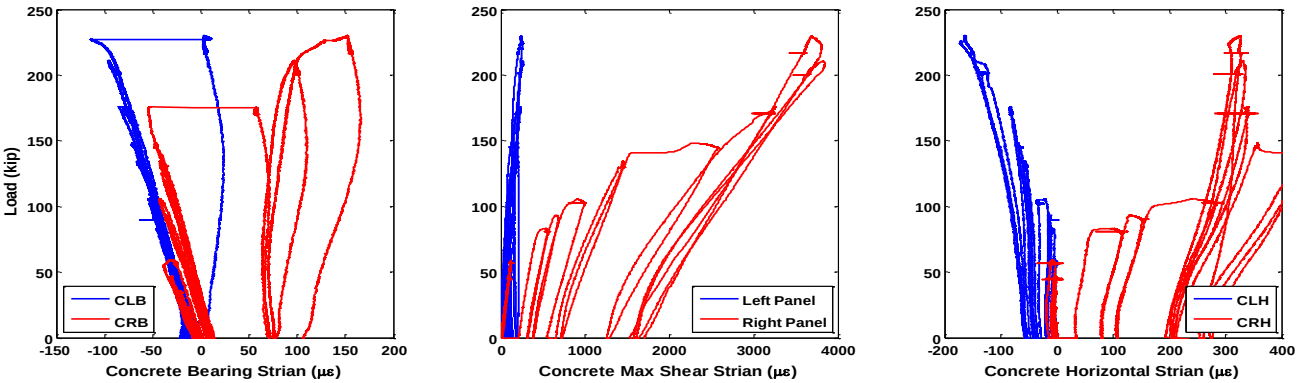

Figure 5.46 Critical Strain Readings from the Concrete Panel

(a) Axial Strain at the Bearing, (b) Maximum Shear Strain Calculated from the Rosettes, (c) Longitudinal Strain from the Rosette

5.5 DISCUSSION OF EXPERIMENTAL RESULTS

5.5.1 General Observations

Figure 5.47 shows the condition of each specimen at the conclusion of the test. The undamaged girder experienced web buckling. This failure happened suddenly and caused extensive yielding on clearly defined yield lines on the entire height of the web as it deformed out of plane. The redistribution of load after failing also caused a pair of plastic hinges, circled in Figure 5.47a, to form in the bottom flange. Due to simulated corrosion damage on the web, the buckling of the damaged girder was localized in the reduced section. The buckled shape on the reduced section of the damaged girder looks identical to that on the entire web of the damaged girder. It is confined to the height of the damage. Like the buckling of the undamaged girder, the damaged girder also failed suddenly, without noticeable yielding and deformed out of plane. The intact portion of the web experienced virtually no damage. There was only minor yielding at the end of the damaged section, indicated with an arrow in Figure 5.47b. The damage also caused only one plastic hinge to form in the bottom flange at the end of the damage, circled.

The repaired girder did not fail. Instead it experienced extensive flexural yielding, indicated with an arrow in Figure 5.47c. Cracking developed in each panel through the entire test, Figure 5.47d, but the panel remained intact. No significant out of plane movement was noted. This demonstrates the remarkable ability of the UHPC to prevent bearing failure in corroded steel girders.

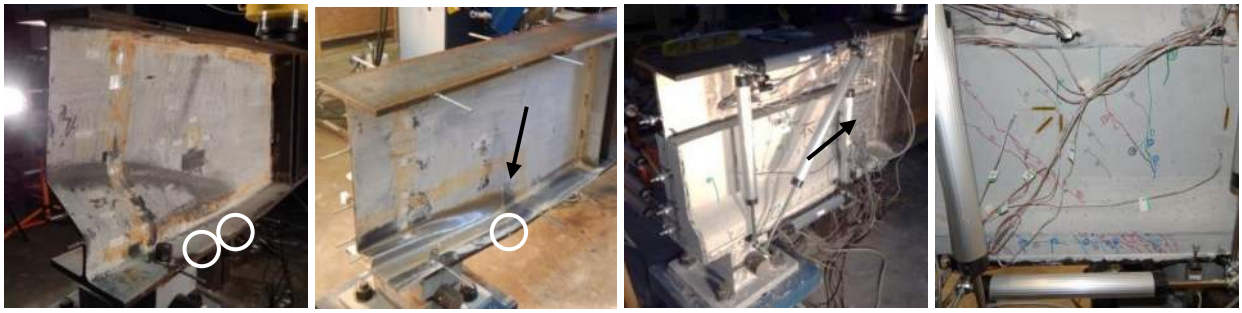

(a) (b) (c) (d)

Figure 5.47 Appearance of the Failed Girders

(a) Undamaged, (b) Damaged, (c) Repaired, (d) UHPC Cracking

5.5.2 Load-Displacement Relationships

Figure 5.48 shows the superimposed load displacement relationships from the three girders. The bearing capacity for the undamaged girder was 180 kip. Imposed corrosion damage caused a 76% drop in capacity, only 43 kip in the damaged girder. The inclusion of the UHPC repair prevented failure at the bearing, proving that corrosion rehabilitation using this method is possible. As the repaired girder began yielding in flexure, the highest capacity recorded was 230 kip. This is over five times the capacity of the damaged girder, and over 28% higher than the baseline undamaged girder.

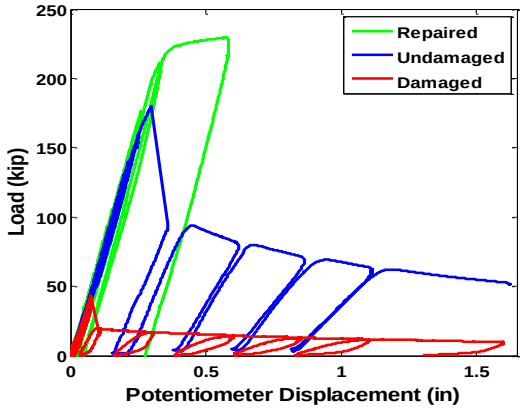

Figure 5.48 Load Displacement Relations for the Three Tested Girders

The stiffness of the three girders was all similar. Neither the applied damage nor the UHPC repair had a significant effect the stiffness of the girder. The corrosion damage caused a 10% reduction in stiffness, from 640 kip/in in the undamaged girder to 573 kip/in in the damaged girder. This slight reduction in stiffness would transfer loading to adjacent girders in a bridge structure. The repair saw this stiffness restored to 674 $^{kip}/_{in}$.

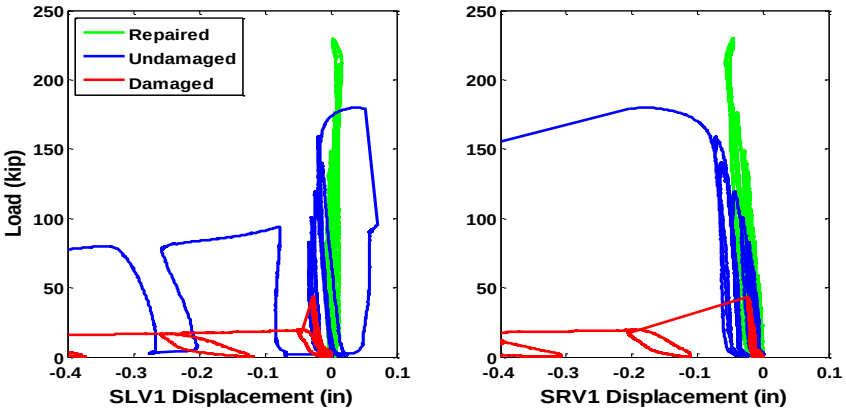

Figure 5.49 Vertical Displacement of the Top Flange at the Bearing

(a) Left Side Vertical Bearing Potentiometer, (b) Right Side Vertical Bearing Potentiometer

Figure 5.49 compares the vertical displacement of the top flange at the bearing. It can be seen that the inclusion of damage significantly effects the vertical deformation of the girder at the bearing. Introduction of the damage decreased the stiffness 50% from -3,360 $^{kip}/_{in}$ in the undamaged girder to -1,740 $^{kip}/_{in}$ in the damaged girder. The repair also had a significant impact on the vertical stiffness of the girder at the bearing. Stiffness increased to over three times the stiffness of the damaged girder and 65% higher than the undamaged girder on the right side, -5,550 $^{kip}/_{in}$. The left side saw virtually no vertical displacement.

Shear strains calculated from the shear box of potentiometers at the girder end are compared in Figure 5.50. The average shear straining rate for the undamaged girder was found to be -19.1 $^{\mu\varepsilon}/_{kip}$. Shear straining rate of the girder end was found to increase 64% in the damaged girder to -30.2 $^{\mu\varepsilon}/_{kip}$. This was obviously caused by the increased deformations which resulted from the corrosion damage. The addition of the UHPC repair made the end of the girder stiffer. The resulting shear straining rate was -7.1 $^{\mu\varepsilon}/_{kip.}$ This was 76% less than damaged girder, and 63% less than the undamaged girder.

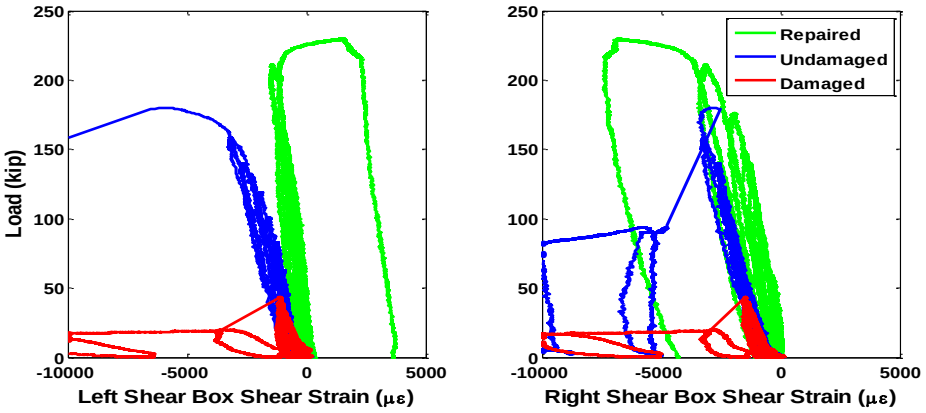

Figure 5.50 Shear Strains Calculated from the Shear Box

(a) Left Side Shear Box, Right Side Shear Box

5.5.3 Strain Data

Axial strain distributions at equivalent loads for the three girders are shown in Figure 5.51. Axial strains on the reduced section of the damaged girder (Wx11) were 3.4 times larger than strains in the undamaged girder at similar loads. Axial strain in the reduced portion of the damaged girder prior to failure was -1,630 με; the undamaged girder only read -475 με at that load. The maximum strain at the time of failure was also found to be significantly less than the undamaged girder at the time of failure. This suggests that the reduced thickness increased instability in the web.

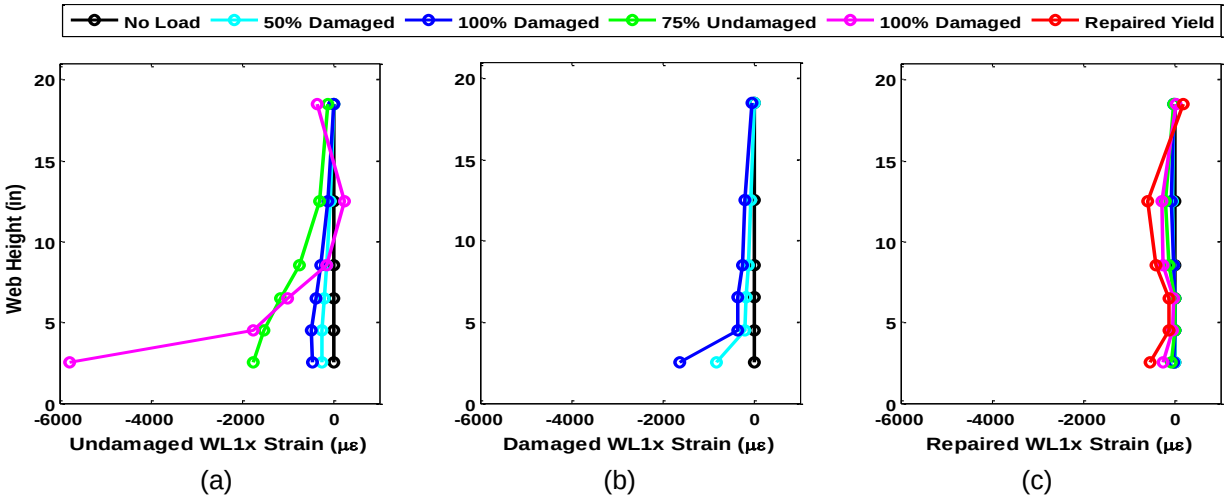

Figure 5.51 Axial Bearing Strain Distribution in the Girders

(a) Undamaged Girder, (b) Damaged Girder, (c) Repaired Girder

The gauges found Wx11 strains in the reduced section of the repaired girder to be on average 5% of the strain in the undamaged girder. This is remarkable, as the strain in the repaired girder includes 70% section loss. Axial strain at the bottom of the web prior to buckling of the web of the undamaged girder read -5,780 με. The same load on the repaired section induced an axial strain of -270 με, despite being on a thinner section of web. The concrete is capable of greatly reducing the strain in the damage web.

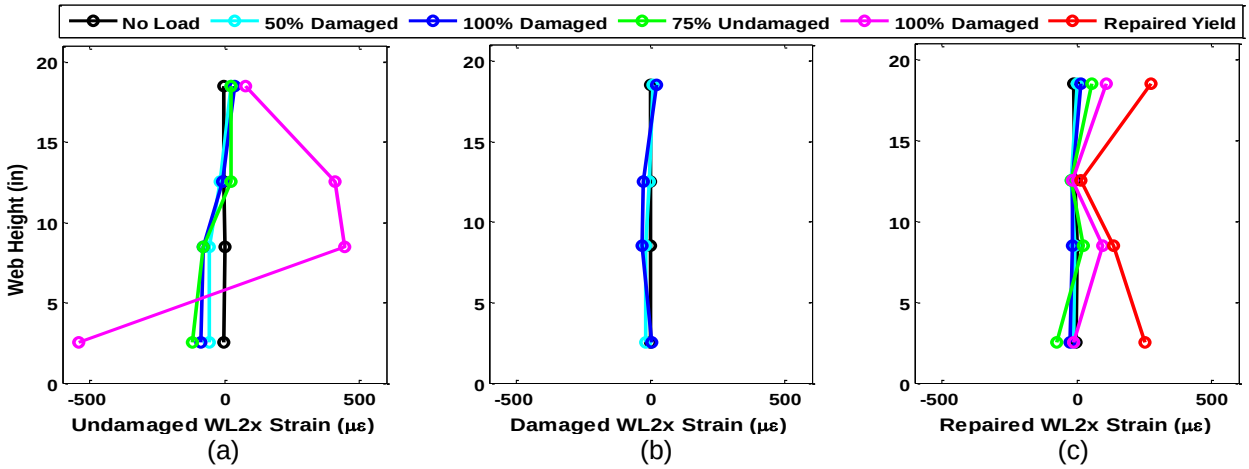

Figure 5.52 Distribution of Vertical Web Strains at the End of the Panel

(a) Undamaged Girder, (b) Damaged Girder, (c) Repaired Girder

Figure 5.52 shows a plot of vertical strains in the web of the girder 10 in from the edge of the bearing. These gauges were intended to detect any possible changes in strain of the girder from the corrosion damage and the application of the repair. No major changes were apparent. Strains in the damaged girder were actually less than the undamaged girder at similar loads despite section loss. This suggests that the load carrying mechanism of a corroded girder may actually change. The repair was also found to reduce vertical strains. Tensile strains seen at peak load of the undamaged girder are from the formation of the buckled shape. Tensile strains in the repaired girder are likely from the tilt of the top flange mentioned.

The development of shear strain in the web of the girder is plotted in Figure 5.53. The corrosion damage resulted in an 8% increased strain rate. The average shear strain development in the undamaged girder was 14.2 $^{\mu\varepsilon}/_{kip}$, while the damaged girder increased to 15.3 $^{\mu\varepsilon}/_{kip}$. The addition of the UHPC repair decreased the shear strain development to 9.0 $^{\mu\varepsilon}/_{kip}$. This resulted in far lower shear strains in the web. At the peak load, the damaged girder had an average maximum shear strain of 2,540 με. At a similar load, the repaired girder only had a shear strain of 1,470 με.

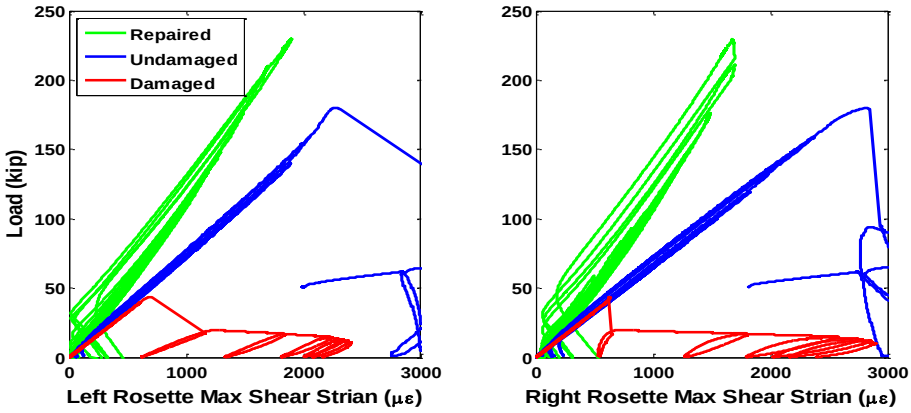

Figure 5.53 Maximum Shear Strain in the Webs of the Girders

(a) Left Side Strain Gauge Rosette, (b) Right Side Strain Gauge Rosette

Plots of the four flexural strain relationships are presented in Figure 5.54. There was an increase in straining rate from the reduction of the flange thickness in the damaged girder. It resulted in a 29% increase of F1 flexural straining rate from 1.72 $^{\mu\varepsilon}/_{kip}$ to 2.22 $^{\mu\varepsilon}/_{kip}$ and a 5% increase in the F2 straining rate from 3.32 $^{\mu\varepsilon}/_{kip}$ to 3.88 $^{\mu\varepsilon}/_{kip}$. The less pronounced increase at F2 is due to the gauge being on at the transition to the damage. Straining rates at the F3 and F4 gauges showed a 5% decrease in the damaged girder. Strain rate at the F3 gauge was 5.70 $^{\mu\varepsilon}/_{kip}$ in the undamaged girder and 5.35 $^{\mu\varepsilon}/_{kip}$ in the damaged girder. F4 straining rates were 7.57 $^{\mu\varepsilon}/_{kip}$ and 7.24 $^{\mu\varepsilon}/_{kip}$ in the undamaged and damaged girders, respectively. After failure the type of strain at the F1 location differed from the undamaged to damaged girders. This is due to the formation of a double plastic hinge in the bottom flange of the undamaged girder.

Strain rates were seen to increase at all gauge locations in the bottom flange. This increase was most dramatic under the end of the concrete panel. Strain rates in the F1 and F2 locations were 5% and 30% larger, respectively, than the damage girder. The comparison for F1 and F2 is made to the damaged girder to account for the increased rate from the section loss. The flexural straining rates for F1 and F2 locations in the repaired girder were 2.33 $^{\mu\varepsilon}/_{kip}$ and 5.01 $^{\mu\varepsilon}/_{kip}$, respectively. This increase in strain rate confirms that the panel and bottom flange work as a composite member to carry the load. The straining rates in the F3 and F4 in the repaired girder increased 9% in the repaired girder compared with the undamaged girder. The comparison for these locations is made with the undamaged girder as they were both on full thickness and were loaded to higher loads. Straining rates for the F3 and F4 locations in the repaired girder were 6.03 $^{\mu\varepsilon}/_{kip}$ and 8.45 $^{\mu\varepsilon}/_{kip}$, respectively.

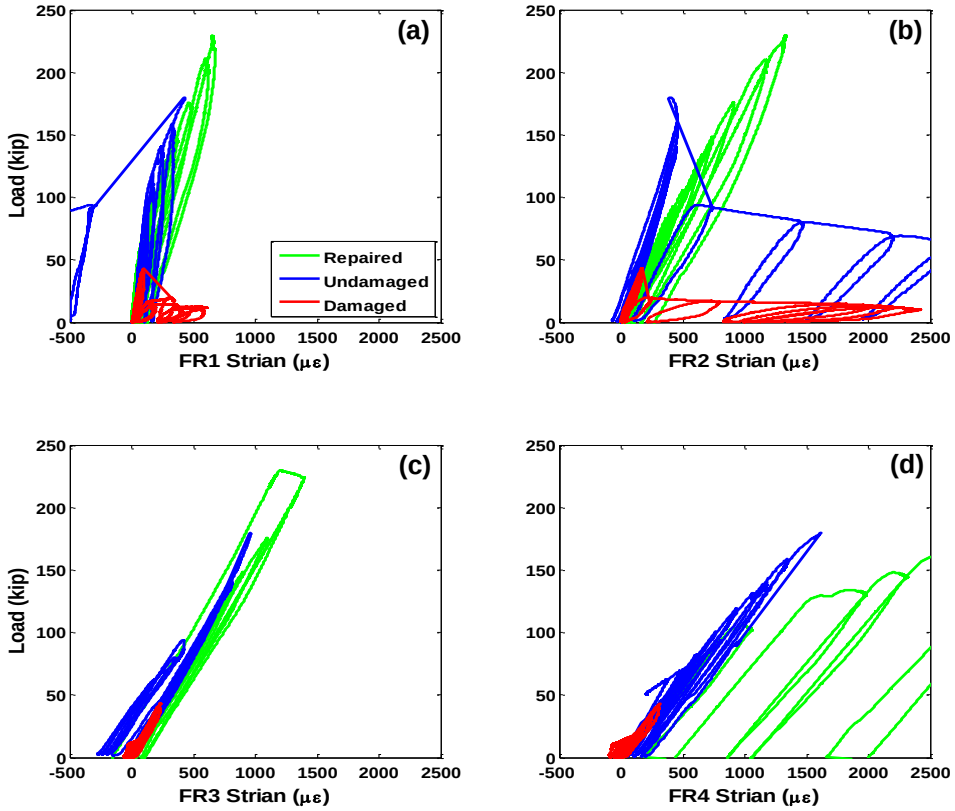

Figure 5.54 Comparison of Flexural Strains in the Girders

(a) Flange Gauge FR1, (b) Flange Gauge FR2, (c) Flange Gauge FR3, (d) Flange Gauge FR4

6 Finite Element Simulations

6.1 INTRODUCTION

From the data collected in the large-scale experiments, a finite element model was created. The intent of the model was to predict the load, ductility, strains, and load carrying mechanisms found in the test sufficiently well. This model could be expanded to study different types of repairs on many different types of girders. This chapter is divided into five sections. The first will describe the objectives of the analytical study. The second section will describe the modeling methodologies used to create the finite element model. The third section will compare the results from the finite element analysis to the large scale test data. The fourth will investigate the effect of the inclusion of a deck in the large scale test. The final section will introduce eight repair designs considered for in service bridges.

6.2 OBJECTIVES

A reliable finite element model was necessary to study possible repair concepts. This model needed to demonstrate the ability to represent real-life performance of bridge girders. LS-Dyna, a general-purpose finite element program, was selected as the software to perform the analysis (LSTC, 2012a).

This finite element model was created and validated from the data acquired from the large-scale experiment. This would provide a means of tuning the finite element model, and learning its limitations. Investigations of girders with composite and non-composite decks were then performed.

Once validated, the model would be used to analyze full-scale rolled and plate girders. These girders had severe levels of corrosion applied to the webs, flanges and

stiffeners. Eight repair designs were introduced to rehabilitate the damage. This was intended to show the versatility of the UHPC repair concept.

6.3 CREATION OF THE FINITE ELEMENT MODEL

6.3.1 General Model Setup

A quasi-static Finite Element Analysis (FEA) was performed utilizing 1-, 2-, and 3-dimensional elements, contact definitions, global and contact damping, material nonlinearities, and has considerations for large deformations. The model used input units of inches for length, seconds for time, and pounds for force. This resulted in mass units of lb*s^2/in and stress measured in psi.

The girders were constructed from thin, four-node plate elements. This allowed for more efficient calculations compared to solid elements. The elements were rigorous enough to capture local phenomena such as web buckling and formation of tension fields. Bearings and concrete were modeled using eight-node hexahedral solid elements. Shear studs and the restraining chain were modeled as three-node beam elements.

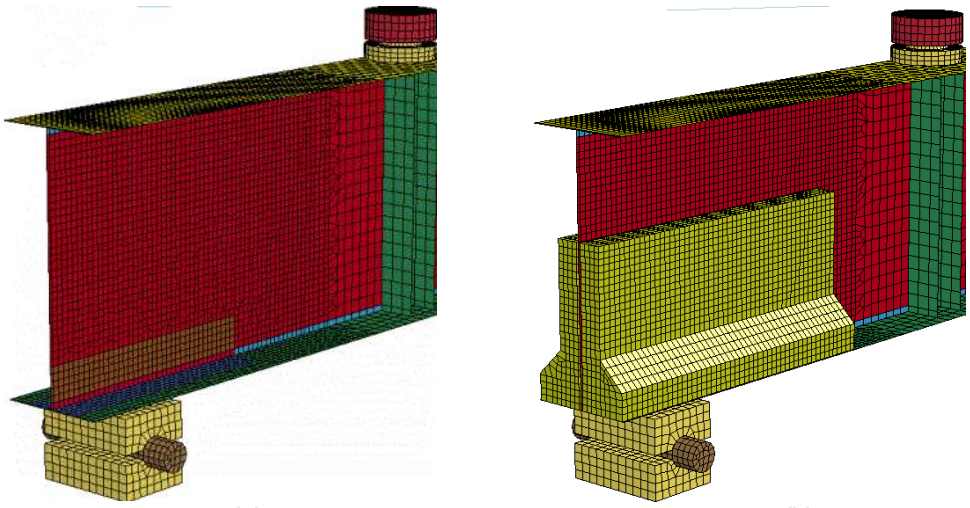

(a) (b)

Figure 6.1 The Finite Element Model of the Damaged and Repaired Girders

(a) Studied End of the Damaged Girder, (b) Studied End of the Repaired Girder

The steel girder was modeled using 6,474 nodes and 6,307 shell elements. The chain for the lateral bracing utilized 53 nodes and 48 truss elements. The addition of the UHPC panel added 15,848 nodes, 12,250 solid elements for the concrete, and 408

beam elements for the studs. Figure 6.1 shows the models of the girder with and without concrete encasement.

The mesh in the region of the studied end utilized a fine mesh. Elements were approximately $^1/_2$ in square. This resulted in 38 elements in the height of the web, and 16 elements on the width of the flange. This fine mesh extended 30 in longitudinally on the girder. This allowed the repair to be placed on the fine mesh. The fine mesh transitioned to a medium mesh before the point of loading, and to an even coarse mesh after the loading point. The medium mesh utilized approximately 1 in square elements, and the coarse mesh utilized 2 in square elements. The coarser meshes were used in order to reduce computation time. Figure 6.2 shows the transitions of the mesh.

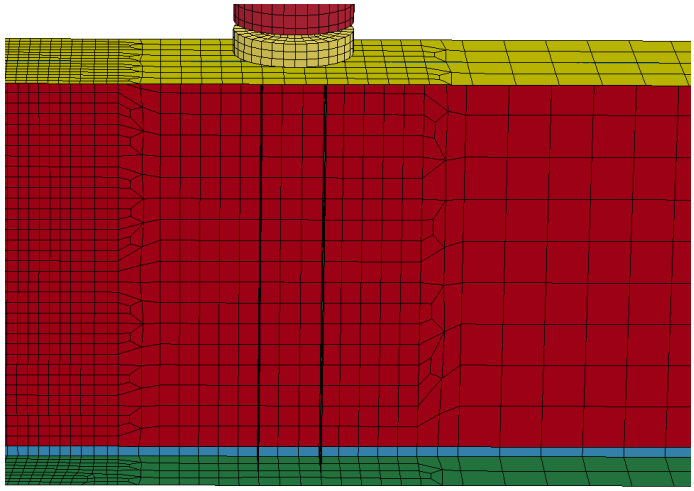

Figure 6.2 Transitions in the Finite Element Mesh

The bottom and top row of elements on the web had increased thickness to account for the fillet occurring from the rolling process. This row is seen as the line of blue elements in Figure 6.2. Damage was included by reduction of the thickness of the element. Plate elements for the web and stiffeners defined the mid-surface of the steel so no undue eccentricity is present. Plate elements for the bottom and top flanges modeled the top and bottom surfaces, respectively. This prevented the flange elements from penetrating the web. This resulted in the height of the modeled web being $2t_f$ less than the finished height. The webs and flanges were modeled as entirely plane, with no initial imperfections.

The analysis was carried out on a Dell® Precision T3600 PC with an eight-core, 3.6 GHz Intel® Xenon® E5-1620 processor, and 16 GB of RAM. The undamaged and damaged girders required 10.5 core-hours to complete. The addition of the UHPC increased computation to 33 core-hours.

LS-Dyna uses a keyword based input method which organizes inputs based on functions. Each keyword has multiple cards which are used to input specific functions used. For instance, the *ELEMENT keyword organizes all types of 1-, 2-, and 3-dimensional elements, and includes the cards _BEAM, _SHELL, and _SOLID, among others. There is also a keyword for material formulations, *MAT, contact options, *CONTACT, element formulations, *SECTION, and many others. Cards are specified by calling the keyword followed by the card. For instance, elastic materials are called using *MAT_ELASTIC. Each card has variables responsible for controlling the functions. For example *MAT_ELASTIC: E controls the Elastic Modulus.

6.3.2 Boundary Conditions, Loading Mechanisms, and Contact Definitions

6.3.2.1 Boundary Conditions

Boundary conditions and loading mechanisms were modeled as closely to what was used in the test, as these are some of the most critical aspects determining the stiffness and ductility of FE models. The dimensions for the top or bottom bearings were used to create a solid mesh of the bearings. These bearings were made from three elastic parts and fixed on their base to prevent movement. All fixed boundary conditions were applied using singe point constraints (*BOUNDARY_SPC_SET). This allows individual DOF constraints to be applied to each node in a node set. Contact definitions were used between the rod and the top and bottom halves of the bearing. Loads on the girder were read as the sum of the individual nodal force responses. The bearings allowed for the same degrees of freedom for movement of the girder as the bearing used in the test. The mesh used on the bearing can be seen in a comparison of the bearing in Figure 6.3.

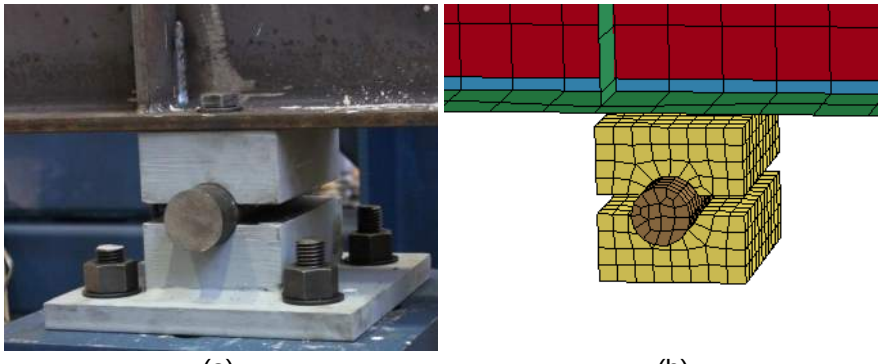

(a) (b)

Figure 6.3 Comparison of the Bearings in the Test and FEM

(a) Roller Bearing Used in the Large-Scale Test, (b) Roller Bearing Used in the Finite Element Model

The lateral restraint system was included to prevent lateral torsional buckling. These were given the same attachment points on the girder and the same attachment location on the load frame in order to maintain the same geometry, but were not tensioned like the ones in the test. Chains would become active if lateral torsional buckling initiated. Ends fixed to the frame used the same single point constraints as the base of the bearings. The lateral restraint system can be seen in Figure 6.4.

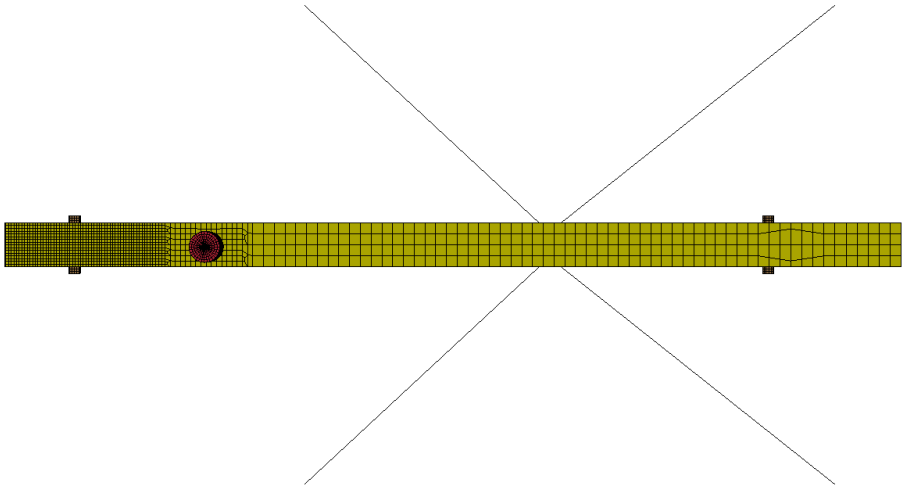

Figure 6.4 Lateral Restrains in the Finite Element Model

6.3.2.2 Loading Mechanisms

In order to model the hydraulic load ram, a two-part system was used to model the tilt saddle. This consisted of an elastic head which would contact the top flange of the girder, and a rigid upper connector to act as the cylinder. The top and bottom haves were shaped to have the same center of rotation and maximum rotation as the tilt saddle. The load was applied $^{3}/_{8}$ in off-center on the right side of the girder. Off-centered loading was intended to counter the exclusion of eccentricities in the web. The load was applied on the right side of the girder to force deformations to the same side seen in the large-scale tests.

Loads were applied to the beam through displacing the top surface of the rigid half of the load ram, the maroon shape in Figure 6.5. This was applied to the entire surface to simulate the plane displacement of the hydraulic load ram. Displacements were applied using the *BOUNDARY_PERSCRIBED_MOTION_SET card. This applies motion to a set of nodes. A triangular acceleration profile was used to slowly increase the velocity, and then maintain a constant velocity. By controlling the accelerations, no shock waves would be sent through the model.

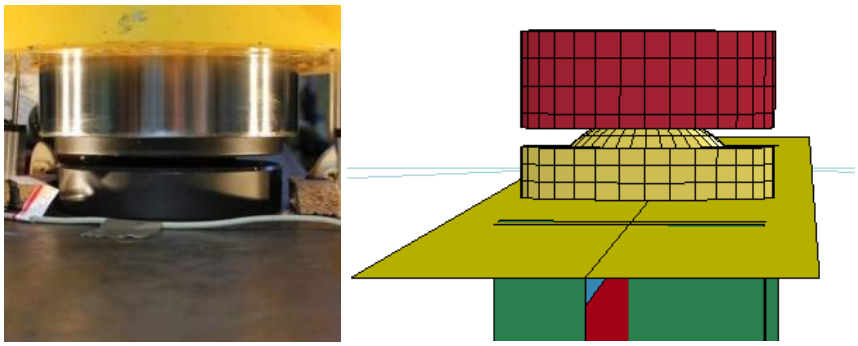

(a) (b)

Figure 6.5 Finite Element Modeling of the Hydraulic Load Ram

(a) Hydraulic Load Ram in the Large-Scale Test, (b) Hydraulic Load Ram in Finite Element Model

6.3.2.3 Contact Definitions

Contact definitions were critical in the formation of the FEM. Force transfer into the main girder was between 3D solid elements and 2D shells. Fortunately, LS-Dyna is capable of handling contact between different orders of elements. All contact was handled using the *CONTACT_AUTOMATIC_SURFACE_TO_SURFACE card. Surface to surface contact tracks nodes on the defined slave surface, and prevents them from penetrating the master surface using a penalty method. This card provides a more rigorous, two-way treatment for contact surfaces. Two-way contact also prevents nodes on the master surface from penetrating the slave surface (DYNAmore, 2015). Surfaces were defined as either a set of shell elements or a segment set of element faces, depending on the type of element. Two-way contact is more accurate than one-way contact, but twice as expensive. This contact definition considers the thickness of shell elements. A standoff based on the shell thickness was provided between all solid and shell elements. This offset can be seen in Figure 6.3b and Figure 6.5b.

Normal behavior of the contact was not considered to be soft, as the modulus of elasticity between the two materials is comparable. This is the default option for contact in LS-Dyna (LSTC, 2012a). Tangential behavior of the contact utilized a penalty method based on a constant friction parameter. Contact between steel and steel was defined as μ=0.50 (Toolbox, 2014). Friction between concrete and steel was reduced to μ=0.45 (Baltay & Gjelsvik, 1990). Contact damping was provided in an effort to eliminate vibrations. This is implemented by providing a percentage of the calculated critical damping coefficient. 20% critical damping was used in all contact definitions.

When considering the model with concrete encasement, four additional contact definitions were required. Contact was not used between the studs and concrete.

Instead, the concrete and studs were considered to be perfectly bonded. This was done by merging nodes of the studs to nodes of the concrete. This was done in lieu of a one-dimensional contact used in concrete reinforcement. This contact would model bond failure and sliding of rebar within the concrete. The heads on the shear studs would not allow significant sliding. Welds between the studs and flanges utilized the same technique of node merging.

6.3.2.4 Shear Stud Constraints

Due to the contact algorithm between solids and shell surfaces, a contact gap was present between the web of the girder and the solid elements of the concrete. This gap was not present on the bottom flange due to the definition of the surface location, discussed in the next section. This gap between the web and concrete needed to be bridged with a beam element for continuity of the stud. This would result in less load transferred to the concrete panel through the studs, and higher stress in the web of the girder.

To attempt to counter this, the two nodes making up the beams spanning the gap were included in individual node sets. One set was made for each stud. These sets had their displacements constrained using the *CONSTRAINED_NODE_SET card. This restricted the x-, y-, and z-translations of the nodes and would help to stiffen this gap.

6.3.2.5 Vibration Damping

In addition to the contact damping, global system level damping was provided (*DAMPING_GLOBAL). The global dampening option provides mass-proportional damping for the entire system (LSTC, 2012a). A damping coefficient of 0.05 of the calculated critical damping was used across the entire model.

6.3.3 Element Formulation

Three element types were used in this model: 1D beam elements, 2D shell elements, and 3D hexahedra. Elements of the same order are differentiated by geometric parameters, such as shell thickness or beam formulation provided in the *SECTION keyword.

6.3.3.1 1D Elements

Beams used in LS-Dyna are defined with three nodes (*ELEMENT_BEAM). Nodes one and two define the beginning and end of the element, respectively, and the third node defines the orientation of the beam (LSTC, 2012a). Orientation is important as it defines the position of the local s- and t- axes. This is important to determine directional shears, or to model differences the strong and weak axis. Orientation of 1D elements are shown in Figure 6.6.

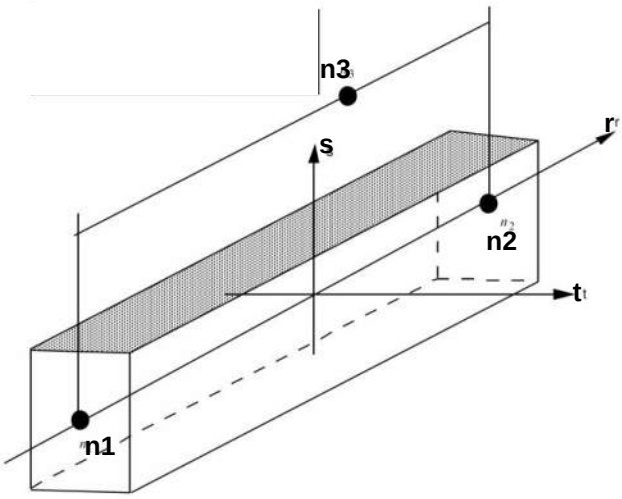

Figure 6.6 Definition of Beam Orientation in LS-Dyna (LSTC, 2012a)

The formulation technique for beam elements used for the studs follows the Hughes-Liu formulation (*SECTION_BEAM: ELFORM=1) with cross section integration. This formulation is desirable for many reasons (LSTC, 2006). This formulation is low-cost and robust. This gives the element a low computational cost and accurate formulation. The formulation uses a local coordinate system and is objective. This means it will not produce stains under rigid body rotation, and existing stress is not affected by rigid body motion. The formulation is based on a degeneration of a hexahedral brick element. This makes Hughes-Liu beams compatible with brick elements. This is important to handle merged nodes of the concrete and studs. The formulation includes finite transverse shear strains. This assumption is critical for the shear in the studs. Two-point Gauss quadrature is used to integrate the beam elements. Shear correction factors of $^5/_6$ are used in the formulations as suggested accounting for over predictions of shear (LSTC, 2012a). The addition of cross section integration allows for stresses to be computed at integration points. This cross section integration defines the size and shape of the beam element being utilized. Studs are defined as a solid circular cross-section of $^3/_8$ in.

Truss elements used for the chain (*SECTION_BEAM: ELFORM=3). These elements only transmit axial force and do not allow bending. Therefore only a cross-sectional area is provided.

6.3.3.2 2D Elements

Shell elements are four node quadrilateral elements (*ELEMENT_SHELL). Shells of the damaged flange include the _OFFSET option. This allows the computational surface of the shell to translate without jogging the mesh. The shell element has a top and bottom surface. The orientation is determined by the numbering of element nodes. Counterclockwise numbering of shell nodes 1-4 determines the top surface (LSTC, 2012a). Fully integrated linear 3D shell elements (*SECTION_SHELL: ELFORM=16) are used in the analysis. While more computationally expensive than the default Belytschko-Tsay element, fully integrated shells provide more accurate representations of complex stress fields. The fully integrated shell utilizes a local coordinate system. This eliminates stresses caused by rigid body motion. The formulation is frame invariant. This maintains the material properties under different material orientations (LSTC, 2006). A transverse shear correction factor of $^5/_6$ is utilized, as recommended in the user manual. Five point Gauss quadrature is used to integrate through the thickness of the shell.

In addition to using the fully integrated formulation, additional accuracy was added to the formulation through the addition of warping stiffness (*HOURGLASS: IHQ=8). This corrects degradations to the solution caused by element warping, and results in a computation time penalty of 25%. This forms extremely robust shell elements capable of correctly predicting the behavior of a twisted beam (DYNAmore, 2015). This behavior is important to estimate post-failure loads.

6.3.3.3 3D Elements

Solid elements used for the concrete and bearings are eight node hexahedra (*ELEMENT_SOLID). Solid elements are formulated using one-point integration (*SECTION_SOLID: ELFORM=1). The one point integration leads to constant stress within an element. Utilizing constant stress elements significantly reduces the formulation cost of these elements. Calculation of the elemental strain matrix is reduced by 25 compared to a fully integrated hexahedra using second order Gauss quadrature (8-point 2×2×2). This is due to fewer computations and the antisymmetric property of the strain matrix at the center of the element. Computational cost savings extend into the nodal strains and forces, reducing the number of operations by a factor

of 16. Because only one constitutive formulation is required at the center of the element, stress calculations for the element are also reduced 8 times (LSTC, 2006).

This element introduces surreptitious zero energy deformation modes. Surreptitious modes occur when an element is able to undergo deformations without causing stress to change in the element. This is caused when using less than second order Gauss quadrature. Surreptitious modes cause internal energy to be wasted deforming the mesh in ways not physically possible. Surreptitious modes can be suppressed through applying hourglass controls. These controls provide resistance to these deformation modes. The Flanagan-Belytschko stiffness based formulation with exact volume integration is used to control surreptitious modes (*HOURGLASS: IHQ=5). This is based off the formulation created by Flanagan and Belytschko (Flanagan & Belytschko, 1981). Stiffness hourglass control is used rather than viscous hourglass control as it performs better in low velocity problems. Viscous damping is useful at high deformation velocities. The exact volume integration helps to provide better results as elements begin becoming highly distorted (DYNAmore, 2015).

6.3.4 Material Formulations

Four material models were used in the model: *MAT_ELASTIC, an elastic material; *MAT_RIGID, a rigid material; *MAT_PIECEWISE_LINEAR_PLASTICITY, a flexible elasto-plastic material; and *MAT_CONCRETE_DAMAGE_REL3, the third iteration of a concrete damage model developed by Karagozian and Case (K&C). Bearings and the spreader beams were modeled using the elastic constitutive model, studs and the girder steel used the piecewise linear plastic formulation, and the concrete followed the K&C model. Girder steel included a more rigorous damage formulation than is standard.

*6.3.4.1 *MAT_ELASTIC*

The elastic material model is a simple three parameter constitutive model. The constitutive formulation uses the Cauchy stress tensor, and the Jaumann rate for stress rate calculations (LSTC, 2006). The Jaumann rate of the Cauchy tensor is given in Equation 6.1. In this equation, σ^{Δ} is the Cauchy stress rate, a superscript dot denotes a time derivative, and ω is the spin tensor. This material model is used for the bearings and the load ram because it is computationally efficient and stresses in these parts are not critical.

$$\sigma^{\Delta} = \dot{\sigma} + \sigma \cdot \omega - \omega \cdot \sigma$$

Equation 6.1 Jaumann Rate of the Cauchy Stress Tensor

The user is required to provide density, Elastic modulus and Poisson's ratio as material inputs. The material was given the properties of steel. The Elastic modulus was defined as 29e6 psi and a Poisson's ratio of 0.3 was used. In order to reduce computation times, mass scaling is introduced to the materials. Minimum time step for calculations are related to the time for a wave to travel through the smallest element. The wave speed through the material is defined as the square root of the Elastic modulus divided by the density. If the density increases, the minimum time step increases (DYNAmore, 2015). The densities of the elastic materials were scaled by a factor of 100 (final density: 0.0734 lb*s^2/in).

*6.3.4.2 *MAT_RIGID*

This material is used to create non-deformable rigid materials. The top bearing was assigned this material. Computational efficiency is further increased by not storing element data from the analysis. This model utilizes the same three input parameters as the elastic material: density, Elastic modulus, and Poisson's ratio. Despite the material being non-deformable, elastic modulus and Poisson's ratio need to be included in order to handle contact definitions. The same values from the elastic material are used to define the rigid material.

*6.3.4.3 *MAT_PIECEWISE_LINEAR_PLASTIC*

This is an elasto-plastic material with an arbitrary stress-strain relationship. This model utilizes the same elastic formulation as the elastic material, and has options for either Cowper Symonds rate effects or an arbitrary user defined rate effects. Due to quasi-static analysis performed, rate effects were not included.

Plastic hardening is determined through one of two ways, a defined yield stress and tangent modulus, or a user defined yield stress vs. plastic strain curve. Plastic strain is updated systematically through checking the current element stress against the current material yield stress. If the element stress exceeds yield, then the effective plastic strain is incremented according to Equation 6.2 (LSTC, 2012b). In this equation, s^* is the current deviatoric stress, σ_y is the current yield stress, and G and E_{tan} are the shear and current tangent modulus.

$$\Delta\varepsilon_{eff}^{p} = \frac{\left(\frac{3}{2}s_{ij}^{*}s_{ij}^{*}\right)^{1/2} - \sigma_y}{3G + E_{tan}}$$

Equation 6.2 Effective Plastic Strain Incrimination in Elasto-Plastic Material

This material has an option for failure based on a maximum allowable plastic strain. An additional damage model is also available by using the *MAT_ADD_EROSION card. This option allows the user to define element deletion criteria based on maximum stress, principal strains and other stress-strain criteria, or invoke more complex damage evolution formulations. The GISSMO (General Incremental Stress-State dependent damage MOdel) damage model was implemented using this card. Originally developed for the automotive and sheet metal forming industries, GISSMO is an incremental damage accumulation model useful for describing damage in metals. The model tracks a damage parameter which increments from zero. The stress in the element is reduced as the parameter increases, representing softening. When the parameter reaches a user defined value, typically one, the element is deleted. The GISSMO model has the added benefit of allowing the plastic strain when damage initiates and the ultimate strain to be functions of the stress triaxiality factor (LSTC, 2012b). Stress triaxiality is the ratio of equivalent stress to mean stress ($^{\sigma e}/_{\sigma m}$). Instability defines the strain where damage based softening initiates. The failure relation defines the material rupture strain. This provides a much more powerful way of capturing damage progression in thin metals, such as those in the girder.

A basic formulation was used for the steel for the studs. The values for the elastic modulus, Poisson's ratio and density were the same as those used in the elastic material. Because the stud material is essentially perfectly plastic (σ_y=84.1 ksi, σ_u=84.7 ksi), a perfect plastic assumption is made with σ_y=84,400 psi. Failure was defined as ε_f=0.3 based on the manufacturer's value.

$$\varepsilon_{true} = \ln(1 + \varepsilon_{eng})$$
$$\sigma_{true} = \sigma_{eng}(1 + \varepsilon_{eng})$$
$$\varepsilon_p = \varepsilon_{true} - \frac{\sigma_{true}}{E}$$

Equation 6.3 Calculation of the Plastic Strain for the Finite Element Model

The girder material used the user defined plasticity option and the GISSMO model to model failure. The plastic strain relation was derived from the undamaged-B coupon stress strain relationship. This coupon had values of yield and ultimate strength nearest the calculated average. The values calculated from the coupon test were based on engineering stress and strain. Values for finite element analysis need to be in terms of true stress and true strain. These are based on instantaneous area rather than initial area. The series of equations required to calculate the plastic strain are given in Equation 6.3. The engineering and true stress strain relations for the undamaged-B coupon are plotted in Figure 6.7a with the finite element stress strain relation used. The

stress in the plastic strain equation cannot decrease; therefore it is terminated at the maximum stress. Softening after that point was handled by the damage model. The same values for the elastic modulus, Poisson's ratio and density from the elastic material are used. 29e6 psi was used for the elastic modulus instead of 33e6 psi as the authors were not confident with the latter value.

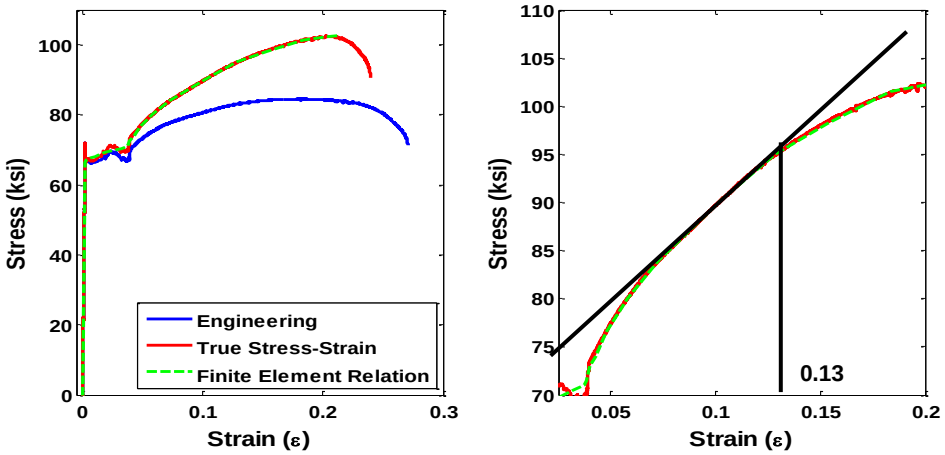

Figure 6.7 Stress Strain Relations of the Undamaged-B Girder Steel

(a) Full Stress Strain Relation, (b) Determination of the Instability Strain

The relation of triaxiality vs. instability strains and failure strains were adapted from data in available material (Effelsberg, et al., 2012). In this paper, typical parameters for the GISSMO model were identified and tested against two other damage models: Gurson and Von Mises. The triaxiality relations given in the paper were then scaled to the observed instability and ultimate strains. The uniaxial tension specimen has a triaxiality factor of 0.5, so the values were scaled at this point. Instability was defined as the point of observable curvature leading to ultimate strength, shown in Figure 6.7b as 0.13. Ultimate strain was scaled to 0.239. The relation of triaxiality with instability and failure strains is shown in Figure 6.8.

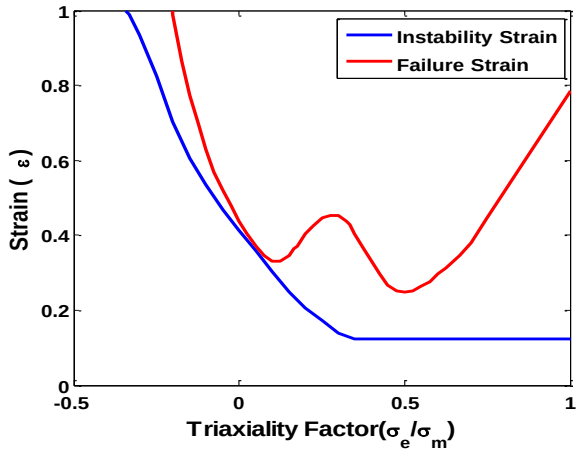

Figure 6.8 Instability and Failure Strain Relations Used in GISSMO Damage Model

*6.3.4.4 *MAT_CONCRETE_DAMAGE_REL3*

This is the K&C concrete damage model. It is a three invariant model (I_1, J_2, J_3) that uses three shear failure surfaces, to represent material yielding, peak strength, and third residual capacity (y, m, and r, respectively) (Malvar, et al., 1997). Each of these curves relates stress difference (σ_1-σ_3) to pressure (-tr(**σ**)/3), and follows the relations given in Equation 6.4. A plot of these surfaces can be seen in Figure 6.9. The high residual strength is part of what defines UHPC. The flow rule used in the constitutive relation can be either associated or non-associated, and is related to the fractional dilatancy parameter prompted in the model. Fractional dilatancy of zero results in non-associated plastic flow, while a value of one gives associated plastic flow (LSTC, 2012b).

$$\Delta\sigma_i = a_{0_i} + \frac{p}{a_{1_i} + a_{2_i} p}, \qquad i = y, m, r$$

Equation 6.4 Equation for the Three Failure Surfaces in the Concrete Damage Model

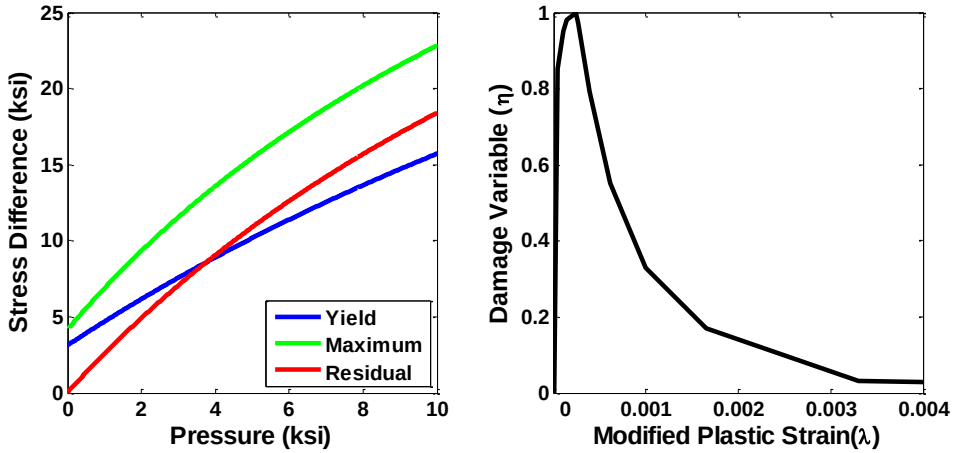

Figure 6.9 Critical Functions Defining the Concrete Damage Model

Damage progression in this model uses a modified plastic strain parameter, λ. This parameter begins to be incremented after the stress state reaches yield. This parameter is related to the effective plastic strain, element pressure, and a damage scaling exponent. The damage exponent depends on the stress state: compressive, tensile, or triaxial tension. The modified plastic strain parameter is then the independent variable of a damage function, η(λ). The damage variable η begins at zero with λ=0 and then reaches a maximum of one, then decreases back to zero. Before the maximum of the damage function, the value is used to interpolate between the yield and maximum surfaces. After maximum, the variable interpolates between the residual and the maximum surfaces (LSTC, 2012b). This interpolation function is plotted in Figure 6.9b.

Maximum aggregate width is input to determine crack formation and progression. This model does not track and document crack formations. Instead, an 'effective plastic strain' variable, δ, is used. This is a damage variable calculated from the modified plastic strain, λ, as shown in Equation 6.5 (LSTC, 2012b). The modified plastic strain is zero when no damage has occurred, one at the maximum strength surface, and two when transitioning to the residual strength surface. A crack can be visualized from a fringe plot of the δ parameter. This damage eventually spreads thorough the entire concrete material, so earlier stages are indicative of crack patterns.

$$\delta = \frac{2\lambda}{(\lambda + \lambda_m)} \leq 2$$

Equation 6.5 Calculation of Effective Plastic Strain

The model includes an option for automatic parameter generation which the user only needs to provide the unconfined compressive strength. The automatic parameter

generation feature does not always provide a robust and reliable model for UHPC, and so it was not used.

The concrete damage model requires an equation of state (*EOS_ TABULATED_COMPACTION). This equation of state relates element pressure and bulk unloading modulus to the volumetric strain. These relationships were modified from the relationship generated from automatic parameter generation. These were scaled uniformly so that the initial bulk modulus when combined with the Poisson's ratio produced the initial loading modulus from the concrete.

A constitutive relationship had been produced and validated for a concrete with compressive strength of 3,300 psi for a previous project. In order to create a concrete with strength of 16,000 psi the automatic parameter generation feature was used to produce parameters for both concrete strengths. Scale factors were then found to change variables of the yield surfaces, and damage scaling exponents from the automatically generated 3,300 psi concrete to the validated concrete. These scaling factors were then applied to the automatically generated 16,000 psi concrete to create a validated model, whose parameters can be found in Table 6.1. The damage function was taken from existing research on constitutive modeling of UHPC being performed at UConn by Man Xu.

Table 6.1 Selected Parameters from the 16 ksi Concrete Damage Model

LS-Dyna Parameter	Parameter Description	Value
PR	Poisson's Ratio	0.200
FT	Uniaxial Tensile Strength Tensile	1305 psi
A0	Maximum Shear Failure Parameter A0	4145 psi
A1	Maximum Shear Failure Parameter A1	0.3513
A2	Maximum Shear Failure Parameter A2	1.848e-5 psi^{-1}
OMEGA	Fractional Dilatancy (Flow Associativity)	0.50
K0	Initial Bulk Unloading Modulus	3.059e6 psi

6.4 COMPARISON TO LARGE-SCALE TESTS

The finite element model was found to predict all critical aspects of the large scale tests. Failure loads, displacements, strains, post-failure loads, and ductility were found to be accurate. The following sections describe the performance of the model in each of the categories on which data was collected in the large scale test.

6.4.1 General Observations

Failure mechanisms and failed shapes were well predicted. Figure 6.10 shows the deformed shapes for each of the specimens. Each of the deformed shapes predicted by the FEA accurately predicts the deformed shapes of the test girders. The coloring seen on the concrete panel in Figure 6.10c indicates predicted cracking pattern from the FEA. The cracking on the large-scale test is outlined in Figure 6.10f for comparison. The mesh on the repaired girder is included to show the shear deformation between the end of the concrete panel and the load ram.

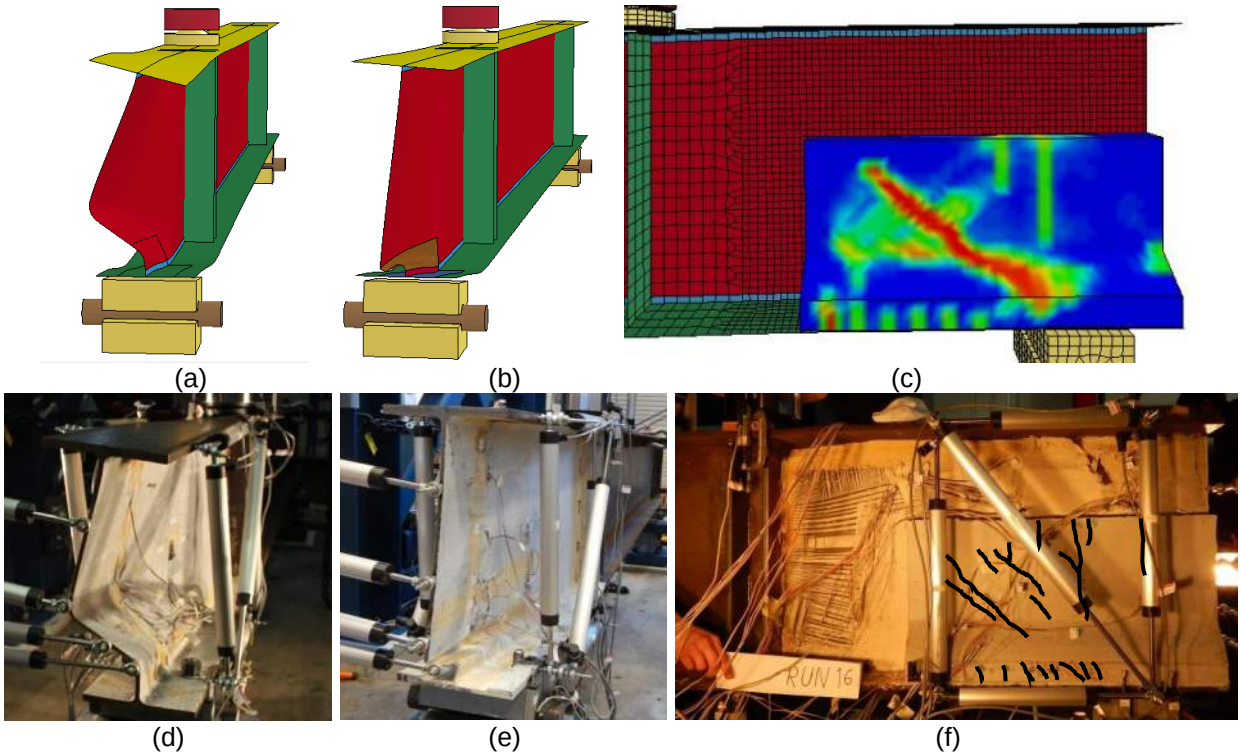

Figure 6.10 Comparisons of the Deformed Shapes of the Girders

(a) FEA of Undamaged Girder, (b) FEA of Damaged Girder, (c) FEA of Repaired Girder, (d) Large-Scale Test of Undamaged Girder, (e) Large-Scale Test of Damaged Girder, (f) Large-Scale Test of Repaired Girder

The finite element model was able to predict the formation of the plastic hinges in the bottom flange of the undamaged and damaged girders. Figure 6.11 shows a comparison of the bottom flange of the undamaged and damaged girders at the conclusion of the FEA and the large-scale test. The finite element model showed higher rotation of the bearing in the undamaged girder. This caused the plastic hinge near the bearing to form at the bearing, rather than off of the bearing. This could potentially lead to lower predicted compressive strains in the flange after failure.

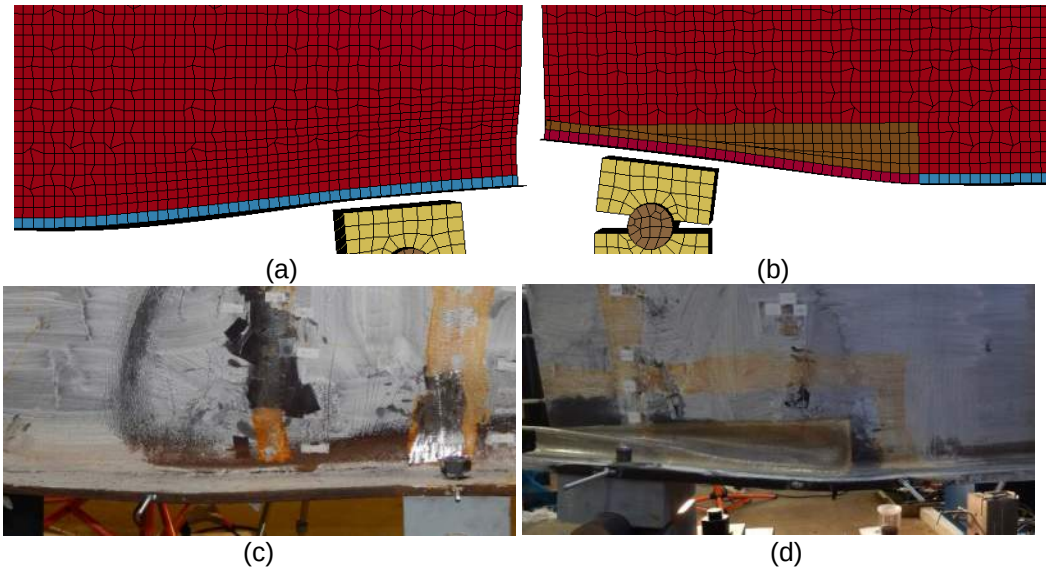

Figure 6.11 Appearance of the Bottom Flange Plastic Hinges

(a) Undamaged Girder from FEA, (b) Damaged Girder from FEA, (c) Undamaged Girder from Large-Scale Experiment, (d) Damaged Girder from Large-Scale Experiment

Crack formation in the finite element model occurred in a similar fashion as in the large-scale test. Figure 6.12 shows the progression of cracking in the left panel, as well as the final crack predictions of both panels. Figure 6.12e shows the scale of the effective plastic strain, δ, used in the figures. Blue indicates regions in the concrete remaining in the elastic region. As the fringe level becomes green, the concrete reaches maximum strength and crack development is possible. At a fringe level of red, the concrete is on its residual strength surface, and cracks have formed. The first signs of yielding actually formed in the bevel at a load of 56 kip. This is seen as the cyan in Figure 6.12a. A vertical crack at the bearing next became possible at 115 kip, Figure 6.12b. Vertical flexural cracks in the bottom of the panel then became possible along with the beginning of shear cracking in the main panel at 192 kip, Figure 6.12c. This shear crack became prominent at a load of 216 kip, Figure 6.12d. The crack predictions at peak load, 268 kip, are shown for the left and right panel in Figure 6.12f-g.

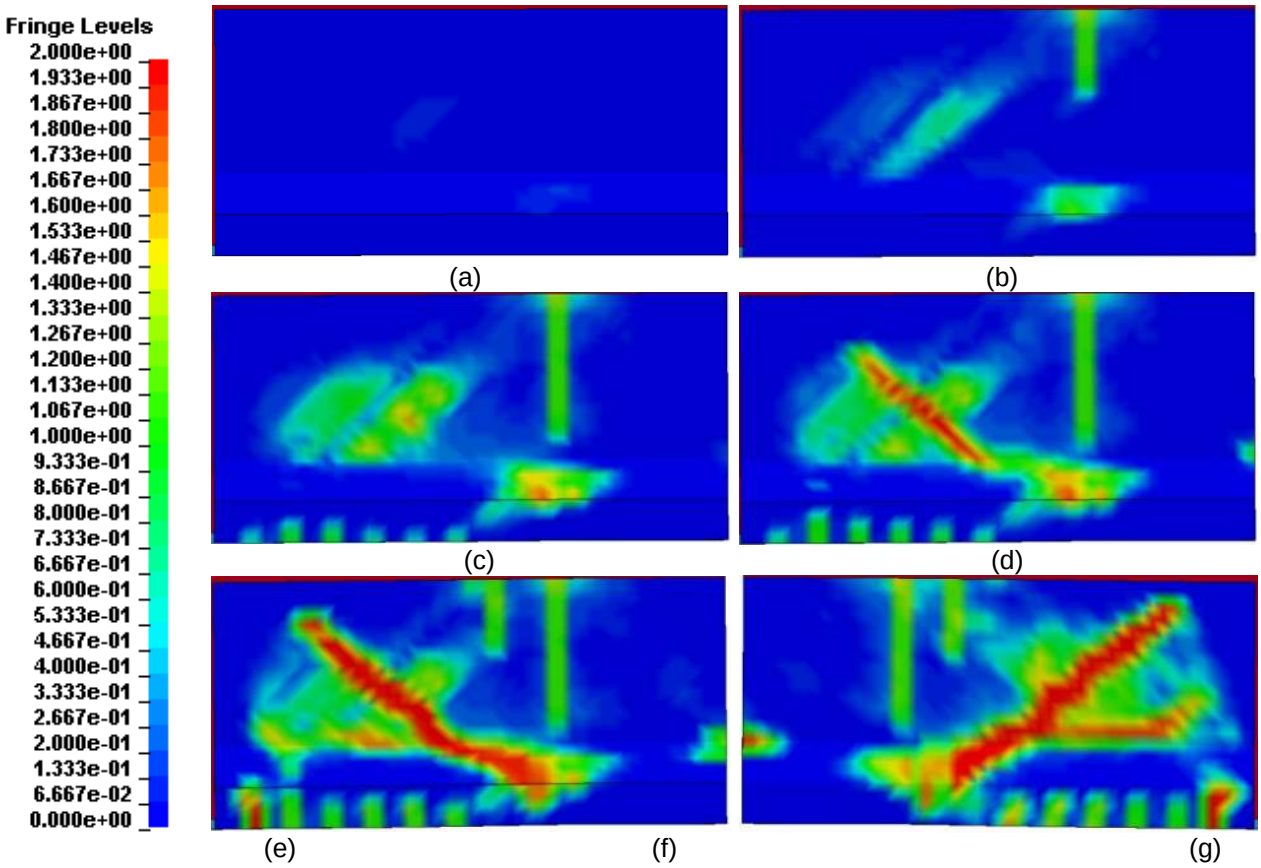

Figure 6.12 Finite Element Crack Development Prediction

(a) Initial Concrete Yielding 56 kip, (b) Vertical Crack Formation off Bearing 115 kip, (c) Cracking Initiating at the Bottom of the Panel, Main Shear Crack Initiating 192 kip, (d) Shear Crack of Main Panel 216 kip, (e) Damage Scale of δ, (f) Final Appearance (L) 268 kip, (g) Final Appearance (R) 268 kip

Figure 6.13 shows a plot of the Von Mises stress distribution in each of the girders at their peak loads. The fringe level used is presented above the figures. A fringe level of red indicates levels of yielding stress. Yield level stresses are visible in the undamaged girder, Figure 6.13a, in the two areas where whitewash damage was evident, at the edge of the bearing and at the top of the web by the load ram. The damaged girder in Figure 6.13b shows concentrated stress in the reduced section. The repaired girder, Figure 6.13c, shows yield level stress on the entire height of the girder from the end of the panel to the stiffeners, as was seen with the whitewash in the test. Stress is still seen concentrated in the reduced section in the repaired girder. This could cause erroneous strains in the base of the girder. This is likely due to the gap between the steel and concrete required for contact. This resulted in a small ($^{Tw}/_{2}$) stud element to span this gap. This likely resulted in a less than efficient force transfer between the girder and the panel.

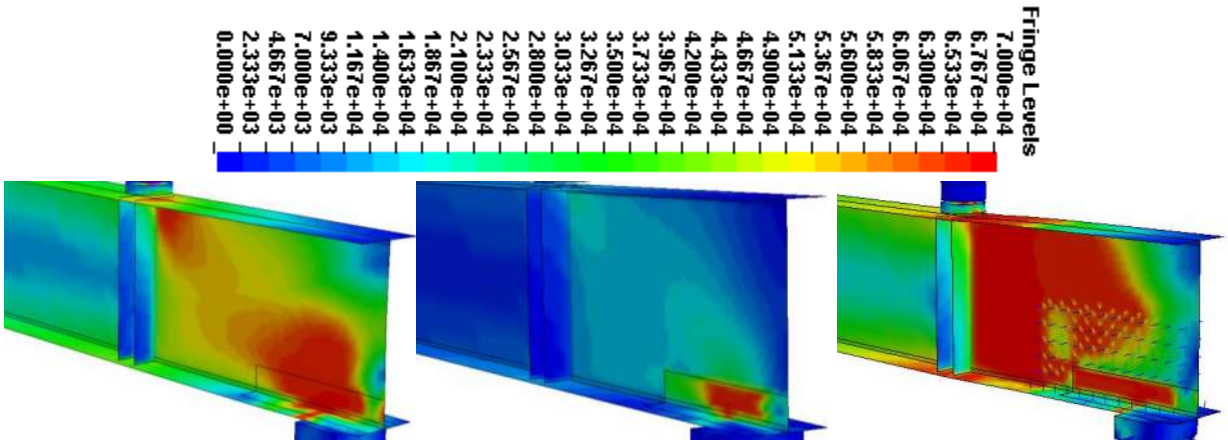

(a) (b) (c)

Figure 6.13 Von Mises (Equivalent) Stress Distribution in the FE Girders

(a) Undamaged Girder Prior to Buckling, 193 kip, (b) Damaged Girder Prior to Buckling, 56 kip, (c) Repaired Girder at Peak Load, 268 kip

6.4.2 Load-Displacement Relationships

Figure 6.14 shows the finite element load displacement relations superimposed on the large scale test data. Failure loads of the girders in the finite element models of the undamaged, damaged and repaired girders were 193 kip, 56 kip, and 268 kip, respectively. This resulted in an over prediction of load of 7%, 29%, and 16% for the undamaged, damage and repaired girders, respectively. One possible source of error is the lateral restraint system used in the large-scale experiment. These applied a downward force on the girder, which was not accounted for in the load. The larger over-prediction of the damaged girder was due to an additional 20 mil being removed from one side of the damage pattern. This resulted in eccentricity and resulted in premature failure of the girder.

Stiffness predictions of the FEA were 767 $^{kip}/_{in}$ for the undamaged girder, 694 $^{kip}/_{in}$ for the damaged girder, and 786 $^{kip}/_{in}$ for the repaired girder. These were 19% higher than the tested values. Over prediction of the stiffness of the system is common in FEA. In addition to exclusion of imperfections which reduce stiffness, slack in the system and residual stress in the tests are not accounted for in FEA (Maggi, et al., 2005). Increases in stiffness also occur from lower degrees of freedom from the modeling process, which increases apparent stiffness (Lepi, 1998). The models did show the same pattern of stiffness changes with respect to damaged and repaired stiffness. The stiffness of the repaired girder was proportionally less than the other two, 15% higher vs 20%, because of the issue with the contact gap.

Post-failure load carrying capacity of the undamaged girder was perfectly predicted. The post-failure capacity of the damaged girder was overestimated by approximately 20%. This is due to the offset of damage in the test girder, and the extreme deformation required of damage in the mesh. This extreme displacement field in linear elements causes element behavior to be overly stiff.

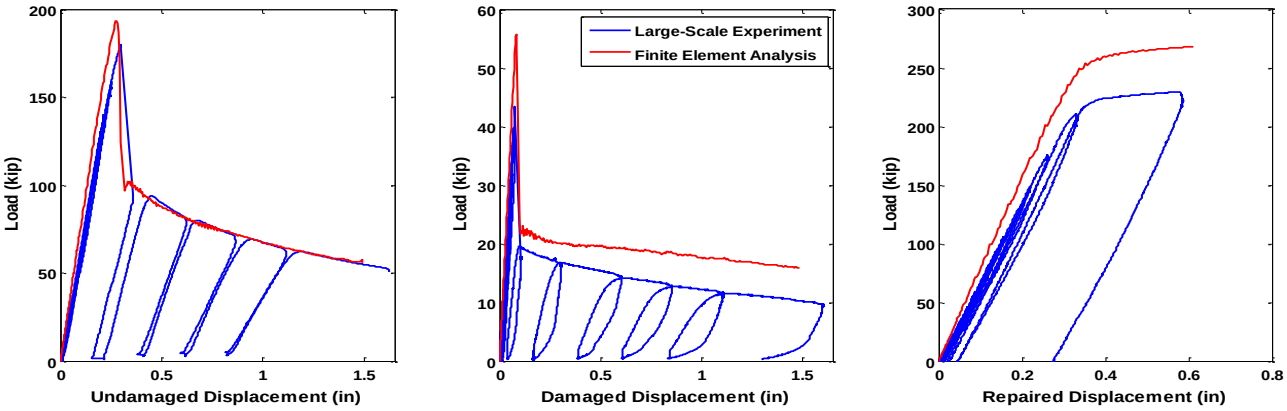

Figure 6.14 Comparisons of the Load Displacement Relations of the Girders

(a) Undamaged Girder, (b) Damaged Girder, (c) Repaired Girder

Figure 6.15 shows vertical displacements of each of the girders at the bearing. The performance of the FEA predicting undamaged and damaged bearing deformations are nearly perfect. At peak load in the undamaged girder, the same divergence is seen between the left and right side. Progression of post-failure deformations for the undamaged and damaged girders is properly predicted.

Predictions for the repaired girder had the same initial stiffness but then diverged. This is likely due to the high overall stiffness of the system. Average error between the readings at peak was only 59 mil.

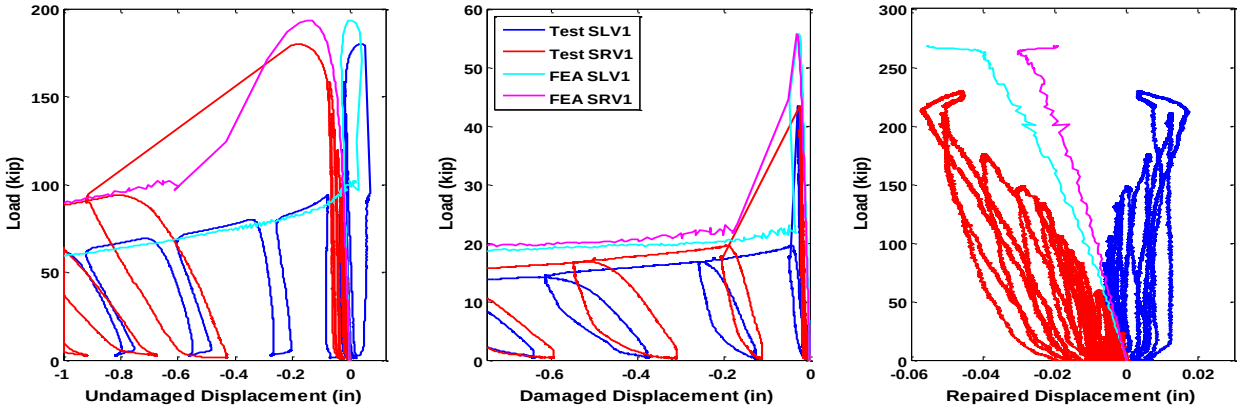

Figure 6.15 Vertical Displacement of Girders at the Bearing

(a) Undamaged Girder, (b) Damaged Girder, (c) Repaired Girder

The shear deformations in the potentiometer shear box are compared in Figure 6.16 for the three girders. The behavior for the undamaged girder was well predicted. Loading rates, failure development, and post failure behavior show the same trends. The damaged girder was also well predicted. The right side showed the same softer response as in the test, and post failure development followed the same trend. The repaired girder showed good predictions for both sides for initial loading rate. As loading progressed, the finite element model did not predict the reversal of direction of the shear strain observed on the left side.

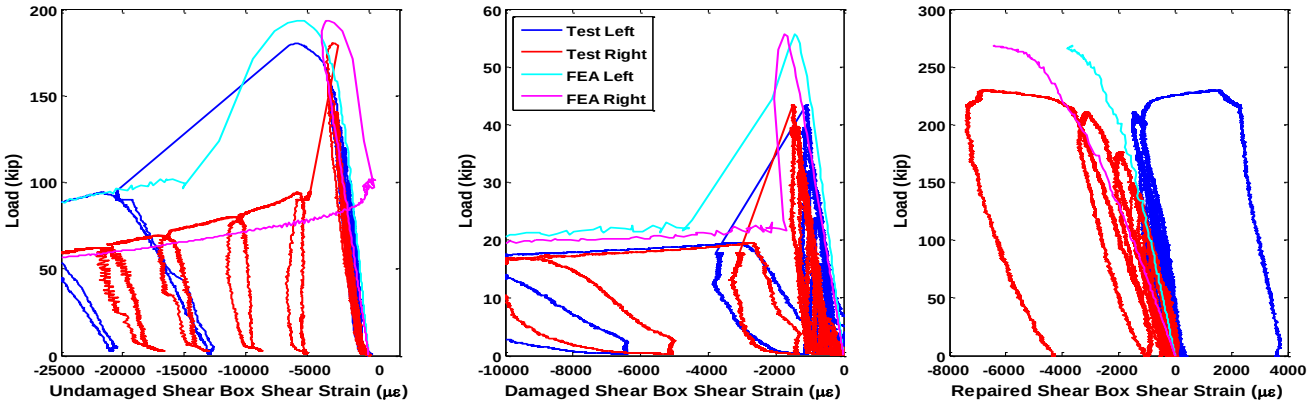

Figure 6.16 Comparison of Shear Box Deformation of the Girders

(a) Undamaged Girder, (b) Damaged Girder, (c) Repaired Girder

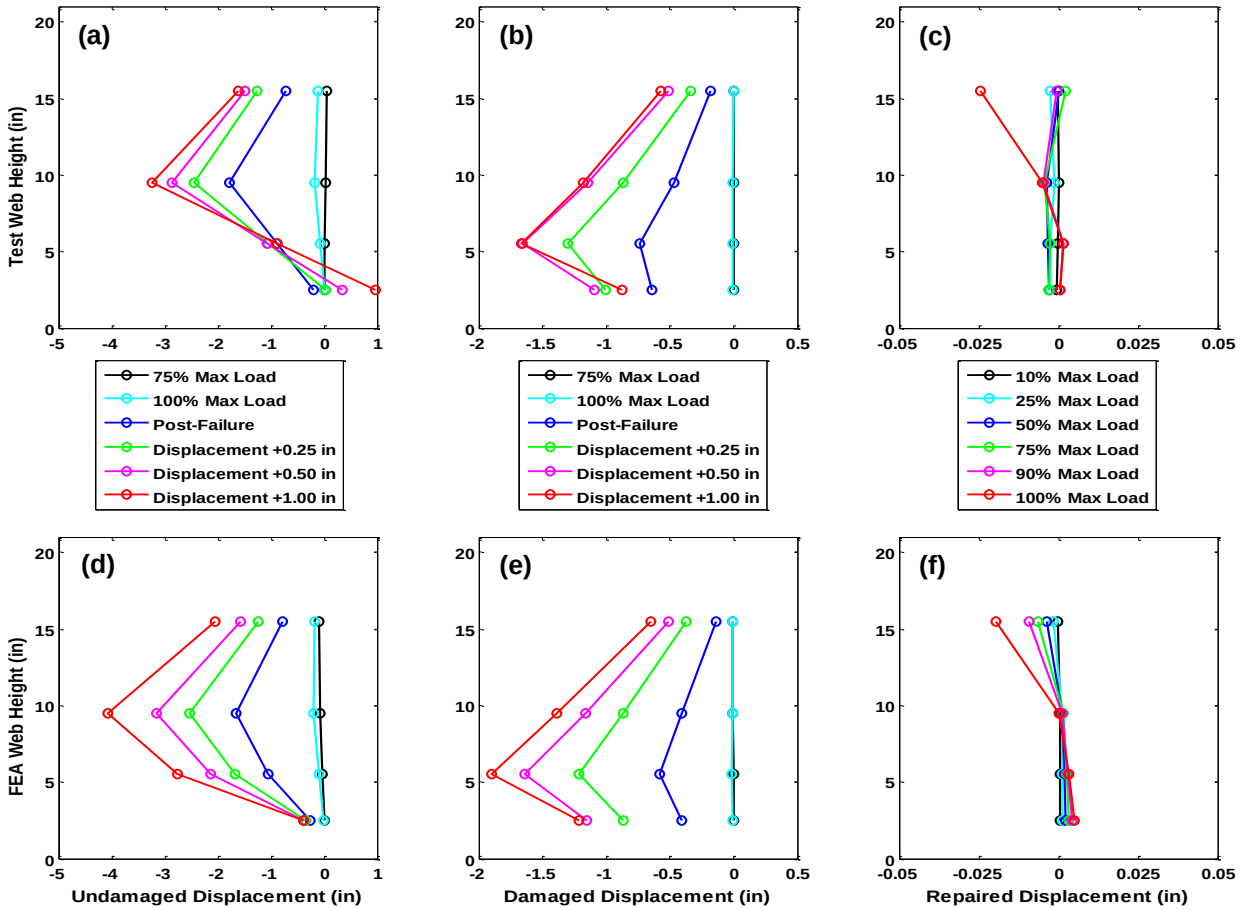

Figure 6.17 Comparison of the Web Deformations in the Girders

(a) Undamaged Girder, Large-Scale Test, (b) Damaged Girder, Large-Scale Test, (c) Repaired Girder, Large-Scale Test, (d) Undamaged Girder, FEA, (e) Damaged Girder, FEA, (f) Repaired Girder, FEA

The deformed shapes of the girders from the large-scale test and the FEA are compared in Figure 6.17. The performance of all three girders was well predicted by the FEA. The only noticeable difference is the movement of the W1 potentiometer in the undamaged girders. Because the FEA did not see the same displacement of the bearing as the test did, the overall displacements predicted by the FEA were larger. The magnitude of difference between the W1 and W3 potentiometers remained consistent.

6.4.3 Strain Data

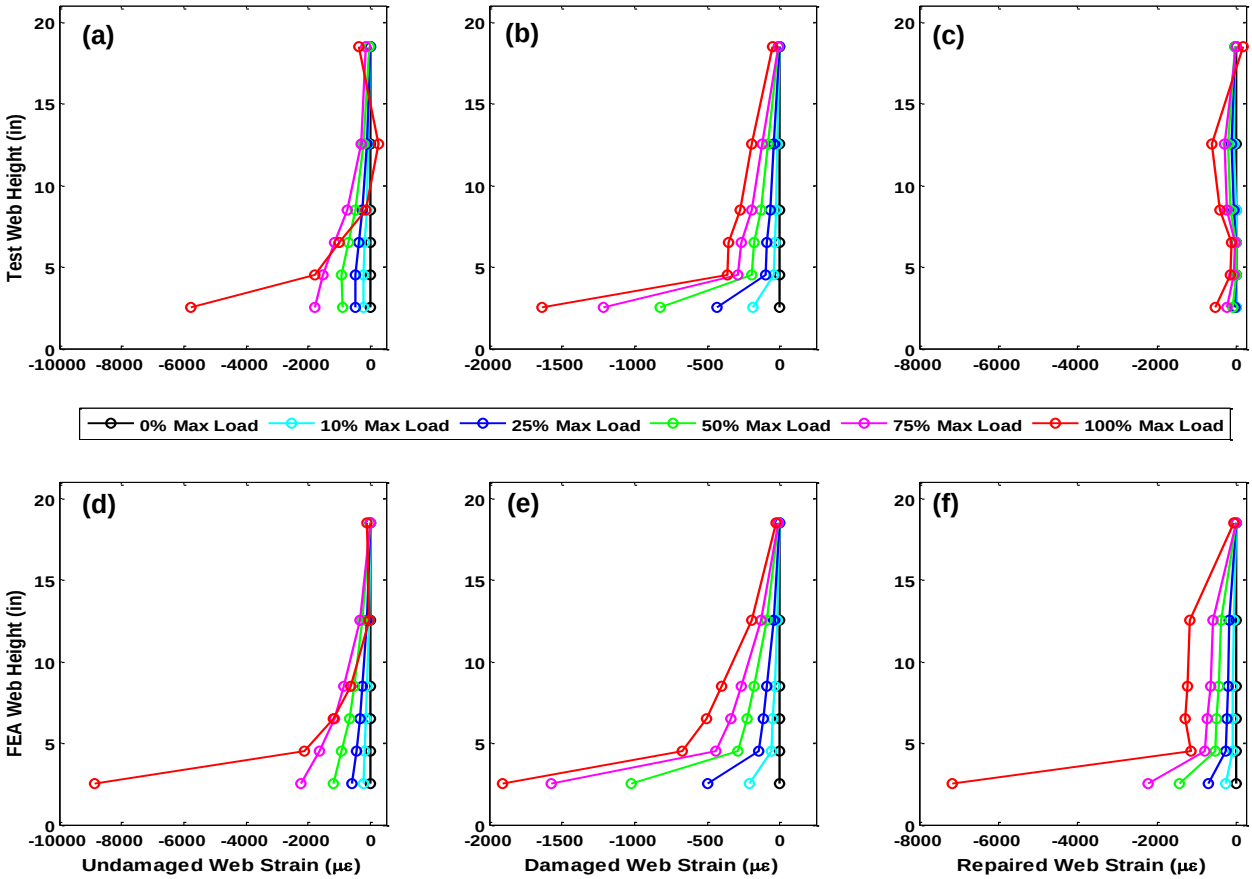

Figure 6.18 Comparison of the Axial Strain Distributions

(a) Undamaged Girder, Large-Scale Test, (b) Damaged Girder, Large-Scale Test, (c) Repaired Girder, Large-Scale Test, (d) Undamaged Girder, FEA, (e) Damaged Girder, FEA, (f) Repaired Girder, FEA

The distribution of axial strains on the height of the web is presented in Figure 6.18. The development of the strains in the undamaged girders and damaged girders show good agreement between the test results and the FEA. The development of tensile strains 60% up the height of the web at peak load are seen in both the test and the FEA. The strains in the reduced section of the repaired girder were over predicted because of the contact gap and saw large concentration in the reduced section. Despite this, the FEA still showed strains lower in the undamaged girder at higher loads.

Figure 6.19 shows the comparison of the maximum shear in the web recorded by the strain gauge rosettes. The initial rate of strain developments in all the girders were well predicted by the FE models. The FEA in the repaired girder saw an increased rate of shear strain development after a load of 150 kip. This was not seen in the large-scale experiment, and was caused by the contact gap.

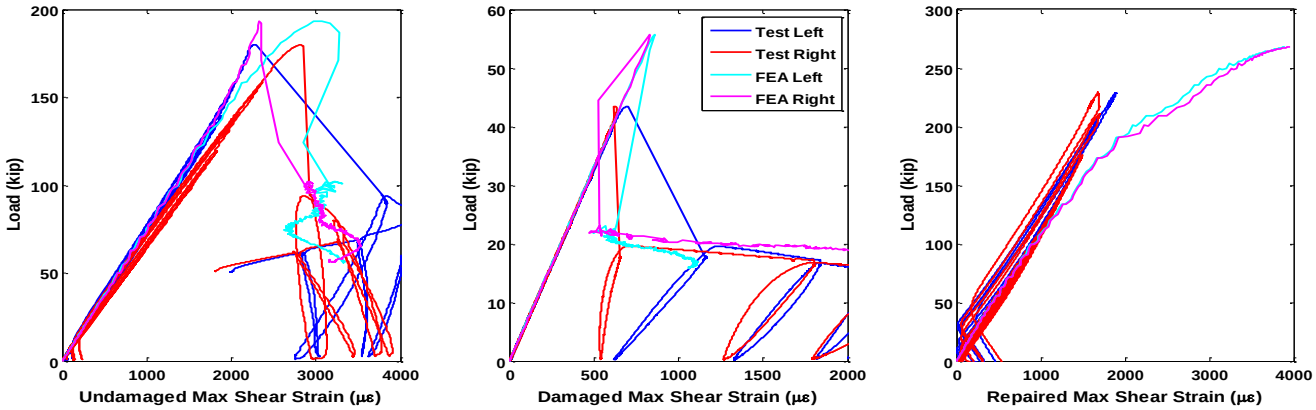

(a) (b) (c)

Figure 6.19 Comparison of Steel Max Shear Strains in the Girders

(a) Undamaged Girder, (b) Damaged Girder, (c) Repaired Girder

Figure 6.20 shows a comparison of the bottom flange strains extracted from the FEM with strains from the tests. Loading rates of the F1 and F2 gauges all showed lower straining rates in the FEA than in the test. Despite this, the same trends can be seen in this plot as was seen in the large-scale experiment. After the undamaged and damaged girders buckle, strains corresponding to F3 and F4 show little change. F1 and F2 strains on the undamaged girder show the same sign of the double plastic hinge. This shows that the FEM used is capable of capturing all critical information for the undamaged girder. The damaged FE girder shows signs of a double, rather than single plastic hinge formation, but these strains do not continue as loading progresses. The strains in the repaired F2 gauge show an increased rate of loading compared to the undamaged and damaged girders, but the increase was not as marked as it was in the physical tests.

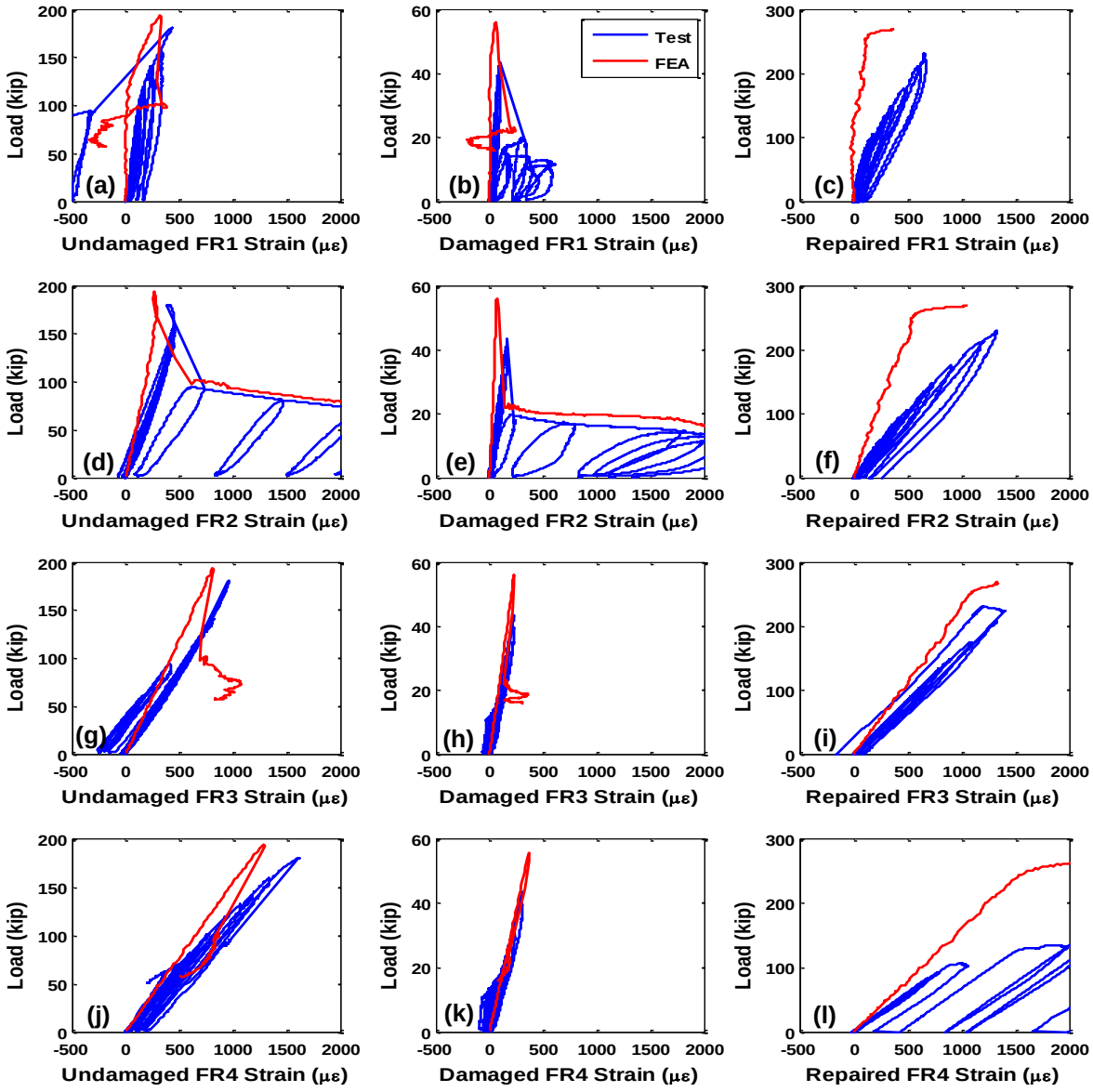

Figure 6.20 Comparison of the Flange Strains in the Girders

(a) Undamaged F1 Flexural Strains, (b) Damaged F1 Flexural Strains, (c) Repaired F1 Flexural Strains, (d) Undamaged F2 Flexural Strains, (e) Damaged F2 Flexural Strains, (f) Repaired F2 Flexural Strains, (g) Undamaged F3 Flexural Strains, (h) Damaged F3 Flexural Strains, (i) Repaired F3 Flexural Strains, (j) Undamaged F4 Flexural Strains, (k) Damaged F4 Flexural Strains, (l) Repaired F4 Flexural Strains,

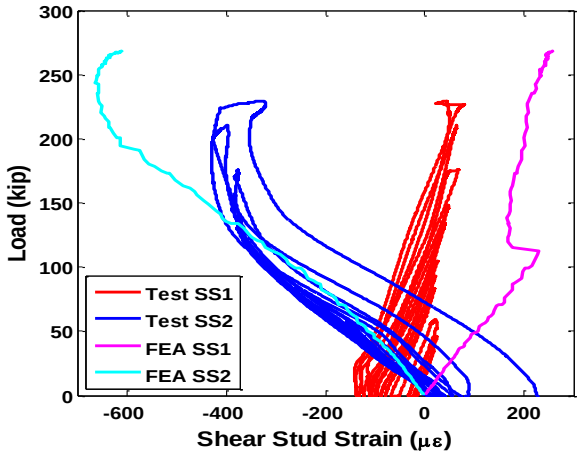

Figure 6.21 Comparison of Axial Strain in the Shear Studs

Figure 6.21 shows the development of axial strains in the shear studs in both the test and the FEA. The development of strains in each of the studs was well predicted. SS1 showed a higher loading rate, but did not climb to excessive strains. The SS2 showed the same change in strain direction around the same load. This shows the ability of the FEA to determine stud loading.

The three graphs in Figure 6.22 show development of the strains in the concrete panel. Development of bearing and shear strains showed higher rates of strain development compared to the test data. The horizontal strains in the FEA developed in agreement with the test data until crack formation.

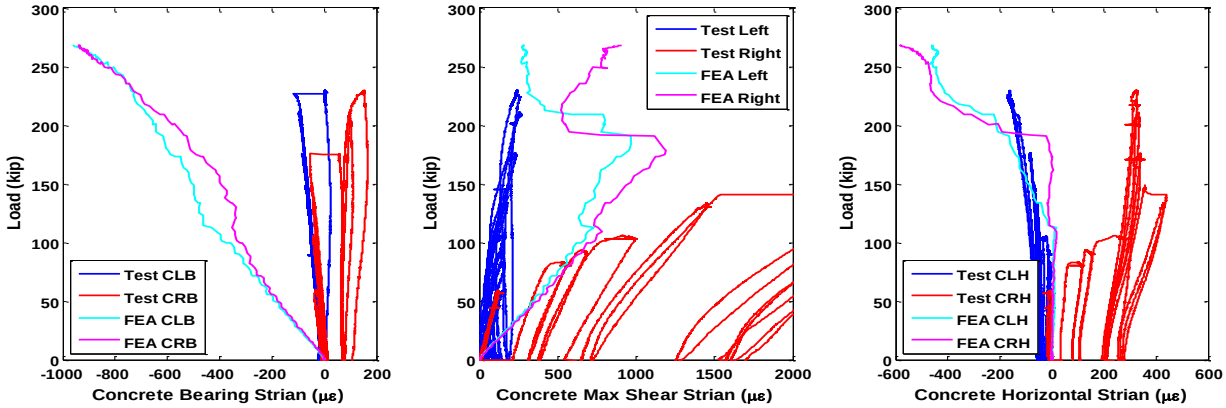

Figure 6.22 Comparison of Strains in the Concrete

(a) Concrete Bearing Strain, (b) Concrete Maximum Shear Strain, (c) Concrete Horizontal Strains

6.5 EFFECT OF THE ADDITION OF A DECK

The effect on the results of not including the bridge deck in the test had to be determined. Two additional series of models were made including a bridge deck. These models included a slab of elastic material to simulate the deck. Dimensions of the deck were derived from the tributary width and thickness of the girder from the rolled girder plans (Bridge No. 00352, 1955). The deck was $3^5/_8$ in thick and $45^5/_8$ in wide with an elastic modulus equivalent to 4,000 psi concrete. An elastic material was chosen because the concrete material would require reinforcement to prevent premature failure. Figure 6.23 shows the deck installed on the girder.

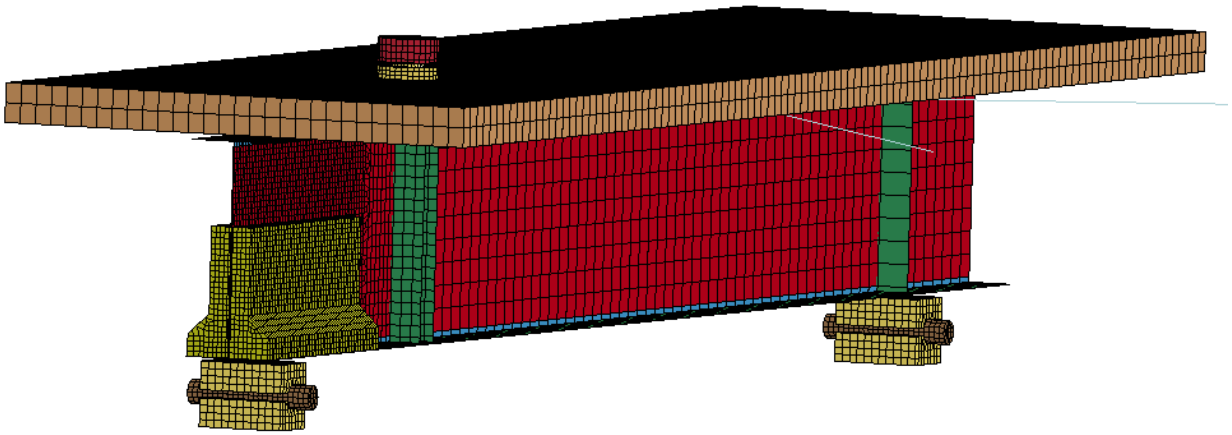

Figure 6.23 Repaired Girder with Deck

6.5.1 Non-Composite Deck

To model the deck as non-composite, the elastic deck interacted with the beam top flange using standard contact (*CONTACT_AUTOMATIC_SURFACE _TO_SURFACE). This contact allowed slippage between the deck and flange. Bending stresses (-200 psi - 200 psi) in the undamaged, non-composite girder are shown in Figure 6.24. The presence of independent bending stresses in the deck and girder show non-composite action in the system.

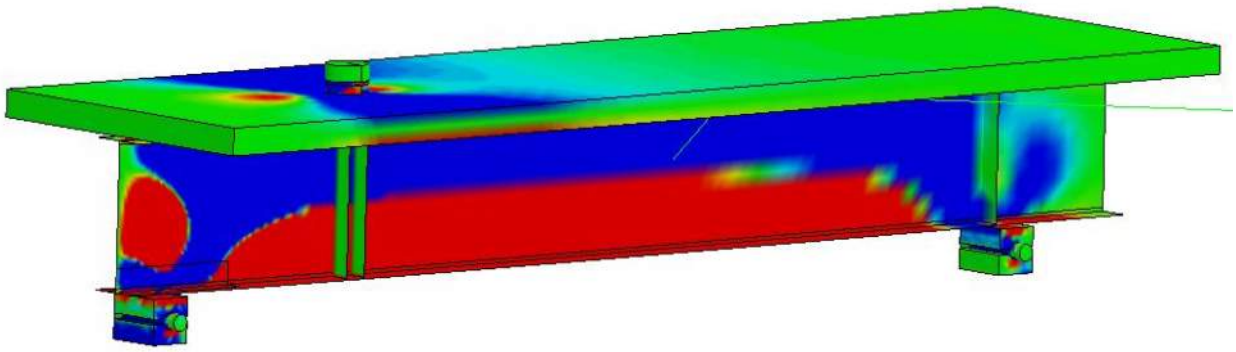

Figure 6.24 Flexural Stresses in the Undamaged, Non-Composite Girder

The deformed shapes of the three non-composite girders are shown in Figure 6.25. The shapes look identical to the girders without the deck. Note the slipping between the deck and top flange. This is evidence of the non-composite action.

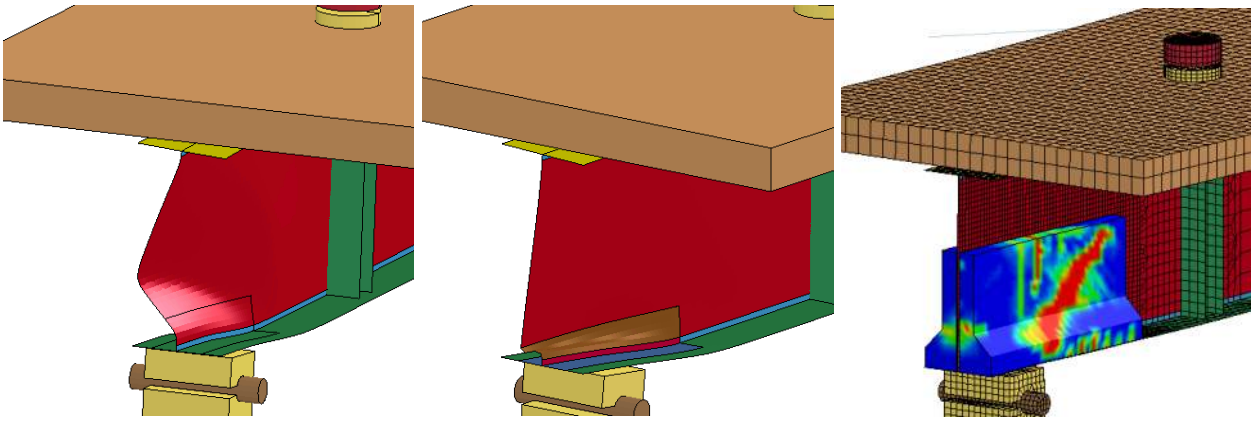

(a) (b) (c)

Figure 6.25 Deformed Shapes of the Non-Composite Girders

(a) Undamaged Girder, (b) Damaged Girder, (c) Repaired Girder

A comparison of the load displacement relationship of the bare and non-composite finite element models is presented in Figure 6.26. The non-composite girders all showed 5% lower capacities compared with the bare girders. This is likely due to increased effect of the eccentricity by twisting of the deck. No noticeable difference in initial stiffness was observed in the three girders. Softening was noted in both the undamaged and repaired girders after a load of 150 kip. This softening is caused by a larger area of plastic strains forming at the bearing prior to failure

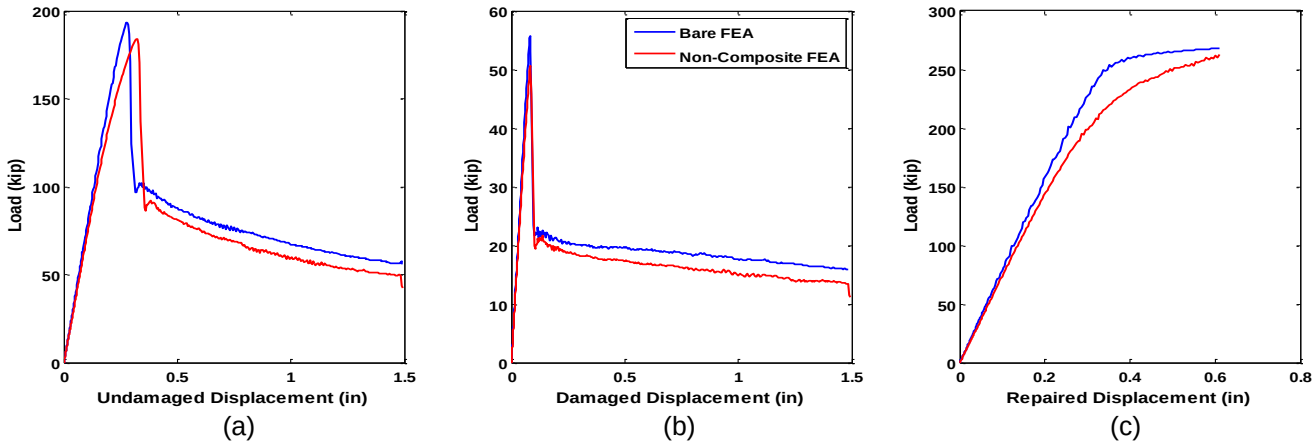

Figure 6.26 Load-Displacement Comparison of the Non-Composite Girders

(a) Undamaged Girder, (b) Damaged Girder, (c) Repaired Girder

6.5.2 Composite Deck

The same deck was used to model a composite deck. To differentiate this model from the non-composite design, the contact type was changed. Instead of using a standard contact, tied contact was used to connect the deck to the top flange (*CONTACT_TIED_ SURFACE_TO_SURFACE). This maintained a uniform strain between the top flange and the bottom of the deck. In tied contact, the slave nodes are translated to and constrained with the master surface. This tied contact restrains translational degrees of freedom, but leave nodal rotations free. The top flange was considered as the master surfaces while the deck nodes were considered as the slave nodes. Figure 6.27 shows the bending stresses (-200 psi - 200 psi) in the composite girder. The deck is in compression, rather than bending, indicating composite action.

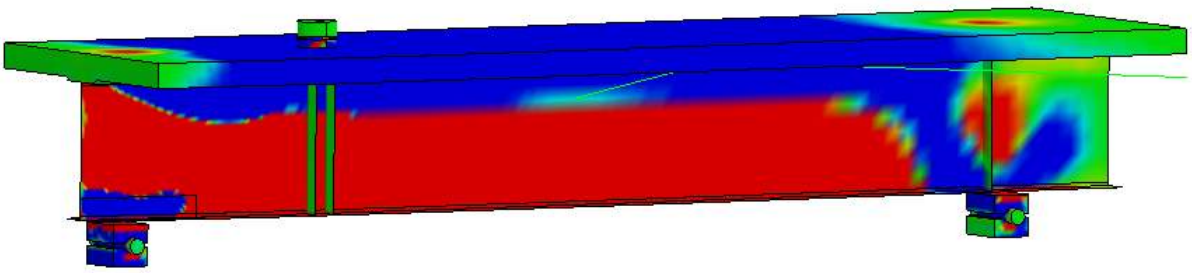

Figure 6.27 Flexural Stresses in the Composite Girder

The deformed shapes of the three composite girders are shown in Figure 6.28. The shapes look identical to the girders without the deck. One minor difference is the lack of

rotation in the top flange caused by the tie constraint. There is no slipping between the deck and top flange. This lack of slip is another indication of composite action.

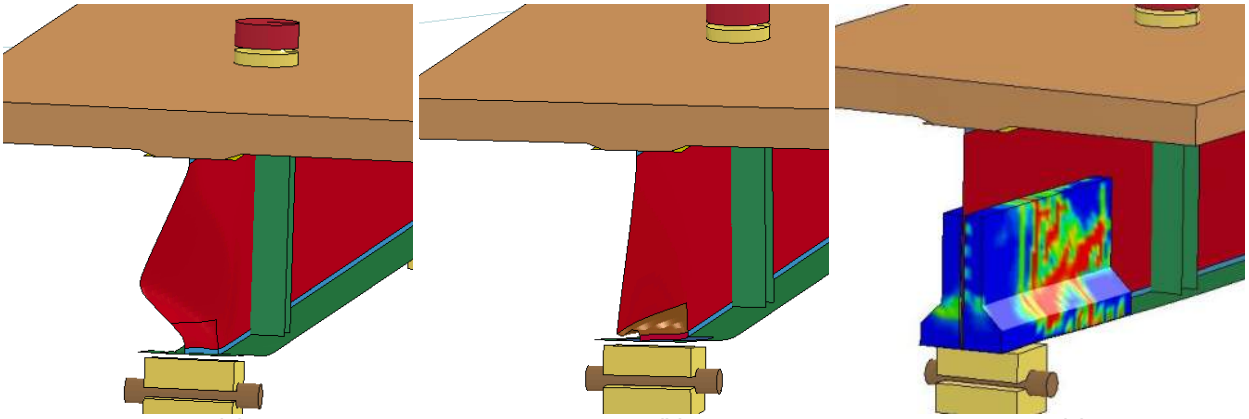

(a) (b) (c)

Figure 6.28 Deformed Shapes of the Composite Girders

(a) Undamaged Girder, (b) Damaged Girder, (c) Repaired Girder

A comparison of the load displacement relationship of the bare and composite finite element models is presented in Figure 6.29. The undamaged and damaged composite girders showed the same 5% reduction of capacity seen in the non-composite girder from deck twisting. The repaired composite girder showed 13% higher capacity compared with the bare girder. This is due to the increased bending moment of inertia and added stiffness of the composite deck. This increased bending moment is also responsible for the increased stiffness observed in the three girders.

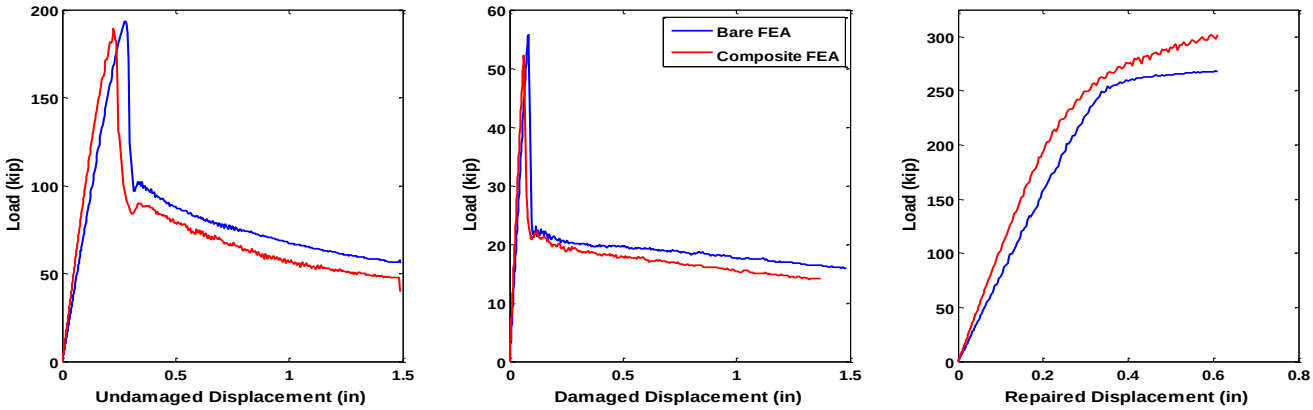

(a) (b) (c)

Figure 6.29 Load Displacement Relations of the Composite Girders

(a) Undamaged Girder, (b) Damaged Girder, (c) Repaired Girder

6.6 ANALYTICIAL STUDY OF REPAIR METHODS

The goal of these analyses was to demonstrate that this repair technique can be adapted to a variety of girder types, and was capable of restoring the capacity lost due to corrosion. Eight designs were developed for three basic types of typical girder ends. In order to prove the method, two conservative assumptions were made: 1) the damage was more severe than indicated in the inspection reports; and 2) that the strength of the UHPC was equivalent to the strength used at the time of study in the half-scale experiment, 16 ksi.

6.6.1 Required Changes to the Existing FEM

Structurally deficient bridges in this country have an average age of 65 years (Davis & Goldberg, 2013). Because of this, the stress-strain properties of the steel modeled had to reflect the steel of the time. These steels were typically either A36 or A7. Strength and ductility of these historic steels are inferior to steel employed today. Therefore steel properties were modified to approximate older steels (Fisher, 1964) (Desai, 1969) (Bruneau & Zahrai, 1997). Figure 6.30 shows a comparison of the modern and historic steel properties used in the two FE models.

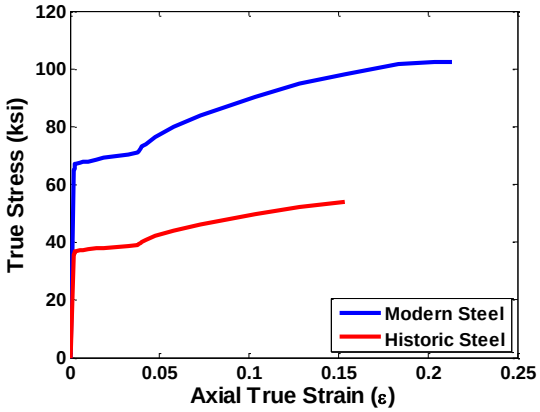

Figure 6.30 Stress Strain Comparison of Modern and Historic Steels Used

In an effort to reduce computation time, the girders were cut approximately at 15% of their span length. This resulted in a change of the loading protocol. Loading was applied by displacing the cut end of the girder. Because the section cut was not at mid-span, symmetric boundary conditions would not apply. A rotational spring was included at the end of the girder to simulate the internal moment. This was done using the *LOAD_MOTION_NODE and *CONSTRAINED_NODAL_RIGID_BODY cards. This monitored the rotation of the cut plane and assigned a moment linearly proportional to

the rotation. This moment was distributed to the entire cut section through the rigid body. The value of the spring constant was found by performing a bending analysis of the entire beam using SAP2000 (CSI, 2012). Displacement, rotation, and moment were found at the location on the cut and a spring constant calculated to match rotation and moment at a given displacement. The rolled girder required a spring constant of 1.380e9 $^{kip\text{-}ft}/_{rad}$ and the plate girder required 1.047e9 $^{kip\text{-}in}/_{rad}$. Lateral restraints were provided on the top and bottom flange at the bearing cut to maintain plane loading.

In addition to the boundary conditions, considerations for the deck had to be made. The deck was not modeled in order to reduce computation time. The deck provides resistance to local flange buckling, which must be accounted for. To model this, each row of nodes in the top flange were given a nodal set constraint (*CONSTRAINED_NODE_SET). This prevented the top flange from buckling locally while allowing flexural displacement of the girder.

Distributed loads were added (*LOAD_SEGMENT_SET) to the top flange to simulate the load of the deck load design lane over each beam's effective width. A second distributed load was added near the bearing to simulate the design tandem.

6.6.2 Design and Selection of the Girders and Damage

The verified FE model was then utilized to create three models of full scale bridge girder ends of bridges in the state of Connecticut. This consisted of a plate girder bridge in Hartford, CT (Bridge No. 03399D, 1962), and a rolled girder bridge in Waterford, CT (Bridge No. 00352, 1955). The plate girder was detailed with a composite deck. In lieu of modeling the deck, the top flange of the girder was thickened based on the tributary width of the girder and the modular ratio of the steel and concrete. The rolled girder did not detail a composite deck. Stiffening of the top flange was not performed. Two series of models were created from the rolled girder, with and without bearing stiffeners.

Both bridges are currently structurally deficient. A level of damage was applied to each of the girders which exceeded the damage reported in either of the inspection reports (Kristoff, 2011) (Pawlikowski, 2012). This increase in the severity of damage was intended to demonstrate the ability of the UHPC repair method to restore capacity to even the most severe level of corrosion. A section loss of 75% was applied to all vertical elements in the damage pattern. The flange was given an equivalent thickness of section loss as the web. Dimensions of the damage were based on more severe lengths and heights of damage in the inspection reports. The thicknesses used in the plates of the model are given in Table 6.2.

Table 6.2 Dimensions Used in the Full-Scale FEA

	Rolled Girder	Plate Girder
Undamaged Web Thickness (in)	0.650	0.375
Damaged Web Thickness (in) [Loss]	0.163 [-75%]	0.094 [-75%]
Undamaged Bottom Flange Thickness (in)	1.020	0.750
Damaged Bottom Flange Thickness (in) [Loss]	0.535 [-48%]	0.469 [-38%]
Top Flange Thickness (in)	1.020	8.917
Undamaged Bearing Stiffener Thickness (in)	0.500	1.000
Damaged Bearing Stiffener Thickness (in) [Loss]	0.125 [-75%]	0.250 [-75%]
Undamaged Interior Stiffener Thickness (in)	N/A	0.313
Damaged Interior Stiffener Thickness (in) [Loss]	N/A	0.078 [-75%]
Height of Increased Damage (in) [vs. D]	14.57 [0.40D]	17.18 [0.32D]
Length of Increased Damage (in) [vs. D]	16.25 [0.45D]	12.53 [0.23D]
Height of Reduced Damage (in) [vs. D]	3.65 [0.10D]	4.90 [0.09D]
Total Length of Damage (in) [vs. D]	51.25 [1.42D]	51.50 [0.95D]

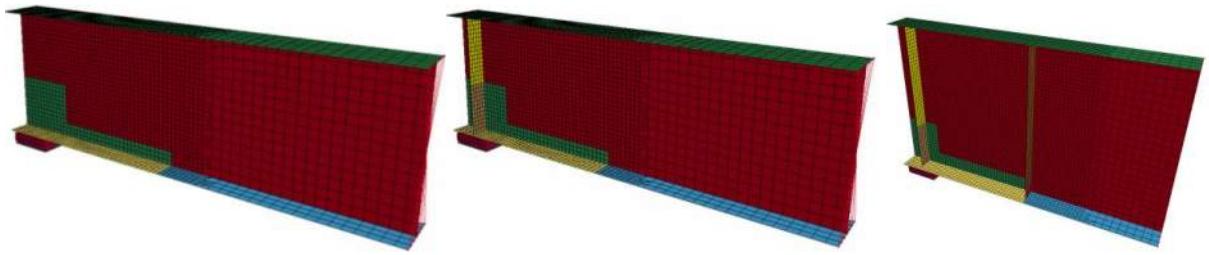

(a) (b) (c)

Figure 6.31 Finite Element Models of the Damaged Girders

(a) Rolled Girder without Bearing Stiffener, (b) Rolled Girder with Bearing Stiffener, (c) Plate Girder

Table 6.3 Baseline Capacities of the Modeled Girders

Girder Model	Undamaged Limit State	Undamaged Capacity (kip)	Damaged Limit State	Damaged Capacity (kip) [% Lost]
Rolled Girder w/o Stiffener	Flexural Yield	234	Buckling of Web	17.7 [-92.4%]
Rolled Girder w/ Stiffener	Flexural Yield	243	Web/Stiffener Buckling at Bearing	79.7 [-67.2%]
Plate Girder	Tension Field Tearing at Bearing	475	Web/Stiffener Buckling at Bearing	97.5 [-79.5%]

The models with the damage pattern for the rolled and plate girders are shown in Figure 6.31. The coloring on the plates is indicative of the thickness of the plate being modeled. With the FE model, capacities of the undamaged and damaged girders were able to be found. Table 6.3 shows the undamaged and damaged bearing capacities of the girders predicted by the FE analysis. Contours of Von Mises stress from 0-40 ksi

(yield stress) are shown in Figure 6.32. The localization of stress in each of the damaged girders is apparent. There is also a noticeable stress decrease in the rolled girder with stiffeners at the bearing compared with the rolled bearing without stiffeners

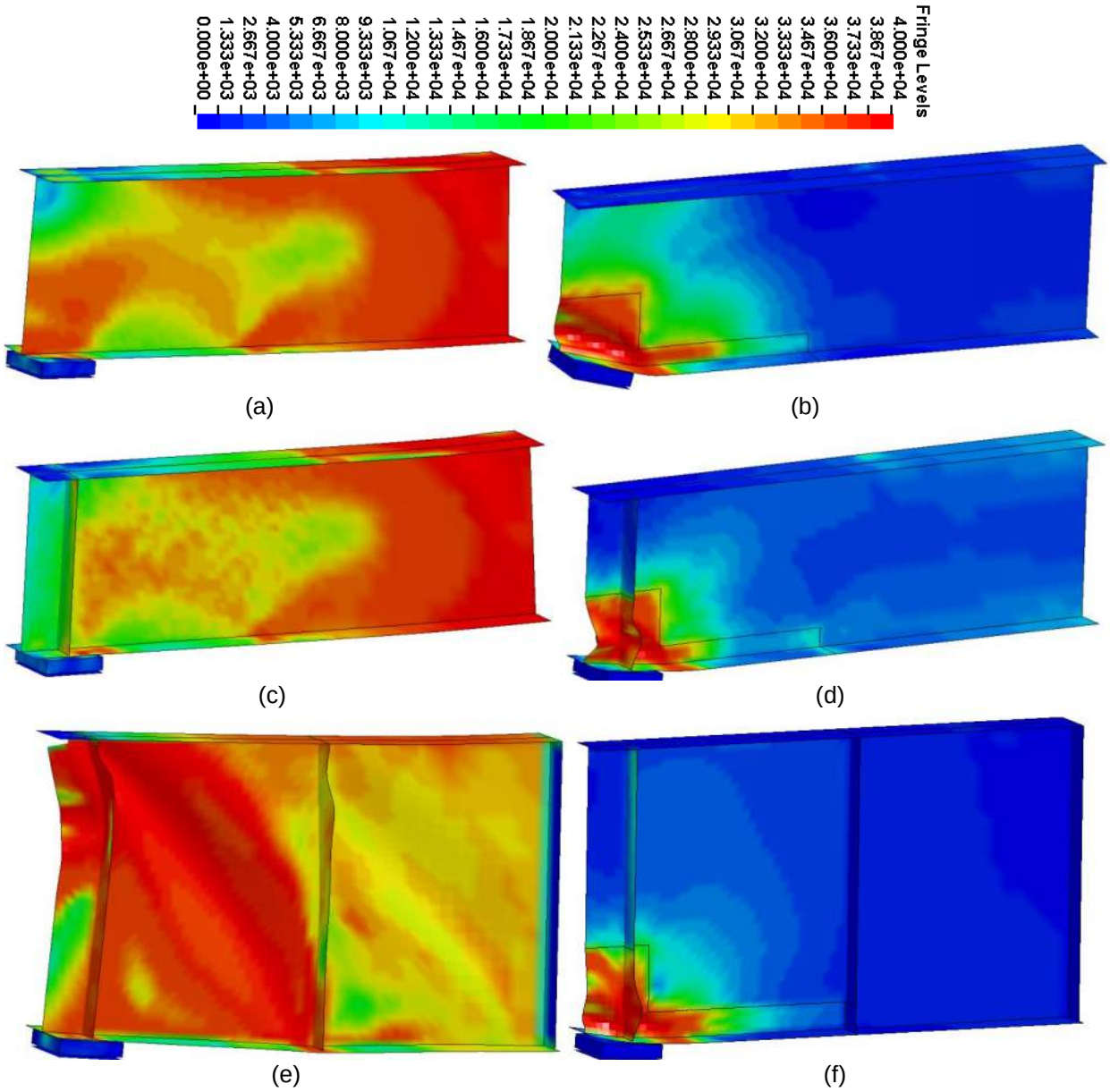

Figure 6.32 Undamaged and Damaged Limit States for the FE Girders

(a) Undamaged Rolled Girder without Stiffeners, (b) Damaged Rolled Girder without Stiffeners, (c) Undamaged Rolled Girder with Stiffeners, (d) Damaged Rolled Girder with Stiffeners, (e) Undamaged Plate Girder, (f) Damaged Plate Girder

6.6.3 Rolled Girder without Bearing Stiffeners

6.6.3.1 Full Height Fill

This method uses a cast of UHPC which covers the entire space between flanges. Shear studs are provided on the top and bottom flanges to secure the panel to the girder, as shown in Figure 6.33a. This method utilized a $2^1/_2$-in thick, $57^1/_2$-in long panel. The top and bottom 3 in of the panel is extended to the width of the flange to provide adequate cover for studs and to prevent water from pooling on the flange. This wider portion is graduately beveled to the $2^1/_2$ in panel thickness at a distance of 6 in from the flanges. 52 $^1/_2$-in diameter, $2^1/_2$ in long studs are used in this repair. Fourteen studs were fixed to the top and bottom flanges on each side of the girder at a $3^3/_4$ in spacing.

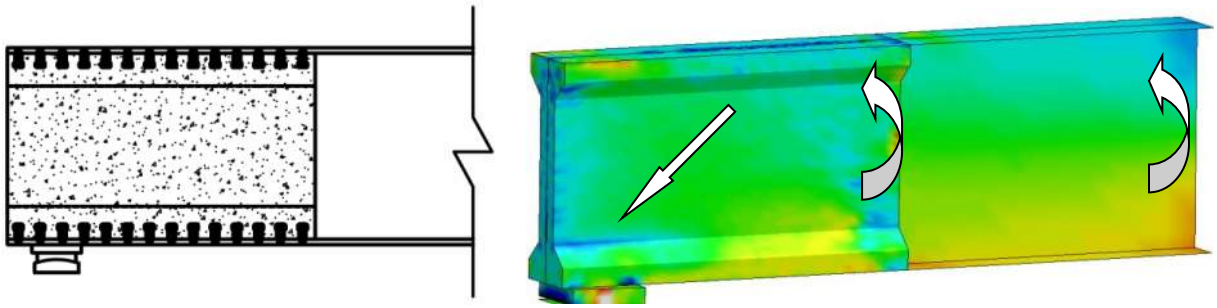

(a) (b)

Figure 6.33 Full Height Fill Repair for Unstiffened Rolled Girders

(a) Schematic of the Full Height Repair without a Bearing Stiffener, (b) Load Carrying Mechanisms in the Full Height Repair

This method carries the load through beam action. This can be visualized in a plot of the triaxiality factor shown in Figure 6.33b. Stress triaxiality is the ratio of equivalent stress to mean stress ($^{\sigma e}/_{\sigma m}$), and defines the general stress state of the element. In the plot, areas in cyan/blue indicate compression; areas of yellow/red indicate tension. Green areas are either areas of shear or stress-free. Bending stresses develop at the end of the repair and is transferred to the bearing through shear, as indicated in the figure.

This method was able to fully rehabilitate the damage, and cause a limit state of flexural yielding, like in the undamaged girder. Two cracks occurred in the concrete panel as a diagonal shear crack from the bearing and a flexural crack towards the end of the panel. The cracking of the panel is shown in Figure 6.34a. Von Mises stress distribution on the girder is shown in Figure 6.34b. This method was able to maintain the stress in the corrosion-damaged area below yield. The capacity of the girder with the

repair increased 19% from the undamaged capacity to 277 kip. The load displacement relations for these repairs are shown in Figure 6.35. These results are summarized in Table 6.4.

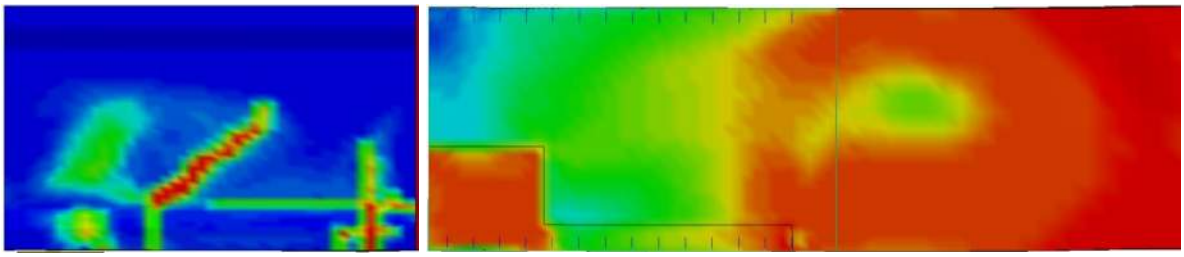

(a) (b)

Figure 6.34 Limit State Condition of the Unstiffened Full Height Repair

(a) Cracking in the Full Height Fill Concrete Panel, (b) Von Mises Stress (0-40 ksi) in the Girder of the Full Height Repair,

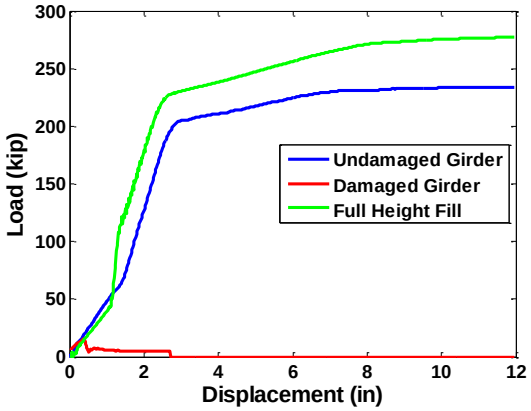

Figure 6.35 Load-Displacement Relation of the Unstiffened Full Height Fill Repair

6.6.3.2 Partial Height Fill

This method uses a cast of UHPC which covers a portion of the web height to the height of the diaphragm. This prevents forming around the bridge diaphragm. Shear studs are provided on the bottom flange and the web to secure the panel to the girder. This was the method tested in the large-scale experiments. A basic schematic of the repair is presented in Figure 6.36a. The analysis was performed with a $2^1/_2$-in thick, 19-in tall, $57^1/_2$-in long panel, with the same bevel design as the full height fill. 116 $^1/_2$-in diameter, $2^1/_2$ in long studs were utilized in this design. Fourteen studs were fixed to the bottom flange, and 44 studs were fixed to the web on each side of the girder at a $3^3/_4$ in spacing, both vertically and longitudinally. Four rows of studs were used. The lower three rows were within the extended height of the corrosion, therefore terminated $17^1/_2$

in from the end of the girder. The top row extended over the damage and to the end of the girder. Studs on the web were staggared $1^1/_4$ in horizontally and vertical to avoid stress concentration.

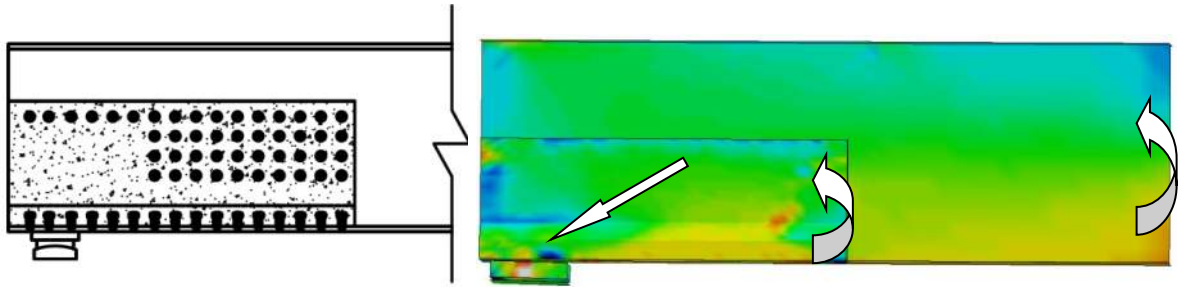

(a) (b)

Figure 6.36 Partial Height Fill Repair for Unstiffened Rolled Girders

(a) Schematic of the Partial Height Repair without a Bearing Stiffener, (b) Load Carrying Mechanisms in the Partial Height Repair

Like the full height fill repair, this method carries the load through beam action, shown in Figure 6.36b. Bending stresses develop at the end of the repair and is coupled with a shear strut at the bearing.

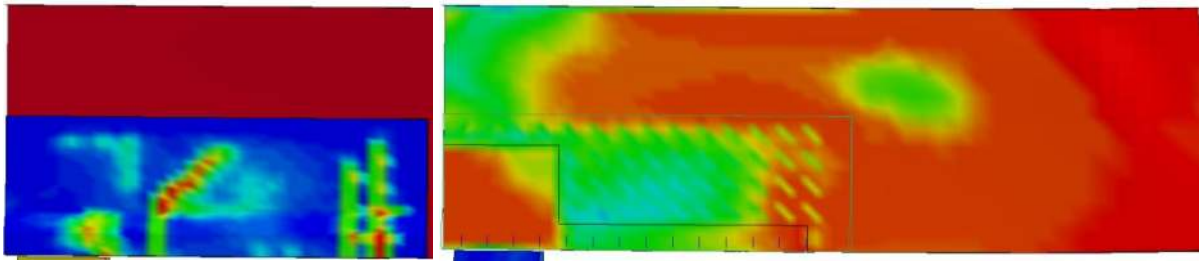

(a) (b)

Figure 6.37 Limit State Condition of the Unstiffened Partial Height Repair

(a) Cracking in the Partial Height Fill Concrete Panel, (b) Von Mises Stress (0-40 ksi) in the Girder of the Partial Height Repair

This method was able to fully rehabilitate the damage, and cause flexural yielding like in the undamaged girder. Three types of cracks occurred in the concrete panel. A diagonal shear crack formed at the bearing, a flexural crack towards the end of the panel, and vertical crack at the top of the panel at the edge of the bearing. This is the same pattern of cracking observed in the large-scale test. The cracking of the panel is shown in Figure 6.37a. Von Mises stress distribution on the girder is shown in Figure 6.37b. The capacity of the girder with the repair increased 17% from the undamaged capacity to 274 kip. The load displacement relation for this repair is shown in Figure 6.38. These results are summarized in Table 6.4.

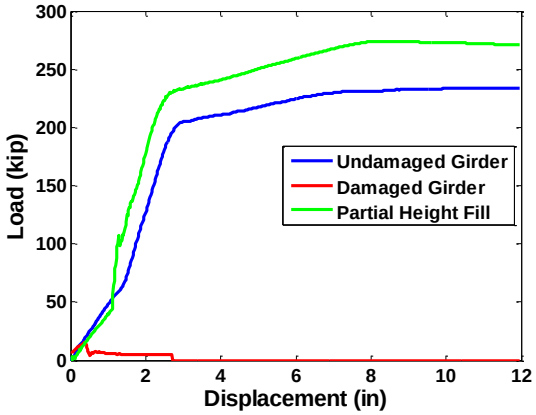

Figure 6.38 Load-Displacement Relation of Unstiffened Full Height Fill Repair

6.6.3.3 L-Shaped Fill

This method is a hybrid of the full height and partial height methods aimed to capitalize on the compressive strength of the UHPC material. A full height of UHPC is provided at the bearing, but only a sufficient height of UHPC is provided to cover the corrosion damage that extends along the girder. Shear studs are only provided on the bottom and top flange, as shown in Figure 6.39a. The full height fill of concrete outside of the stiffener is still provided. This method utilized a $2^1/_2$-in thick cast only $16^1/_2$-in long. After that length the height was terminated at the top of the 6 in bevel for the remaining 41 in. Only 36 $^1/_2$-in diameter, $2^1/_2$ in long studs were used. Fourteen studs were fixed to the bottom flange, and four to the top flange on each side of the girder at a $3^3/_4$ in spacing.

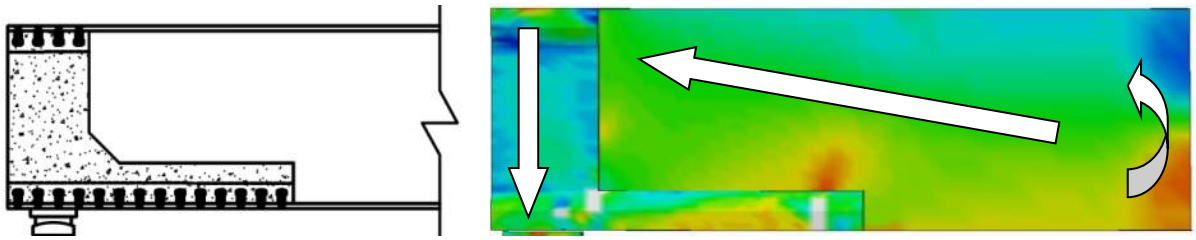

(a) (b)

Figure 6.39 L-Shaped Fill Repair for Unstiffened Rolled Girders

(a) Schematic of the L-Shaped Repair with a Bearing Stiffener, (b) Load Carrying Mechanisms in the L-Shaped Repair

This method carries loads predominantly through column action at the bearing. Negligible bending stresses do develop in the bevel section, but the majority of the load is carried through shear in the girder to the top of the bearing and taken down through the full height portion of the panel. This mechanic is illustrated in Figure 6.39b.

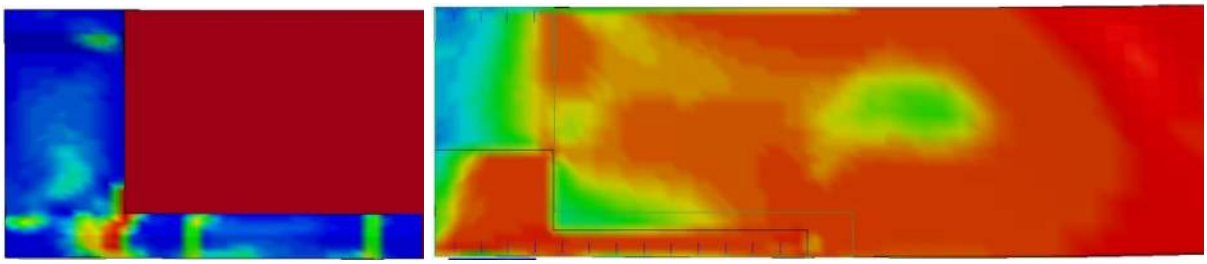

(a) (b)

Figure 6.40 Limit State Condition of the Unstiffened L-Shaped Repair

(a) Cracking in the L-Shaped Fill Concrete Panel, (b) Von Mises Stress (0-40 ksi) in the Girder of the L-Shaped Repair

This method was able to fully rehabilitate the damage, and cause flexural yielding like in the undamaged girder. Two cracks occurred in the concrete panel. A vertical crack formed at the reduction of height. Flexural cracking was also noted along the length of the bevel. The cracking of the panel is shown in Figure 6.40a. Von Mises stress distribution on the girder is shown in Figure 6.40b. The capacity of the girder with the repair increased 16% from the undamaged capacity to 271 kip. The load displacement relation for this repair is shown in Figure 6.41. These results are summarized in Table 6.4.

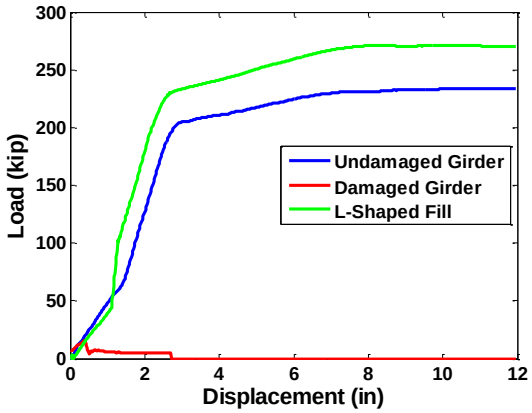

Figure 6.41 Load-Displacement Relation of the Unstiffened L-Shaped Fill Repair

6.6.4 Rolled Girder with Bearing Stiffeners

6.6.4.1 Full Height Fill

This method uses a cast of UHPC which covers the entire web from flange to flange. Shear studs are provided on the top and bottom flanges to secure the panel to the girder, as shown in Figure 6.42a. The fill of concrete outside of the stiffener does not

require studs to be installed on the flanges. This is done in consideration of space constraints. This method utilized a $2^1/_2$-in thick, 50 in long panel. The top and bottom 3 in of the panel is extended to the width of the flange to provide adequate cover for studs and to prevent water from pooling on the flange. This wider portion is graduately beveled to the $2^1/_2$ in panel thickness at a distance of 6 in from the flanges. Because the cast outside the stiffener does not include studs, no bevel is required on the top. Only the bottom bevel is needed to prevent water from pooling. 48 $^1/_2$-in diameter, $2^1/_2$ in long studs are used in this repair. Twelve studs were fixed to the top and bottom flanges on each side of the girder at a $3^3/_4$ in spacing.

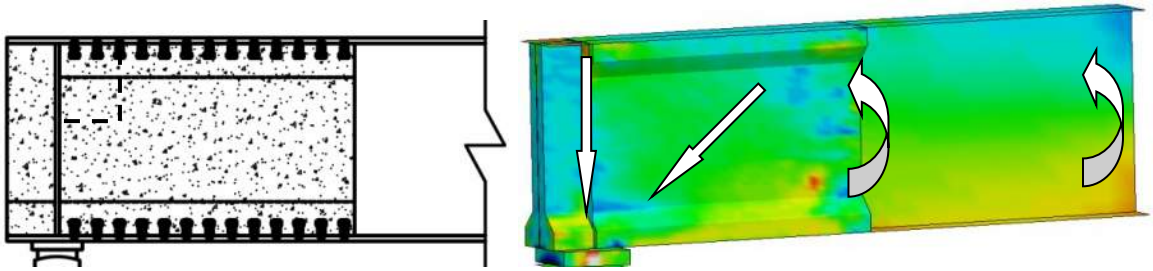

(a) (b)

Figure 6.42 Full Height Fill Repair for Stiffened Rolled Girders

(a) Schematic of the Full Height Repair with a Bearing Stiffener, (b) Load Carrying Mechanisms in the Full Height Repair

This method carries the load through beam action. This can be visualized in a plot of the triaxiality factor shown in Figure 6.42b. Bending stresses develop at the end of the repair and is coupled with a compressive field at the bearing. The cast of UHPC on the outside of the stiffener experiences pure axial compression. A second model was created with a section of the fill removed from the top of the bearing for consideration of the bridge diaphragm.

This method was able to fully rehabilitate the damage, and cause a limit state of flexural yielding, like in the undamaged girder. Two cracks occurred in the concrete panel as a diagonal shear crack from the bearing and a flexural crack towards the end of the panel. The cracking of the panel is shown in Figure 6.43a/c for the repair without and with the diaphragm hole, respectively. No difference was seen in the cracking or stress distribution in the girder from the diaphragm hole. Von Mises stress distribution on the girders is shown in Figure 6.43b/d. The capacity of the girder with the repair increased 15% from the undamaged capacity to 278 kip. The load displacement relations for these repairs are shown in Figure 6.44. These results are summarized in Table 6.4.

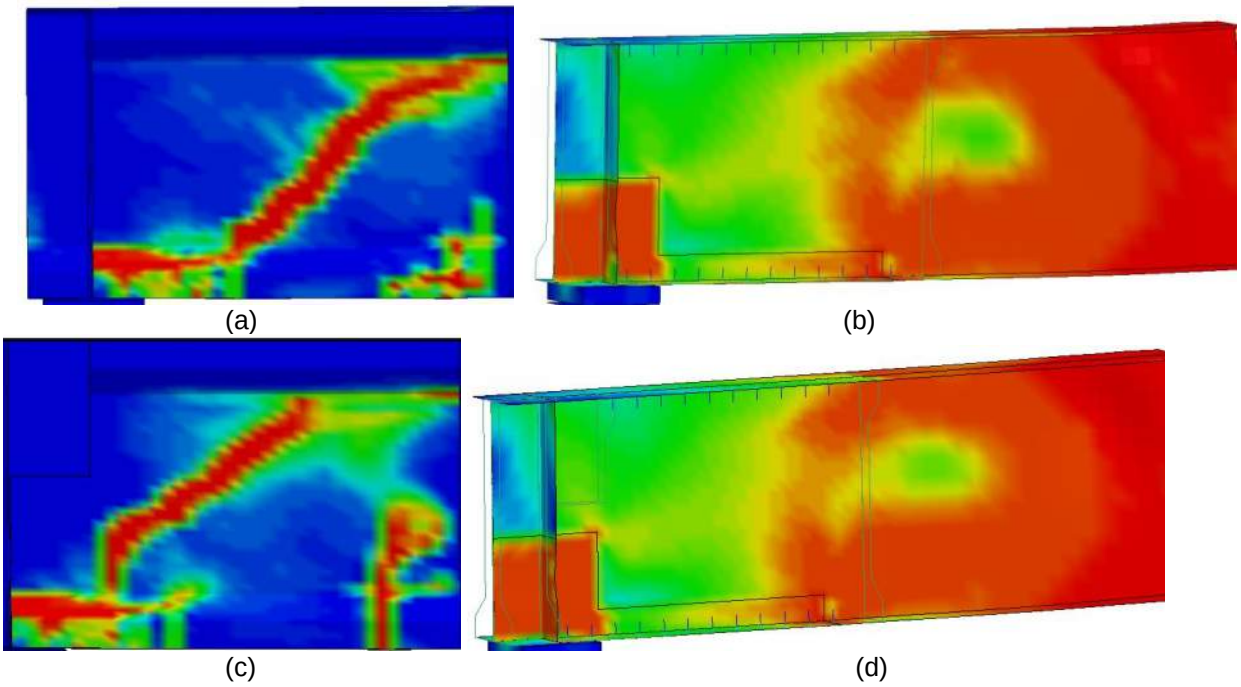

Figure 6.43 Limit State Condition of the Full Height Repair

(a) Cracking in the Full Height Fill Concrete Panel, (b) Von Mises Stress (0-40 ksi) in the Girder of the Full Height Repair, (c) Cracking in the Full Height Fill Concrete Panel with Diaphragm Hole, (d) Von Mises Stress in the Girder of the Full Height Repair with Diaphragm Hole

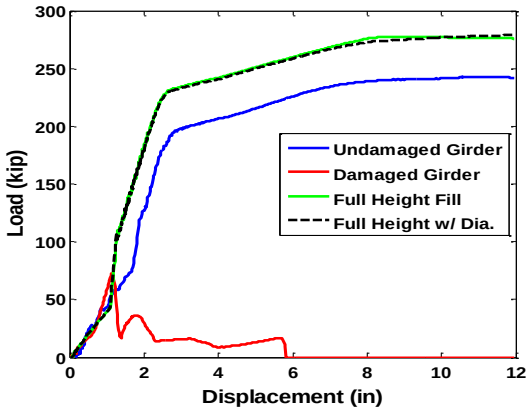

Figure 6.44 Load-Displacement Relation of Full Height Fill Repair

6.6.4.2 Partial Height Fill

This method uses a cast of UHPC which covers a portion of the web height to the height of the diaphragm. This prevents forming around the bridge diaphragm. Shear studs are provided on the bottom flange and the web to secure the panel to the girder, as shown in Figure 6.45a. A full height, stud free fill of concrete outside of the stiffener

still is required. With excessive section loss, there is not sufficient spacing for an adequate number of shear studs to be located to fully develop the repair. This method utilized a $2^1/_2$-in thick, 19-in tall, 50-in long panel, with the same bevel design as the full height fill. 108 studs of $^1/_2$-in diameter and $2^1/_2$ in length were utilized in this design. Twelve studs were fixed to the bottom flange, and 42 studs were fixed to the web on each side of the girder at a $3^3/_4$ in spacing, both vertically and longitudinally. Four rows of studs were used. The lower three rows were within the extended height of the corrosion, therefore terminated 10 in from the stiffener. The top row extended over the damage and to the stiffener. Studs on the web were staggared $1^1/_4$ in horizontally and vertical to avoid stress concentration.

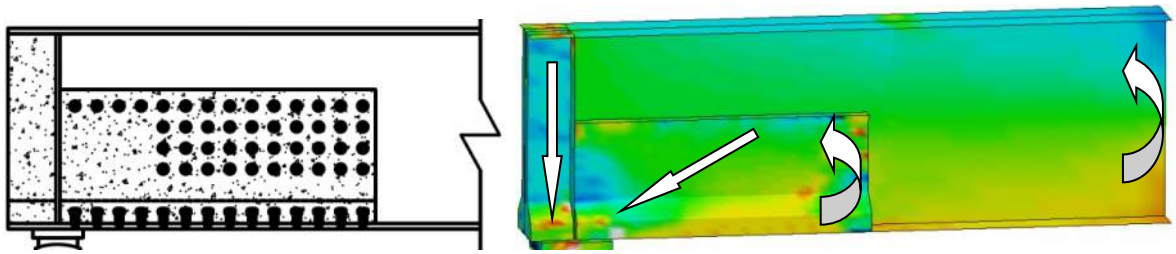

(a) (b)

Figure 6.45 Partial Height Fill Repair for Stiffened Rolled Girders

(a) Schematic of the Partial Height Repair with a Bearing Stiffener, (b) Load Carrying Mechanisms in the Partial Height Repair

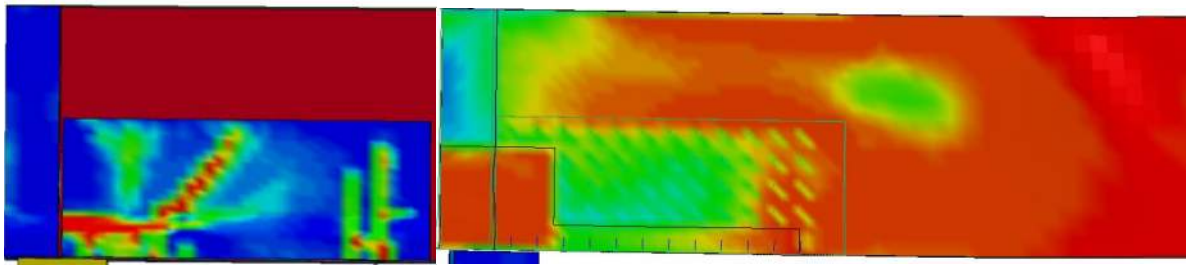

(a) (b)

Figure 6.46 Limit State Condition of the Partial Height Repair

(a) Cracking in the Partial Height Fill Concrete Panel, (b) Von Mises Stress (0-40 ksi) in the Girder of the Partial Height Repair

Like the full height fill repair, this method carries the load through beam action, shown in Figure 6.45b. Bending stresses develop at the end of the repair and is coupled with a compressive field at the bearing. The cast of UHPC on the outside of the stiffener experiences pure axial compression.

This method was able to fully rehabilitate the damage, and cause flexural yielding like in the undamaged girder. Two cracks occurred in the concrete panel as a diagonal shear crack from the bearing and a flexural crack towards the end of the panel. The

cracking of the panel is shown in Figure 6.46a. Von Mises stress distribution on the girder is shown in Figure 6.46b. The capacity of the girder with the repair increased 12% from the undamaged capacity to 272 kip. The load displacement relation for this repair is shown in Figure 6.47. These results are summarized in Table 6.4.

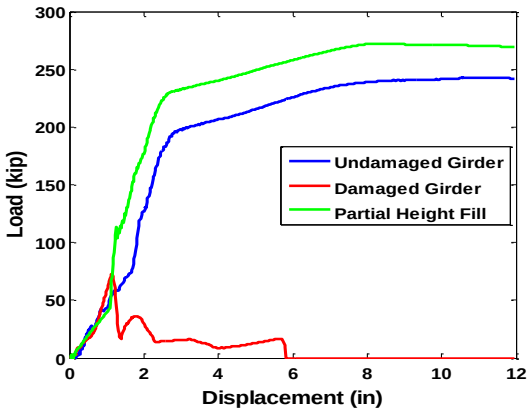

Figure 6.47 Load-Displacement Relation of Full Height Fill Repair

6.6.4.3 L-Shaped Fill

This method is a hybrid of the full height and partial height methods aimed at material optimization. A full height of UHPC is provided at the bearing, but away from the extended height of the corrosion damage, only a sufficient height of UHPC is provided to cover the corrosion damage. Shear studs are only provided on the bottom and top flange, as shown in Figure 6.48a. The full height fill of concrete outside of the stiffener is still provided. This method utilized a $2^{1}/_{2}$-in thick cast only $8^{3}/_{4}$-in long. After that length the height was terminated at the top of the 6 in bevel for the remaining $41^{1}/_{4}$ in. Only 28 $^{1}/_{2}$-in diameter, $2^{1}/_{2}$ in long studs were used. Twelve studs were fixed to the bottom flange, and two to the top flange on each side of the girder at a $3^{3}/_{4}$ in spacing.

This method carries loads predominantly through column action at the bearing. Small bending stresses do develop in the bevel section, but stresses remain largely tensile due to the small height and the joining to the bottom flange. The majority of the load is carried through shear in the girder to the top of the bearing and taken down through the full height and external UHPC panels. This mechanic is illustrated in Figure 6.48b.

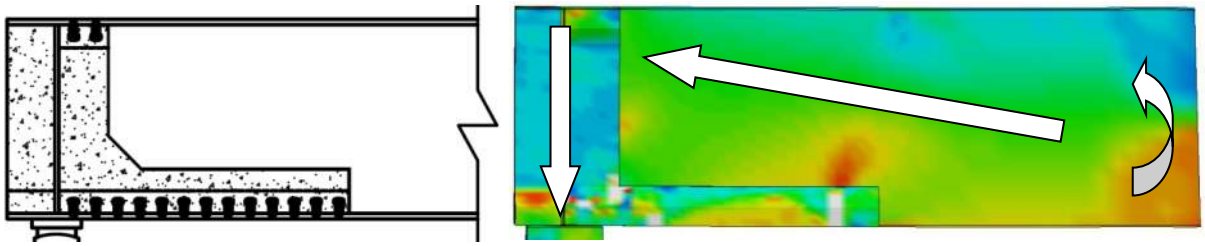

(a) (b)

Figure 6.48 L-Shaped Fill Repair for Stiffened Rolled Girders

(a) Schematic of the L-Shaped Repair with a Bearing Stiffener, (b) Load Carrying Mechanisms in the L-Shaped Repair

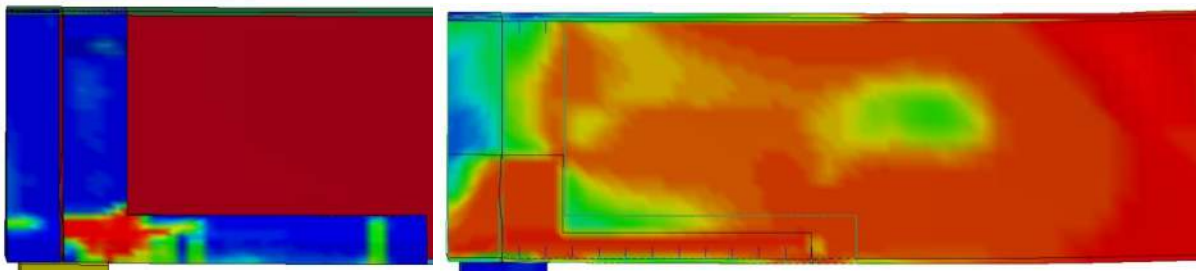

(a) (b)

Figure 6.49 Limit State Condition of the L-Shaped Repair

(a) Cracking in the L-Shaped Fill Concrete Panel, (b) Von Mises Stress (0-40 ksi) in the Girder of the L-Shaped Repair

This method was able to fully rehabilitate the damage, and cause flexural yielding like in the undamaged girder. Two cracks occurred in the concrete panel. A vertical crack formed at the reduction of height early on and spread through the base toward the bearing. Flexural cracking was also noted along the length of the bevel. The cracking of the panel is shown in Figure 6.49a. Von Mises stress distribution on the girder is shown in Figure 6.49b. The capacity of the girder with the repair increased 11% from the undamaged capacity to 269 kip. The load displacement relation for this repair is shown in Figure 6.50. These results are summarized in Table 6.4.

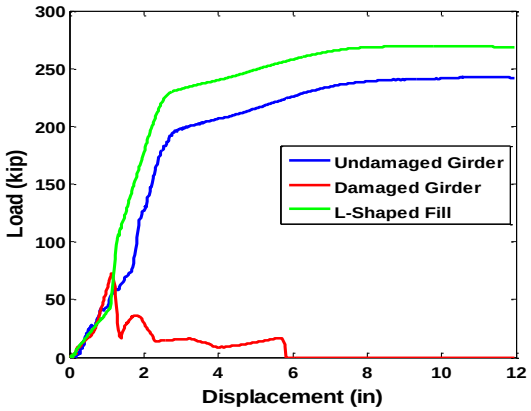

Figure 6.50 Load-Displacement Relation of L-Shaped Fill Repair

6.6.5 Plate Girders

6.6.5.1 Full Panel Fill

This method uses a cast of UHPC to fill the entire first panel of the plate girder which has the corrosion damage. The panel is secured by bearing forces of the flanges and stiffeners, therefore shear studs are not required. The fill of concrete outside of the bearing stiffener does not require studs to be installed on the flanges. A visualization of this repair is shown in Figure 6.51a. This method utilized a $2^1/_2$-in thick panel. The bottom 5 in of the panel is flared to the width of the flange to prevent water from pooling on the flange. A second model was created with a hole in the tops of the panels to allow for penetration of the bridge diaphragm. This is shown by the dotted lines in Figure 6.51.

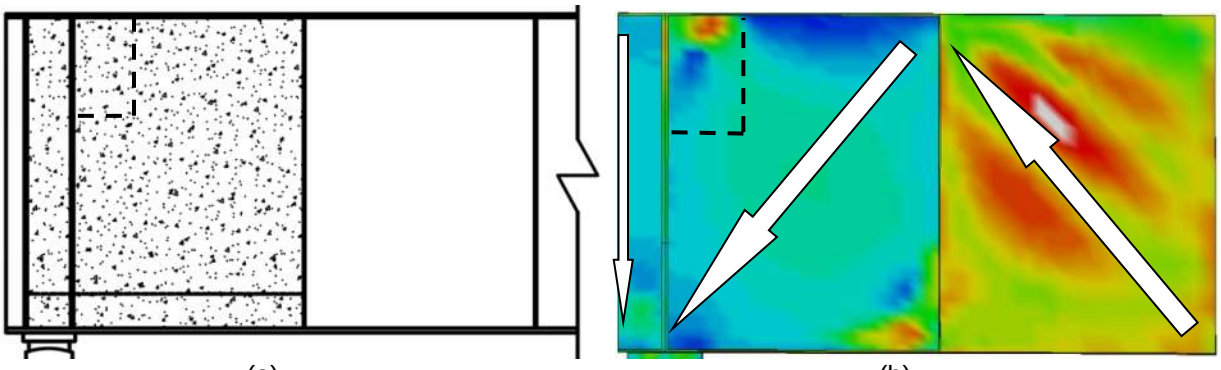

(a) (b)

Figure 6.51 Full Panel Fill Repair for Plate Girders

(a) Schematic of the Full Panel Repair, (b) Load Carrying Mechanism of the Full Panel Repair

This method carries the load with a compressive strut forming in the concrete panel. This can be visualized Figure 6.51b. The panel without the concrete fill develops a tension field as loading progresses. The cast of UHPC on the outside of the stiffener experiences pure axial compression. The inclusion of the hole in the panel to account for the bridge diaphragm did not affect the load path.

This method was able to fully rehabilitate the damage. The load was limited by tearing of the steel at the bottom of the covered panel, initiating at the end of the corrosion. Two cracks occurred in the concrete panel as diagonal cracks perpendicular to principal tension in the panel. One appeared in the middle of the panel and a second that formed with the tearing. This cracking is visible in Figure 6.52a/c for the repair without and with the diaphragm hole, respectively. Presence of the diaphragm hole actually reduced the severity of the cracking. Von Mises stress distribution on the girders is shown in Figure 6.52b/d. The tearing of the web at the corroded section is clearly visible in the circled area. The capacity of the girder with the repair increased 37% from the undamaged capacity to 649 kip. The load displacement relations for these repairs are shown in Figure 6.44. These results are summarized in Table 6.4.

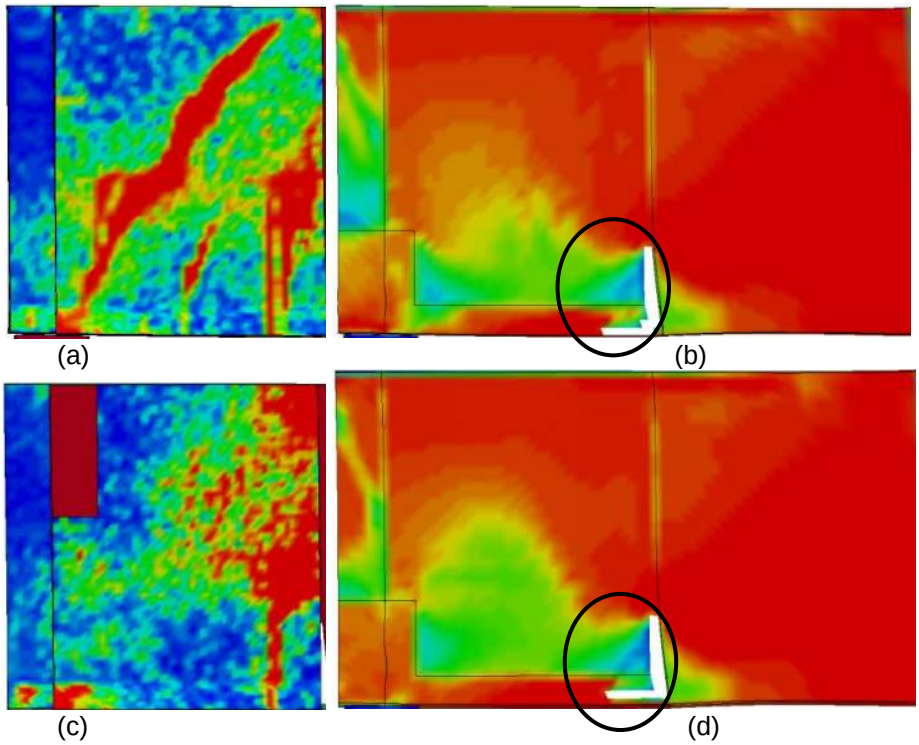

Figure 6.52 Limit State Condition of the Full Panel Repair

(a) Cracking in the Full Panel Fill Concrete Panel, (b) Von Mises Stress (0-40 ksi) in the Girder of the Full Panel Repair, (c) Cracking in the Full Panel Fill Concrete Panel with Diaphragm Hole, (d) Von Mises Stress in the Girder of the Full Panel Repair with Diaphragm Hole

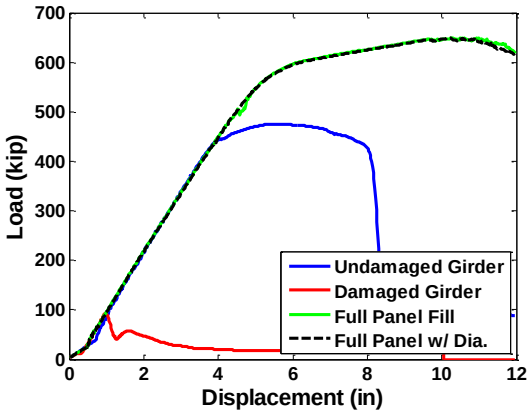

Figure 6.53 Load-Displacement Relation of Full Panel Fill Repair

6.6.5.2 Partial Panel Fill

This method uses a cast of UHPC which only fills a portion of the first panel to the height of the diaphragm. This prevents forming around the bridge diaphragm. Shear studs are included on the web as the top flange can no longer secure the panel, as shown in Figure 6.54a. A full height fill of concrete outside of the stiffener still is required. This method utilized a $2^1/_2$-in thick, 27-in tall cast in the first panel, with the same flare design as the full height fill. 36 $^1/_2$-in diameter, $2^1/_2$ in long studs were included on the web. Two rows of studs were used. Rows were spaced 5 in apart, with $3^3/_4$ in spacing in each row. Studs on the web were staggared $1^1/_4$ in horizontally and vertically to avoid stress concentration.

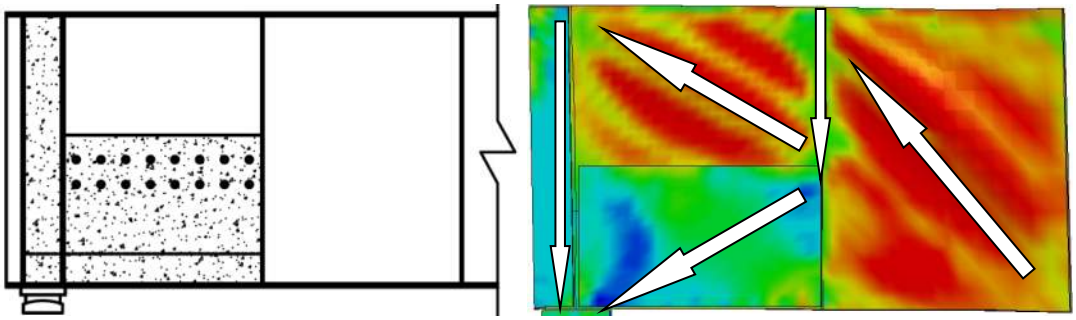

(a) (b)

Figure 6.54 Partial Panel Fill Repair for Plate Girders

(a) Schematic of the Partial Height Repair with a Bearing Stiffener, (b) Load Carrying Mechanisms in the Partial Height Repair

Like the full height fill repair, the concrete panel formed a compressive strut to the bearing and the full height cast acts as a column, as shown in Figure 6.54b. Because the portion of the plate girder is exposed above the concrete panel, a tension field

develops here as well as in the second full panel. Due to the higher shear in this panel, the tension field develops in the half panel first.

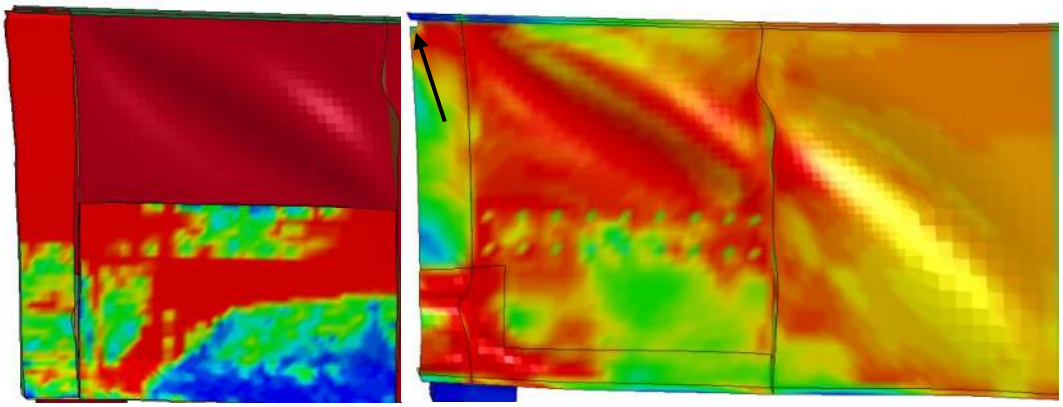

(a) (b)

Figure 6.55 Limit State Condition of the Partial Panel Repair

(a) Cracking in the Partial Height Fill Concrete Panel, (b) Von Mises Stress (0-40 ksi) in the Girder of the Partial Height Repair

This method was able to fully rehabilitate the damage. Because the top of the first panel was exposed, and a tension field developed, the same tearing occurred at the top of the girder at the bearing. This shock caused the full height cast to fail. The half panel of concrete had a diagonal shear crack at the time of failure. With failure of the concrete, the corrosion damaged portion of the web crippled. The cracking of the panel is shown in Figure 6.55a. Von Mises stress distribution on the girder during the buckling at the bearing is shown in Figure 6.55b. The capacity of the girder with the repair increased 6% from the undamaged capacity to 504 kip, and maintained the same level of ductility. The load displacement relation for this repair is shown in Figure 6.56. These results are summarized in Table 6.4.

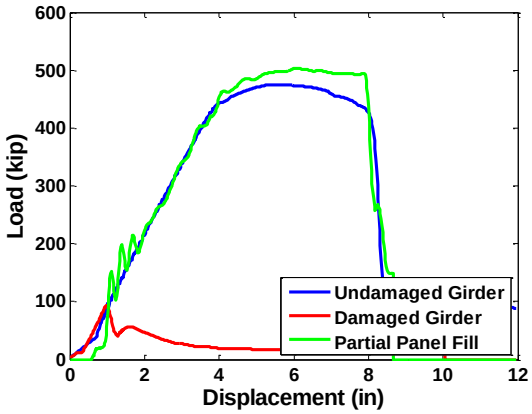

Figure 6.56 Load-Displacement Relation of Full Height Fill Repair

Table 6.4 Summary of Finite Element Results

Girder Model	Rolled Girder w/o Stiffener	Rolled Girder w/ Stiffener	Plate Girder
Undamaged Limit State	Flexural Yield	Flexural Yield	Tension Field Tearing at Bearing
Undamaged Capacity (kip)	234	243	475
Damaged Limit State	Buckling of Web	Web/Stiffener Buckling	Web/Stiffener Buckling
Damaged Capacity (kip) [%]	18 [-92%]	80 [-67%]	98 [-80%]
Full Height/Panel Limit State	Flexural Yield	Flexural Yield	Tearing of Corroded Web
Full Height/Panel Capacity (kip) [%]	277 [+19%]	278 [+15%]	649 [+37%]
Partial Height/Panel Limit State	Flexural Yield	Flexural Yield	Tension Field Tearing/UHPC Column Failure
Partial Height/Panel Capacity (kip) [%]	274 [+17%]	272 [+12%]	504 [+6%]
L-Shaped Limit State	Flexural Yield	Flexural Yield	N/A
L-Shaped Capacity (kip) [%]	271 [+16%]	269 [+11%]	N/A

7 Summary and Conclusion

7.1 SUMMARY

A series of three tests were run in the UCONN Structures Laboratory on large-scale rolled girders. The goal was to perform a proof of concept of a novel method utilizing UHPC to rehabilitate corrosion damage. One girder was undamaged, to determine baseline bearing capacity. A second girder had section loss at the bearing to simulate severe corrosion damage to isolate the effect of corrosion on bearing capacity. A third girder had the same level and pattern of simulated corrosion damage, but included a repair with UHPC. This determined the capacity restored by the repair technique. Each of these tests was instrumented to record data to create a finite element model for use in an analytical study.

The undamaged girder was found to fail due to the buckling of the web at a load of 180 kip. The simulated corrosion at the bottom of the web reduced the capacity of the girder to 43 kip. The failure was still considered to be buckling of the web, but it was isolated in the simulated corrosion. The girder did not fail with the addition of the concrete panel. Instead it experienced flexural yielding, and a maximum load of 230 kip.

A finite element model was created from the experimental study. This model saw good agreement with the data collected from the large scale tests. The model was used to run full-scale simulations of rolled and plate girders. This was done to verify the performance of eight different repair methods on three configurations of bridge girders. All of the girders had extreme levels of corrosion damage to test the limits of this repair. All of the repair methods were found able to recover the initial capacity of the girders with limited panel thickness.

7.2 CONCLUSIONS

- Section loss attributed to corrosion damage at bridge bearing can severely impact the bearing capacity of the girder. Section loss of 70% was found to decrease the bearing capacity 76% in large-scale tests.
- The repair was successful in restoring the bearing capacity of damaged girder. *The capacity of the repaired girder exceeded the capacity of undamaged girder by approximately 25%.* This proved the effectiveness of the repair method.
- The repair method prevented the failure of the girder at the bearing. Only very fine cracks formed on the UHPC panels. Instead, the beam began experiencing extensive flexural yielding.
- The UHPC mix was highly flowable and self-consolidating. It made it easy to cast the panels. The UHPC fully enclosed studs without any fiber segregation.
- When cured at an average temperature of 72° F, compressive strengths of 4 ksi in 12 hours, and 16 ksi in four days were achieved.
- Stiffness of the system was unaffected between the three tests.
- A high level of axial strain was noted to concentrate in the reduced section of the damaged girder. The addition of the concrete drastically lowered this strain demonstrating the successful transfer of loads from the steel web to the UHPC panels.
- The addition of the concrete panels increased the longitudinal strains in the bottom flange. This demonstrates that the concrete panels and the bottom flange formed a composite section.
- The shear studs located far from the bearing had larger axial strains compared to the ones placed at the proximity of the bearing. This suggests that having fewer studs at the bearing, due to corrosion further up the height, may not degrade the performance of the repair.
- Finite element model provided reliable predictions of load-deformation relationship and strains in the girder. The model also displayed correct failure modes, deformed shapes, and concrete cracking pattern.
- Stress was still seen to concentrate in the reduced section of the girder with the application of the concrete in the finite element analysis. This could lead to premature predicted failure. This makes the model conservative.

- The finite element model was used to develop eight repair strategies for three common girder end configurations. These included full height, partial height, and L-shaped repairs for rolled girders with and without stiffeners as well as full panel and partial panel repairs for plate girders.
- The eight repair methods were all able to recover and increase the capacity of the bearing above the undamaged baseline capacity.

7.3 LIMITATIONS IN NEED OF FUTURE STUDY

With the successful completion of this phase of the project, to facilitate the adoption of this repair method with confidence the following items need to be addressed.

Application of UHPC Panel under Dead Load: In order to eliminate jacking the bridge, tests need to confirm that any preexisting stress field in the steel girder will not negatively affect the load restoring capacity of the repair.

Early Lane Opening/Traffic Effect on Curing/Capacity: An investigation must be made on the effect of vibrations caused by the passing of trucks on curing UHPC. This enables estimating the minimum time needed before the bridge is opened to heavy traffic.

Application of the Repair to Full-Scale Plate Girders: Testing of full-scale plate girders with realistic geometry is of significant importance. Casting methods around bearing stiffeners should be investigated.

Verified Durability: The long-term durability of the UHPC panel/shear stud/corroded beam system should be investigated to verify the longevity of the repair.

Understand the Behavior Studs on Thin Webs: Experiments need to be performed on sub-systems to understand the effect of stud pattern, size, web thickness, welding on painted surfaces, and other parameters on the capacity of studs.

Optimized Design/Standard Details: With data obtained from verified finite element models, a more rigorous investigation into optimized design of the repair can be perused. Application on partially crippled webs and clear-through corrosion should also be considered. This would culminate in the development of standard details that can be easily adapted for different girder types and geometries.

The knowledge acquired on these issues will provide engineers and maintenance teams with all the tools required to begin the implementation of the repair on in service bridges.

References

ASCE, 2014. *2013 Report Card for America's Infrastructure,* s.l.: American Society of Civil Engineers.

ASTM, 2013. *ASTM E8-13a: Standard Test Methods for Tension Testing of Metallic Materials,* West Conshohocken: American Standard for Testing and Materials, International.

ASTM, 2014a. *ASTM C230-14a: Standard Specification for Flow Table for Use in Testing Hydraulic Cement,* West Conshohocken: American Society for Testing and Materials, International.

ASTM, 2014b. *ASTM C39-14a: Standard Test Method for Compressive Strength of Cylindrical Concrete Specimens,* West Conshohocken: American Society for Testing and Materials, International.

AZO Materials, 2013. *AISI 12L14 Carbon Steel (UNS G12144).* [Online] Available at: http://www.azom.com/article.aspx?ArticleID=6604 [Accessed April 2014].

Baltay, P. & Gjelsvik, A., 1990. Coefficient of Friction for Steel on Concrete at High Normal Stress. *Journal of Materials in Civil Engineering,* 2(1), pp. 46-49.

Bridge No. 00352, 1955. *Greenwich-Killingly Expressway Rt 1 over Oil Mill Rd.* Waterford: The Clarkeson Engineering Co. Inc..

Bridge No. 03399D, 1962. *RT 84 Onramp over Parking Lot.* Hartford: De Leuw Cather & Brill.

Bruneau, M. & Zahrai, S. M., 1997. Effect of Severe Corrosion on Cyclic Ductility of Steel. *Journal of Structural Engineering,* Volume 123, pp. 1478-1486.

CSI, 2012. *SAP2000 User's Guide.* 15 ed. Berkley: Computer and Structures Inc..

Davis, S. L. & Goldberg, D., 2013. *The Fix We're In For: The State of Our Nation's Bridges 2013,* Washington, DC: Transportation for America.

Desai, S., 1969. *Mechanical Properties of ASTM A572 Grade 65 Steel,* Bethlehem, PA: Lehigh University.

DYNAmore, 2015. *LS-Dyna Support.* [Online] Available at: http://www.dynasupport.com/ [Accessed 2015].

Effelsberg, J. et al., 2012. On Parameter Identification for the GISSMO Damage Model. *12th International LS-Dyna Users Conference,* Volume 12.

Elnashai, A. S., Takanashi, K., Elghazouli, A. Y. & Dowling, P. J., 1991. Experimental Behaviour of Partially Encased Composite Beam-Columns Under Cyclic and Dynamic Loads. *Proceedings Institute of Civil Engineers,* 2(91), pp. 259-272.

FHWA, 2014. *Bridges By Structure Type.* [Online] Available at: http://www.fhwa.dot.gov/bridge/struct.cfm

Fisher, J., 1964. *On the Behavior of Fasteners and Plates with Holes,* Bethlehem, PA: Fritz Engineering Laboratory.

Flanagan, D. & Belytschko, T., 1981. A Uniform Strain Hexahedra and Quadrilateral and Orthogonal Hourglass Control. *International Journal of Numerical Methods in Engineering,* Volume 17, pp. 697-706.

Fung, Y. C. & Tong, P., 2010. *Classical and Computational Solid Mechanics.* Singapore: World Scientific Publishing Co..

He, J. et al., 2012b. Shear Behavior of Partially Encased Composite I-Girder with Corrugated Steel Web: Numerical Study. *Journal of Constructional Steel Research,* Volume 79, pp. 166-182.

He, J., Liu, Y., Chen, A. & Yoda, T., 2012a. Shear Behavior of Partially Encased Composite I-Girder with Corrugated Steel Web: Experimental Study. *Journal of Constructional Steel Research,* Volume 77, pp. 193-209.

Hyashi, K., Ono, S. & Nakamura, S., 2003. Experimental Studies on Retrofit by Partially Encased Concrete to the Steel I-Girder Subjected to Buckling Deformation. *Technical Memorandum of Public Works Research Institute,* Issue 3920, pp. 229-236.

Kauffman, M., 2013. Nearly Ten Percent of Connecticut's Bridges are 'Structurally Deficient'. *Hartford Currant*, 14 May.

Kristoff, W. M., 2011. *In-Depth Inspection of Bridge No. 03399D: I-84 over Parking Lot, Hartford, CT,* : November, 11.

Lepi, S., 1998. *Practical Guide to Finite Elements: A Solid Mechanics Approach.* New York: Marcel Dekker, Inc..

LSTC, 2006. *LS-Dyna Theory Manual.* Livermore: Livermore Software Technology Corp..

LSTC, 2012a. *LS-Dyna Keyword Manual,* Livermore: Livermore Software Technology Corp..

LSTC, 2012b. *LS-Dyna Material Manual.* Version 971 R6.1.0 ed. Livermore: Livermore Software Technology Corp..

Maggi, Y. I., Goncalves, R. M., Leon, R. T. & Ribeiro, L. F., 2005. Parametric Analysis of Steel Bolted End Plate Connectionos Using Finite Element Modeling. *Journal of Constructional Steel Research,* 61(5), pp. 689-708.

Malvar, L. J., Crawford, J. E., Wesevich, J. W. & Simons, D., 1997. A Plasticity concrete Material Model for Dyna 3D. *International Journal of Impact Engineering,* Volume 19.

Malvar, L. J., Crawford, J. E., Wesevich, J. W. & Simons, D., 1997. A Plasticity Concrete Material Model for Dyna-3D. *International Journal of Impact Engineering,* 19(9-10), pp. 847-873.

Nakamura,, S. & Narita, N., 2003. Bending and Shear Strength of Partially Encases Compisite I-Girders. *Journal of Constructional Steel Research,* Volume 59, pp. 1435-1453.

Nakamura, S., Momiyama, Y., Hosaka, T. & Homma, K., 2002. New Technologies of Steel/Concrete Composite Bridges. *Journal of Constructional Steel Research,* Volume 58, pp. 99-130.

NPR, 2013. *Transcript: Obama's State of the Union Address Prepared for Delivery.* [Online]
Available at: http://www.npr.org/2013/02/12/171841852/transcript-obamas-state-of-the-union-as-prepared-for-delivery

Pawlikowski, D., 2012. *Routine & Special Inspections on Structure No. 00352A, Interstate 95 over Oil Mill Rd,* : January, 11.

Reinhorn, A. M. & Bracci, J., 1992. *Multi-Axis Load Cell Design and Construction,* Buffalo: University of Buffalo.

Toolbox, E., 2014. *Friction and Coefficients of Friction.* [Online] Available at: http://www.engineeringtoolbox.com/friction-coefficients-d_778.html

Yuan, J. & Graybeal, B. A., 2014. *Bond Behavior of Reinforcing Steel in Ultra-High Performance Concrete,* FHWA-HRT-14-090: October.

Appendix A. Load Cell Development

A.1 INTRODUCTION

This appendix outlines the design, manufacture, and calibration procedure of the load cells created for the experiment. In total, four load cells were prepared. Only two were calibrated for the current experiment. This appendix is divided into three sections. The first section outlines the design of the load cells including a basic review of the background literature and the design of the load cell with finite element analysis. The second section discusses the manufacture of the load cells including machining, selection and soldering of the strain gauges, and assembly of the completed cells. The final section covers the calibration procedures of the axial, shear, and moment circuits.

A.2 LOAD CELL DESIGN

A.2.1 Basic Design from Literature

The design of the load cell was based off a design of a smaller load cell developed at the University of Buffalo (Reinhorn & Bracci, 1992). The design utilized a steel cylinder with a reduced cross-section in the middle of the height. This concentrated the highest strains in this reduced section, allowing for more accurate measurements. The load cell measured force and moments by converting full bridge strain readings. The gauges were positioned in such a way that the effects of other forces are canceled.

The load cell developed at the University of Buffalo was designed for relatively small capacity. It was manufactured from a $4^1/_2$-in diameter steel rod. The rod was machined so that the interior diameter was $2^1/_2$ in, and the reduced measuring area was 2 in tall and $^1/_4$-in thick. It had an axial capacity of ±40 kip, shear capacity of ±5 kip, and moment capacity of ±40 kip-in. This load cell is shown in Figure A.2.1.

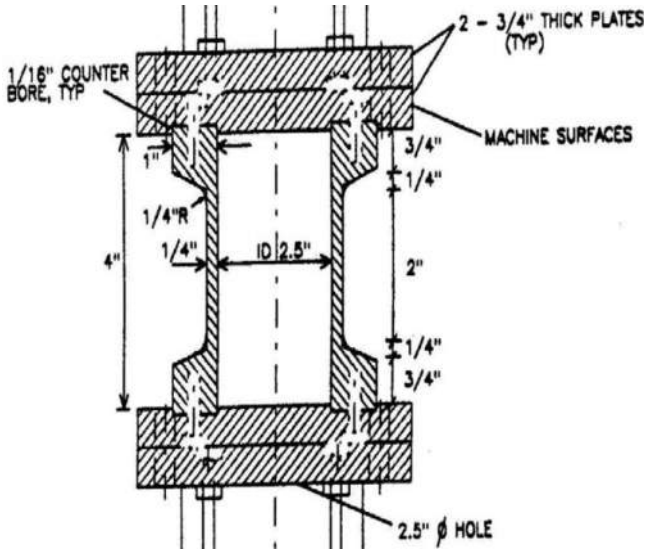

Figure A.2.1 Basic Load Cell from the University of Buffalo (Reinhorn & Bracci, 1992)

These capacities were too low for the current study so the design had to be scaled up. The general design of the fluted cylinder was modified in order to increase the capacities to ±500 kip axially, ±100 kip in shear, and ±500 kip-in for moment. This design was done using finite element analysis

A.2.2 Design of the High-Capacity Load Cells

In order to increase capacity, the area of steel in the reduced section had to be increased. To determine the required dimensions, finite element analysis was performed on iterations of possible load cell design shapes, and strains maximum strains were limited such that no strain for either of the individual capacities were greater than 1,600 με. This was done so that the material would not reach the proportionality limit and form excessive hysteresis loops.

The load cell was modeled in LS-Dyna (LSTC, 2012a). The load cell was modeled as 13,600 solid elements with elastic properties of steel. The elements were calculated using selectively reduced integration techniques. This formulation is more expensive than the single point integration, but is also more accurate. The selectively reduced elements occasionally experience shear-locking if elements have poor aspect ratios (DYNAmore, 2015). This was not an issue as all the elements were well formed. The model of the load cell is shown in Figure A.2.2a. The load was applied with the *LOAD_NODE_SET card which applies a force to a set of nodes. A rigid plate was included and the center node loaded with either an axial, shear or moment at its center, circled in Figure A.2.2b. The top set of nodes on the load cell were constrained to move with the rigid plate using the *CONSTRAINED_EXTRA_NODES_SET card. This

included these nodes in the rigid body of the plate, and effectively applied the load uniformly on the top surface.

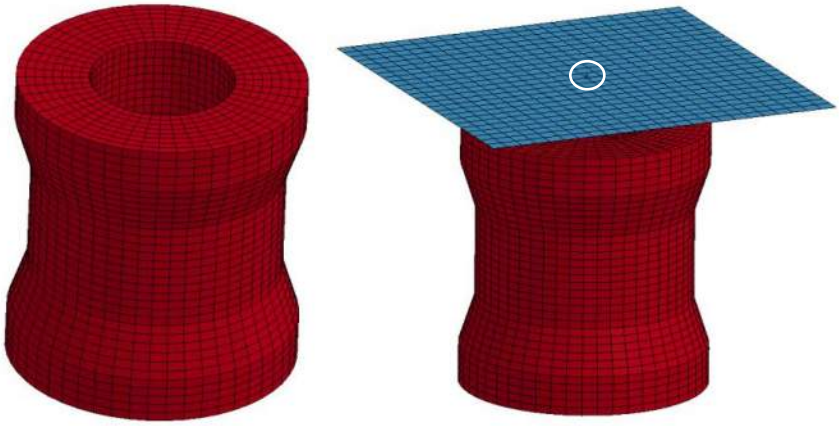

(a) (b)

Figure A.2.2 Finite Element Model of the Load Cell

(a) Load Cell Mesh, (b) Loading Mechanism for the analysis

The load cell model ran four separate analyses: axial load, shear load, moment load, and combined loading. In each of these the maximum effective strain was found on the reduced section away from the sloped edges, where stress concentrates. This was done as this would be where the strain would be measured. Figure A.2.3 shows effective strain contours (0-1,600 με) on the load cell under load capacities. The maximum effective strains on the central area of the cylinder in the cell for axial, shear, and moment were calculated to be 635 με, 814 με, and 540 με, respectively. These were all well below the target of 1,600 με to remain under the proportionality limit of the steel, and any two combined will still be below the limit. One final analysis was run on the load cell assuming all three forces were applied simultaneously. The shear and moment were applied in perpendicular directions to maximize the effect. Under these unlikely conditions the maximum strain was found to be 1,990 με, a sum of the three maximum strains. To assure that the steel would not yield, a minimum yield stress of 55 ksi was needed.

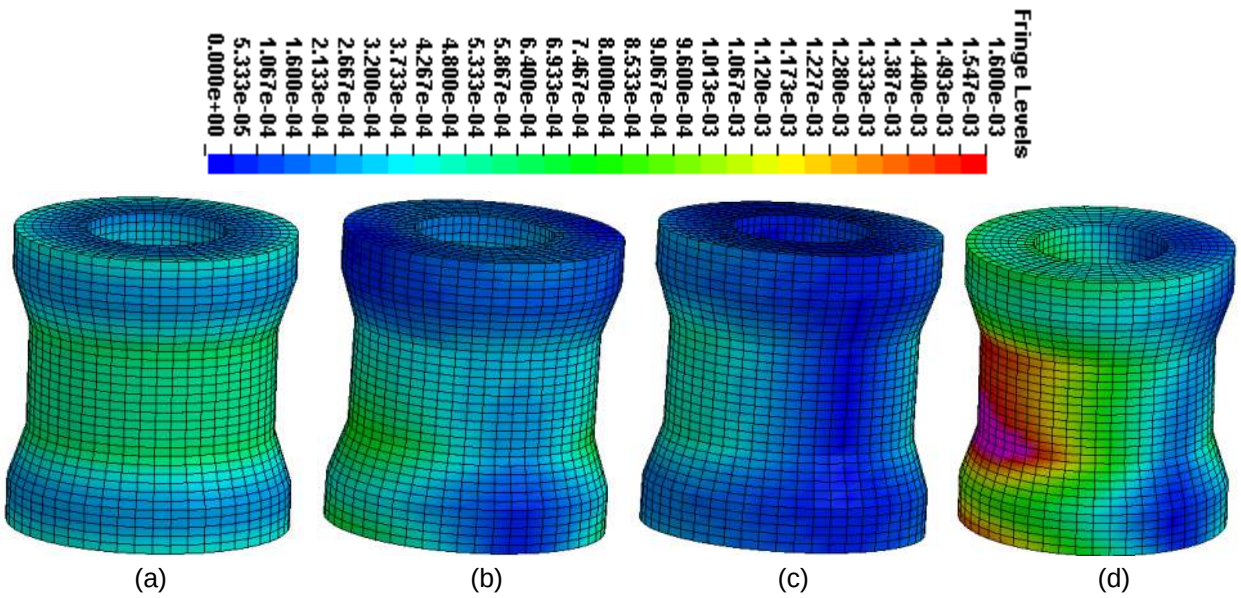

Figure A.2.3 Effective Strain Contours on the Finite Element Model Load Cells

(a) 500 kip Axial Load, (b) 100 kip Shear Load, (c) 500 kip-in Moment, (d) All Loads Combined for Maximum Effect

The finished dimensions of the load cell are shown in Figure A.2.4. The main body of the load cell would require an 8-in diameter steel rod, with an inside diameter of 4 in. The reduced section would have an exterior diameter of 7 in, and be situated in the middle $2^5/_8$ in of the $8^1/_2$ in tall cylinder. Twelve $^3/_4$-16 high-strength heat treated alloy pan-head bolts were used to attach the body to the end plates. These had a total axial capacity of 710 kip. This would allow the cells to be fully effective in tension as well as compression.

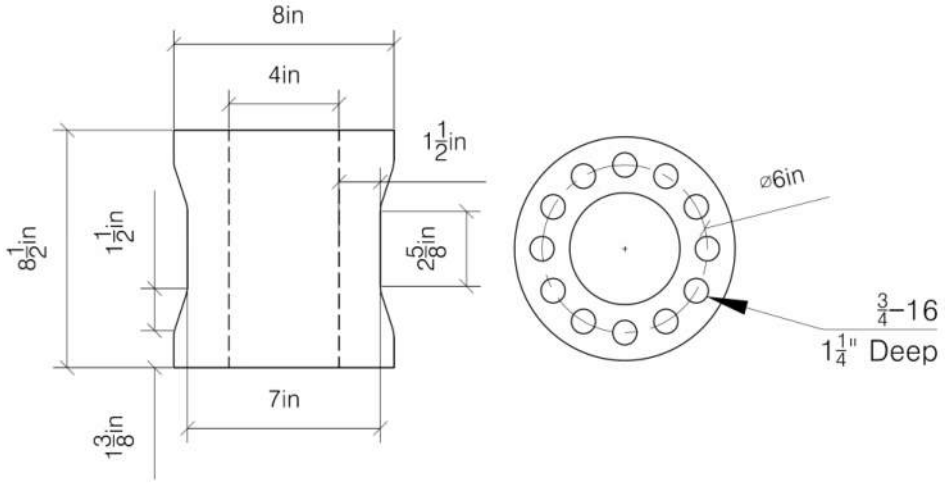

Figure A.2.4 Dimensions of the Designed 500 kip Load Cell

The end plates of the load cell were designed as 16 in × 16 in × 3 in plate. This was done in order to provide a large bearing surface and to ensure the cantilevered portions

of the plate would not bend. Each end plate had a $^1/_2$-in deep recess was provided to seat the ends of the cylinder. A $^1/_{32}$ in oversize was provided on the diameter so that the cylinder would fit snugly, but evenly. The same twelve bolt pattern was included to secure the load cell to the plates. These were through holes with countersinks so that the pan-head screws would sit flush or below the surface of the plate. Two sets of 8 in × 8 in holes were provided for the $1^1/_8$ in floor anchors. One set was provided square to the plate, and a second set was oriented 45° from the first set. A $^7/_8$-9 threaded hole was provided in the center of the plate to allow for the attachment of a hoist ring to move the load cell with the bridge crane in the Structures Lab. Figure A.2.5 shows the design of the base plates and the seating of the load cell within the end plates.

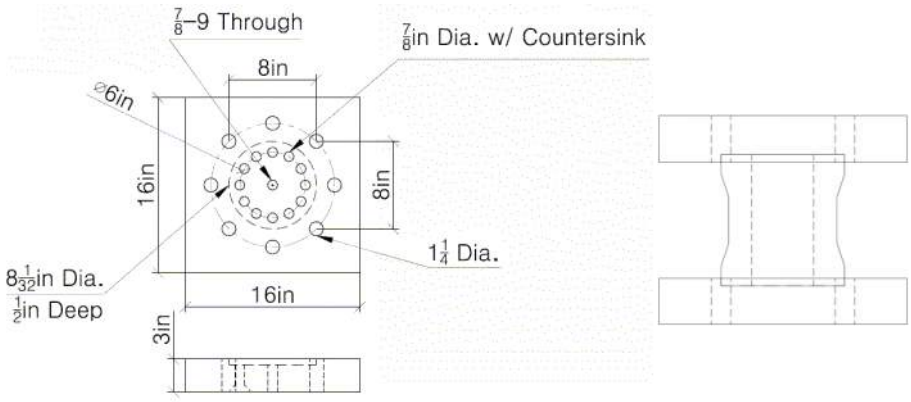

Figure A.2.5 Design of the Load Cell Base Plates

A.3 LOAD CELL MANUFACTURING

A.3.1 Machining

The geometry and yield strength limits set in place by the finite element made the selection of load cell cylinder material difficult. Most round rod with a diameter over 5 in are hot rolled. The hot rolling process results in low yield stresses around 36 ksi. In order to get yield stresses above 50 ksi in round bar, a cold rolled bar needs to be used. Cold rolling typically limits the diameter of the bar. Only one stock cold rolled bar was found with an 8 in diameter. This was a 12L14 alloy steel. This is an easily machined high-strength alloy steel. The high machinability is achieved through 0.25% lead in the alloy. The alloy has a minimum yield stress of 60 ksi, and a minimum tensile strength of 78 ksi (AZO Materials, 2013).

(a) (b) (c)

Figure A.3.1 Machining of the Load Cells from Blanks

(a) The 8 in Rod Cut into Load Cell Blanks, (b) Drilled Cylinder Having Exterior Milled, (c) Finished Exterior of the Cylinder Prepared for Drilling Attachment Holes

The bar ordered was 48 in long, so that four lengths could be cut to make the four load cells, Figure A.3.1a. The bar was then placed in a lathe to machine the exterior and interior of the load cell. The center hole was first drilled out. This was done by using a CNC milling machine. First a hole was drilled through the cylinder. This allowed an end mill to take the hole to the finished diameter. The exterior of the bar was first cleaned to the 8 in finished exterior diameter, Figure A.3.1b. This also allowed the diameter to be uniform on the entire rod. With the finished interior and exterior diameters, the central reduced section was machined. This was done in a lathe. With the dimensions of the load cell finished, the twelve holes for attaching the end plates had to be added, Figure A.3.1c. The holes were first positioned and drilled in the load cell using the CNC milling machine. These drilled holes were $^{11}/_{16}$in. These holes were then tapped with a $^{3}/_{4}$-16 thread. The finished load cell cylinders are shown in Figure A.3.2a.

(a) (b) (c)

Figure A.3.2 Load Cell after the Machining Process

(a) Load Cell after Machining and Drilling, (b) Load Cell and Scribe for Mid-Height Marking, (c) Scribing the Quarter-Points of the Cylinder

With the load cell cylinders finished, the vertical center of the cylinders and the circumferential quarter-points aligned with the hole pattern of the load cell had to be scribed. These scribe marks would act to align the strain gauges on the surface of the cell. These marks had to be accurately positioned to assure that the gauges were positioned with respect to the attachment holes in the end plates. This was done using a scribe mounted on a precision ruler. This allowed the position of the scribe to be located with an accuracy of 0.0005 in. The scribe was set to two levels to scribe the two heights on the cell. First, a horizontal mark was scribed on the entire circumference of the cell to mark the center of the reduced section, Figure A.3.2b. With the horizontal scribe made, the load cell cylinder was placed on its side, and rested on pegs screwed into the top screws. These were rested on metal risers set so that the screw hole would be mid-height on the height of the cylinder. The scribe was repositioned, and a vertical line scribed perpendicular to the first line, Figure A.3.2c. This ensured that the four vertical scribes would be 90° apart and aligned with the hole pattern on the top and bottom of the cell. This way, the cell could be aligned with the mounting holes on the end plates.

The end plates were manufactured from 16 in × 16 in × 3 in grade 50 plate, Figure A.3.3a. The end plates were machined in a CNC machine, Figure A.3.3b. These plates were milled and drilled automatically to the design provided. After the plate was finished being machined, the plates had to be tapped for the hoist ring, Figure A.3.3c. These finished plates were then read to be attached to the load cell cylinders.

(a) (b) (c)

Figure A.3.3 Machining the End Plates

(a) Plates as Supplied by Inframetals, (b) Machining of the End Plates in the CNC Milling Machine,

A.3.2 Strain Gauging

A total of twenty four strain gauges were used on each load cell. These gauges would be wired into five full bridge configurations to measure the axial capacity, and the shear and moment in two perpendicular directions. These gauges were arranged in clusters on the scribe lines as illustrated in Figure A.3.4a. Four clusters of gauges were oriented on the load cell as shown in Figure A.3.4b. Strain gauges were given an alphanumerical designation based on the gauges location on the load cell and the orientation within the cluster. These designations would then be used to identify the strain gauges within the bridge circuits.

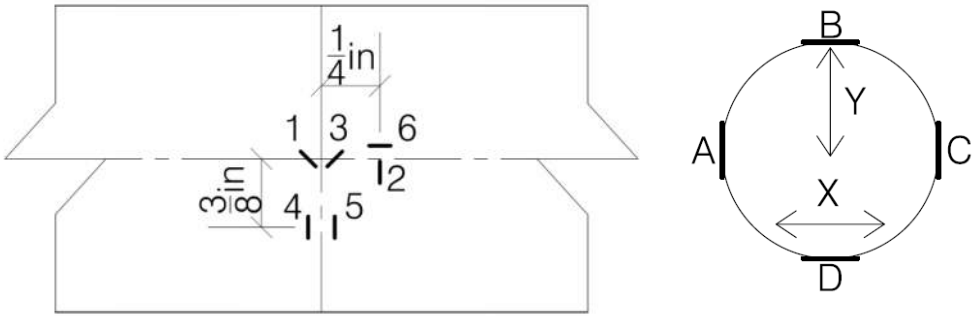

(a) (b)

Figure A.3.4 The Arrangement of Strain Gauges on the Load Cells

(a) Positioning of the Strain Gauges in a Cluster on One Side of the Load Cell, (b) Positioning of the Strain Gauge Clusters on the Load Cell

All gauges were transducer quality strain gauges manufactured by Omega Engineering. Transducer quality strain gauges differ from traditional strain gauges by having higher durability, more consistent resistance, and improved fatigue performance. This ensures that the quality of the readings from the gauge would not degrade as the gauge goes through many cycles of loading. The gauges were constantan foil gauges mounted on polyimide film. Three different rosette pair orientations were required to achieve the arrangement shown in Figure A.3.4a. Gauges were selected such that their grid lengths were comparable. SGT-2D/350M-SY41 dual shear transistor with four terminations was used for used for the 1 and 3 gauges in the cluster. This rosette has two gauges oriented at ±45° and has solder pad terminations. The gauge grid patterns are 0.071 in long, a resistance of 350Ω, and have a gauge factor of 2.05 and are compensated for use on steel. SGT-2/350-XY41 90° biaxial transistor with four terminations was used for used for the 2 and 6 gauges in the cluster. This has two gauges oriented at 0° and 90° with solder terminations. The gauge grid patterns are 0.063 in long, a resistance of 350Ω, and have a gauge factor of 2.14 and is temperature compensated for steel. SGT-2C/350-DY41 dual grid transistor with four terminations was used for used for the 4 and 5 gauges in the cluster. This has two parallel gauges

for bending applications. The gauge grid patterns are 0.075 in long, a resistance of 350Ω, and have a gauge factor of 1.99 compensated for steel.

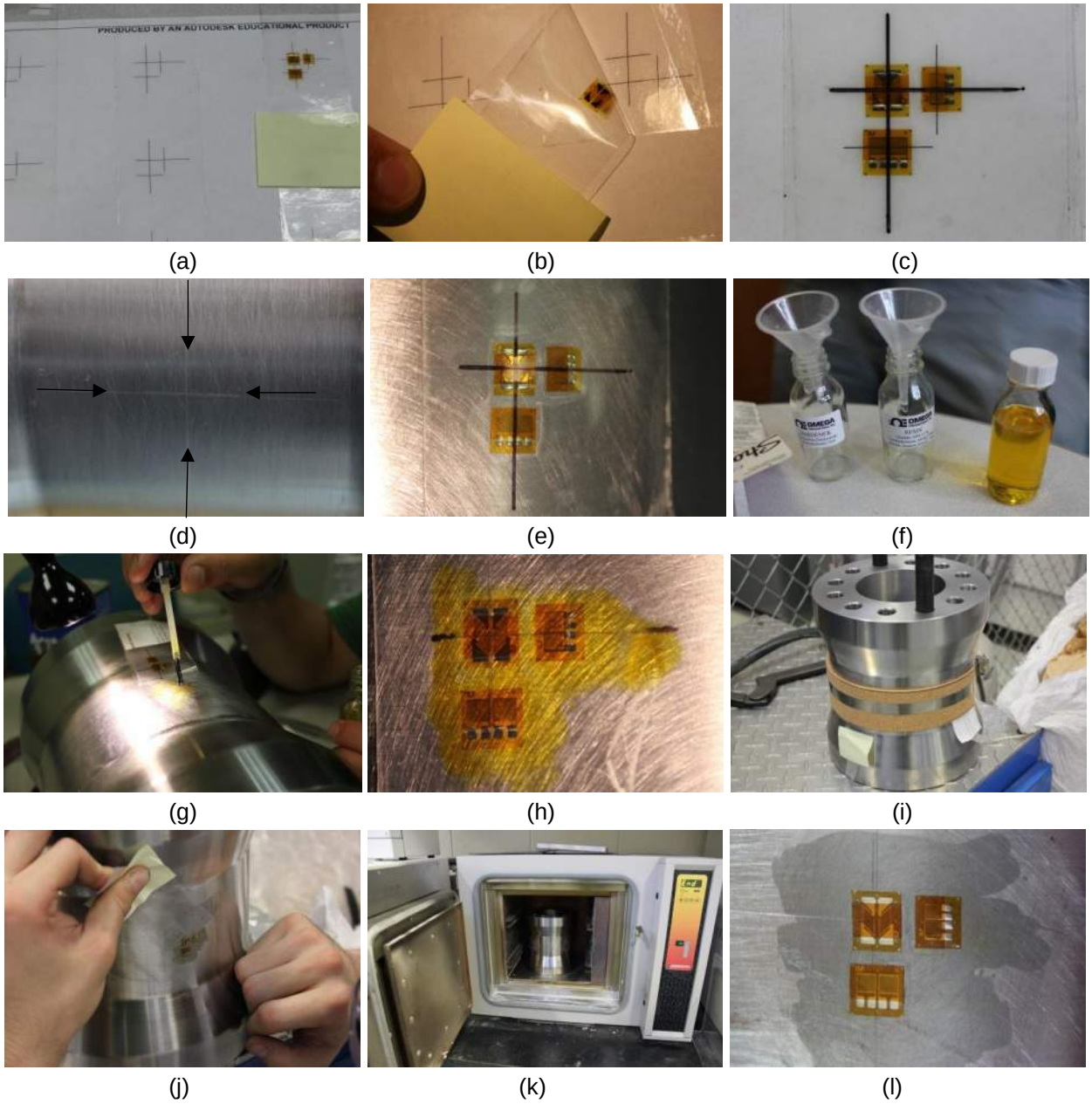

Figure A.3.5 Alignment and Adhesion of the Strain Gauges on the Load Cell

(a) Alignment Grid Used to Position the Strain Gauge Sets, (b) Positioning of Individual Strain Gauges, (c) Completed Arrangment of Strain Gauge Set, (d) Detail of the Alignment Scribe Lines on the Load Cell, (e) Positioned Strain Gauge Set on the Scribe Lines, (f) Heat Cure Adhesive Used to Glue the Gauges, (g) Applying the Adhesive to the Steel and the Gauges, (h) Gauges Adhered to the Load Cell, (i) Clamp System to Maintain Pressure on the Adhered Gauges, (j) Removing the Tape from the Gauges, (k) Heat Curing the Adhesive, (l) Strain Gauges after Heat Curing

Positioning of the gauges was achieved by printing a series of alignment grids to the scaled size to position over the alignment marks, Figure A.3.5a. A strip of clear tape was placed over the grid so that a second piece of tape could be used to hold the position of the gauges. The strain gauges were aligned on the grid and then tape was used to fix the location, Figure A.3.5b. This was repeated for each individual gauge until all three gauges were positioned and aligned on the grid, Figure A.3.5c. The two alignment marks that went through gauges 1 and 3 were marked with a marker to align with the scribe lines on the load cell which are seen in Figure A.3.5d. Figure A.3.5e shows the gauges on the tape with the alignment marks positioned on the load cell. The adhesive used to fix the gauges on the load cell was a two part, heat cured adhesive. This was part of the Omega TT300 two-part heat-cured epoxy adhesive kit for polyimide backed strain gauges, Figure A.3.5f. The adhesive was painted onto the surface of the load cell as well as the backs of the strain gauges, Figure A.3.5g. The adhesive was given fifteen minutes to begin to set before the gauge was set to the surface of the load cell per the manufacturer's instructions. The gauges were then placed back on the adhesive and force applied for a few minutes for the adhesive to set. The gauges after setting are shown in Figure A.3.5h. A band of cork was then fixed over the gauges with a hose clamp to apply constant pressure overnight, Figure A.3.5i. After a night of pressure being applied, the cork and tape were removed from the gauges, Figure A.3.5j. The load cell was then cured in an oven at 212°F for 10 hours in order to set the adhesive, Figure A.3.5k. Figure A.3.5l shows the gauge and the adhesive after the curing process.

A.3.3 Soldering

After the strain gauges were adhered to the surface of the load cell, the full bridge circuits had to be wired to read the axial, shear and moments acting on the load cell. The designs of the Wheatstone bridges are shown in Figure A.3.6. The gauges are positioned such that the strain readings would be increased so that the readings would be more accurate. In the figure the voltage is supplied across the horizontal connection points, and read across the vertical connections in the figure.

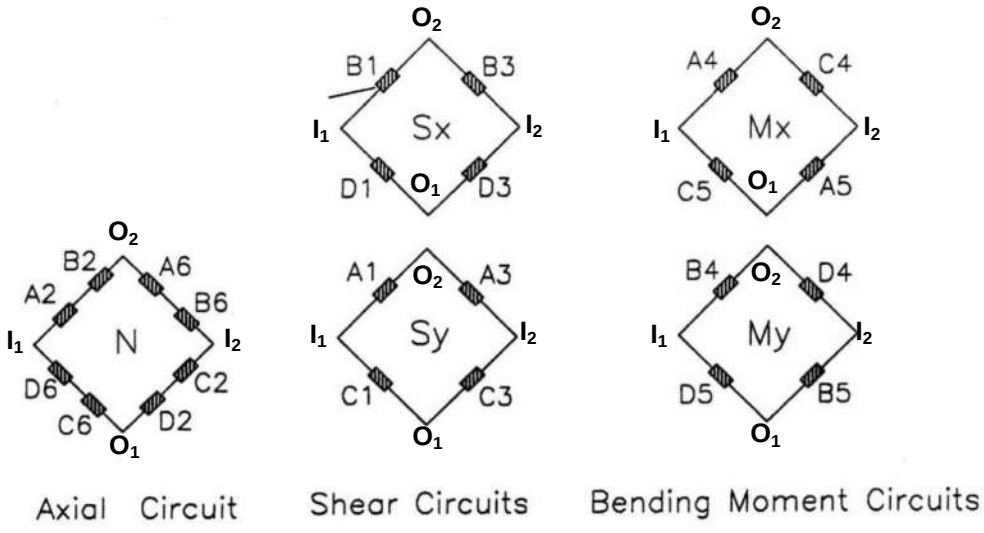

Figure A.3.6 Wiring of the Wheatstone Bridge Circuits in the Load Cell

Due to the small size of the terminal pads on the strain gauges, bondable terminal pads (Omega Engineering BTPC-2) were included on the load cell adjacent to the strain gauges. A 60/40 Tin-Lead solder was used with a fine point soldering iron set to 450°F for all soldering. Lead based solder was used to reduce the temperature required, reducing risk of damage to the gauges. A small coil 32 gauge wire was used to run from the small terminal pads on the strain gauges to the larger ones on the bondable terminal pad, Figure A.3.7a. This provided strain relief and would prevent larger wires from potentially damaging the strain gauges. Terminal pads were also included for completion of the Wheatstone bridge circuits, Figure A.3.7b. Each of the terminal pads were labeled with the location that each of the terminals had to be wired to complete the proper circuit. This prevented errors in wiring the load cell. The Wheatstone bridges were completed with 28 gauge color-coded wires so that each circuit could be identified. The terminal pads after soldering of the 28 gauge wire are shown in Figure A.3.7c-d.

(a) (b) (c) (d)

Figure A.3.7 Numbering and Soldering of the Load Cell Circuits

(a) Strain Gauges Soldered to the Bondable Terminal Pads with Destination Labels, Side B, (b) Terminal Pad for Axial Circuit, (c) Wired Side B Strain Gauge Circuit, (d) Soldered Normal Circuit Termination

The load cells after wiring was finished are shown in Figure A.3.8a. After wiring was completed, the resistances of all of the circuits were verified using a digital multimeter to verify the circuits were complete, and wired correctly. Additional lead wires were then soldered to the circuit terminal pads, Figure A.3.8b. These wires were sent to a five terminal RJ45 Ethernet port, Figure A.3.8c. This Ethernet port would allow fast, easy connections of the load cell to data acquisition systems.

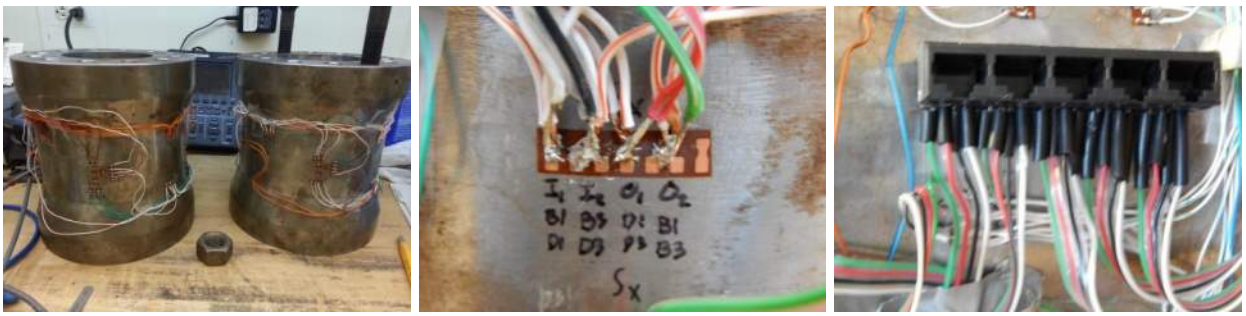

(a) (b) (c)

Figure A.3.8 Final Wiring of the Wheatstone Bridge Circuits

(a) Completed Wiring on the Load Cell Cylinders, (b) Attachment of Leads to the RJ45 Jack, (c) Wiring of the RJ45 Jack for Ethernet Cable Connection

A.3.4 Assembly

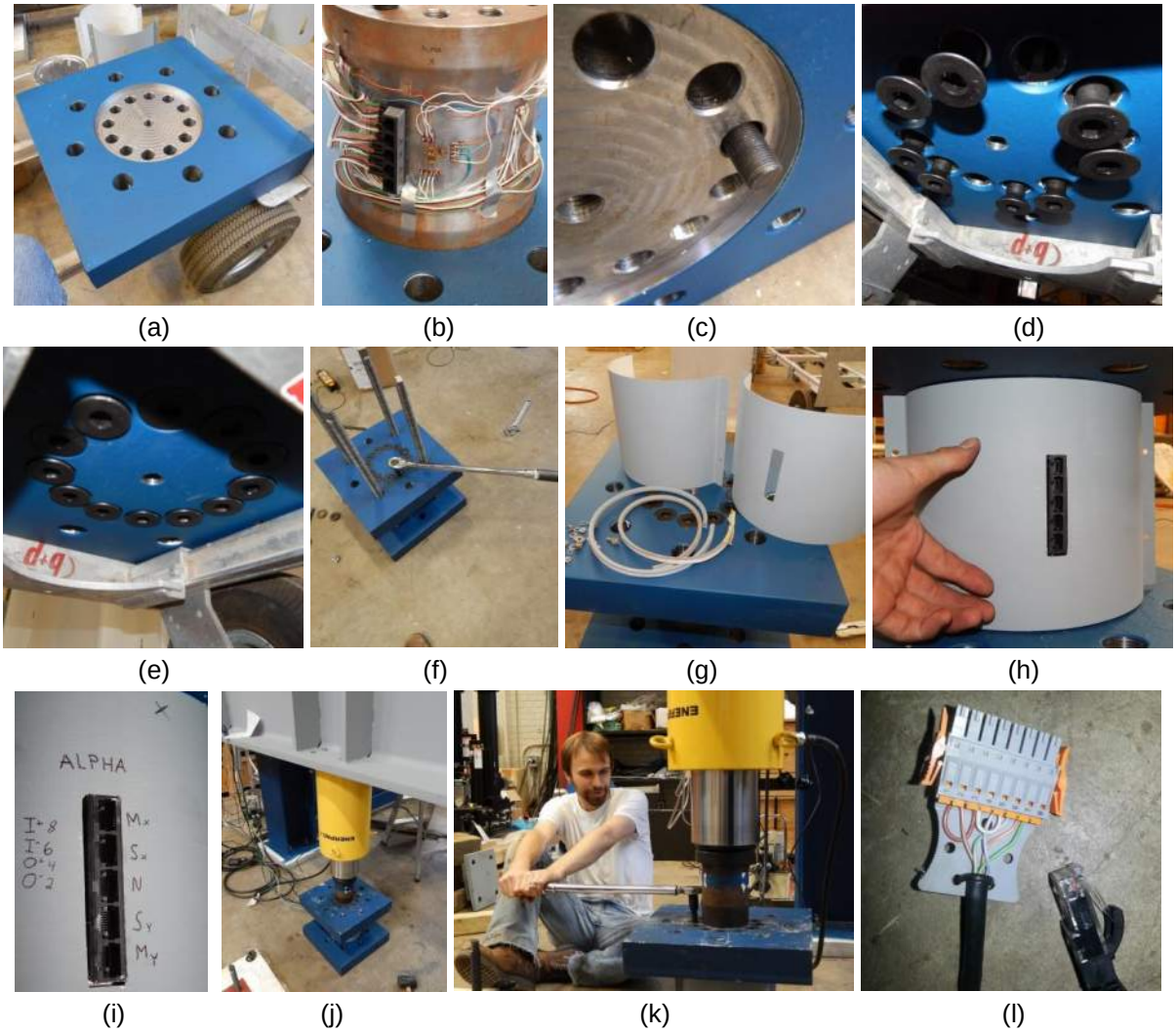

Figure A.3.9 Assembly of the Load Cells

(a) The Primed and Painted Load Cell End Plates, (b) Seating the Load Cell Cylinder on the Base, (c) Penetration of the Pan-Head Bolts through the End Plate, (d) Installation of the Bolts on the Plate, (e) Finished Bolt Installation, (f) Tightening the Bolts with a Torque Wrench, (g) Cylinder Protective Shroud Components, (h) Installation of the Protective Shroud, (i) Marking the Protective Shroud, (j) Applying an Axial Load to the Load Cell, (k) Snugging the Bolts Under Load, (l) Modified Ethernet Cable for Load Cell Data Acquisition

With the load cell cylinders completed and wired assembly of the load cells could begin. The end plates of the load cell were primed with rust inhibiting primer and painted prior to assembly. The end plate was then placed on a raised platform so that the bolt holes could be accessed, Figure A.3.9a. The bottom plate was added first rather than adding the top plate and flipping the assembly to reduce the risk of damage to the cell. The cell was then placed in the recess on the end plate so that the clusters of gauges were aligned with the flat edges of the plate, Figure A.3.9b. This allows for

the axis of measured shear and moment to be aligned with the end plates. The penetration of the bolts through the plate is shown in Figure A.3.9c. This depth was sufficient to fully engage the bolts without bottoming out in the tapped holes. The bolts were then installed on the bottom plate, Figure A.3.9d. The bolts were then tightened, Figure A.3.9e. When tightening the bolts, a star pattern was always used so that the end plates would be evenly seated. After the top plate was installed in a similar manner, the load cell was seated on a floor bolt cluster to provide a reaction so the torque on the bolts could be increased to 250 ft-lb, Figure A.3.9f.

A protective shroud made from two crescent pieces of sheet steel were used to protect the wiring of the load cell and to protect the strain gauges, Figure A.3.9g. One of the crescent plates had a hole to fit the RJ45 jack. The crescent pieces were also cut shorter that the space between end plates to avoid force transfer through the shroud, Figure A.3.9h. After installation of the shroud, the ports were labeled according to the circuit, input and output voltage ports, and the axis of the load cell were also marked, Figure A.3.9i.

After some preliminary axial calibration, it was found that the bolts should be torqued under load. So the load frame was adjusted to allow for the load ram to be used to apply pressure to the cylinder during tightening, Figure A.3.9j. The bolts were then torqued again to 250 ft-lb, Figure A.3.9k. To attach the load cell to the data acquisition system, Ethernet cables were modified by removing one end and wiring the appropriate lines from the circuit to the MX1615, Figure A.3.9l. The load cell was now complete and ready for calibration.

A.4 LOAD CELL CALIBRATION

A.4.1 Axial Calibration

Calibration of the axial circuit was performed using the UCONN Structures Lab's 400 kip SATEC load frame, Figure A.4.1a. The load cell was placed on the bottom platen of the load frame, and centered and squared to the frame, Figure A.4.1b. This assured minimal eccentricity and a more uniform distribution of the axial load on the load cell. To reduce the moment imparted on the load cell a pivot head was used between the top of the load cell and the upper platen of the load frame, Figure A.4.1c. This pivot head was centered on both the load cell and centered to the top platen to reduce eccentricity.

(a) (b) (c)

Figure A.4.1 Installation of the Load Cell in the Load Frame for Axial Calibration

(a) Load Cell in the SATEC Load Frame, (b) Centering the Load Cell on the Bottom Platen, (c) Pivot Head between the Top Platen and the Load Cell

The FlexTest-40 controller coupled with the SATEC frame is capable of programmable control on the hydraulics of the load frame. A multi-step test was programed to run calibration on each of the load cells. This utilized force control, and ran multiple cycles to increasing loads. Three dwell cycles were also performed to determine the creep performance of the load cells. Four cycles were performed at each load step, increasing in 50 kip increments from 50 kip to 350 kip. Loading and unloading was performed over a 15 second period. Unloading was performed to a load of 5 kip. The three dwell cycles each lasting five minutes were performed at 100, 200, and 300 kip. 1 kip was added to all baseline load levels to account for the weight of the load cell. The profile of the loading history used in the experiment is shown in Figure A.4.2.

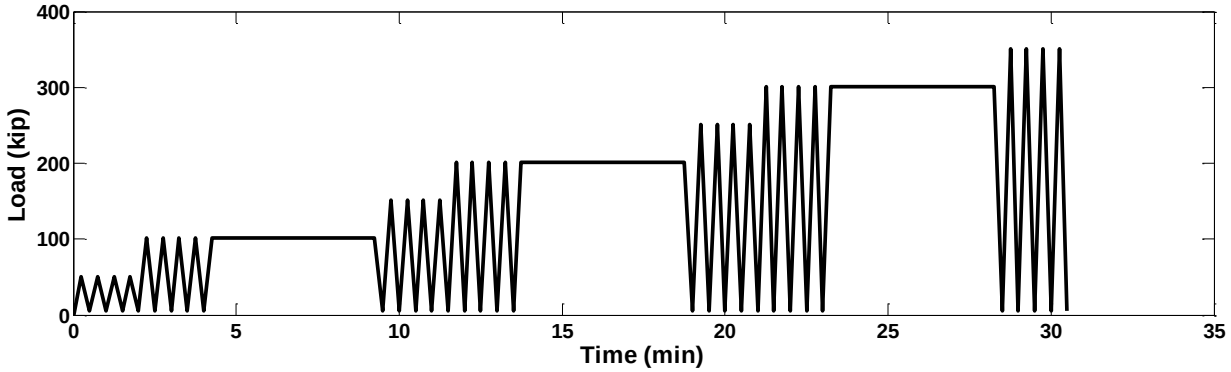

Figure A.4.2 Loading History Used in Load Cell Calibration

Four cycles were performed for each load cell, two cycles in a right-side up orientation (RU1, RU2), and two in an upside-down orientation (UD1, UD2). Through the test, readings of both the load reading from the load frame as well as the $^{mV}/_{V}$ reading from the load cell were recorded simultaneously with the MX 1615. These two values were then plotted against each other to determine the correlation between the bridge reading and the load. This factor was then used as the calibration factor for the

axial circuit. The $^{mV}/_{V}$ vs load graphs for both of the load cells used are presented in Figure A.4.3.

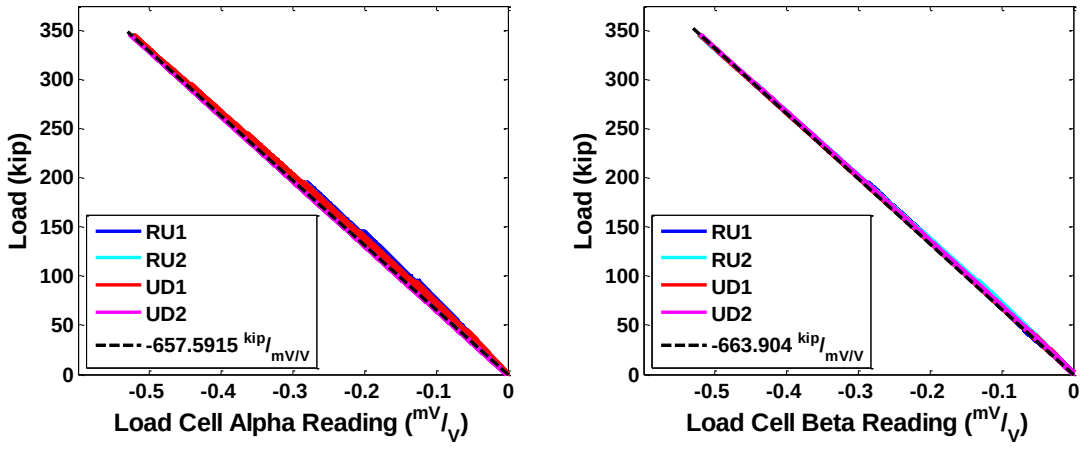

(a) (b)

Figure A.4.3 Calibration Graphs for the Two Load Cells

(a) Calibration Factor Calculation: Load Cell Alpha, (b) Calibration Factor Calculation: Load Cell Beta

Figure A.4.4 shows the error in each load cell based on the predicted values from the pressure in the load ram. The pressure from the 10,000 psi pressure gauge was converted to a force based on the area of the piston. This force was the distributed based on the geometry of the loading. Error was defined as the difference between the load cell reading and the predicted value divided by the full scale range. This range was defined as 1,000 kip as the cell is capable of reading 500 kip in both tension and compression. As can be seen in the figure, the maximum error in load cell Alpha is less than 0.41% of full scale, and load cell Beta is 0.68% of full scale.

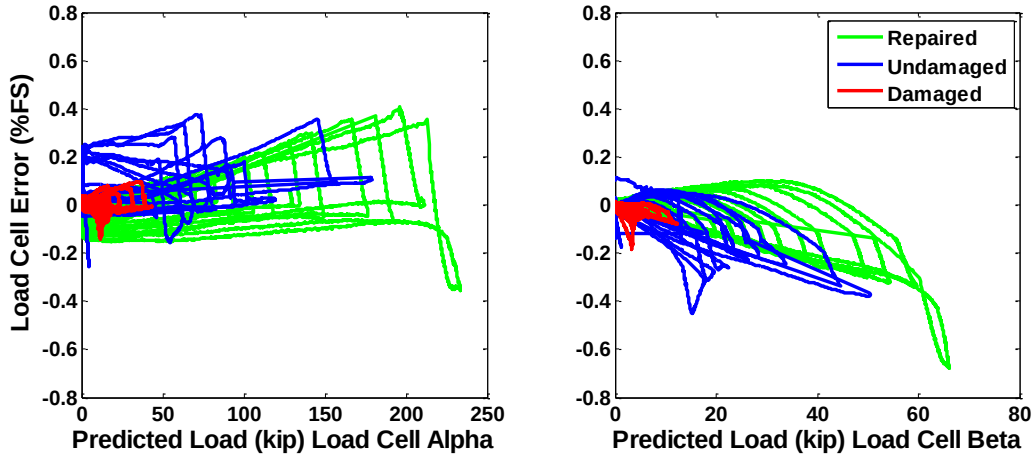

(a) (b)

Figure A.4.4 Full Scale Error for Each Load Cell Based on Predicted Load from Cylinder

(a) Calibration Factor Calculation: Load Cell Alpha, (b) Calibration Factor Calculation: Load Cell Beta

A.4.2 Shear and Moment Calibration

The calibration of the shear and moment circuits of the load cells will be performed with the completion of the remaining two load cells. This is due to the setup required for proper calibration of the circuits. Figure A.4.5 shows a schematic of the test setup for shear and moment calibration. A two-point bending setup will create regions of uniform shear in the two end load cells, and a region of uniform moment in the middle cells. The load limitation of the load applied to the spreader beam in the calibration will be 80 kip. This 80 kip load will produce a shear force of 40 kip in the end load cells and a moment of 480 kip-in in the central load cells. The loading protocol will be similar to that performed on the axial circuit, but using 10 kip increments instead of 50 kip increments.

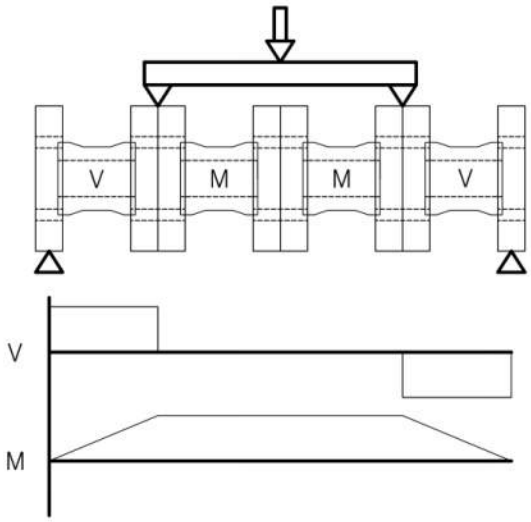

Figure A.4.5 Schematic of the Setup for the Shear and Moment Circuits Calibration

Appendix B. Photos of Damage Progression

B.1 UNDAMAGED GIRDER

B.1.1 Undamaged - Right Side View

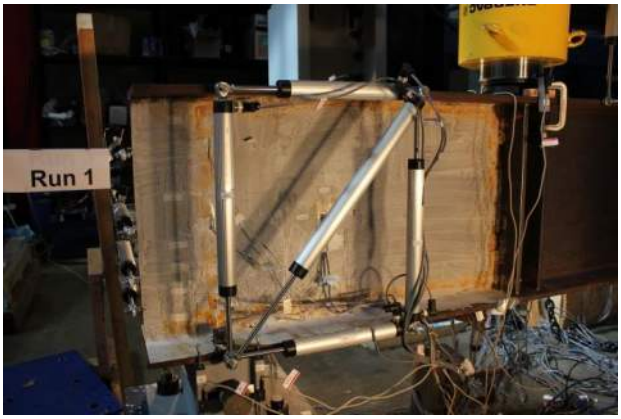

Figure B.1.1 Undamaged Girder Right: 40 kip

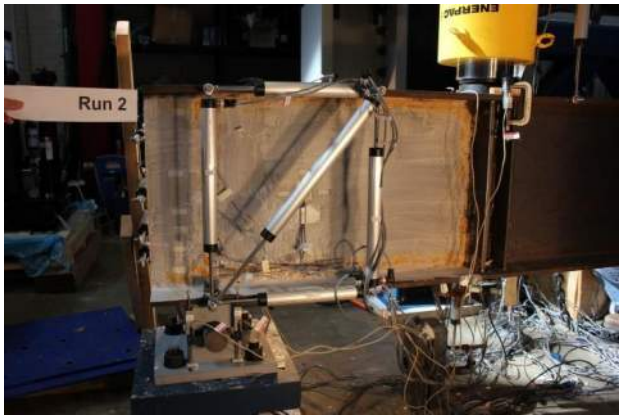

Figure B.1.2 Undamaged Girder Right: 60 kip

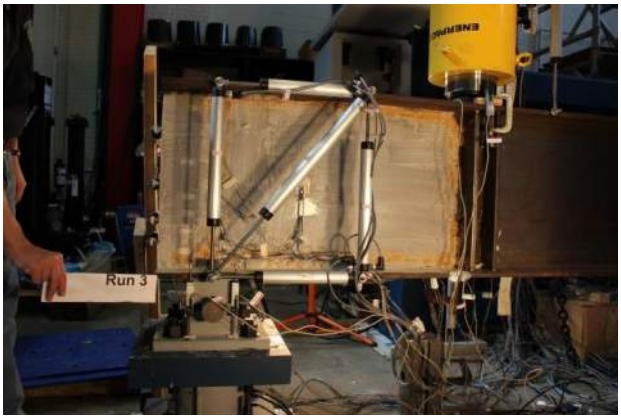

Figure B.1.3 Undamaged Girder Right: 80 kip

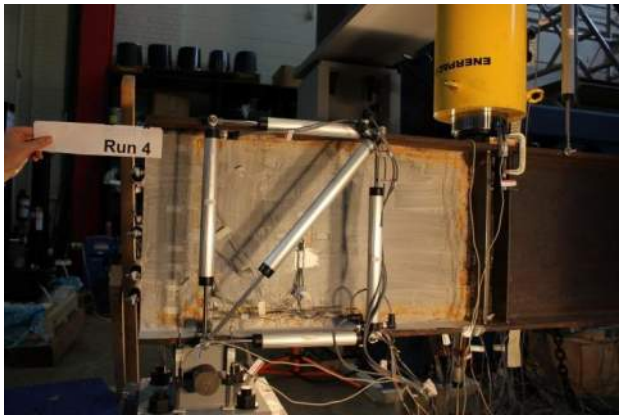

Figure B.1.4 Undamaged Girder Right: 100 kip

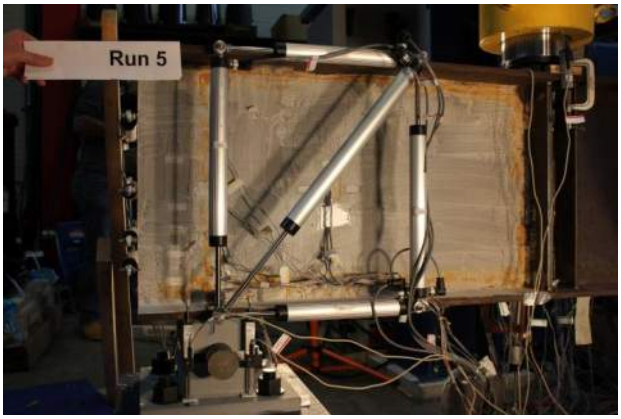

Figure B.1.5 Undamaged Girder Right: 120 kip

Figure B.1.6 Undamaged Girder Right: 140 kip

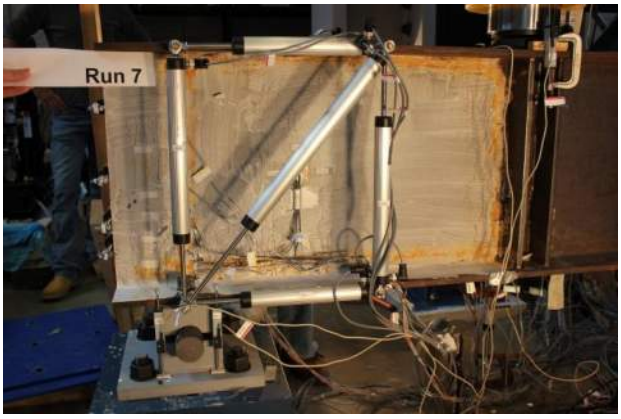

Figure B.1.7 Undamaged Girder Right: 160 kip

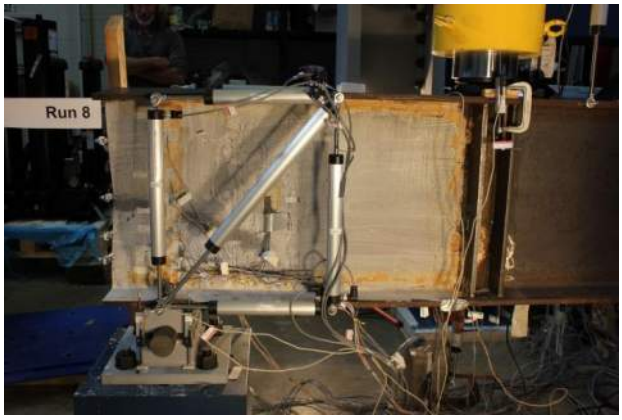

Figure B.1.8 Undamaged Girder Right: Failure

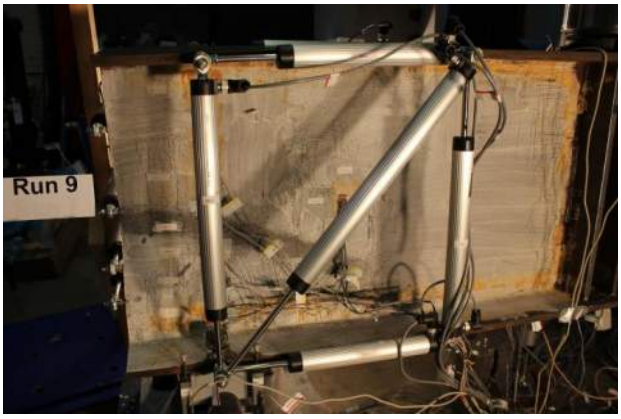

Figure B.1.9 Undamaged Girder Right: +0.25 in

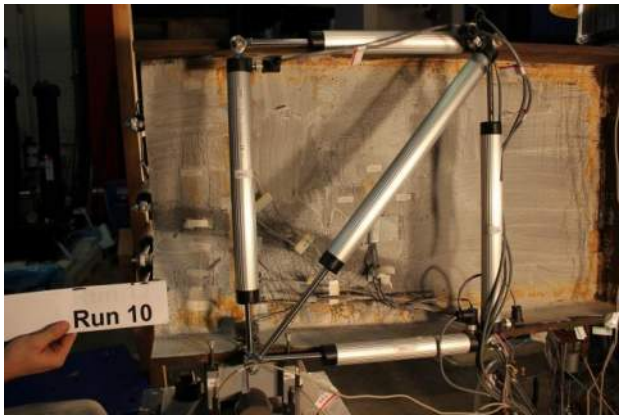

Figure B.1.10 Undamaged Girder Right: +0.50 in

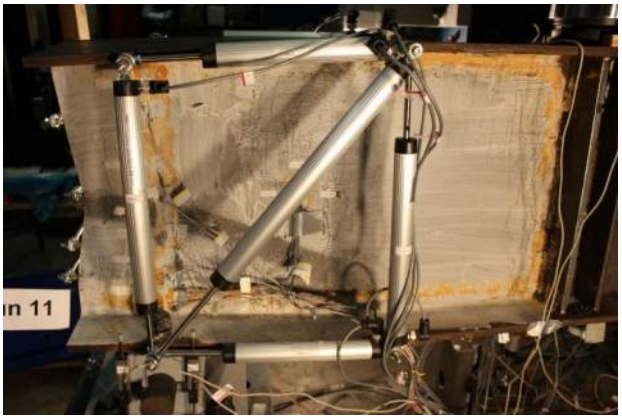

Figure B.1.11 Undamaged Girder Right: +0.75 in

Figure B.1.12 Undamaged Girder Right: Final

B.1.2 Undamaged - Left Side View

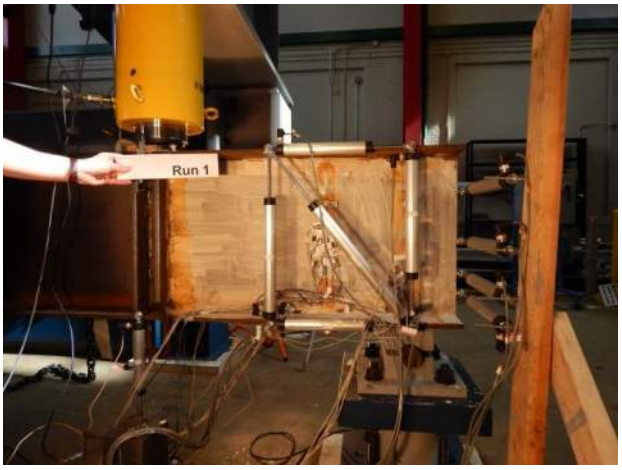

Figure B.1.13 Undamaged Girder Left: 40 kip

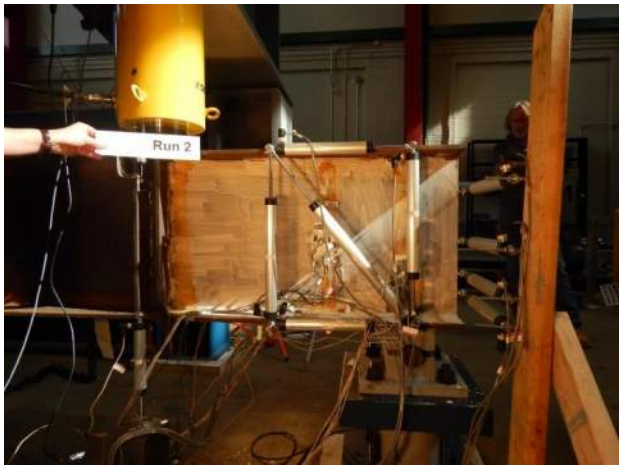

Figure B.1.14 Undamaged Girder Left: 60 kip

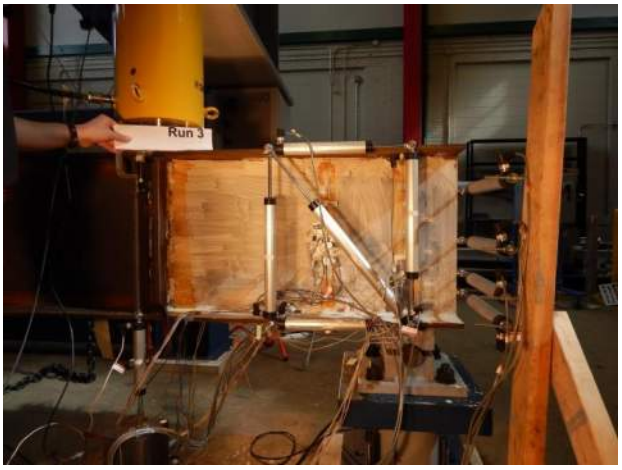

Figure B.1.15 Undamaged Girder Left: 80 kip

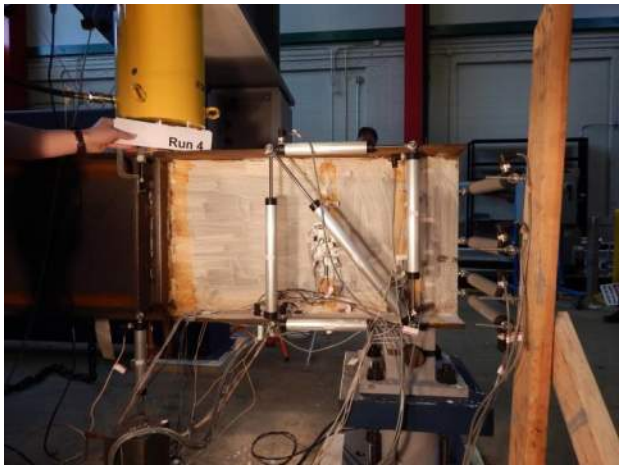

Figure B.1.16 Undamaged Girder Left: 100 kip

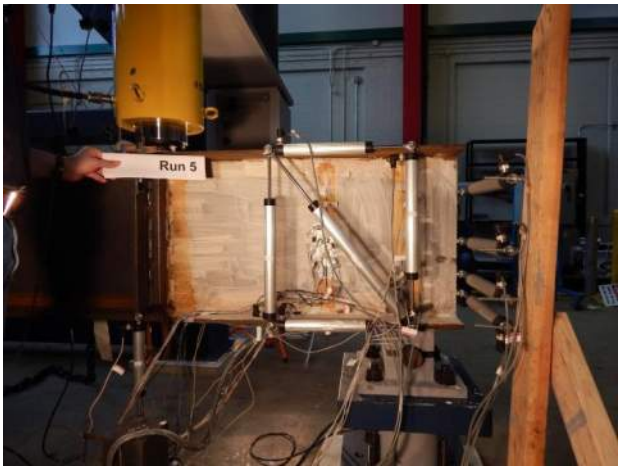

Figure B.1.17 Undamaged Girder Left: 120 kip

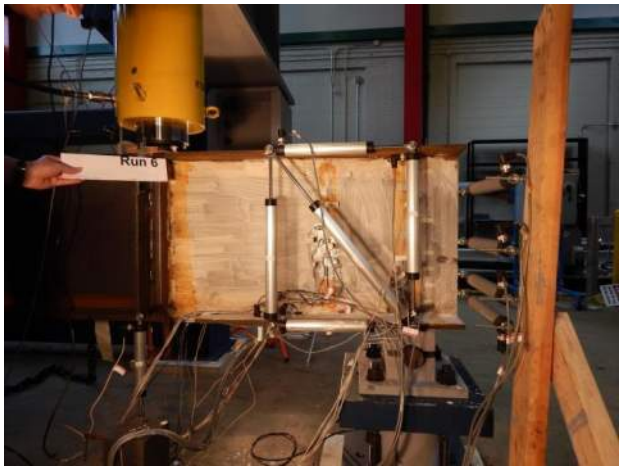

Figure B.1.18 Undamaged Girder Left: 140 kip

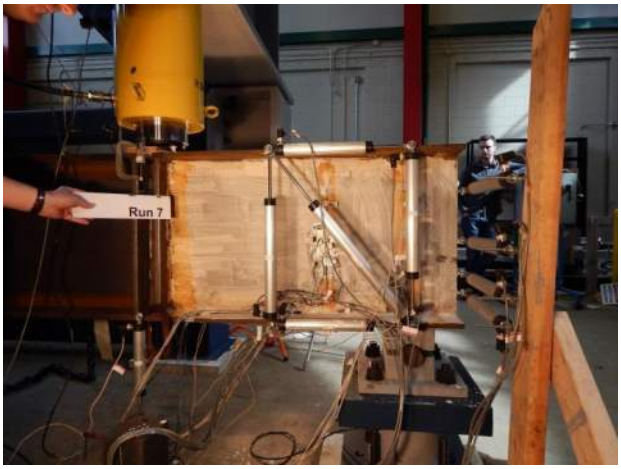

Figure B.1.19 Undamaged Girder Left: 160 kip

Figure B.1.20 Undamaged Girder Left: Failure

Figure B.1.21 Undamaged Girder Left: +0.25 in

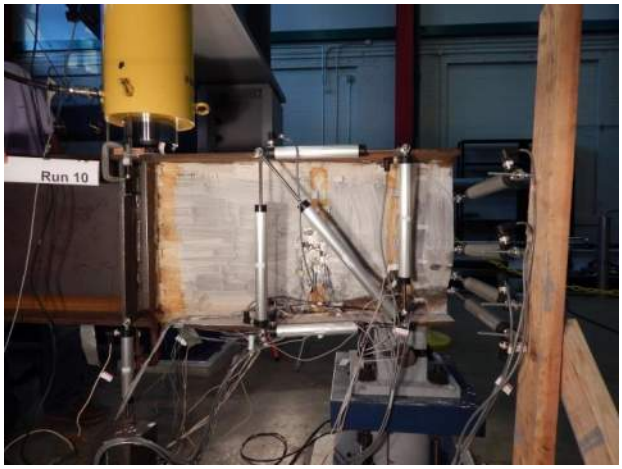

Figure B.1.22 Undamaged Girder Left: +0.50 in

Figure B.1.23 Undamaged Girder Left: +0.75 in

Figure B.1.24 Undamaged Girder Left: +1.25 in

B.1.3 Undamaged - Longitudinal View

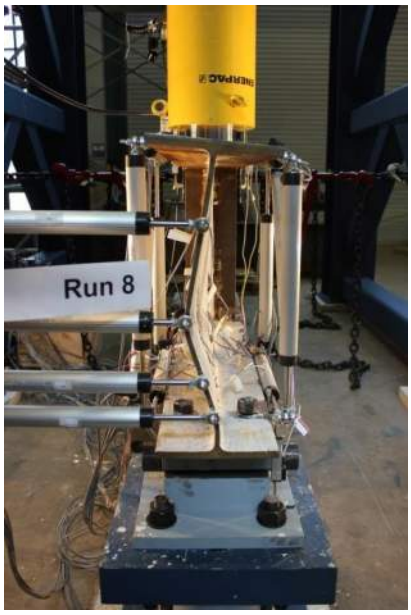

Figure B.1.25 Undamaged Girder Longitudinal: Failure with Load

Figure B.1.26 Undamaged Girder Longitudinal: +0.25 in with Load

Figure B.1.27 Undamaged Girder Longitudinal: +0.25 in without Load

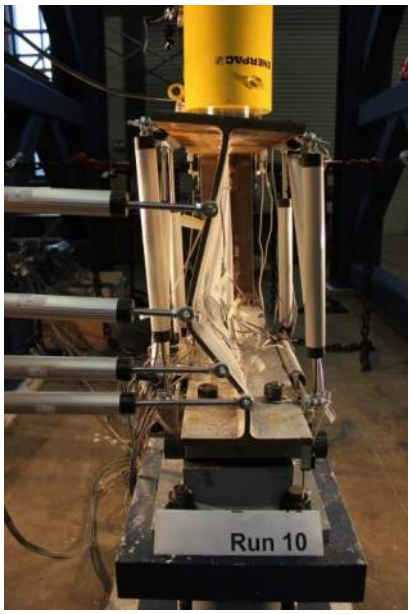

Figure B.1.28 Undamaged Girder Longitudinal: +0.50 in with Load

Figure B.1.29 Undamaged Girder Longitudinal: +0.50 in without Load

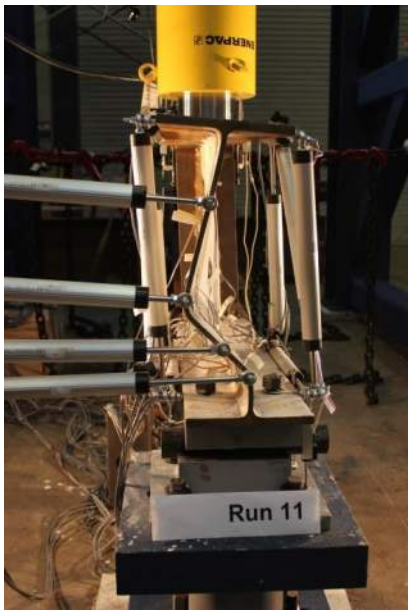

Figure B.1.30 Undamaged Girder Longitudinal: +0.75 in with Load

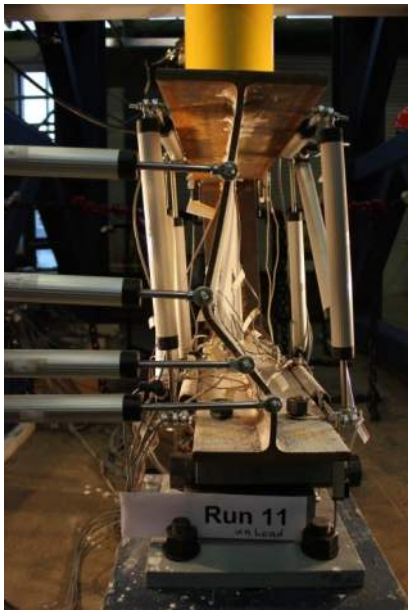

Figure B.1.31 Undamaged Girder Longitudinal: +0.75 in without Load

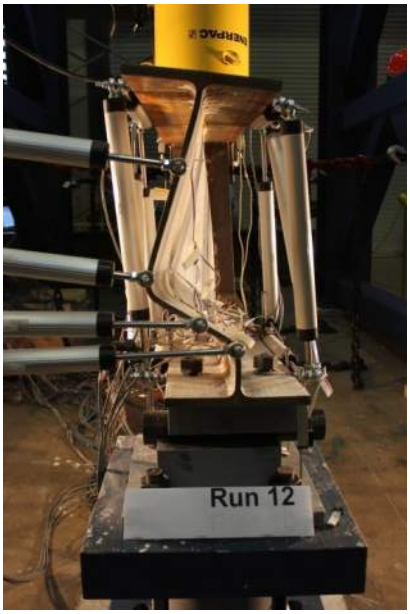

Figure B.1.32 Undamaged Girder Longitudinal: +1.25 in with Load

Figure B.1.33 Undamaged Girder Longitudinal: +1.25 in without Load

B.1.4 Undamaged - Bearing View

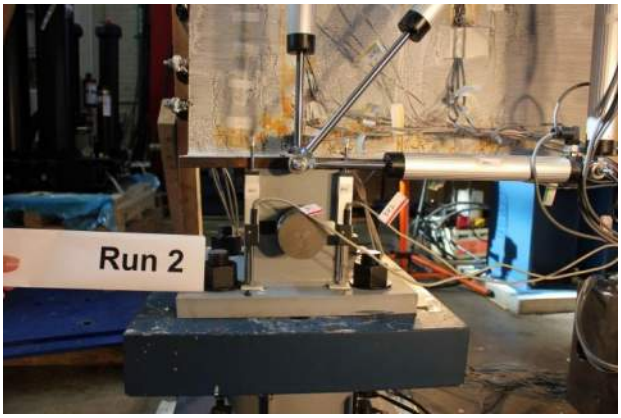

Figure B.1.34 Undamaged Bearing: 60 kip

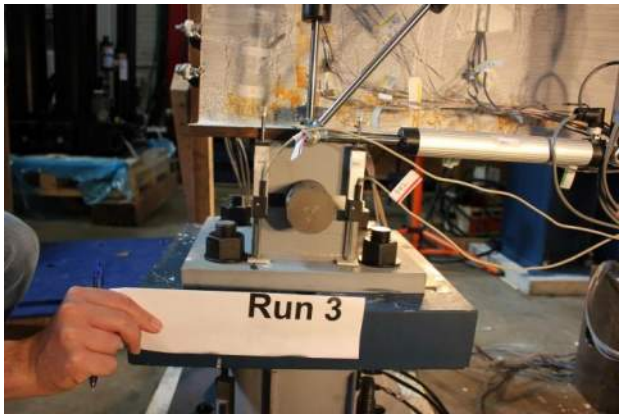

Figure B.1.35 Undamaged Bearing: 80 kip

Figure B.1.36 Undamaged Bearing: 100 kip

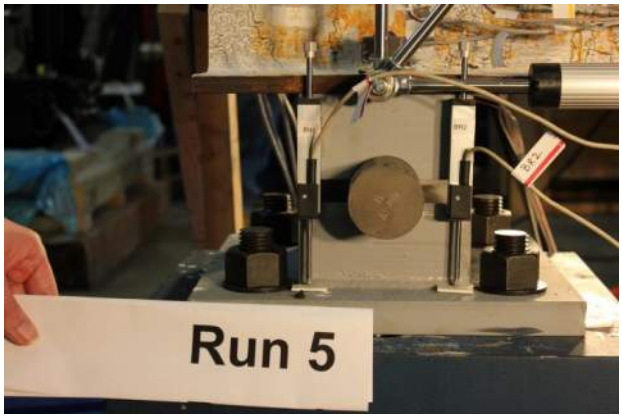

Figure B.1.37 Undamaged Bearing: 120 kip

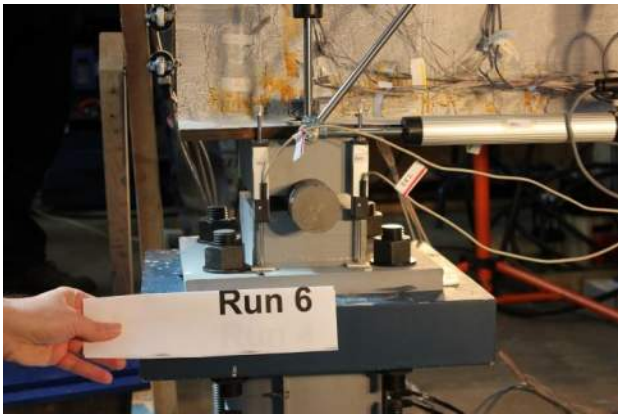

Figure B.1.38 Undamaged Bearing: 140 kip

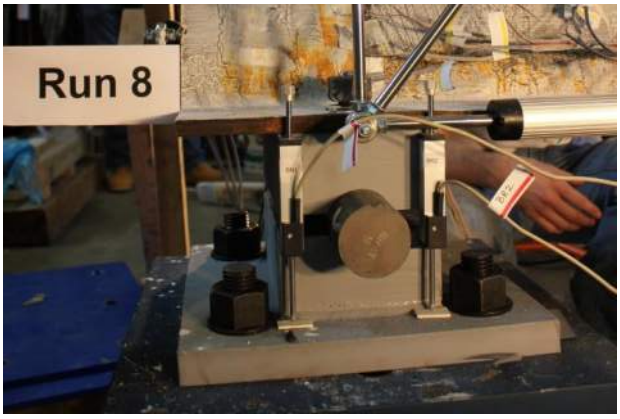

Figure B.1.39 Undamaged Bearing: Failure

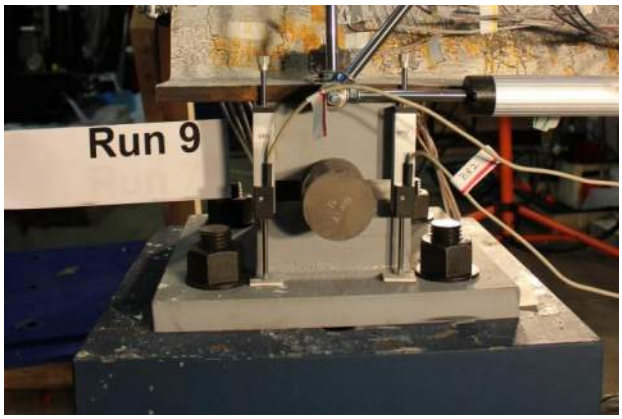

Figure B.1.40 Undamaged Bearing: +0.25 in

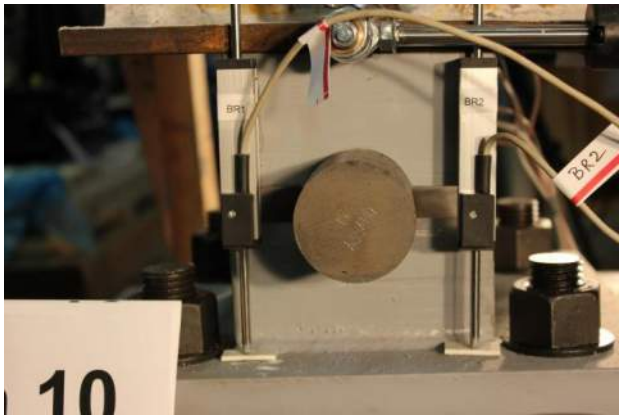

Figure B.1.41 Undamaged Bearing: +0.50 in

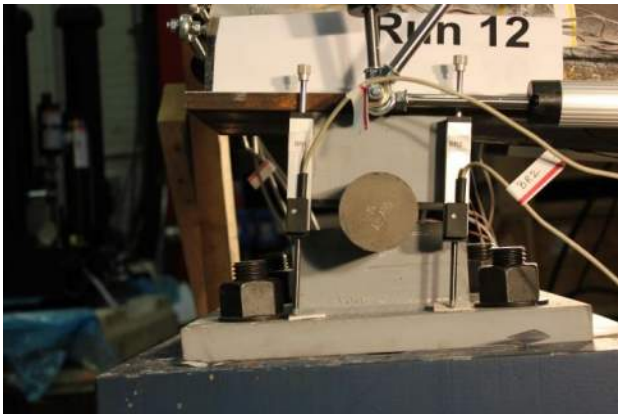

Figure B.1.42 Undamaged Bearing: +1.25 in

B.2 DAMAGED GIRDER

B.2.1 Damaged - Right Side View

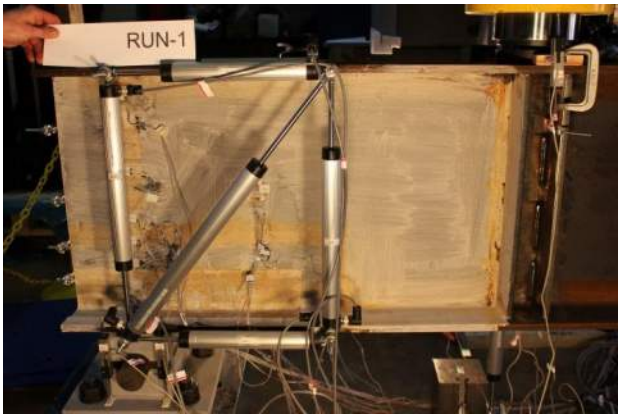

Figure B.2.1 Damaged Girder Right: 8 kip

Figure B.2.2 Damaged Girder Right: 16 kip

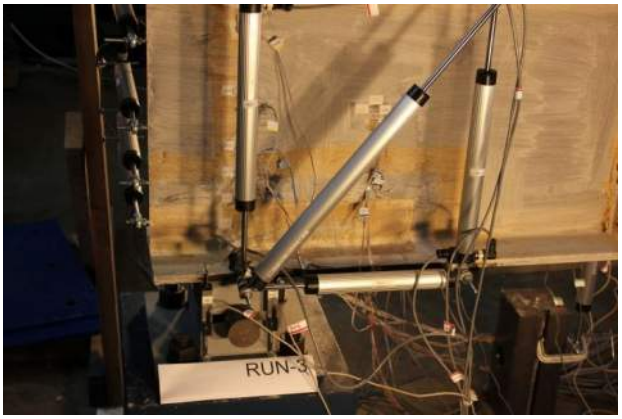

Figure B.2.3 Damaged Girder Right: 24 kip

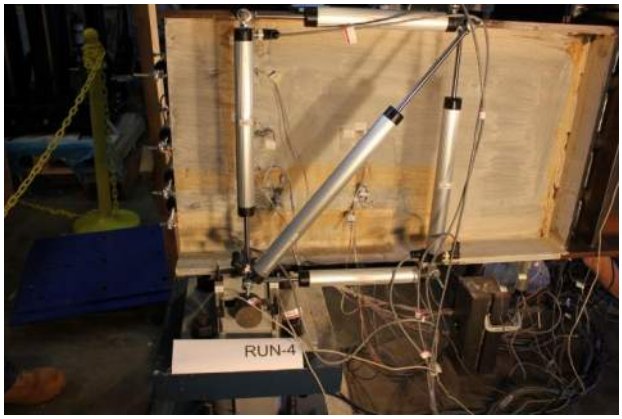

Figure B.2.4 Damaged Girder Right: 32 kip

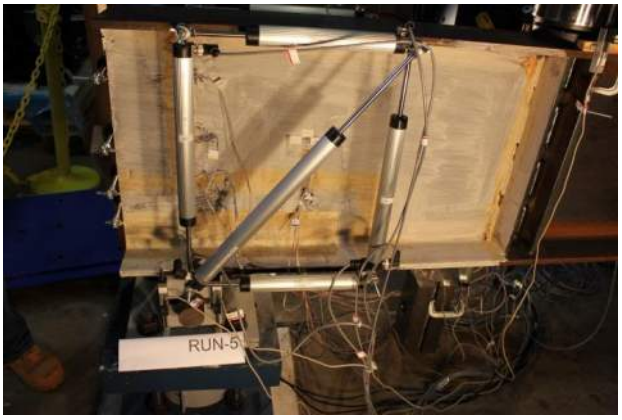

Figure B.2.5 Damaged Girder Right: 40 kip

Figure B.2.6 Damaged Girder Right: Failure

Figure B.2.7 Damaged Girder Right: +0.25 in

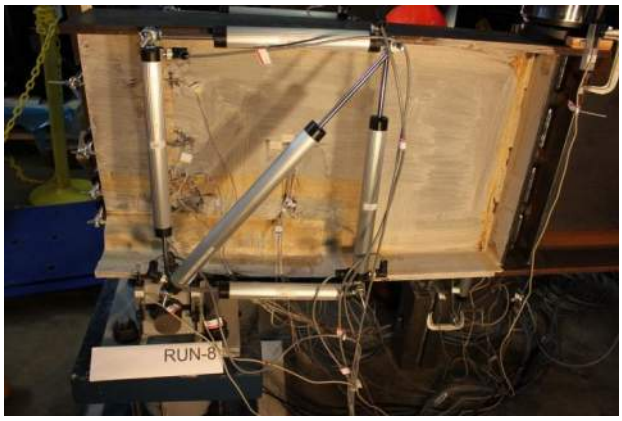

Figure B.2.8 Damaged Girder Right: +0.50 in

Figure B.2.9 Damaged Girder Right: +0.75 in

Figure B.2.10 Damaged Girder Right: +1.00 in

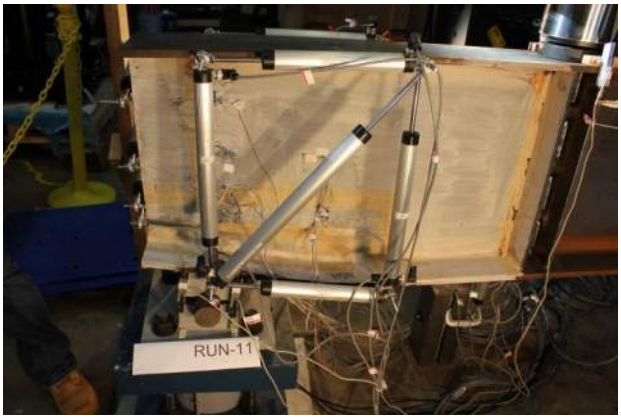

Figure B.2.11 Damaged Girder Right: +1.50 in

B.2.2 Damaged - Left Side View

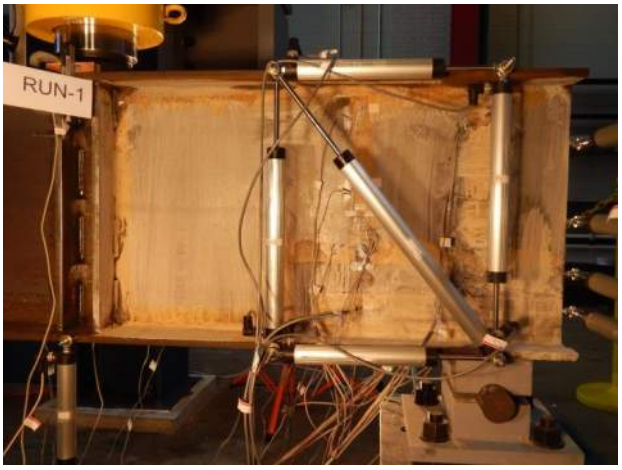

Figure B.2.12 Damaged Girder Left: 8 kip

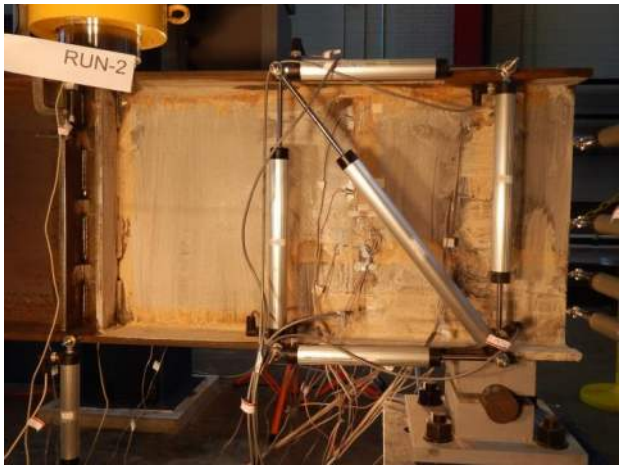

Figure B.2.13 Damaged Girder Left: 16 kip

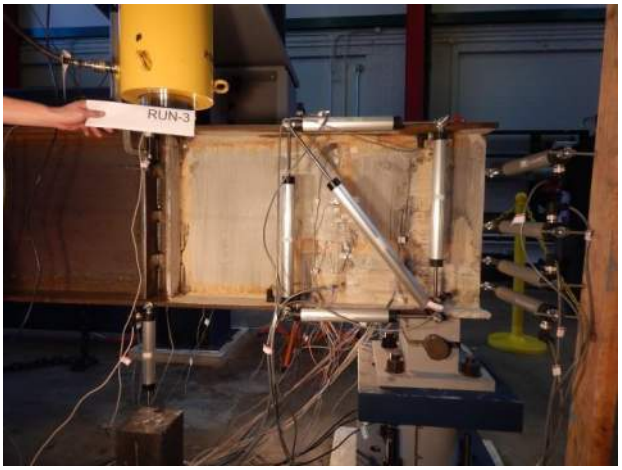

Figure B.2.14 Damaged Girder Left: 24 kip

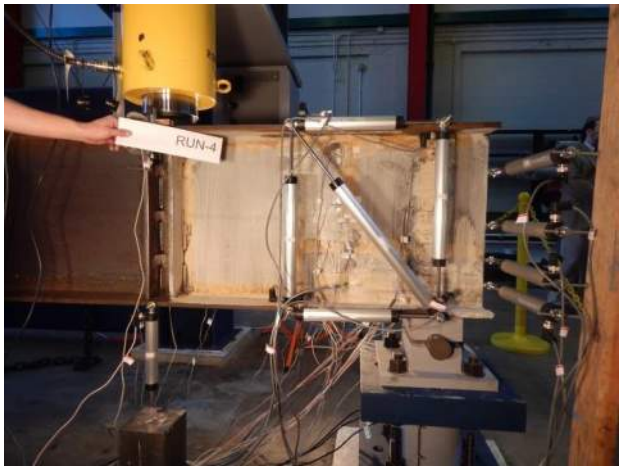

Figure B.2.15 Damaged Girder Left: 32 kip

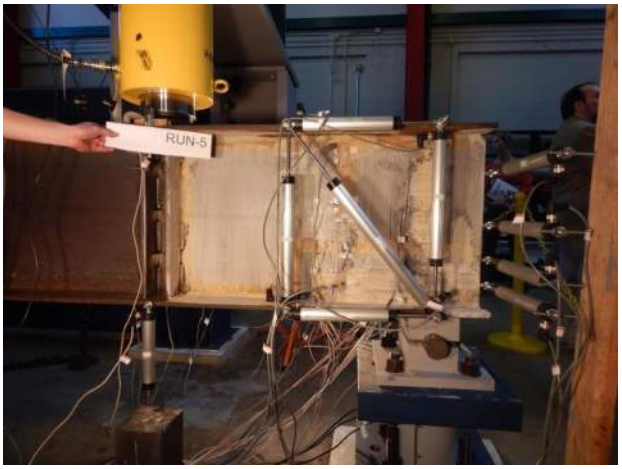

Figure B.2.16 Damaged Girder Left: 40 kip

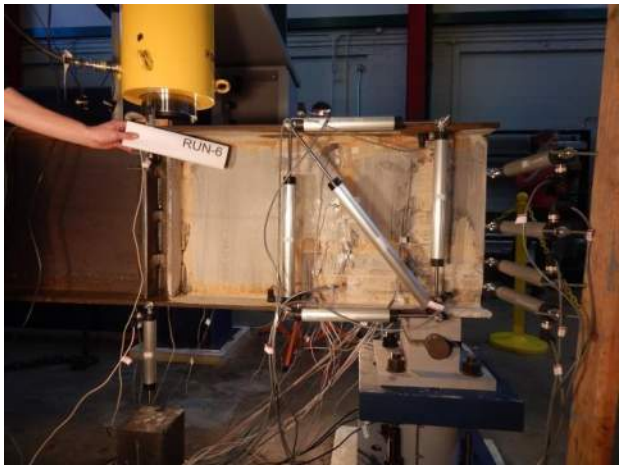

Figure B.2.17 Damaged Girder Left: Failure

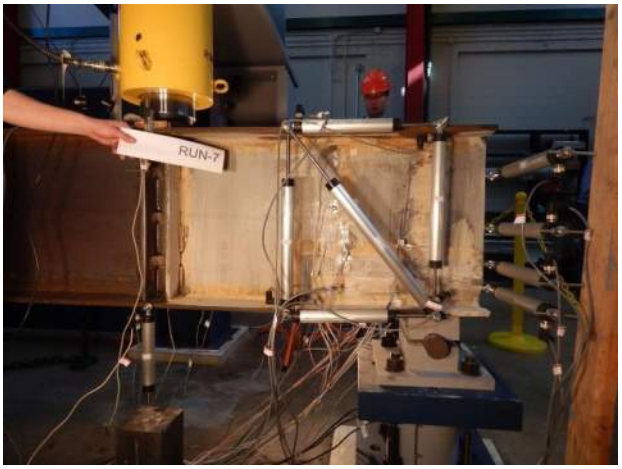

Figure B.2.18 Damaged Girder Left: +0.25 in

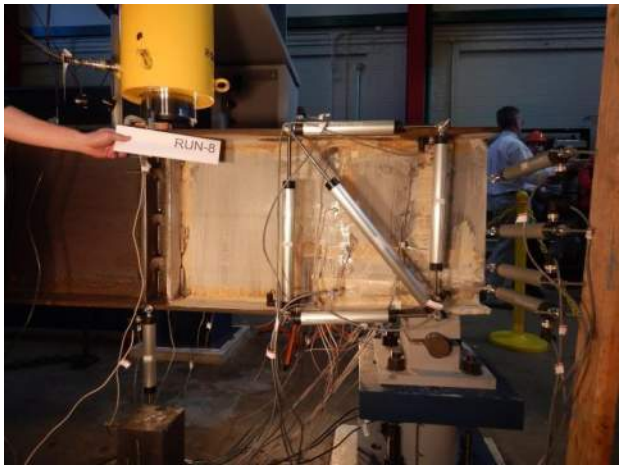

Figure B.2.19 Damaged Girder Left: +0.50 in

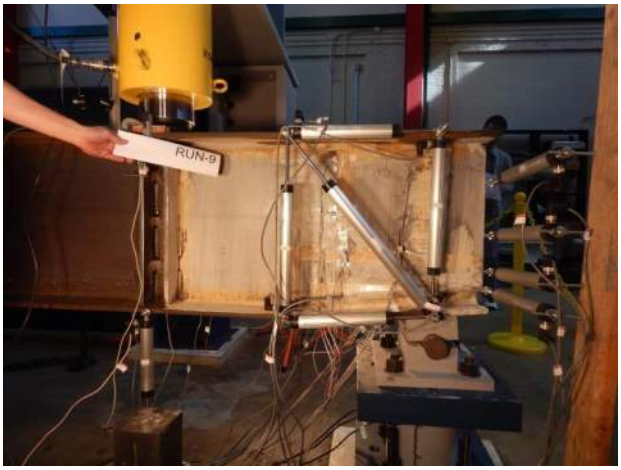

Figure B.2.20 Damaged Girder Left: +0.75 in

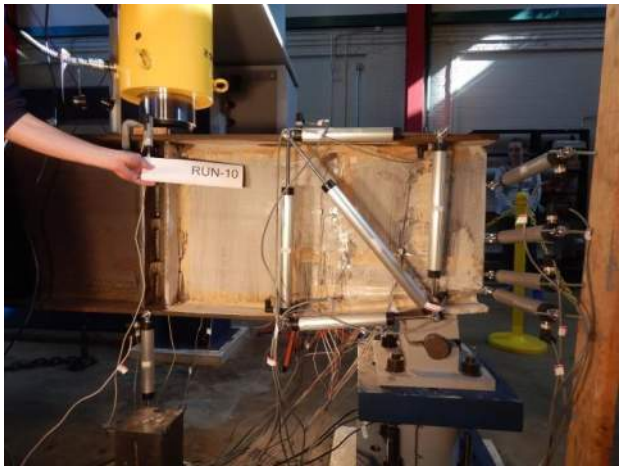

Figure B.2.21 Damaged Girder Left: +1.00 in

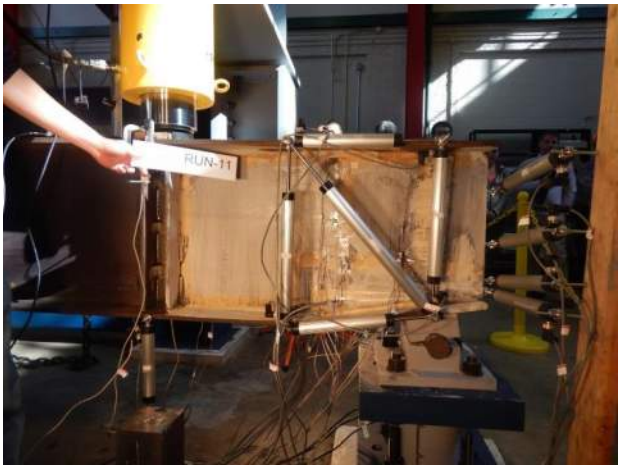

Figure B.2.22 Damaged Girder Left: +1.50 in

B.2.3 Damaged - Longitudinal View

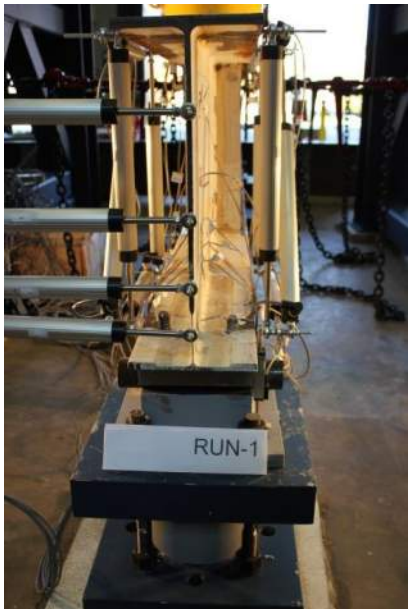

Figure B.2.23 Damaged Girder Longitudinal View: 8 kip

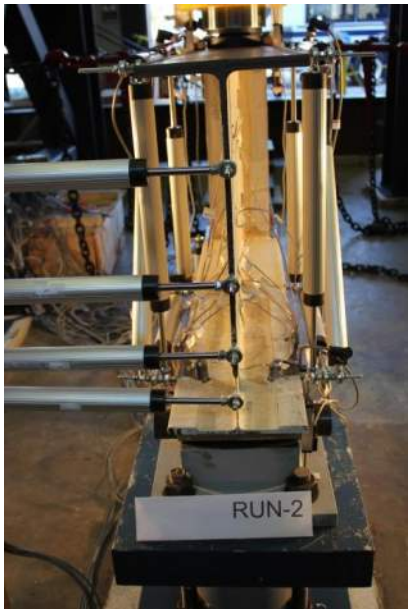

Figure B.2.24 Damaged Girder Longitudinal View: 16 kip

Figure B.2.25 Damaged Girder Longitudinal View: 24 kip

Figure B.2.26 Damaged Girder Longitudinal View: 32 kip

Figure B.2.27 Damaged Girder Longitudinal View: 40 kip

Figure B.2.28 Damaged Girder Longitudinal View: Failure

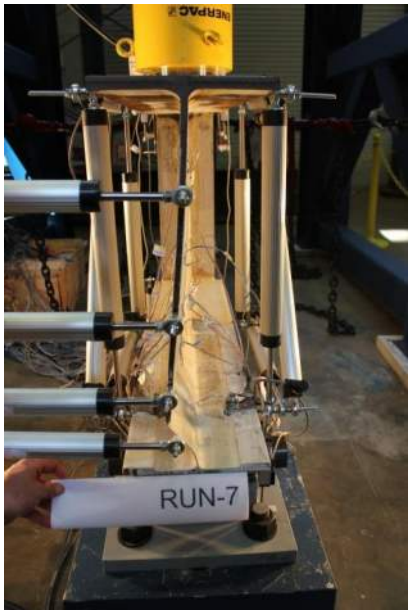

Figure B.2.29 Damaged Girder Longitudinal View: +0.25 in

Figure B.2.30 Damaged Girder Longitudinal View: +0.50 in

Figure B.2.31 Damaged Girder Longitudinal View: +0.75 in

Figure B.2.32 Damaged Girder Longitudinal View: +1.00 in

Figure B.2.33 Damaged Girder Longitudinal View: +1.50 in

B.2.4 Damaged - Bearing View

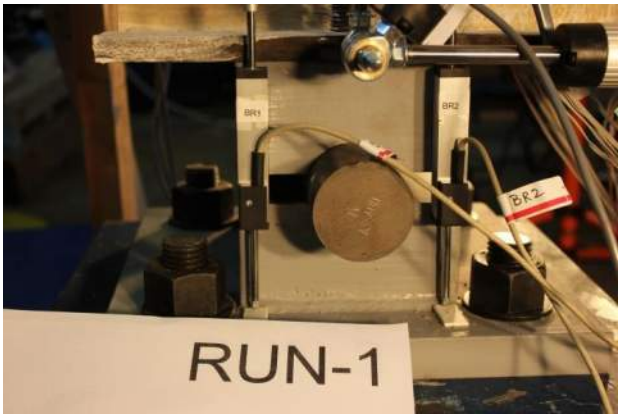

Figure B.2.34 Damaged Girder Bearing: 8 kip

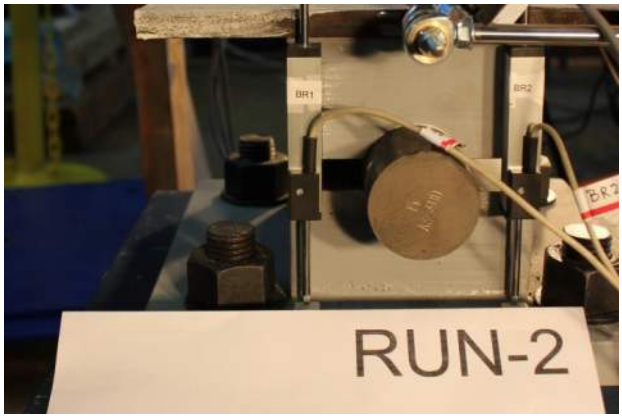

Figure B.2.35 Damaged Girder Bearing: 16 kip

Figure B.2.36 Damaged Girder Bearing: 24 kip

Figure B.2.37 Damaged Girder Bearing: 32 kip

Figure B.2.38 Damaged Girder Bearing: 40 kip

Figure B.2.39 Damaged Girder Bearing: Failure

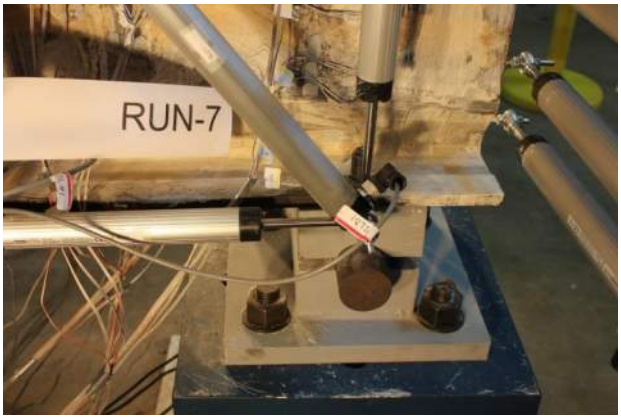

Figure B.2.40 Damaged Girder Bearing: +0.25 in

Figure B.2.41 Damaged Girder Bearing: +0.50 in

Figure B.2.42 Damaged Girder Bearing: +0.75 in

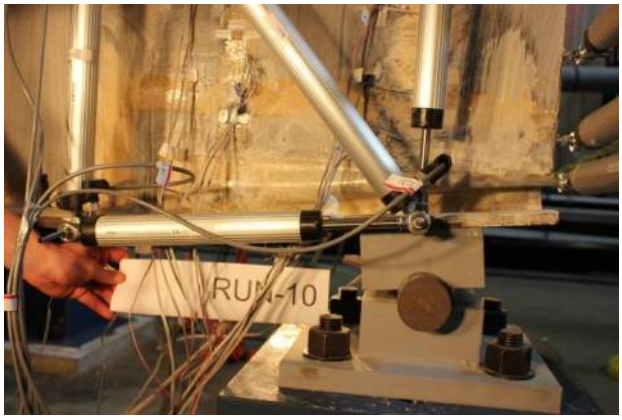

Figure B.2.43 Damaged Girder Bearing: +1.00 in

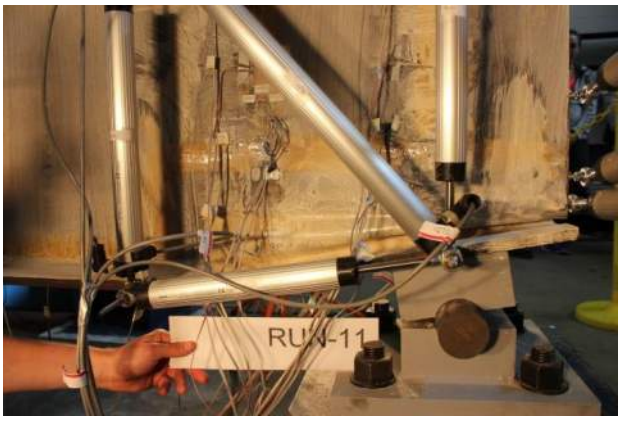

Figure B.2.44 Damaged Girder Bearing: +1.50 in

B.3 REPAIRED GIRDER

B.3.1 Repaired - Right Side View

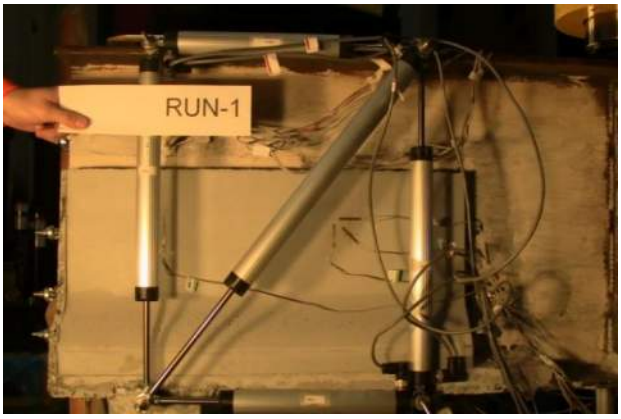

Figure B.3.1 Repaired Girder Right: 12 kip

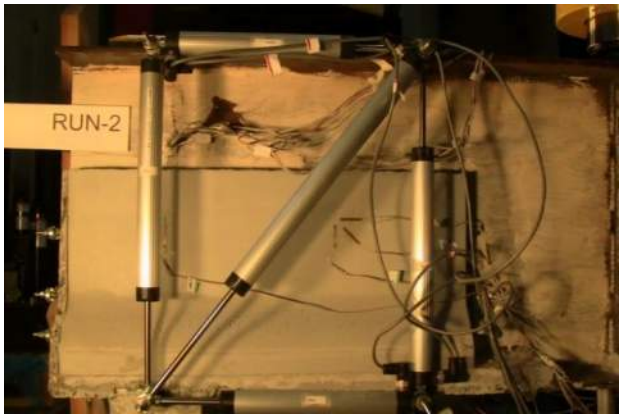

Figure B.3.2 Repaired Girder Right: 24 kip

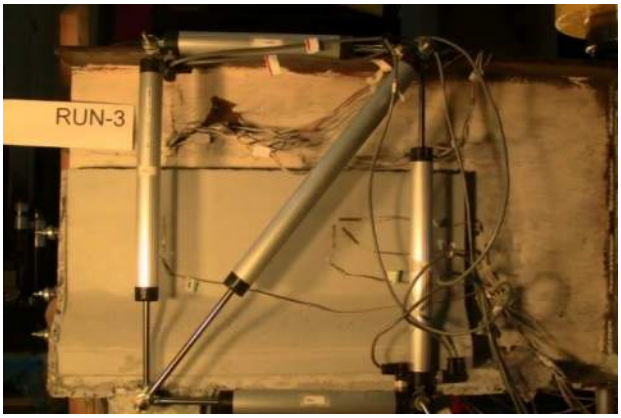

Figure B.3.3 Repaired Girder Right: 36 kip

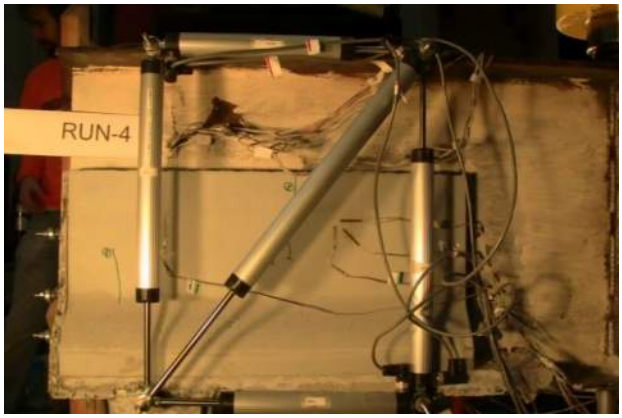

Figure B.3.4 Repaired Girder Right: 48 kip

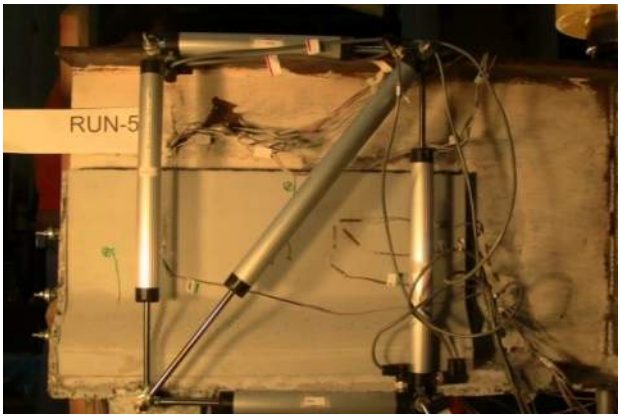

Figure B.3.5 Repaired Girder Right: 60 kip

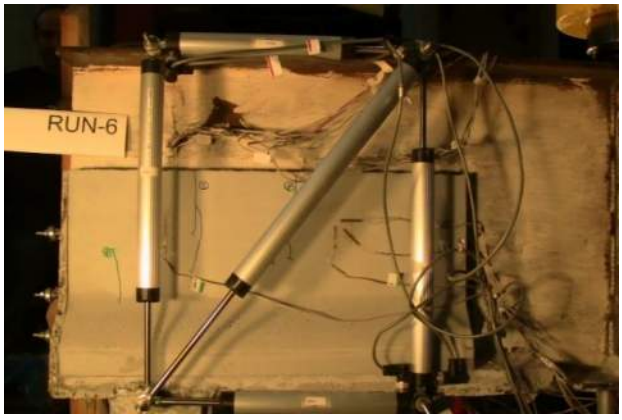

Figure B.3.6 Repaired Girder Right: 72 kip

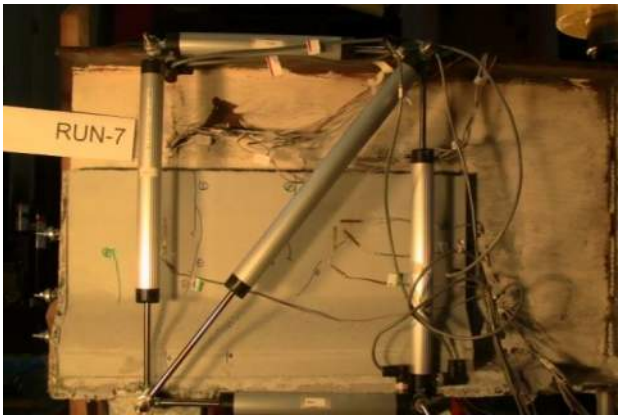

Figure B.3.7 Repaired Girder Right: 84 kip

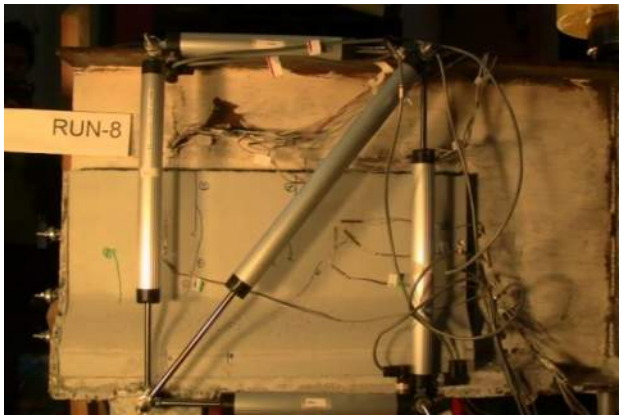

Figure B.3.8 Repaired Girder Right: 96 kip

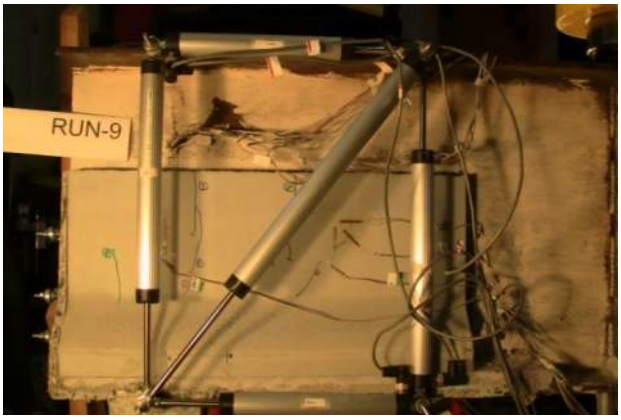

Figure B.3.9 Repaired Girder Right: 108 kip

Figure B.3.10 Repaired Girder Right: 120 kip

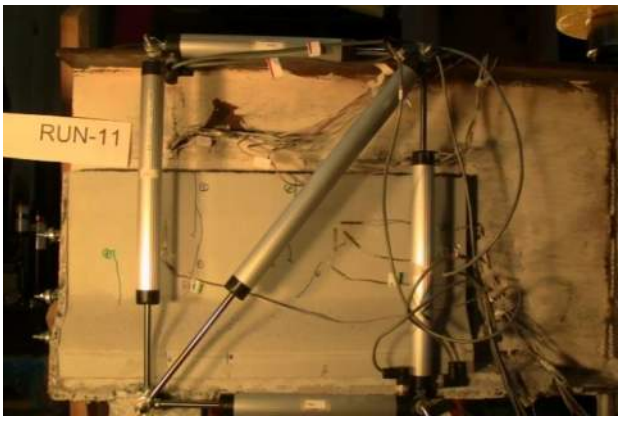

Figure B.3.11 Repaired Girder Right: 140 kip

Figure B.3.12 Repaired Girder Right: 160 kip

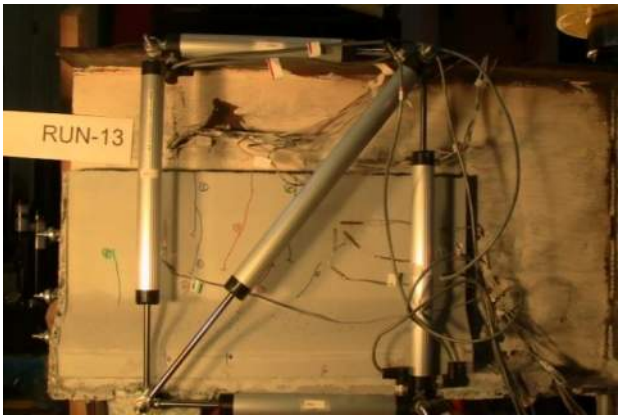

Figure B.3.13 Repaired Girder Right: 180 kip

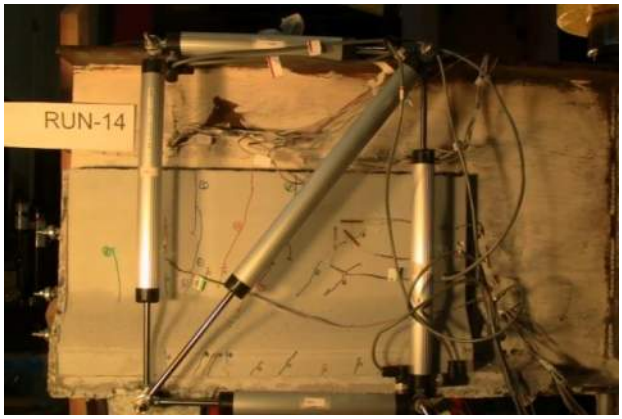

Figure B.3.14 Repaired Girder Right: 200 kip

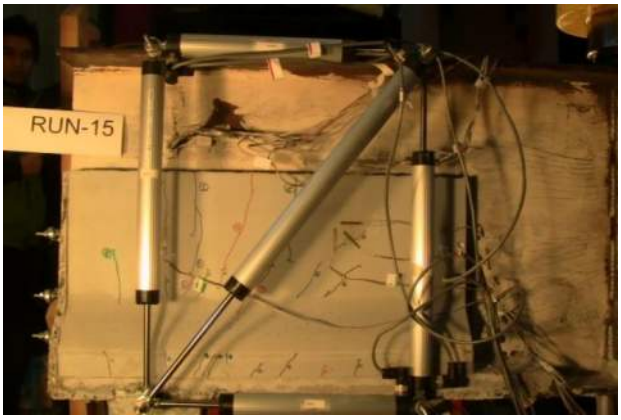

Figure B.3.15 Repaired Girder Right: 220 kip

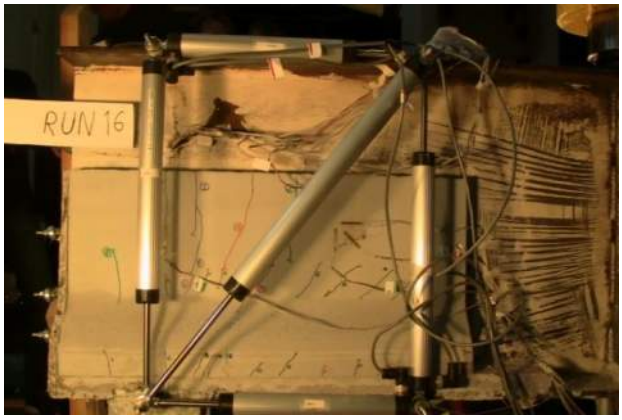

Figure B.3.16 Repaired Girder Right: 230 kip

B.3.2 Repaired - Left Side View

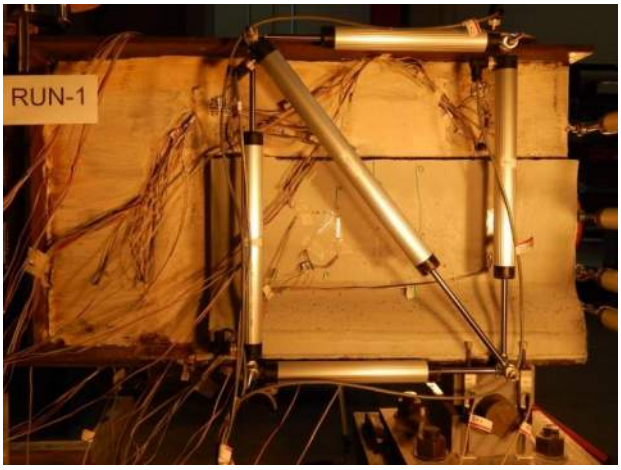

Figure B.3.17 Repaired Girder Left: 12 kip

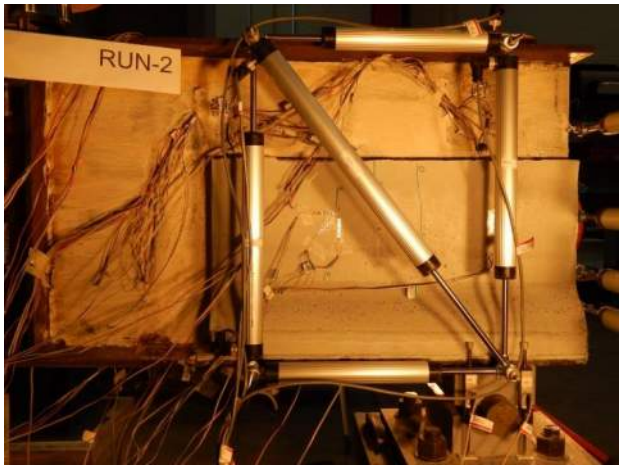

Figure B.3.18 Repaired Girder Left: 24 kip

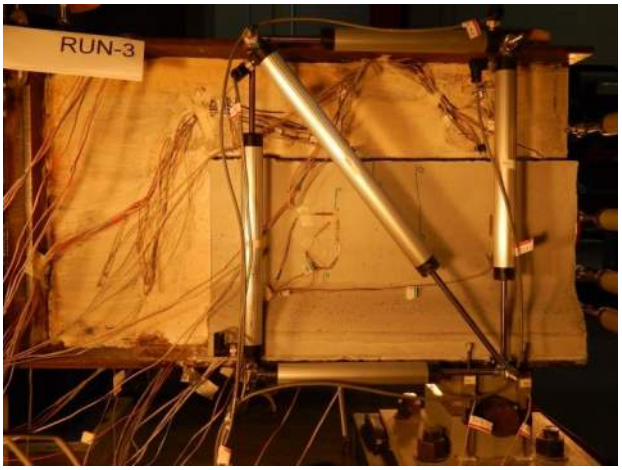

Figure B.3.19 Repaired Girder Left: 36 kip

Figure B.3.20 Repaired Girder Left: 48 kip

Figure B.3.21 Repaired Girder Left: 60 kip

Figure B.3.22 Repaired Girder Left: 72 kip

Figure B.3.23 Repaired Girder Left: 84 kip

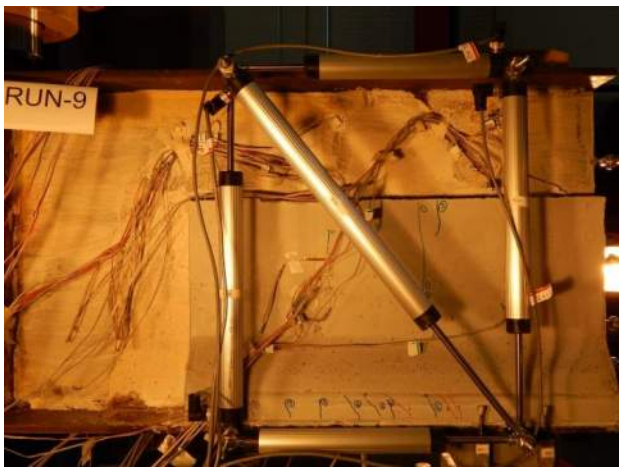

Figure B.3.24 Repaired Girder Left: 108 kip

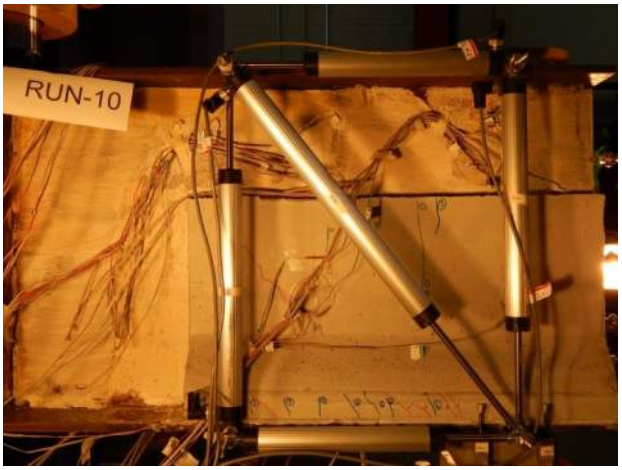

Figure B.3.25 Repaired Girder Left: 120 kip

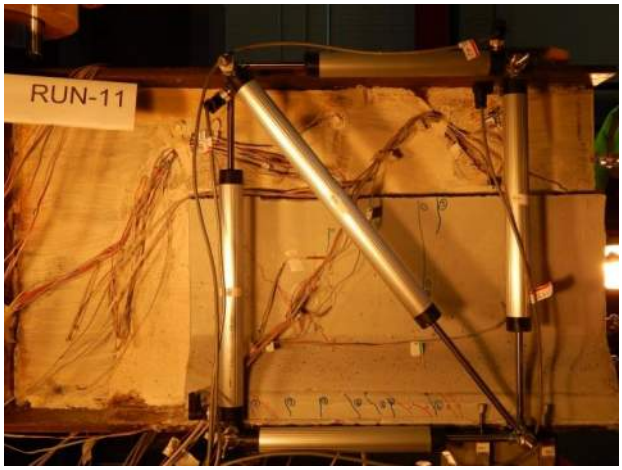

Figure B.3.26 Repaired Girder Left: 140 kip

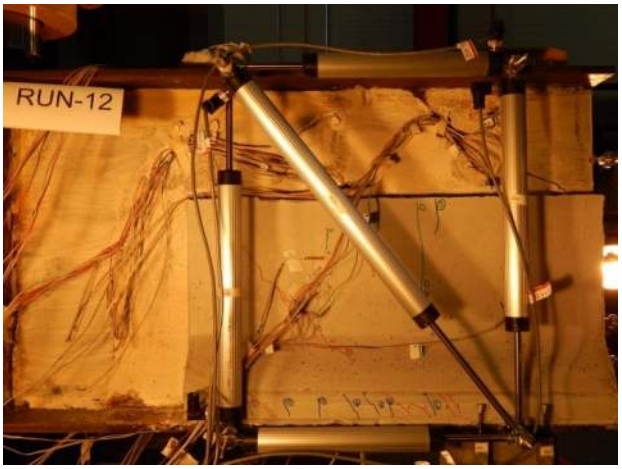

Figure B.3.27 Repaired Girder Left: 160 kip

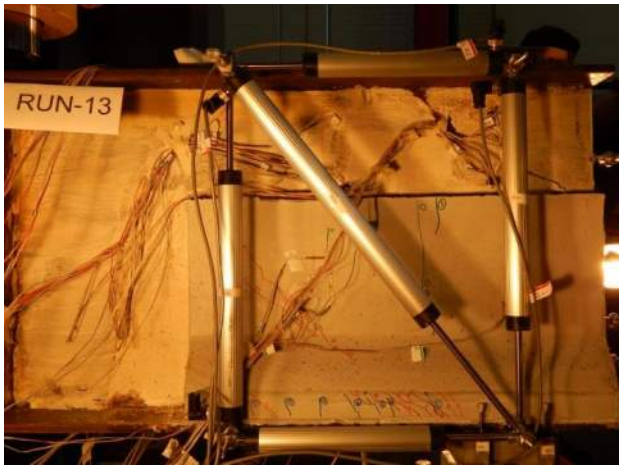

Figure B.3.28 Repaired Girder Left: 180 kip

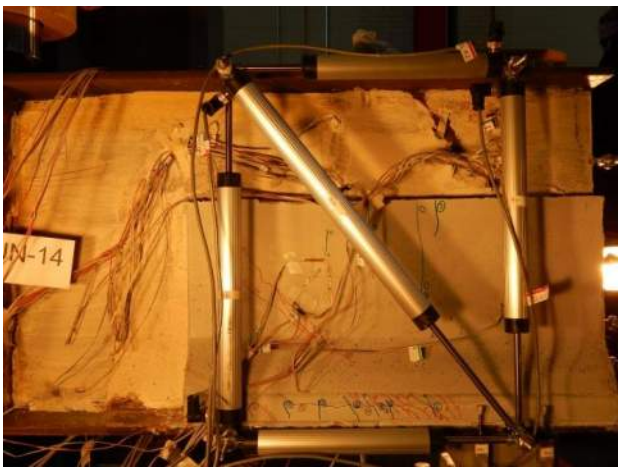

Figure B.3.29 Repaired Girder Left: 200 kip

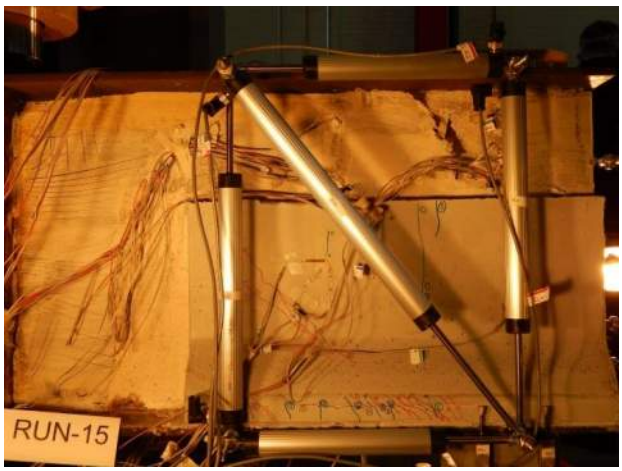

Figure B.3.30 Repaired Girder Left: 220 kip

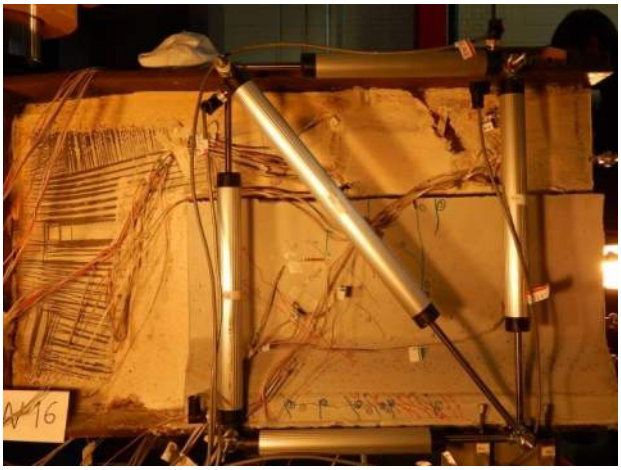

Figure B.3.31 Repaired Girder Left: 230 kip

Appendix C. Data from Large-Scale Tests

C.1 UNDAMAGED GIRDER

C.1.1 Force Data

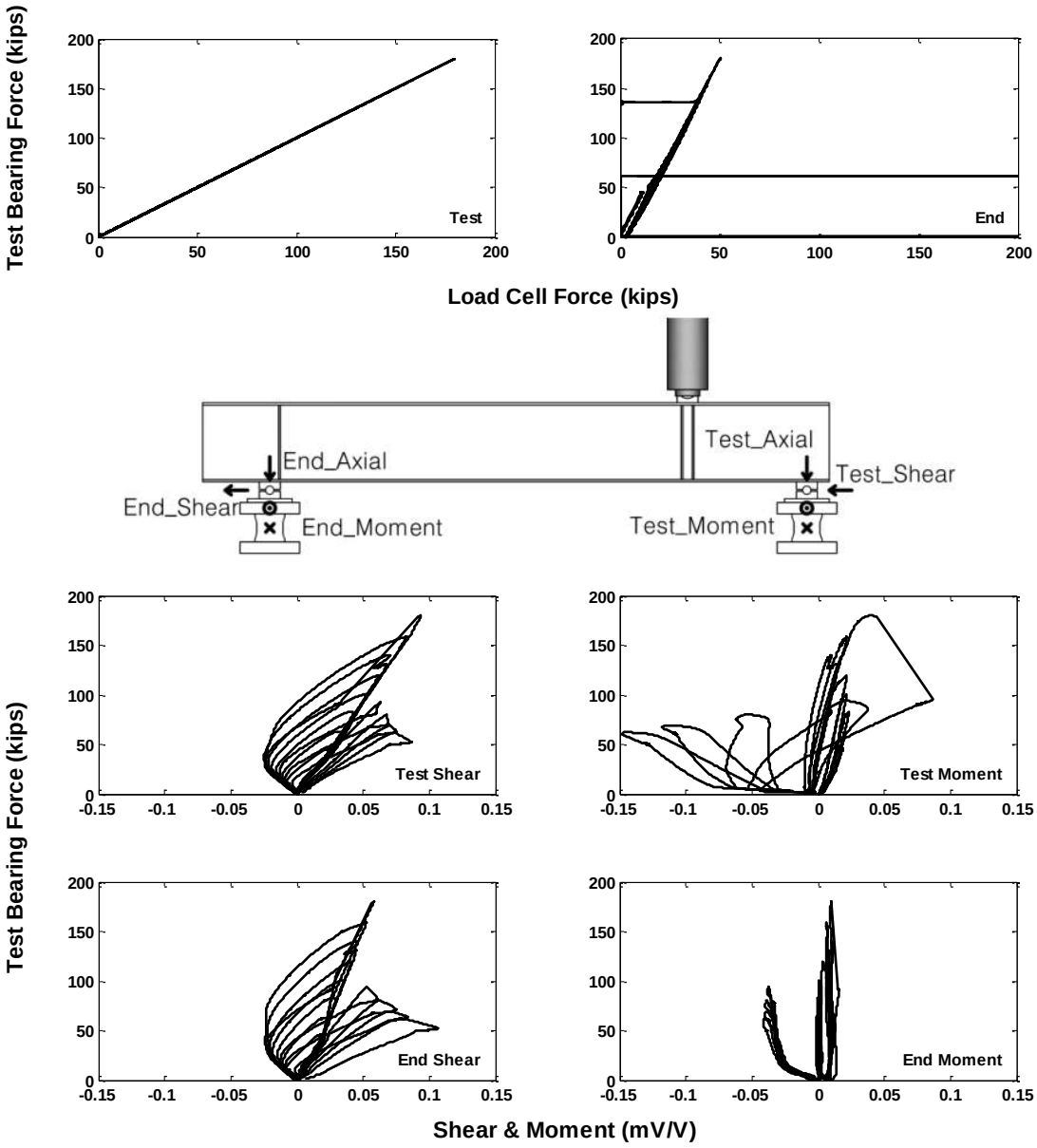

Figure C.1.1 Undamaged Girder Load Cell Axial Force and Shear/Moment mV/V Readings

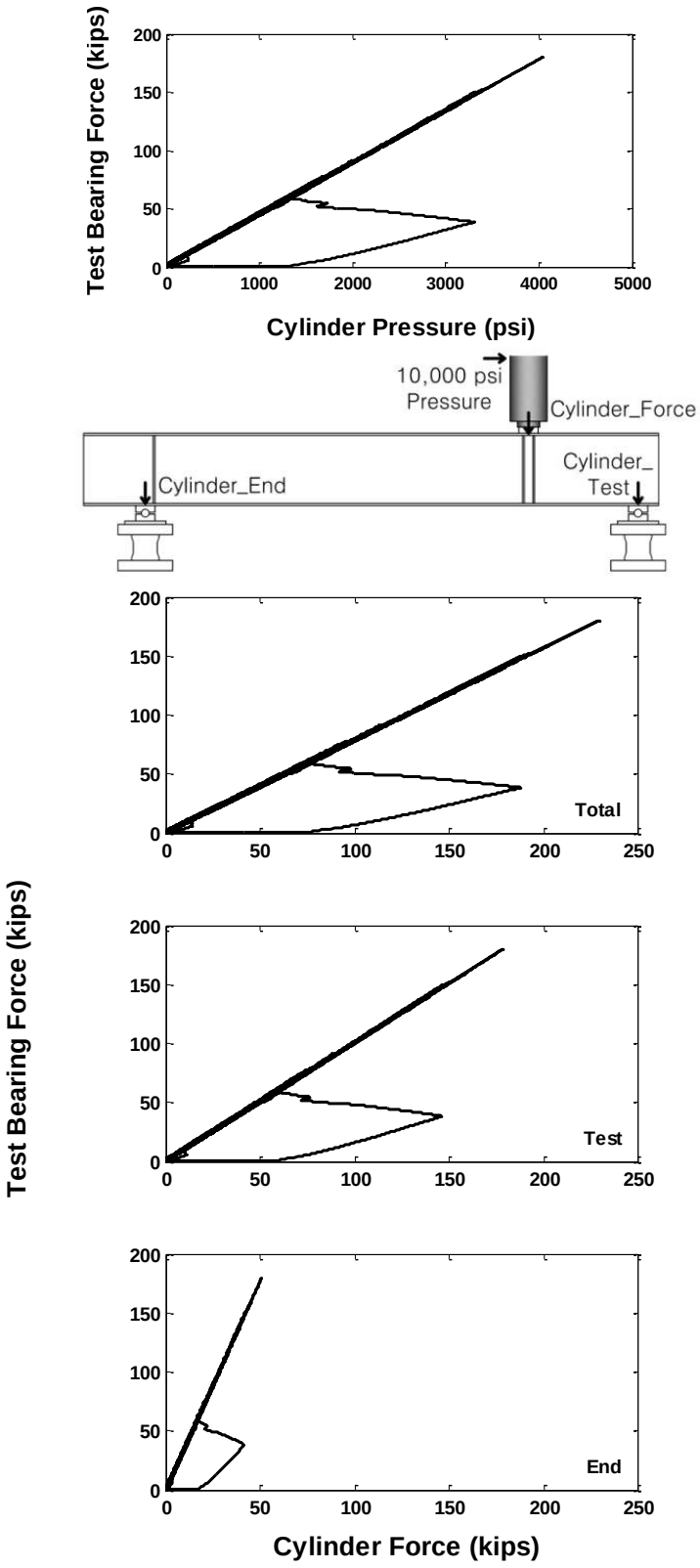

Figure C.1.2 Undamaged Cylinder Pressure and Converted Force Readings

C.1.2 Displacement Data

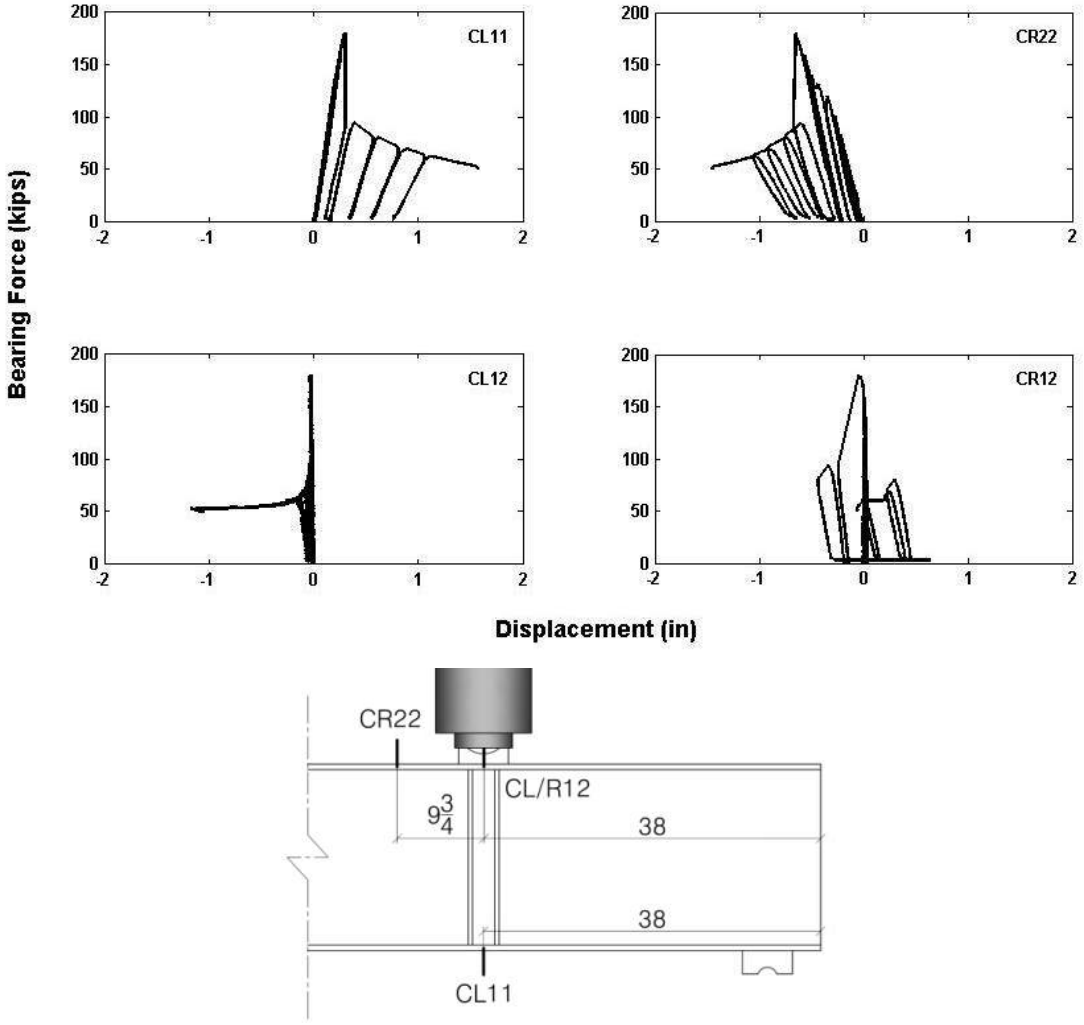

Figure C.1.3 Undamaged Girder Vertical Displacements at the Loading Point

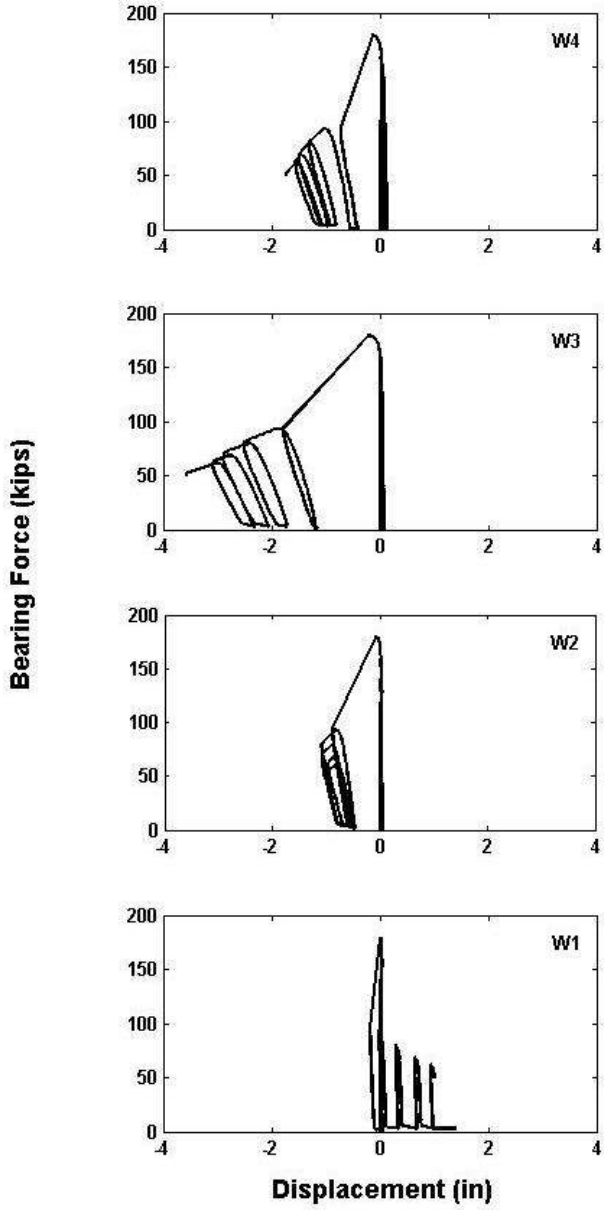

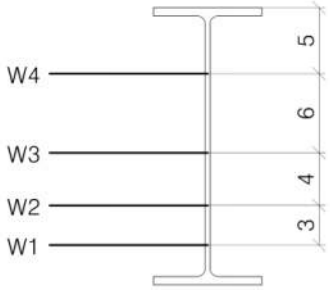

Figure C.1.4 Undamaged Girder Lateral Web Displacements

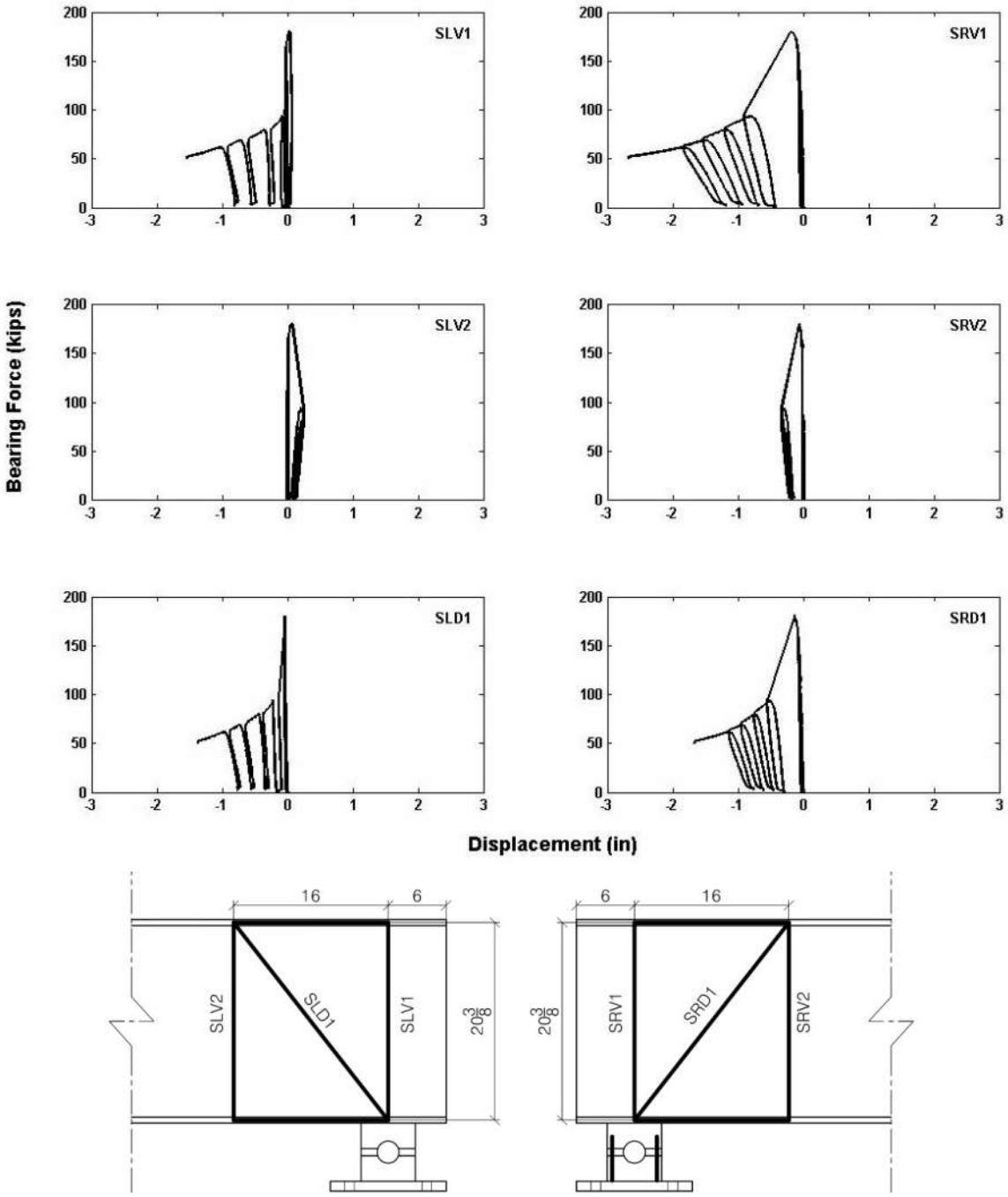

Figure C.1.5 Undamaged Girder Shear Box Potentiometer Displacements: Vertical and Diagonal

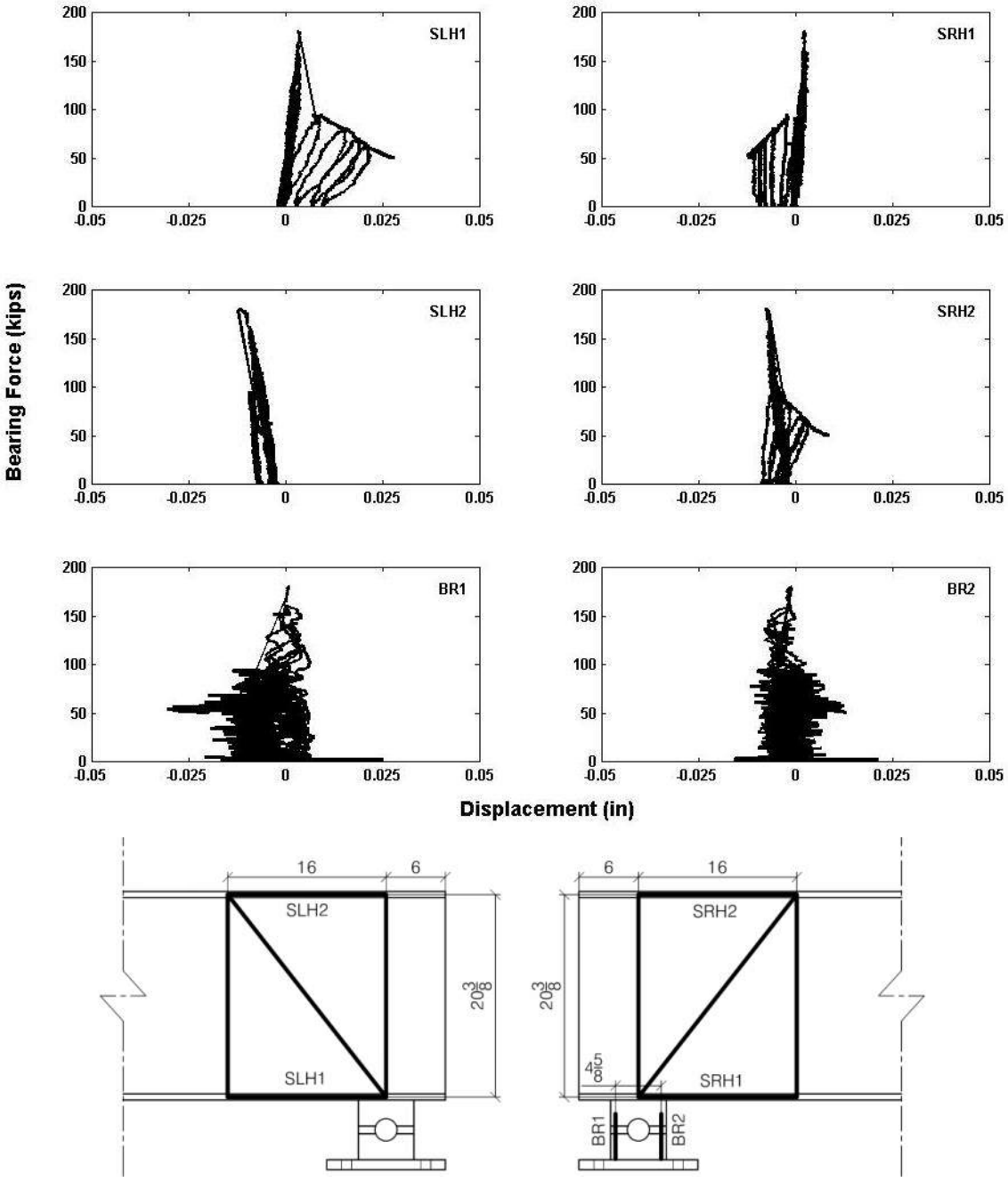

Figure C.1.6 Undamaged Shear Box Potentiometer Displacements, Horizontal and Bearing

C.1.3 Strain Data

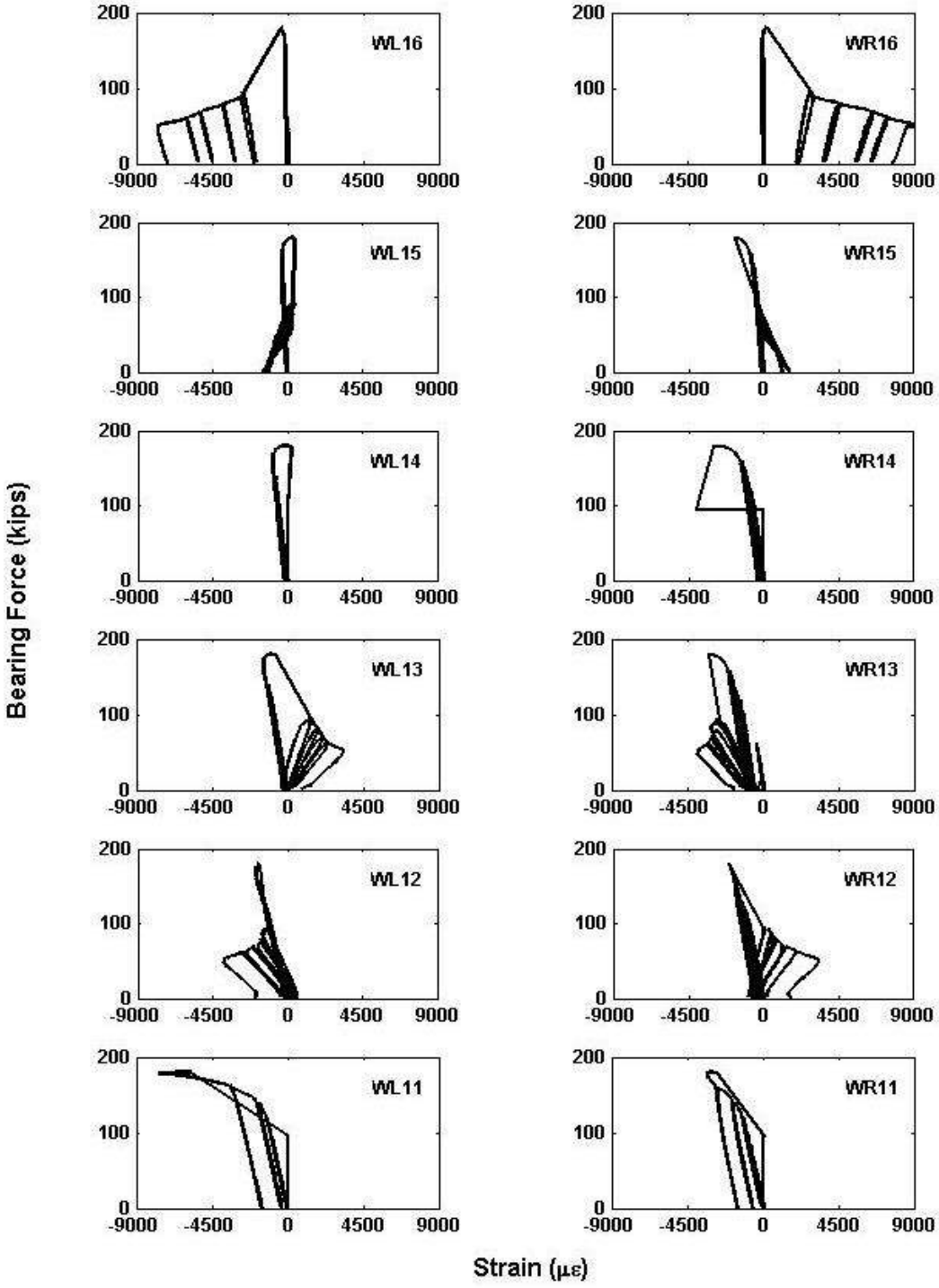

Figure C.1.7 Undamaged Girder WL/R1x Axial Web Strains

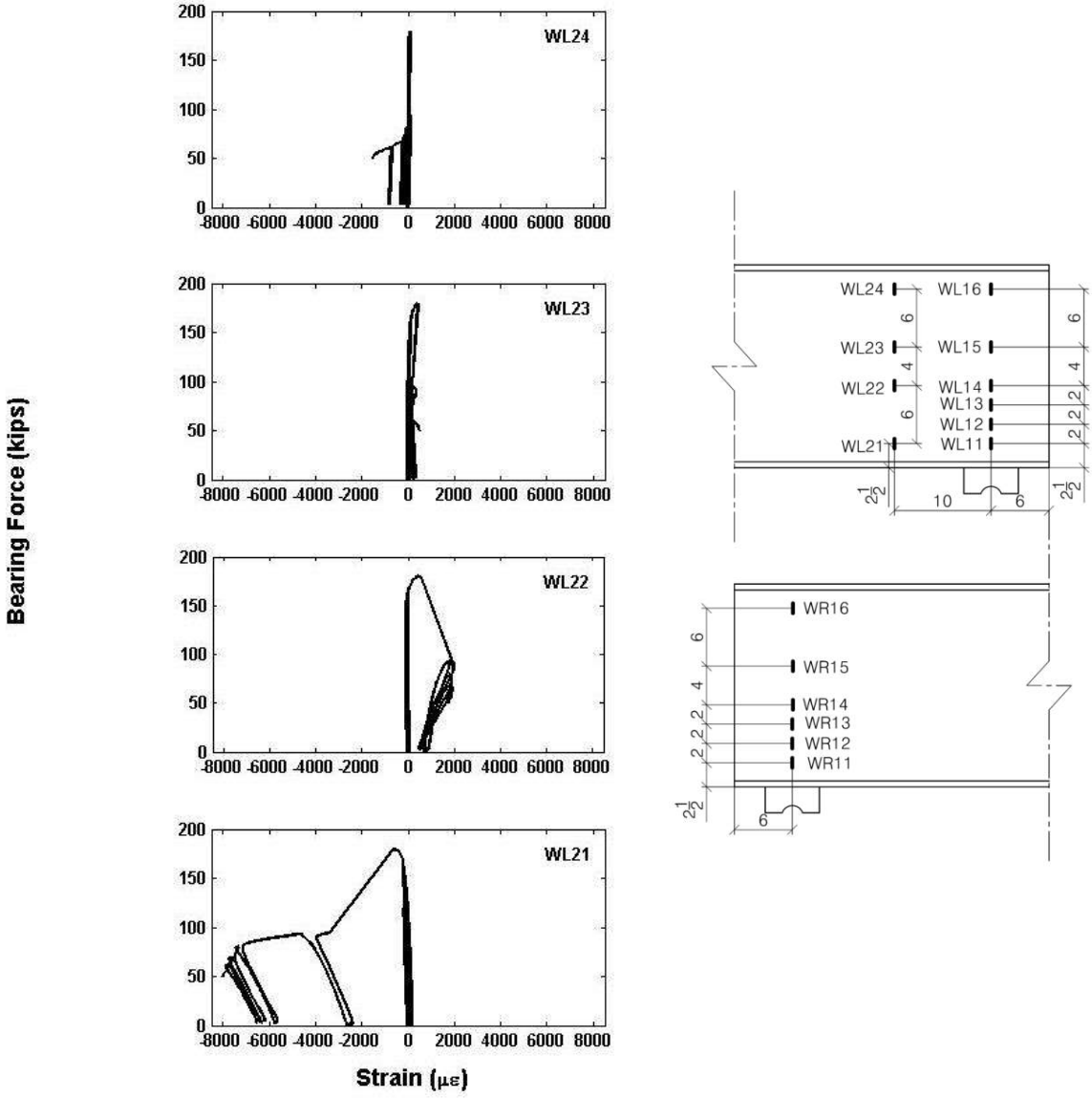

Figure C.1.8 Undamaged Girder WL2x Axial Web Strains

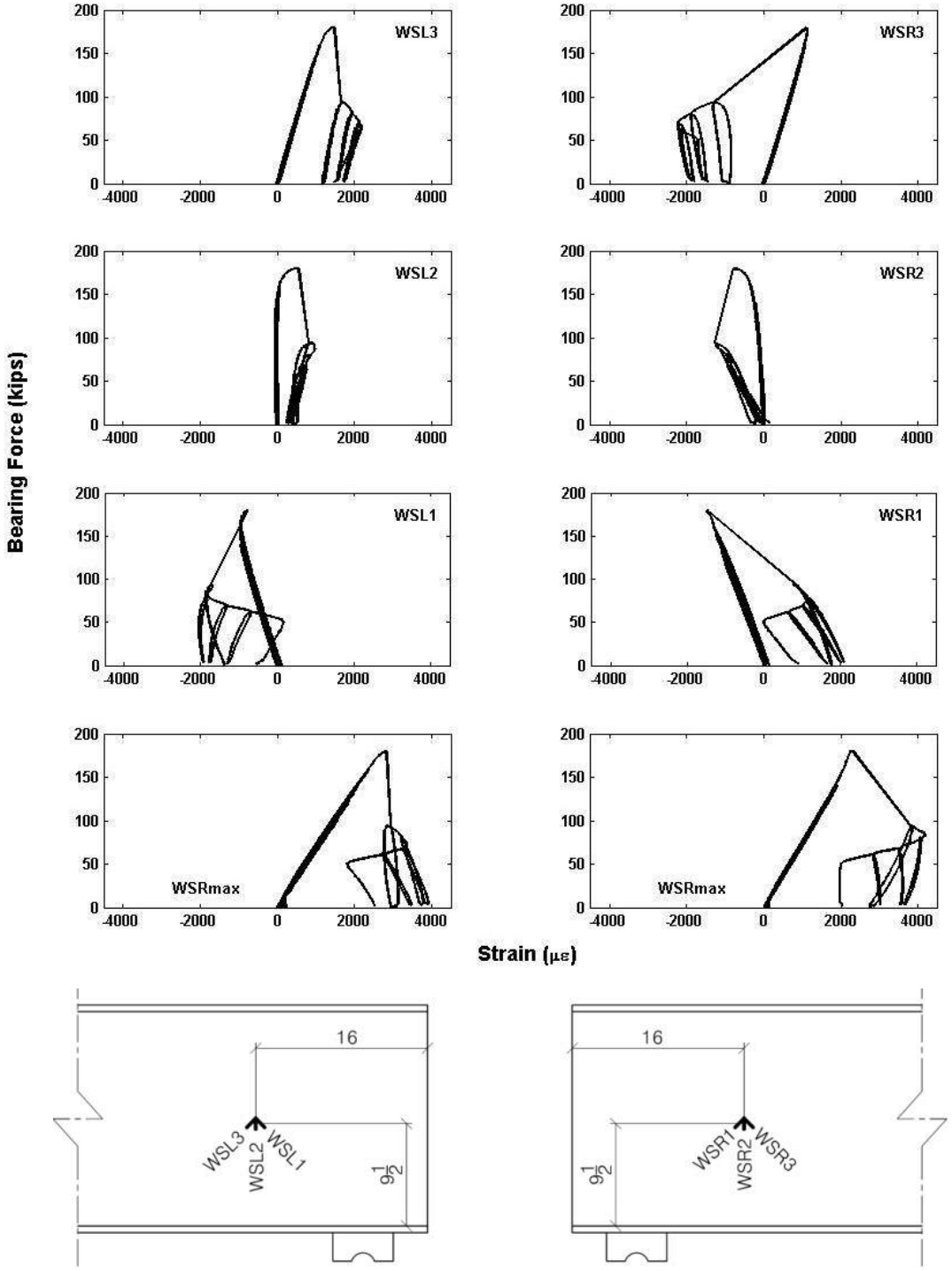

Figure C.1.9 Undamaged Girder Web Rosette Gauge Strains and Maximum Strain

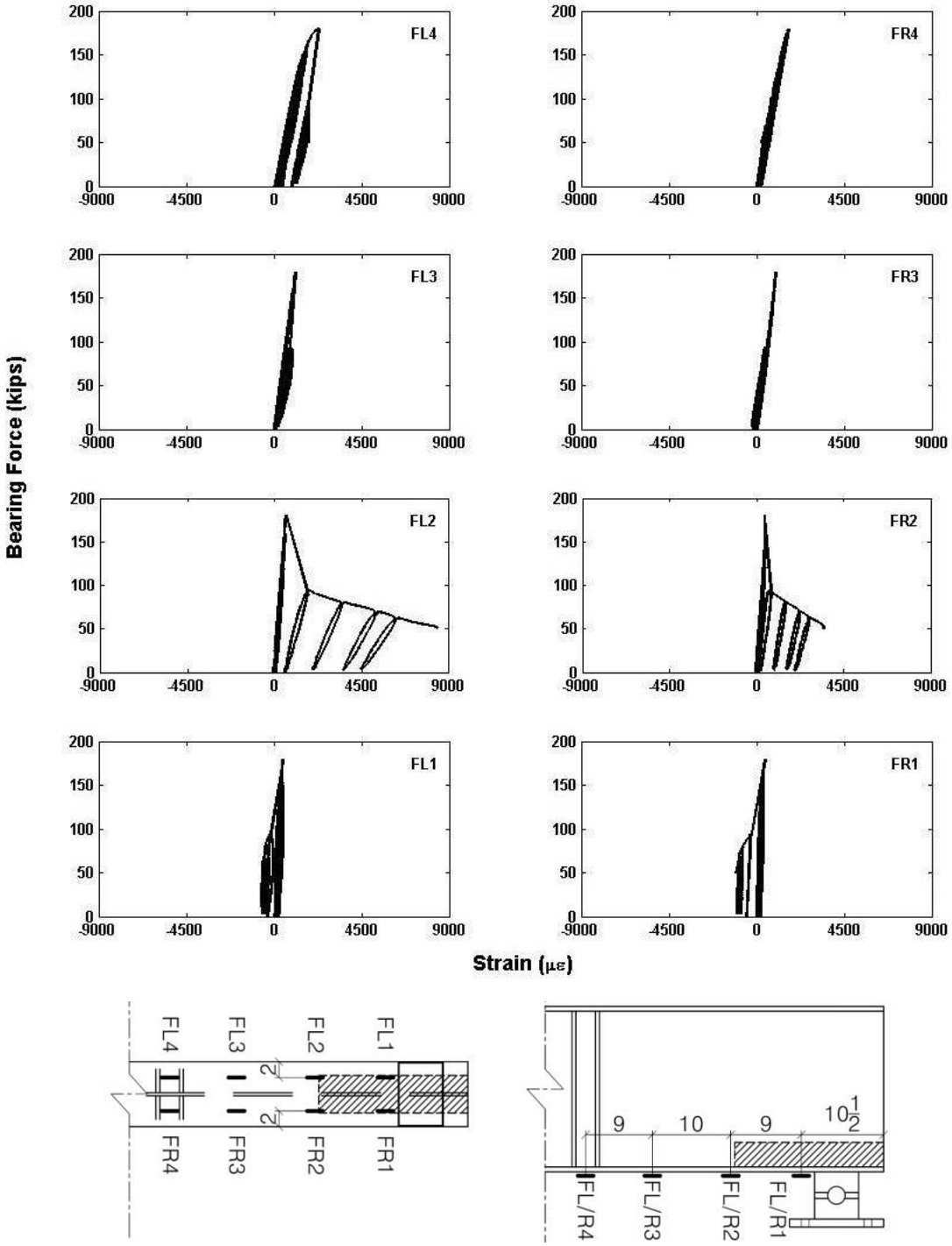

Figure C.1.10 Undamaged Girder Flange Strains

C.2 DAMAGED GIRDER

C.2.1 Force Data

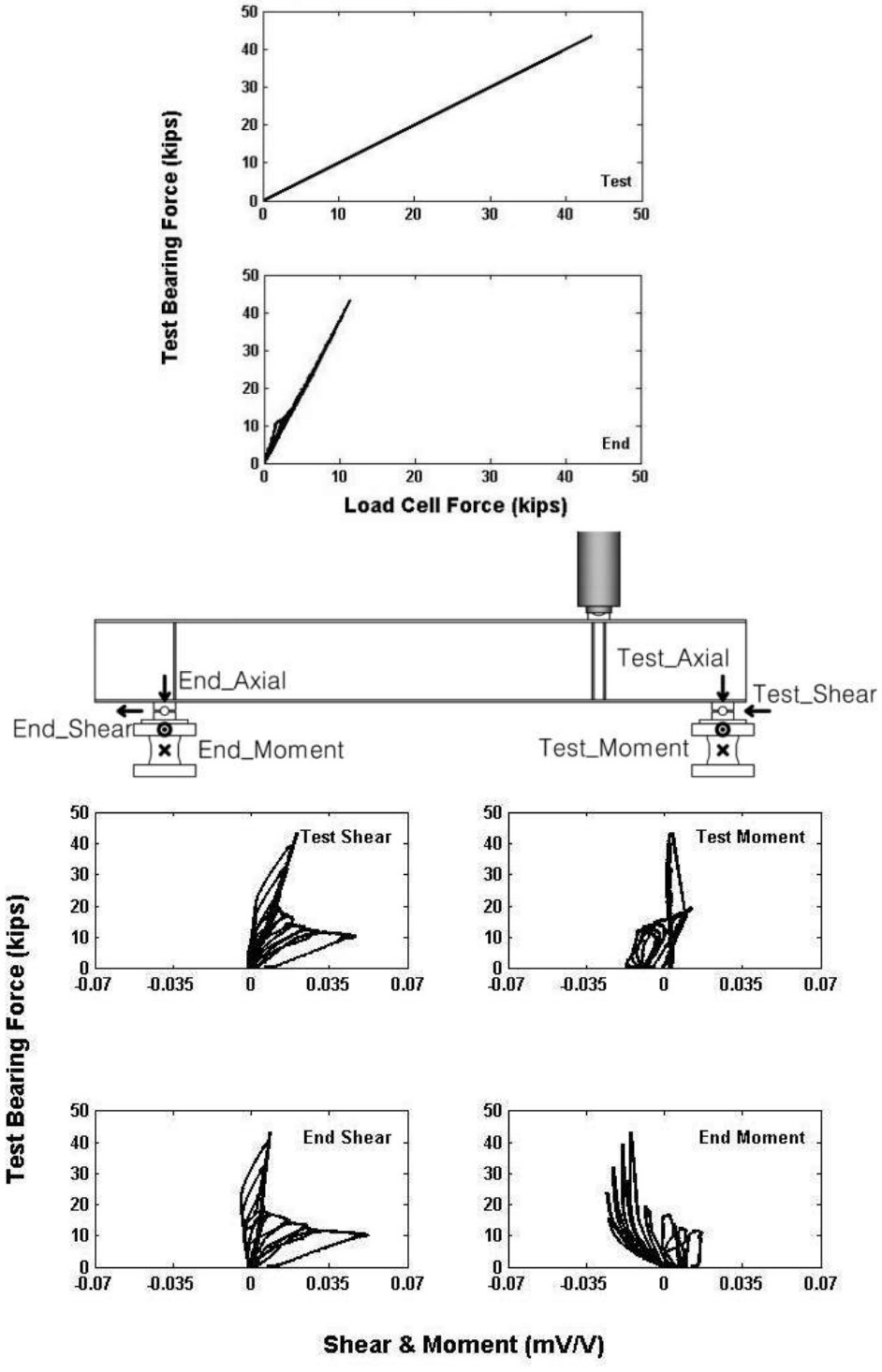

Figure C.2.1 Damaged Girder Load Cell Axial Force and Shear/Moment mV/V Readings

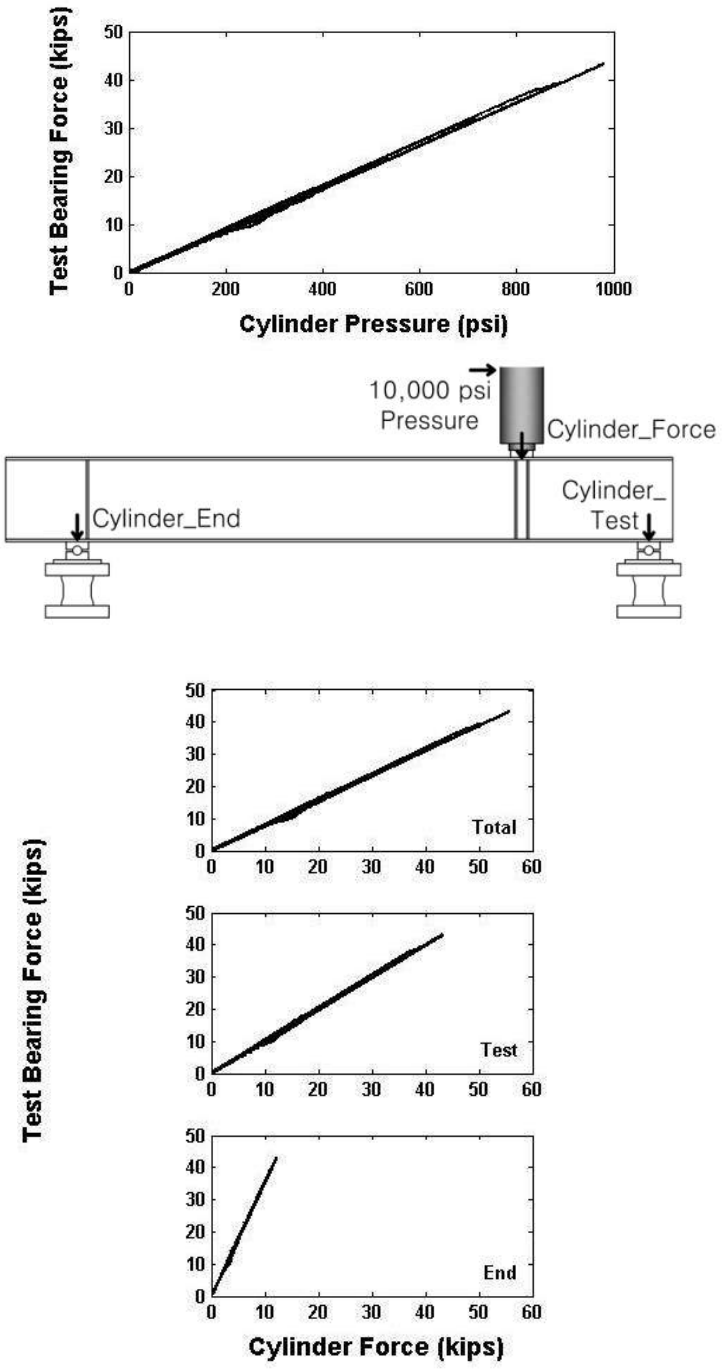

Figure C.2.2 Damaged Girder Cylinder Pressure and Converted Force Readings

C.2.2 Displacement Data

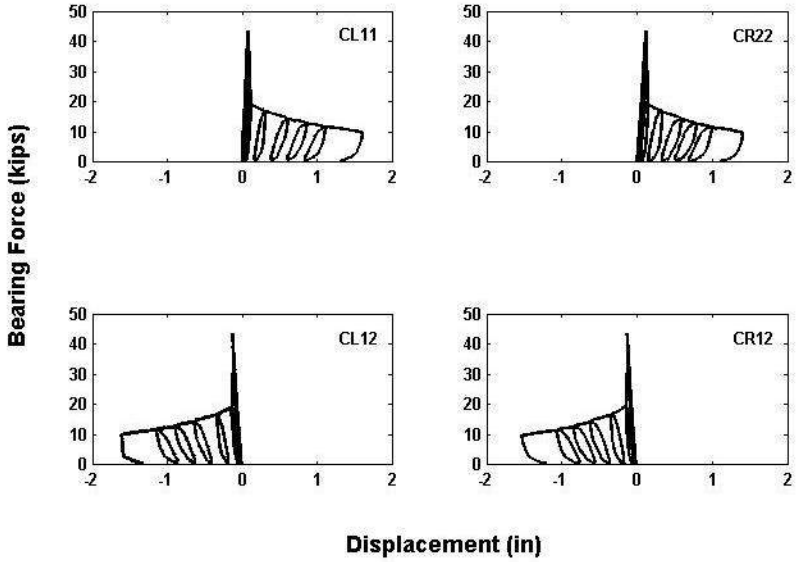

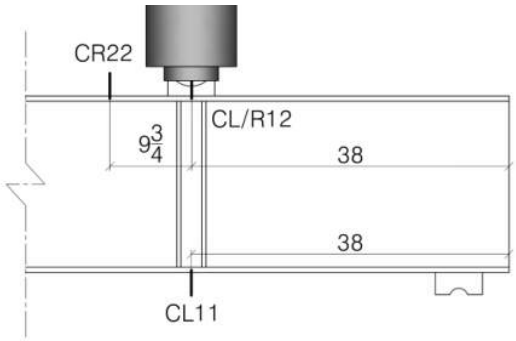

Figure C.2.3 Damaged Girder Vertical Displacements at the Loading Point

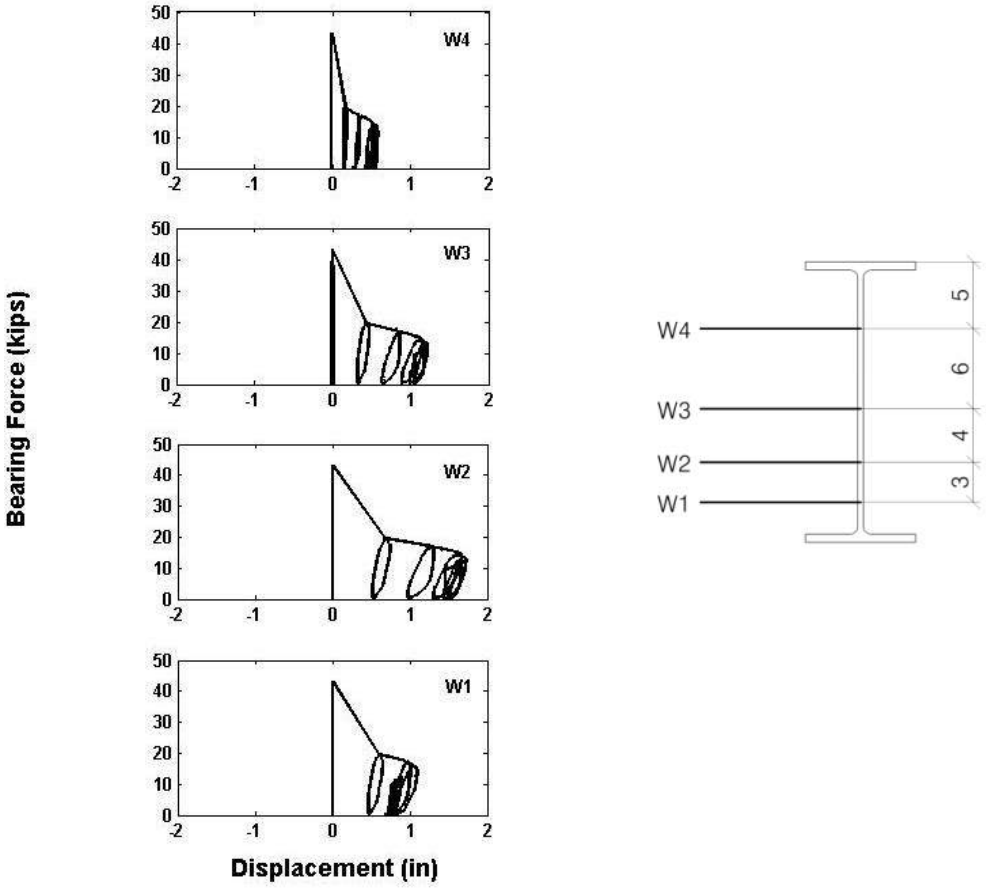

Figure C.2.4 Damaged Girder Lateral Web Displacements

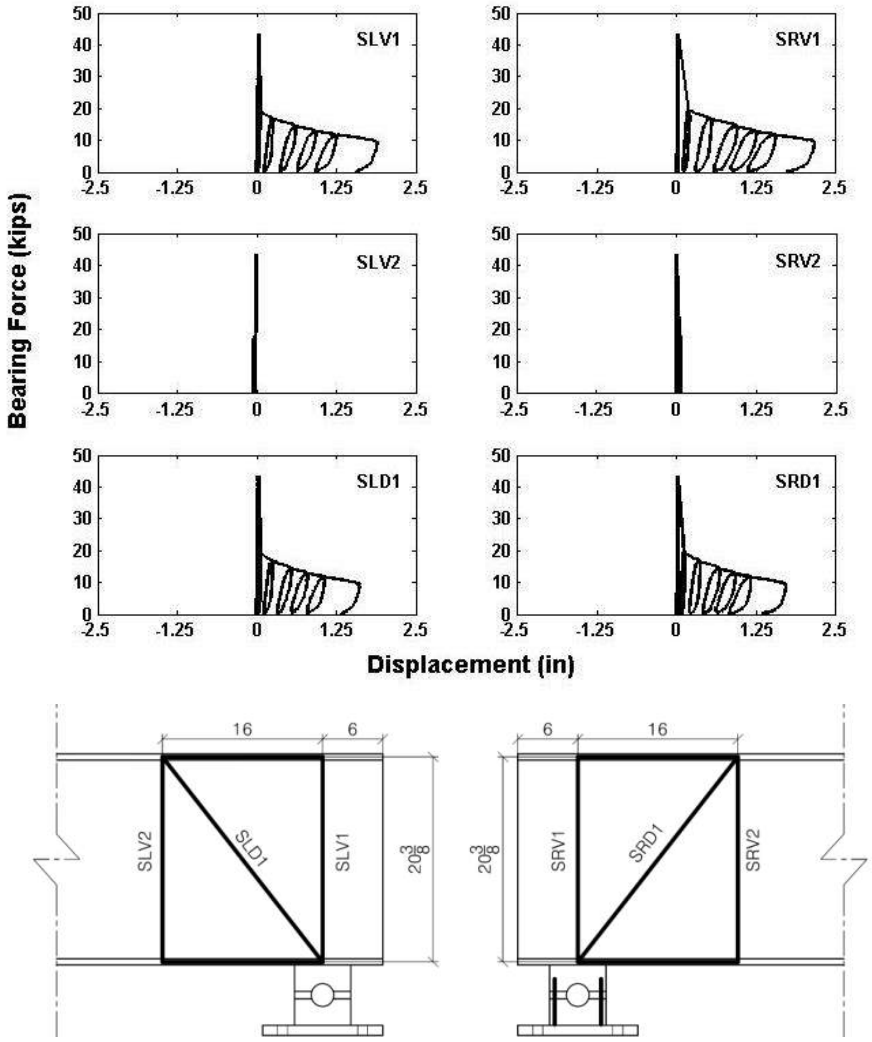

Figure C.2.5 Damaged Girder Shear Box Potentiometer Displacements, Vertical and Diagonal

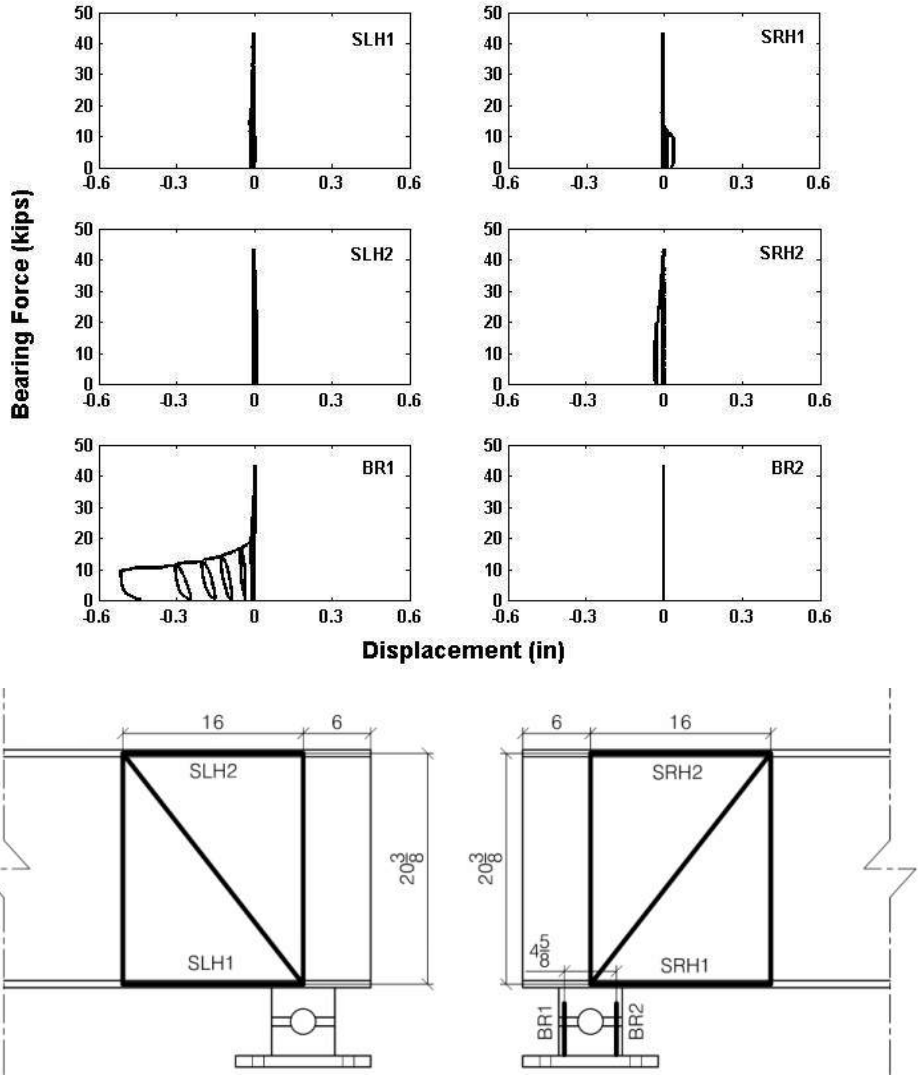

Figure C.2.6 Damaged Girder Shear Box Potentiometer Displacements, Horizontal and Bearing

C.2.3 Strain Data

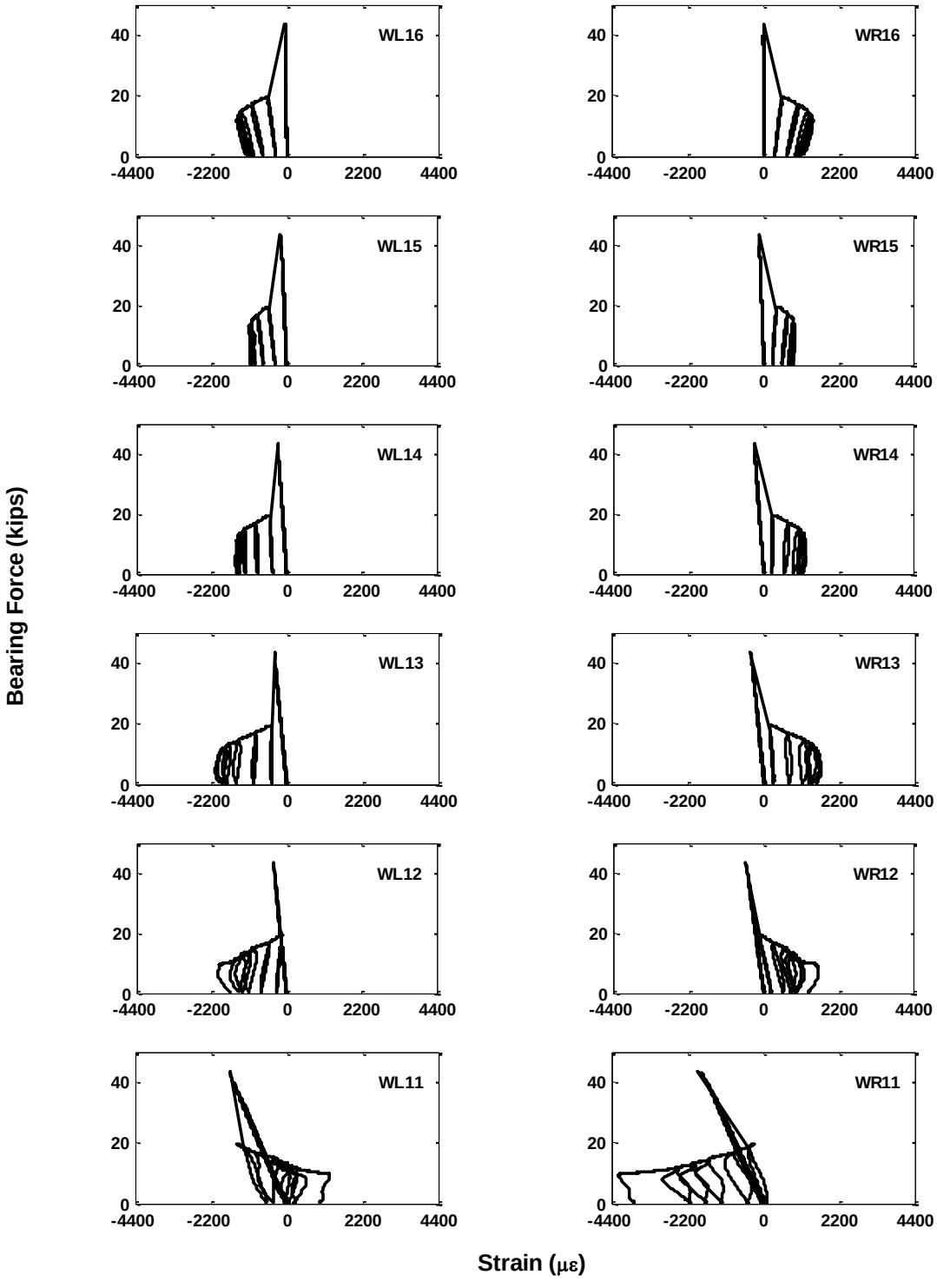

Figure C.2.7 Damaged Girder WL/R1x Axial Web Strains

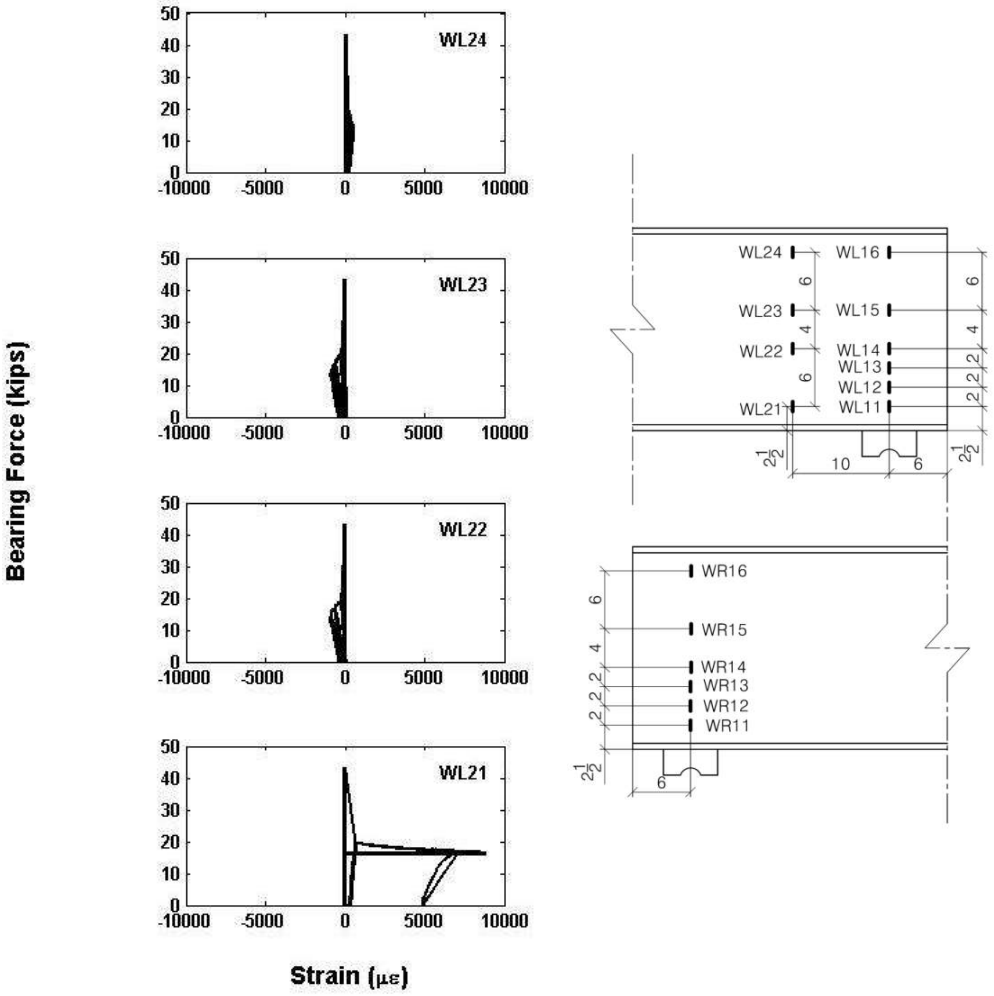

Figure C.2.8 Damaged Girder WL2x Axial Web Strains

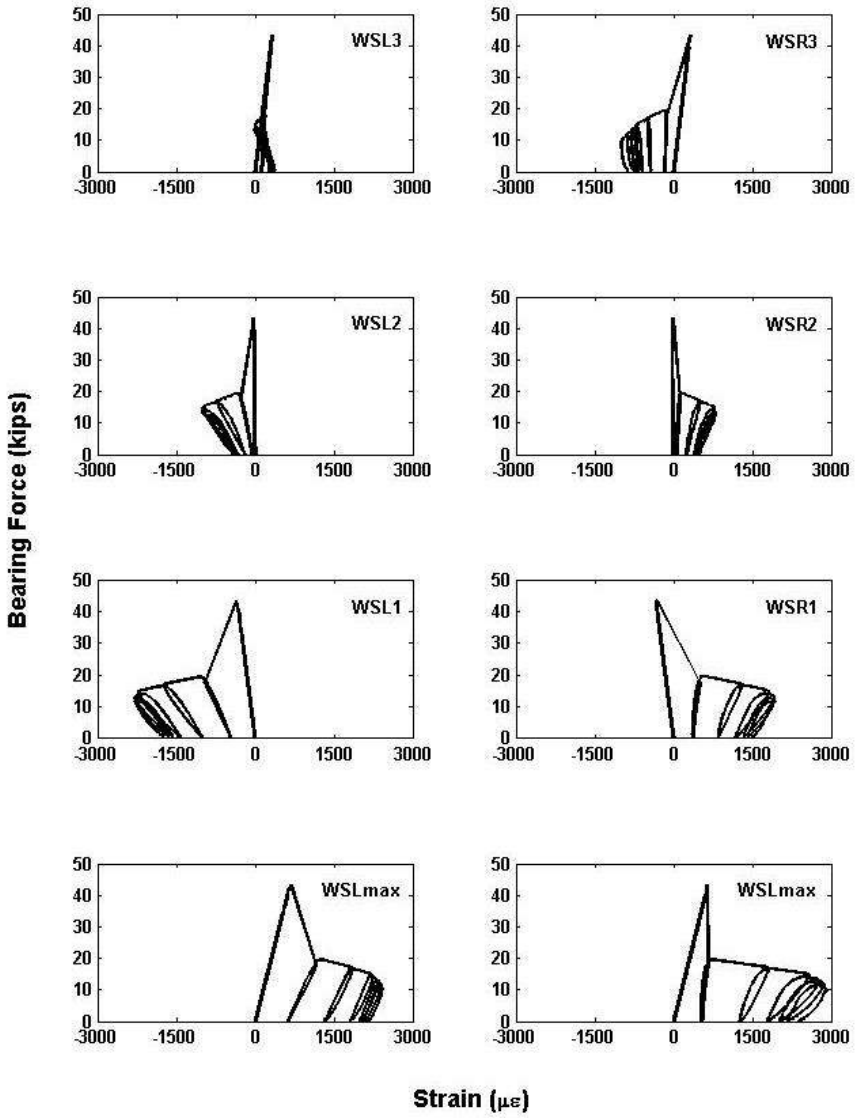

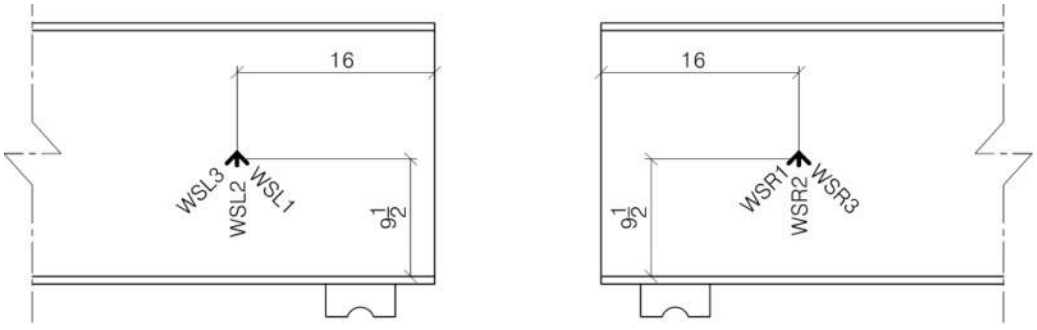

Figure C.2.9 Damaged Girder Web Rosette Gauge Strains and Maximum Strain

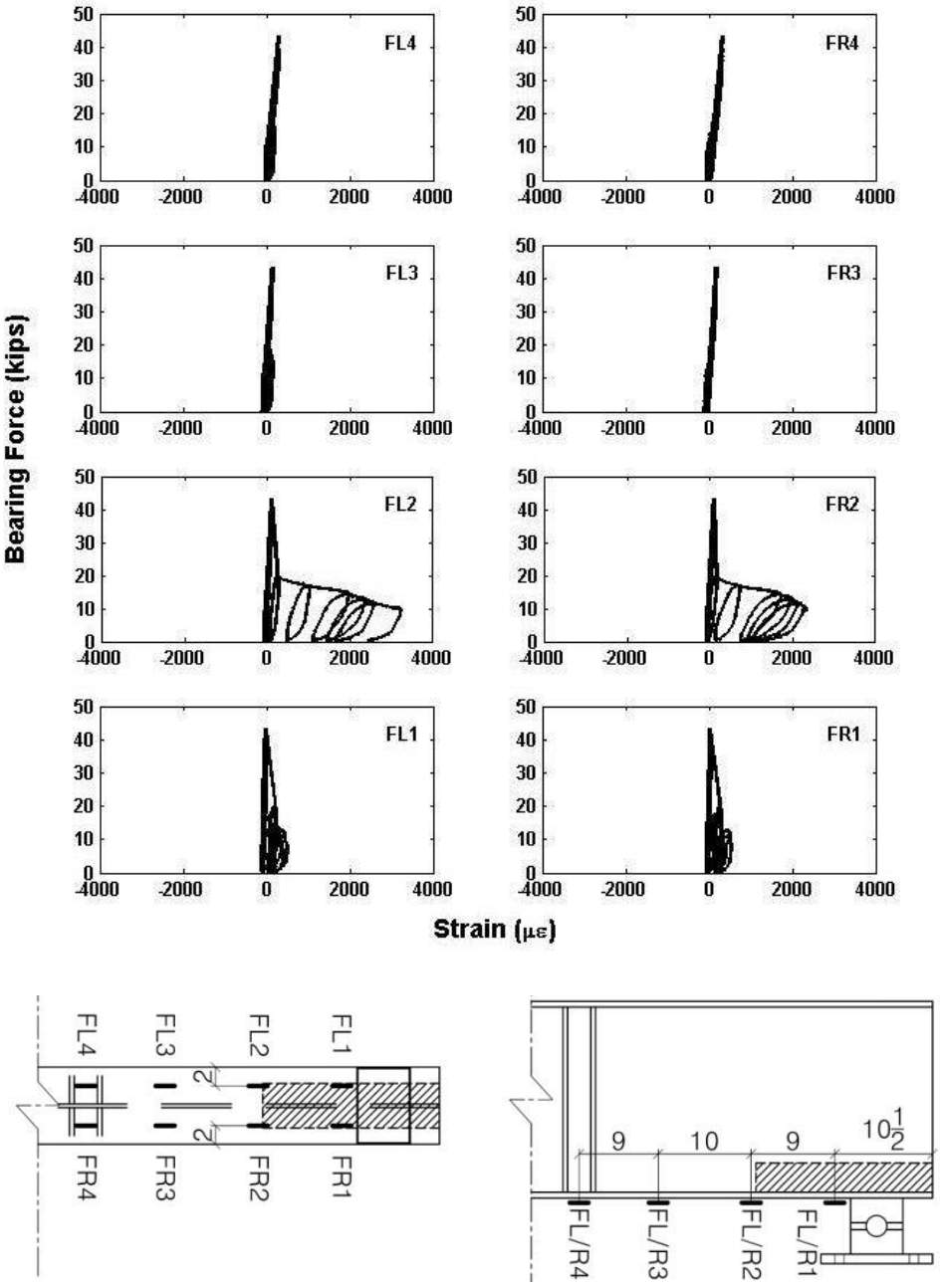

Figure C.2.10 Damaged Girder Flange Strains

C.3 REPAIRED GIRDER

C.3.1 Force Data

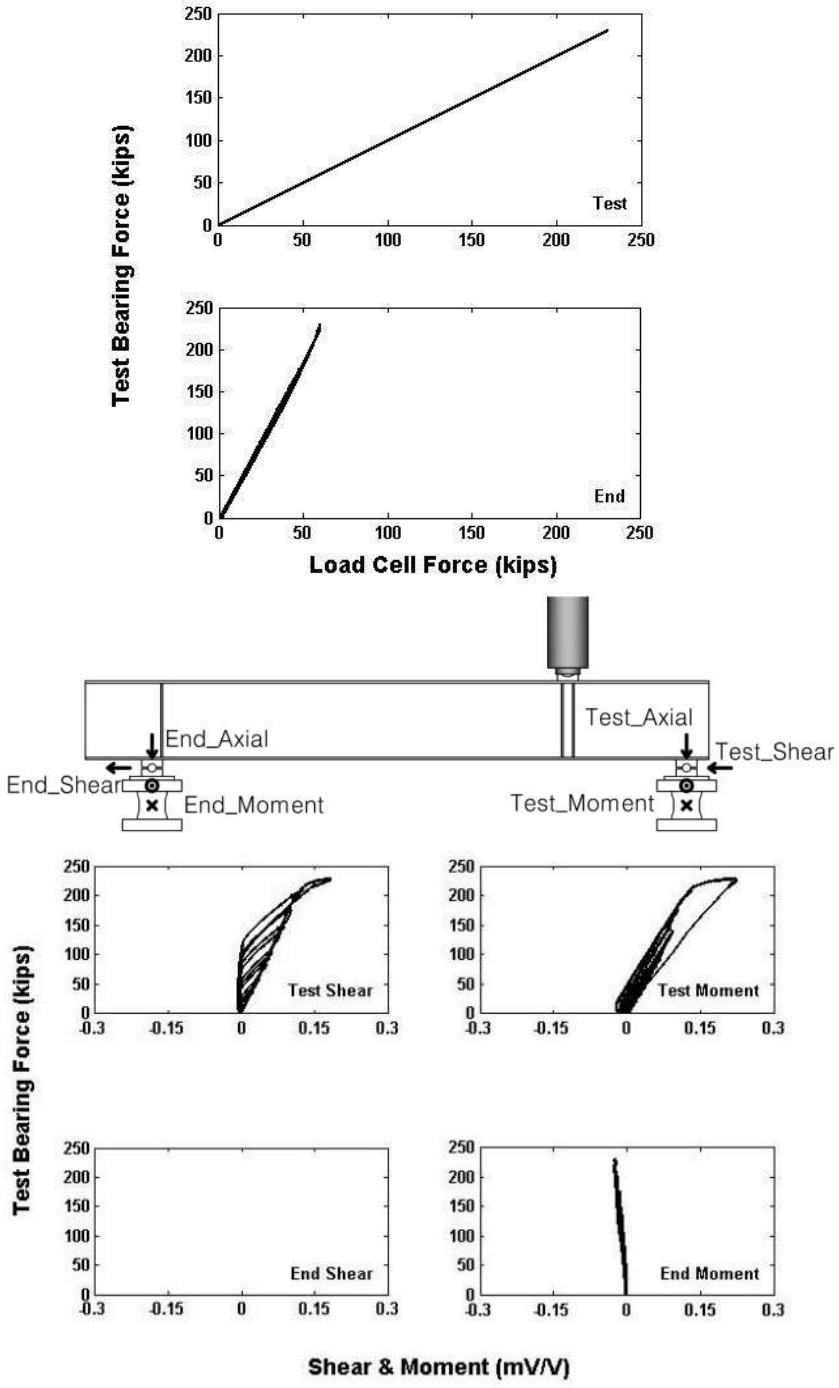

Figure C.3.1 Repaired Girder Load Cell Axial Force and Shear/Moment $^{mV}/_{V}$ Readings

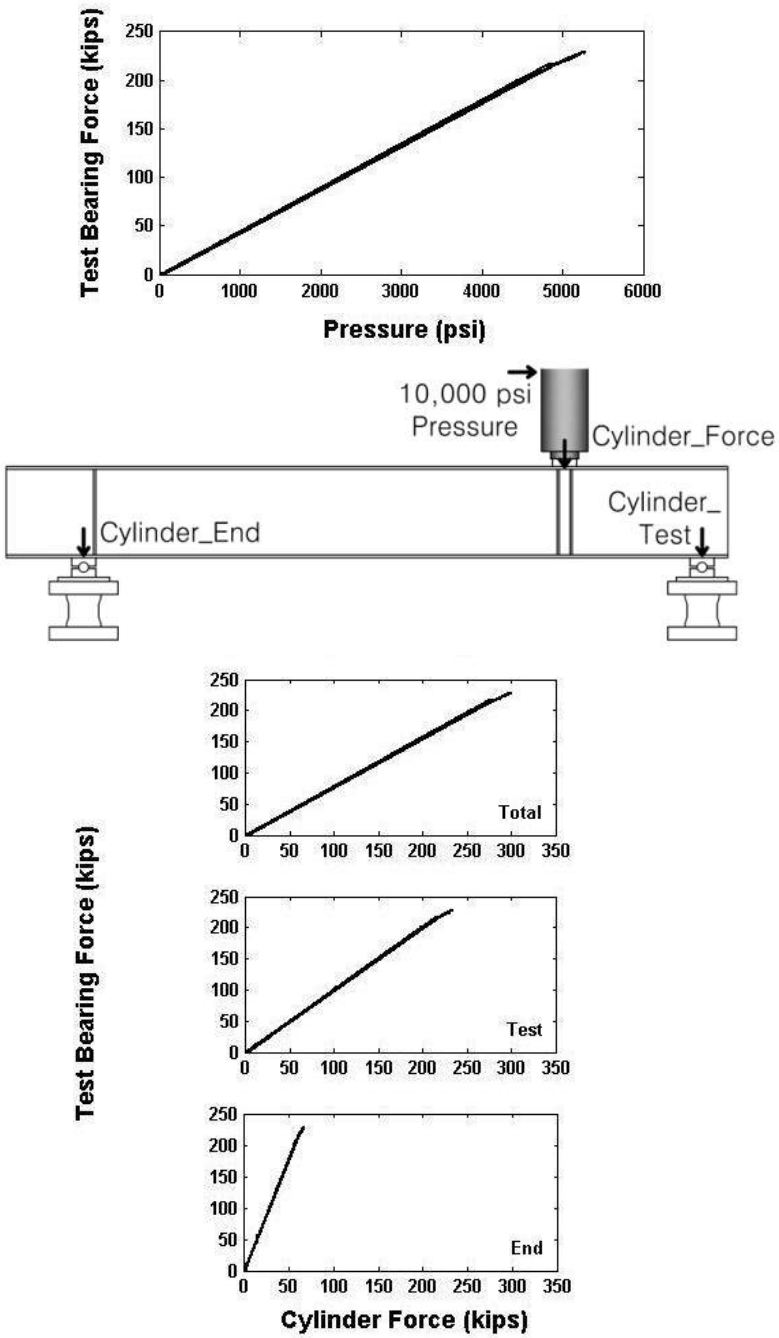

Figure C.3.2 Repaired Girder Cylinder Pressure and Converted Force Readings

C.3.2 Displacement Data

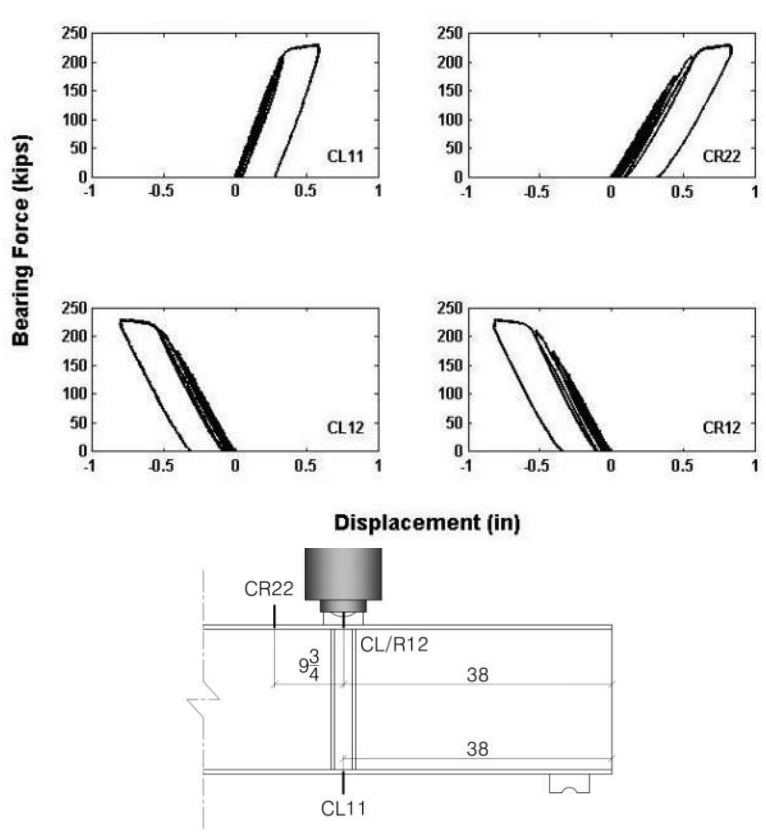

Figure C.3.3 Repaired Girder Vertical Displacements at the Loading Point

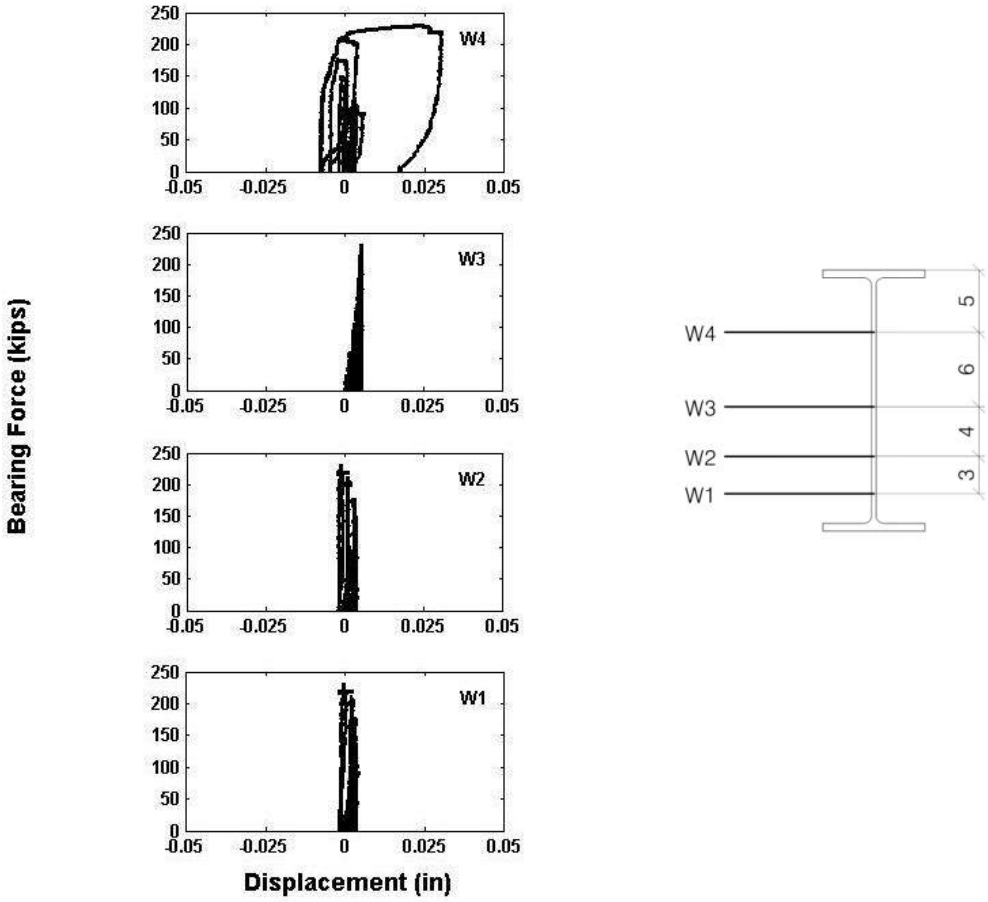

Figure C.3.4 Repaired Girder Lateral Web Displacements

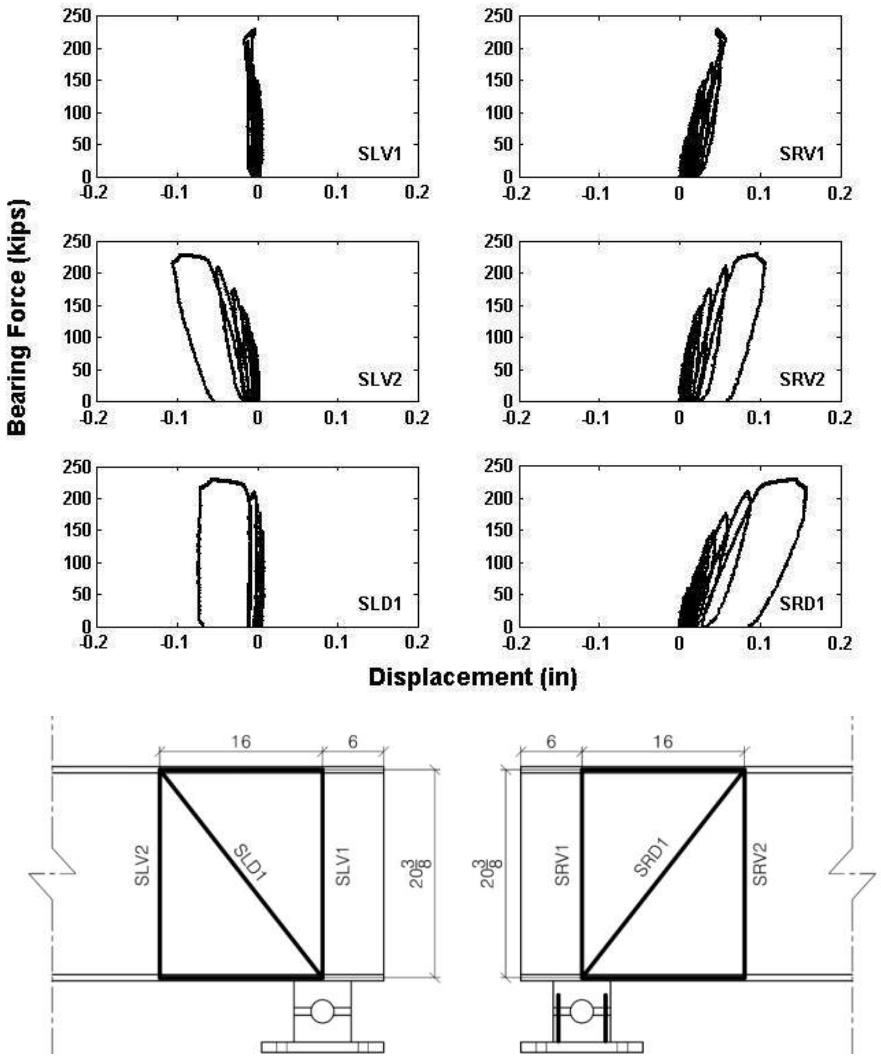

Figure C.3.5 Repaired Girder Shear Box Potentiometer Displacements, Vertical and Diagonal

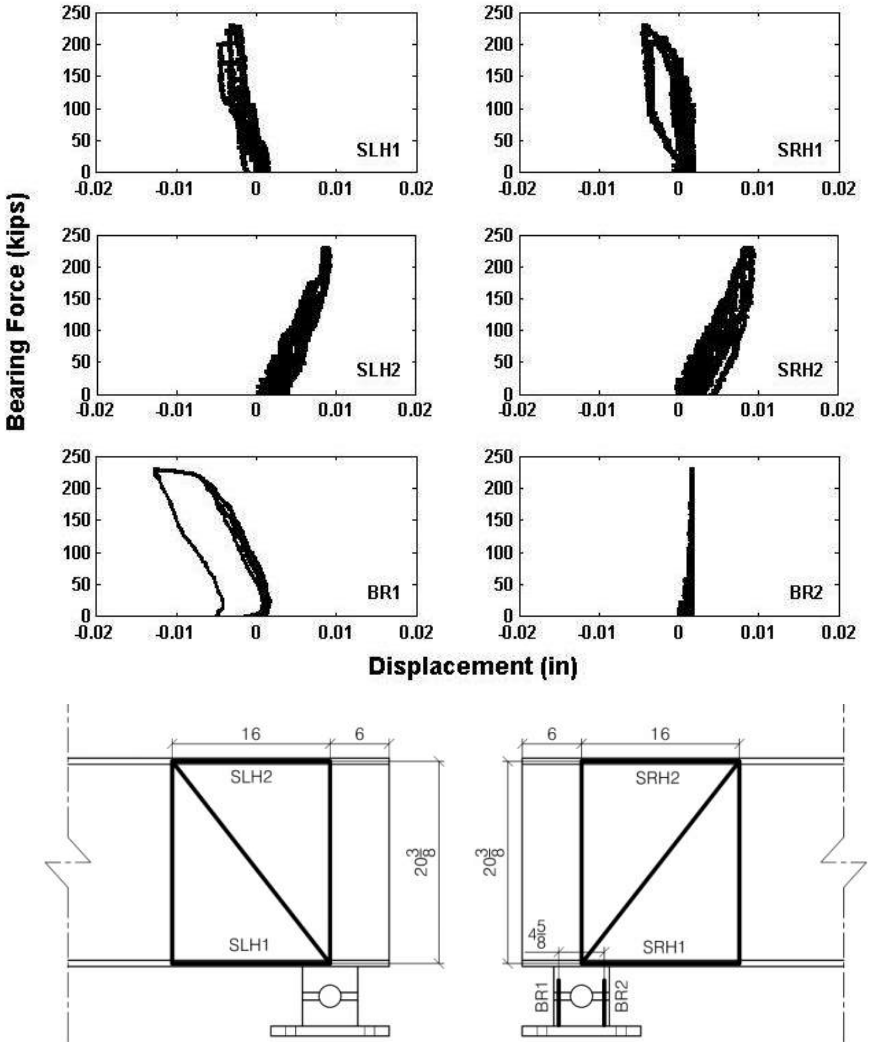

Figure C.3.6 Repaired Girder Shear Box Potentiometer Displacements, Horizontal and Bearing

C.3.3 Strain Data

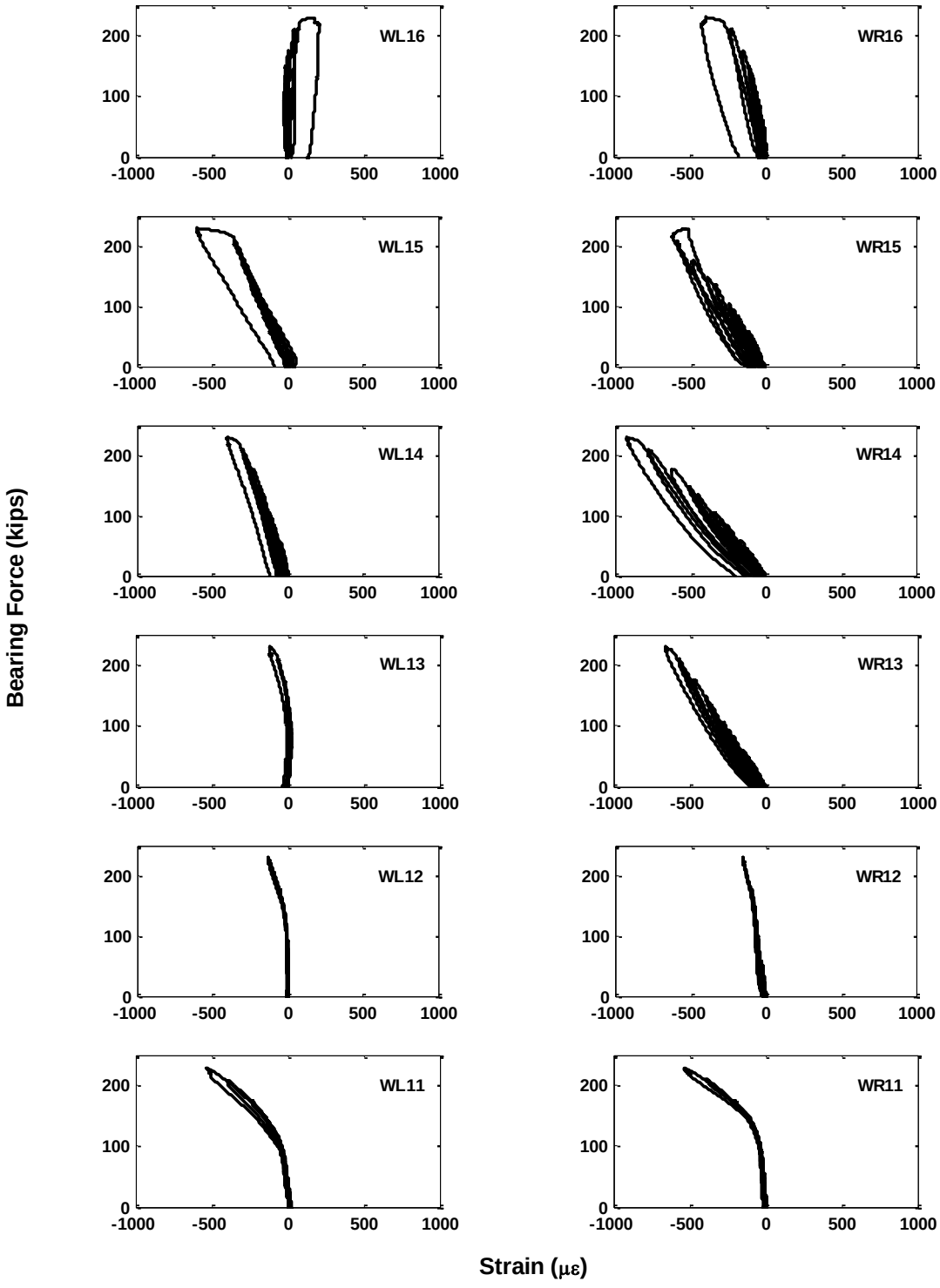

Figure C.3.7 Repaired Girder WL/R1x Axial Web Strains

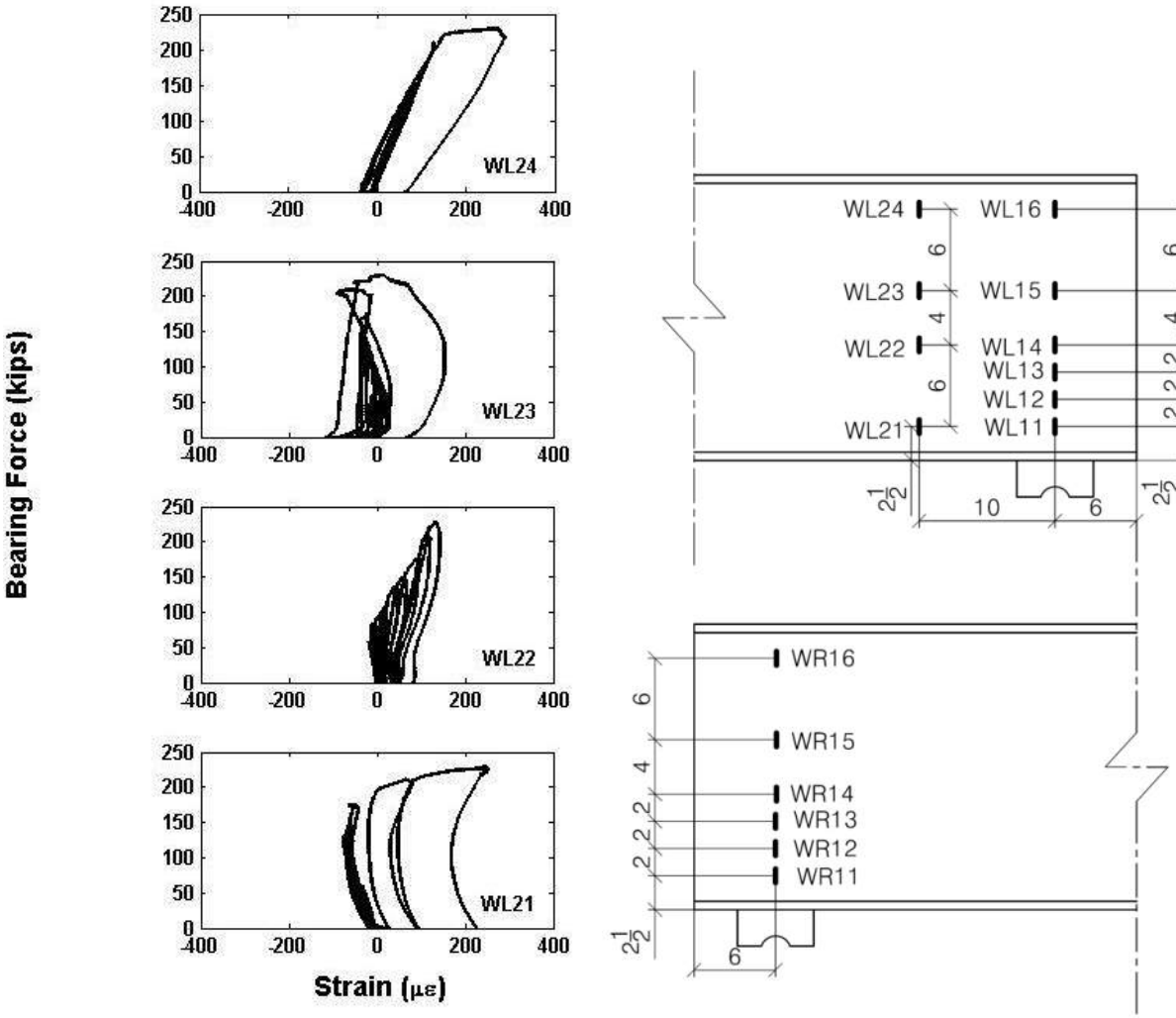

Figure C.3.8 Repaired Girder WL2x Axial Web Strains

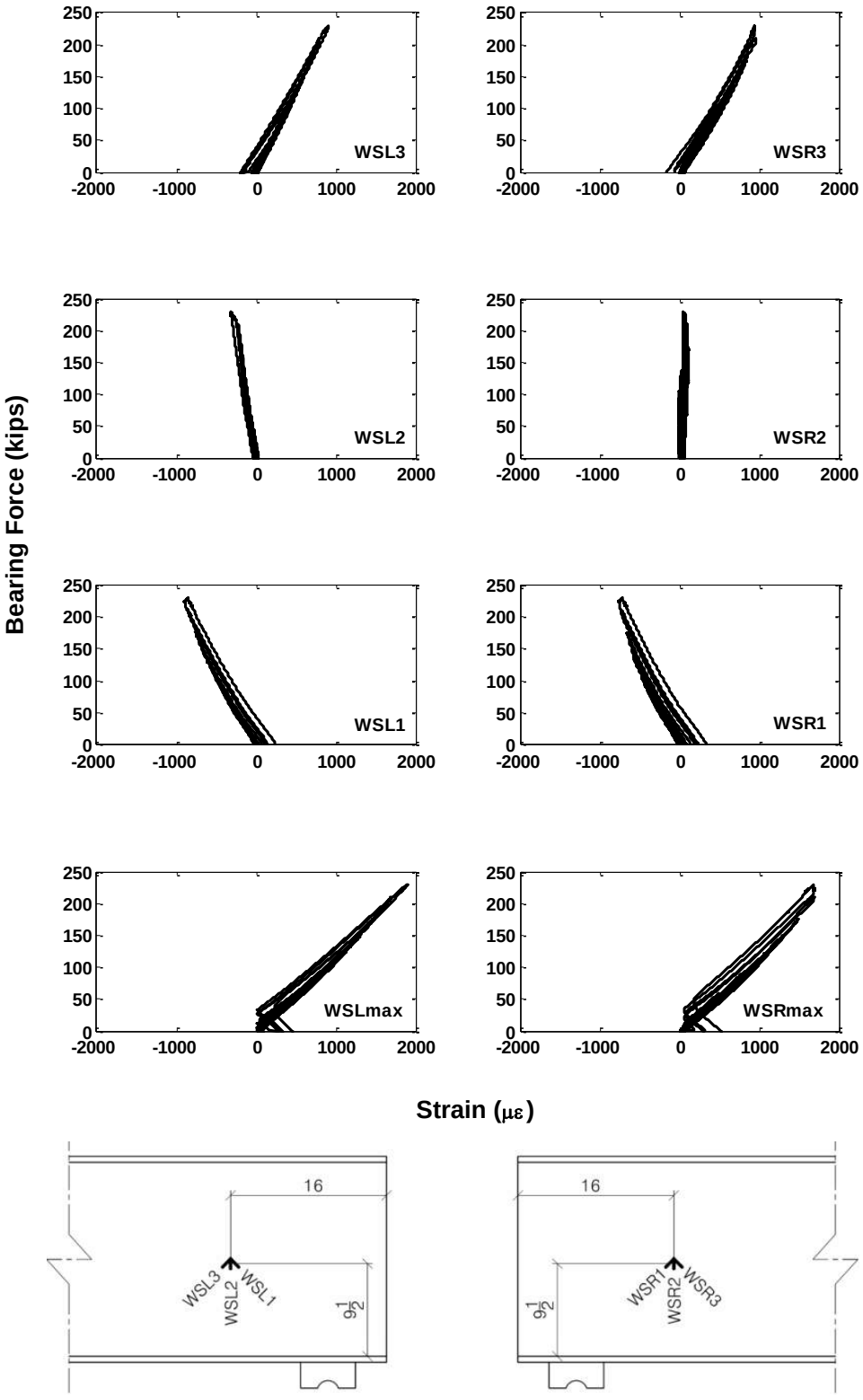

Figure C.3.9 Repaired Girder Web Rosette Gauge Strains and Maximum Strain

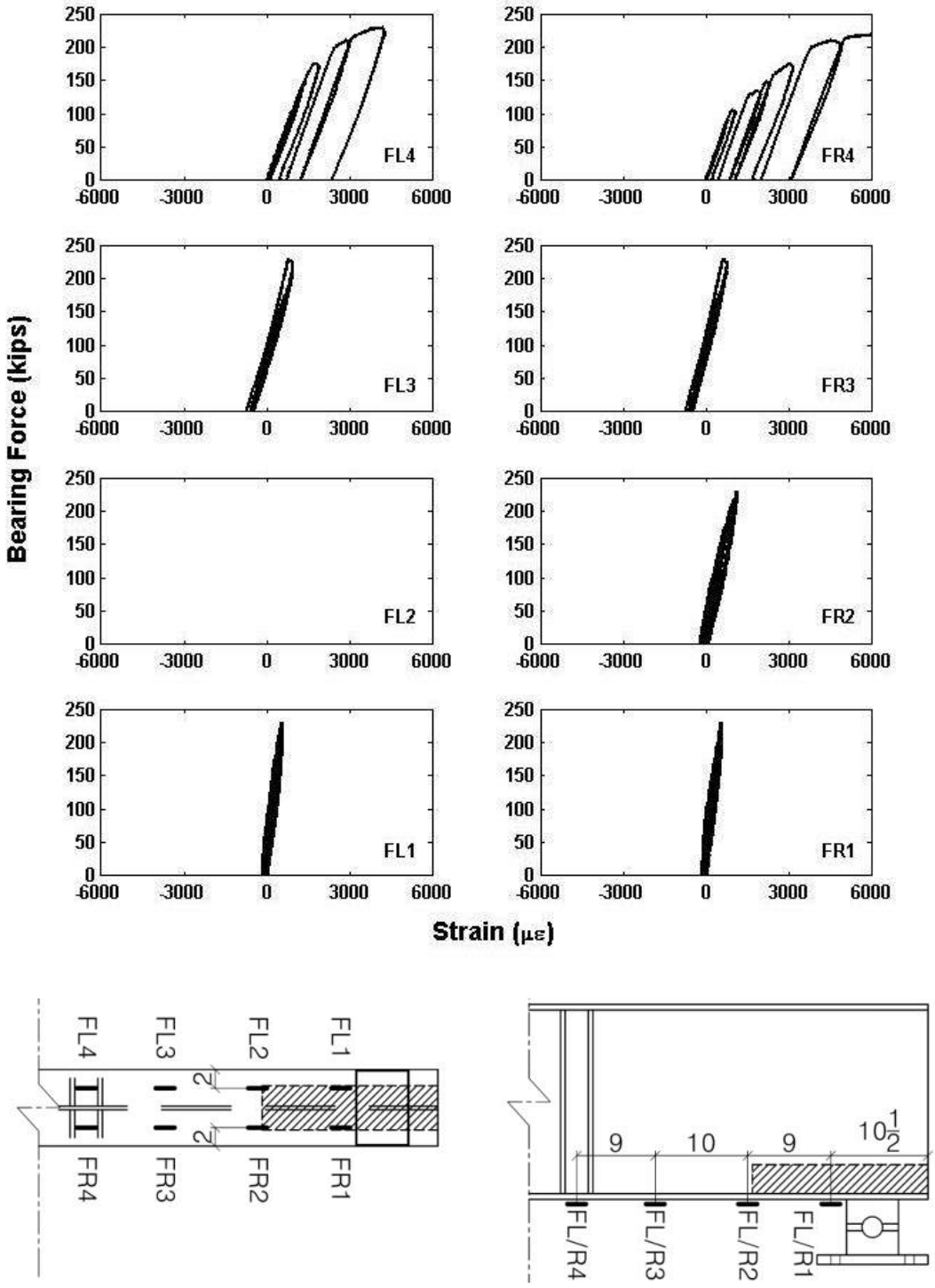

Figure C.3.10 Repaired Girder Flange Strains

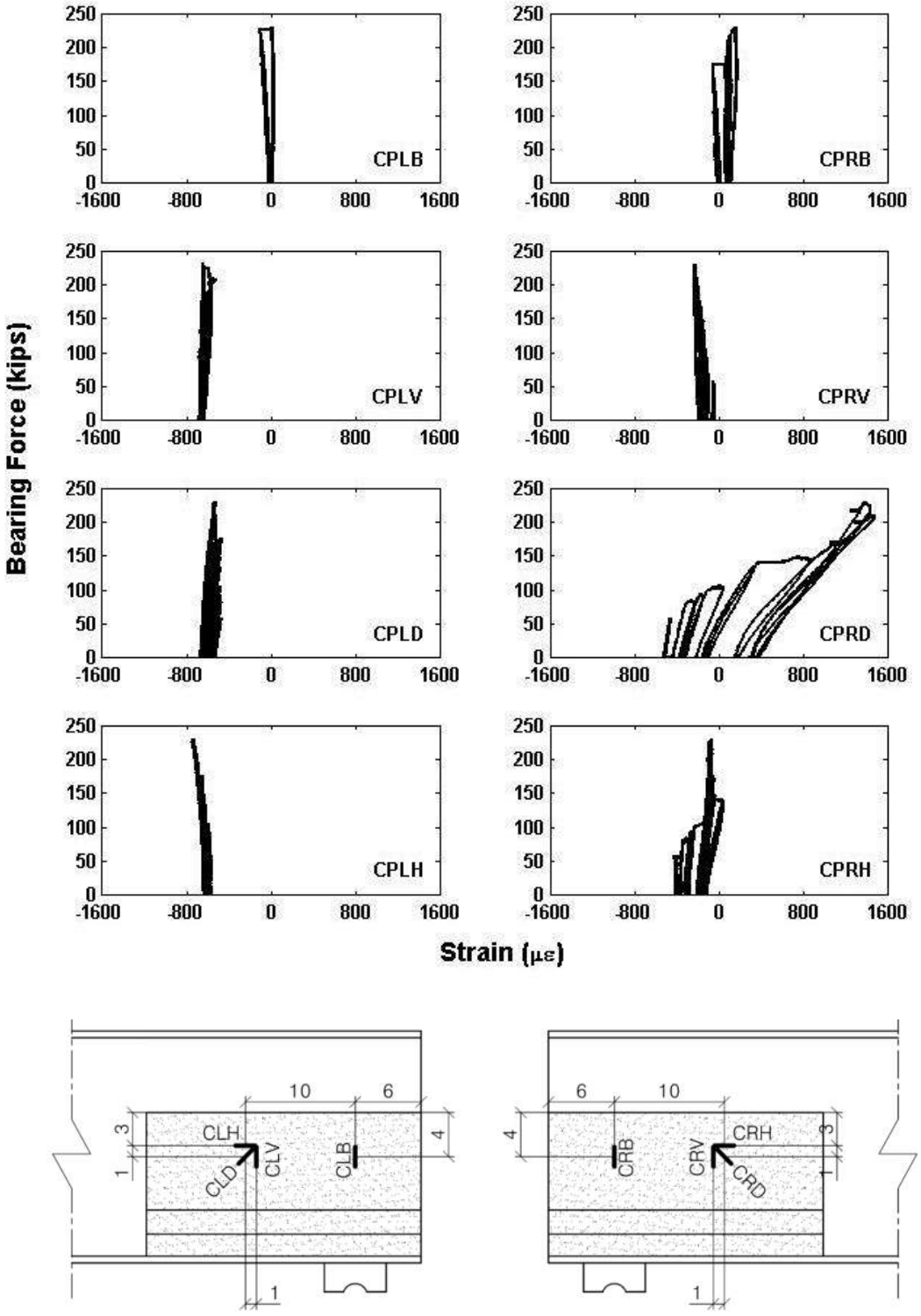

Figure C.3.11 Repaired Girder Concrete Strains

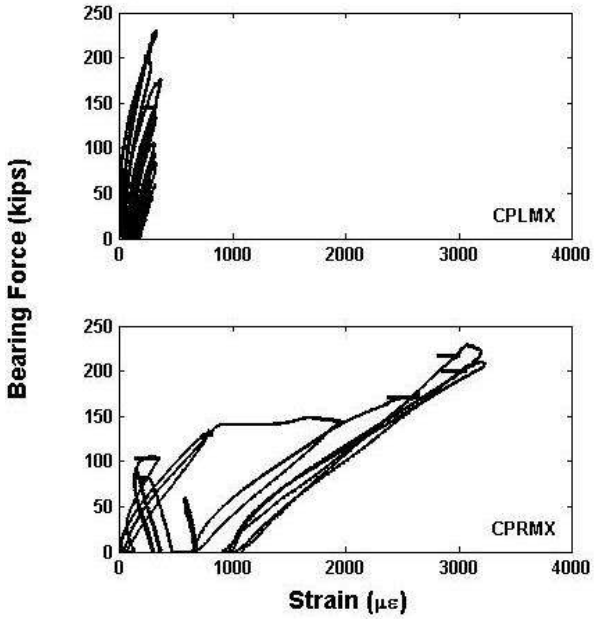

Figure C.3.12 Repaired Girder Maximum Concrete Shear Strains Calculated From the CH/CD/CV Strain Gauge Rosette

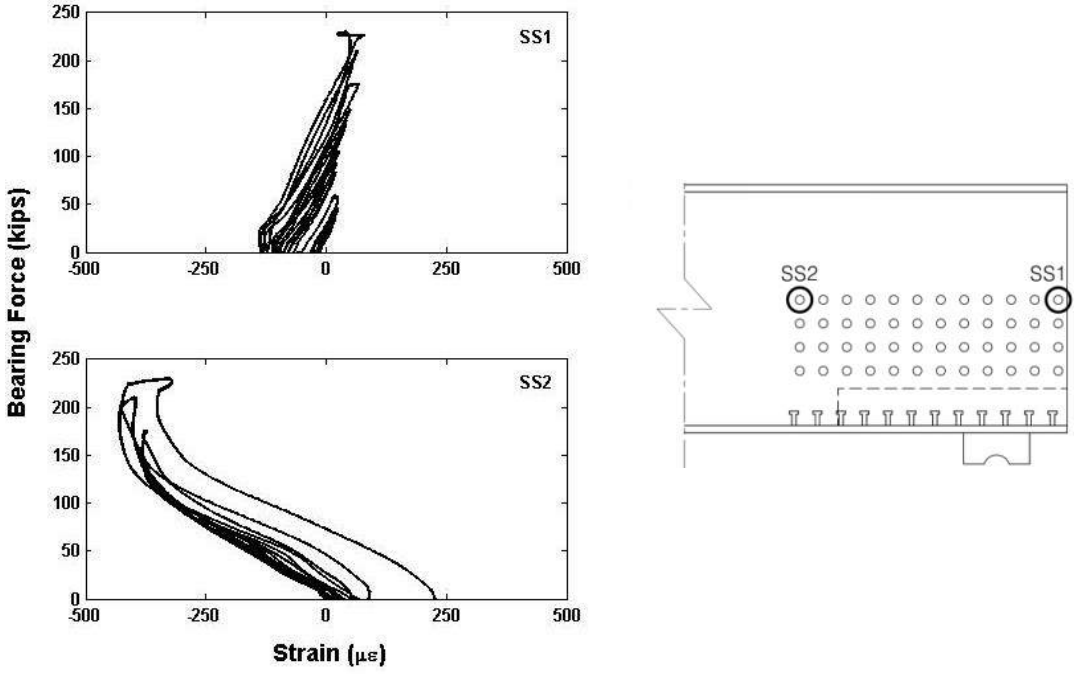

Figure C.3.13 Repaired Girder Shear Stud Axial Strain

Appendix D. Finite Element Results

D.1 UNDAMAGED GIRDER

D.1.1 Undamaged - Girder Von Mises Stress Distribution (0 - 70 ksi)

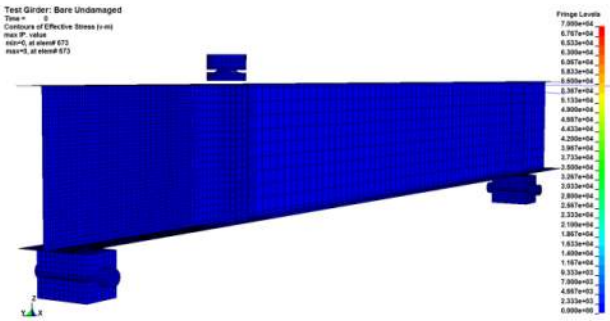

Figure D.1.1 Undamaged Von Mises: 0 kip

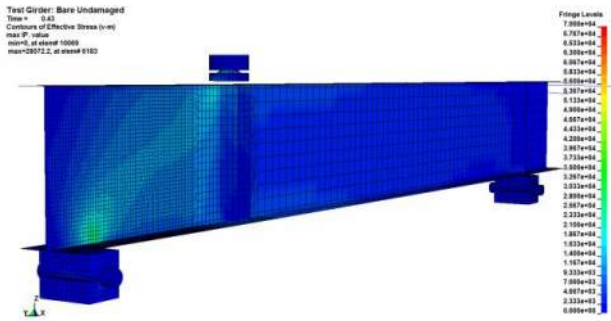

Figure D.1.2 Undamaged Von Mises: 40 kip

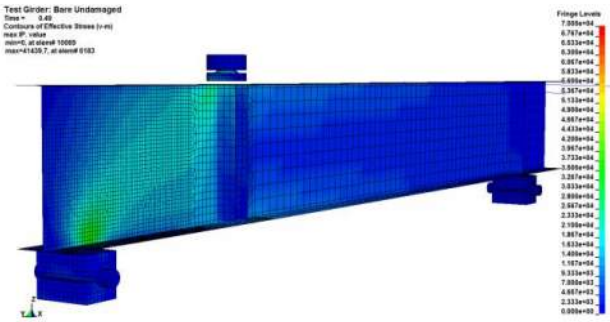

Figure D.1.3 Undamaged Von Mises: 60 kip

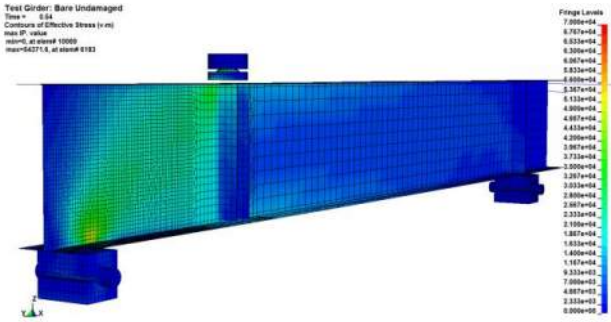

Figure D.1.4 Undamaged Von Mises: 80 kip

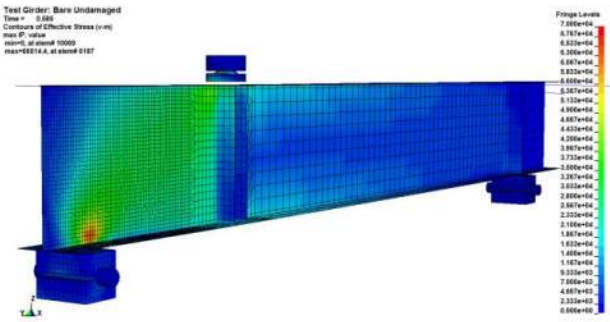

Figure D.1.5 Undamaged Von Mises: 100 kip

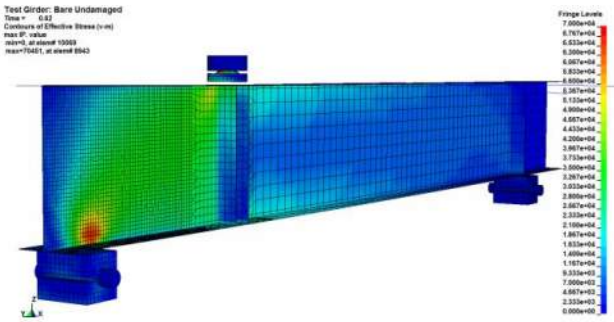

Figure D.1.6 Undamaged Von Mises: 120 kip

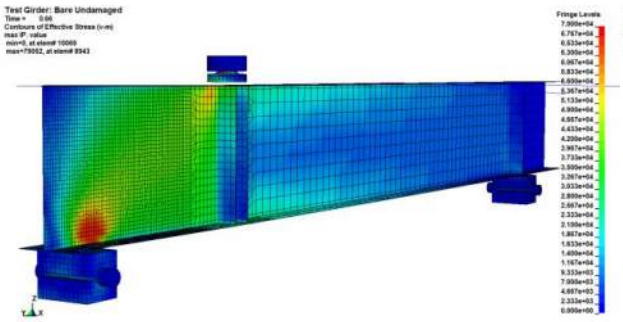

Figure D.1.7 Undamaged Von Mises: 140 kip

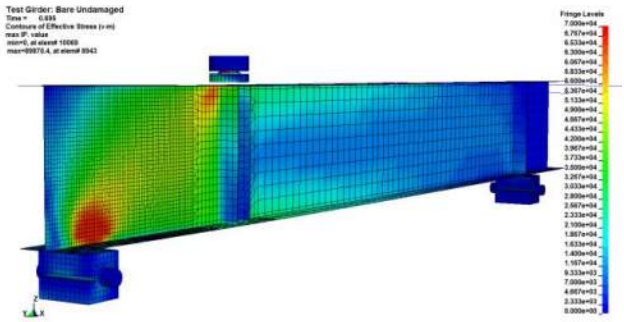

Figure D.1.8 Undamaged Von Mises: 160 kip

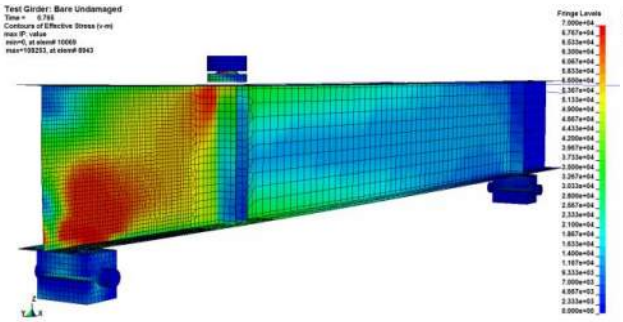

Figure D.1.9 Undamaged Von Mises: 193 kip

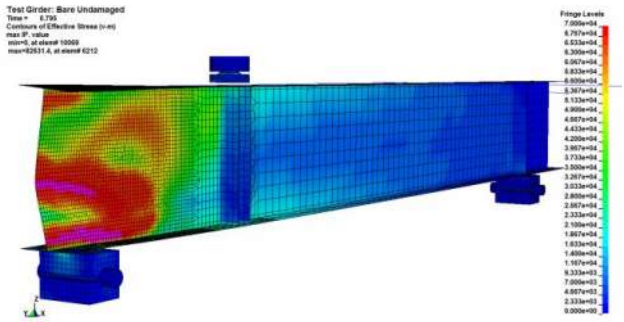

Figure D.1.10 Undamaged Von Mises: Failure

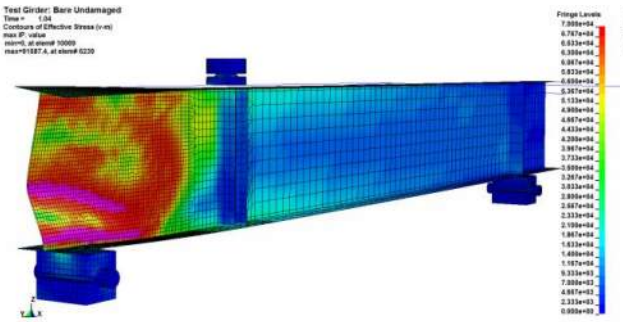

Figure D.1.11 Undamaged Von Mises: +0.25 in

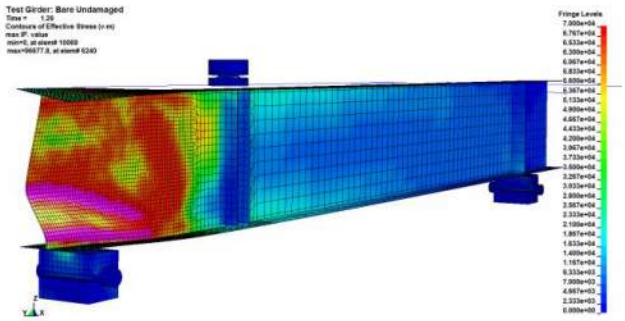

Figure D.1.12 Undamaged Von Mises: +0.50 in

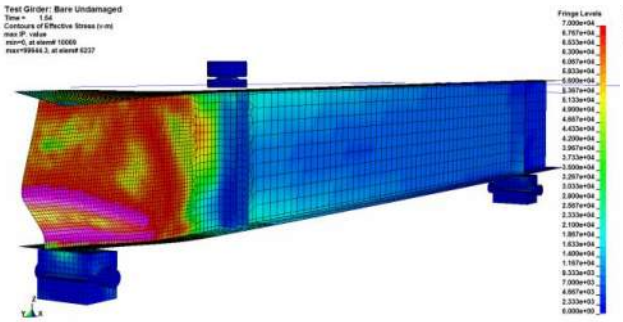

Figure D.1.13 Undamaged Von Mises: +0.75 in

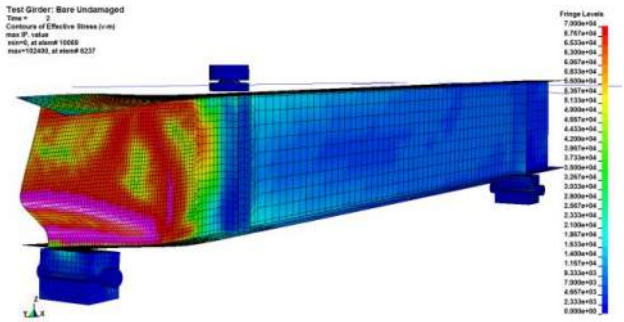

Figure D.1.14 Undamaged Von Mises: +1.25 in

D.1.2 Undamaged - Girder Plastic Strain Development (0 - 45,000 με)

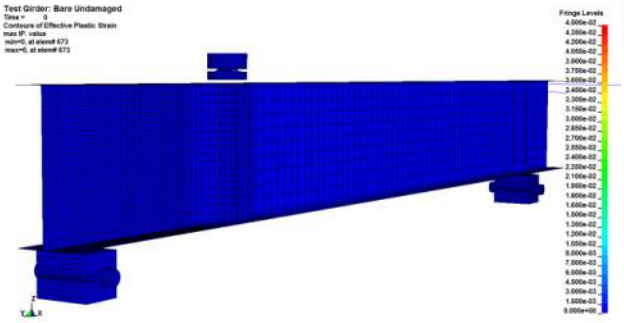

Figure D.1.15 Undamaged Plastic Strain: 0 kip

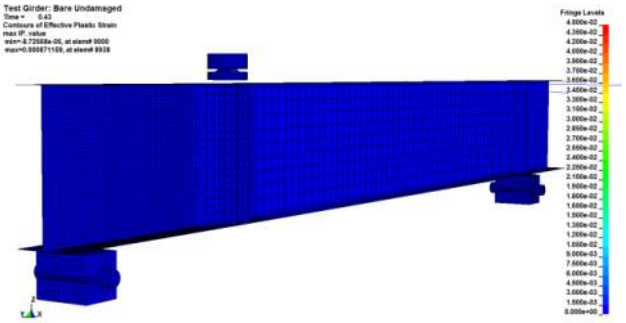

Figure D.1.16 Undamaged Plastic Strain: 40 kip

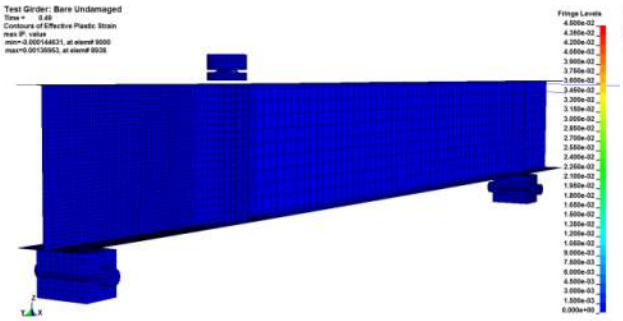

Figure D.1.17 Undamaged Plastic Strain: 60 kip

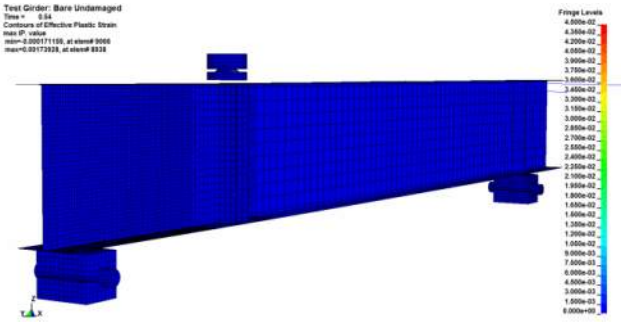

Figure D.1.18 Undamaged Plastic Strain: 80 kip

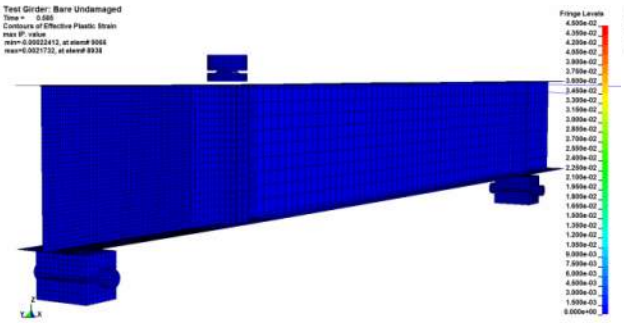

Figure D.1.19 Undamaged Plastic Strain: 100 kip

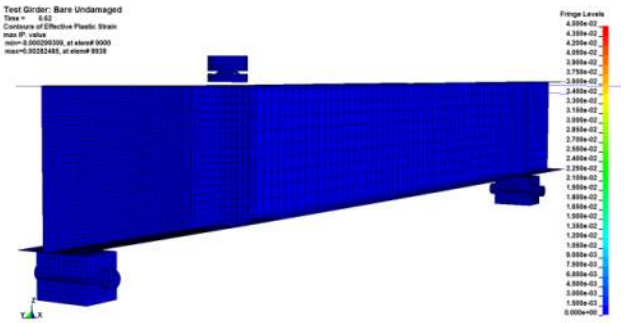

Figure D.1.20 Undamaged Plastic Strain: 120 kip

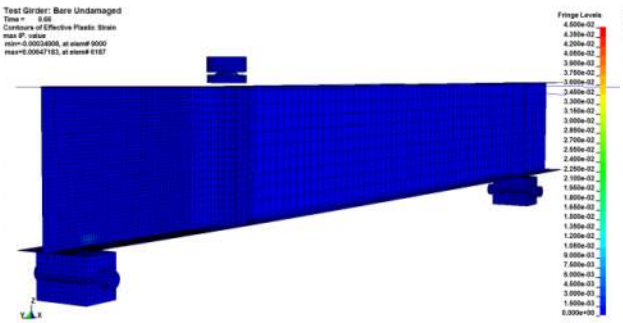

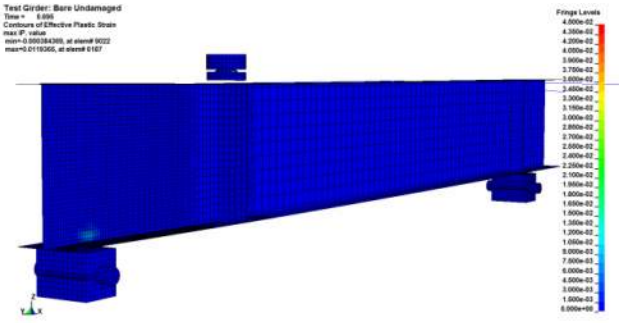

Figure D.1.21 Undamaged Plastic Strain: 140 kip

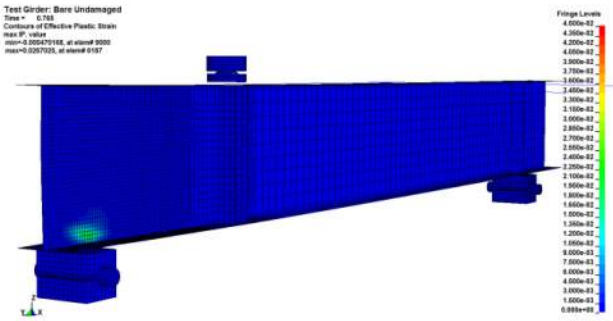

Figure D.1.22 Undamaged Plastic Strain: 160 kip

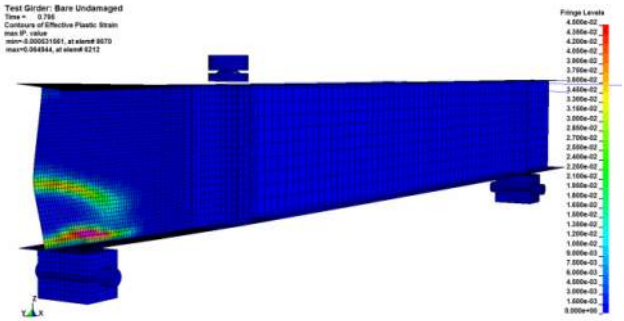

Figure D.1.23 Undamaged Plastic Strain: 193 kip

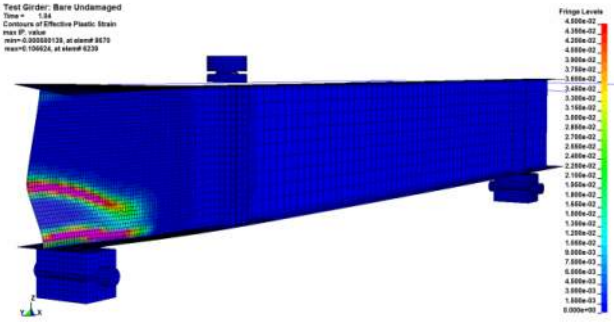

Figure D.1.24 Undamaged Plastic Strain: Failure

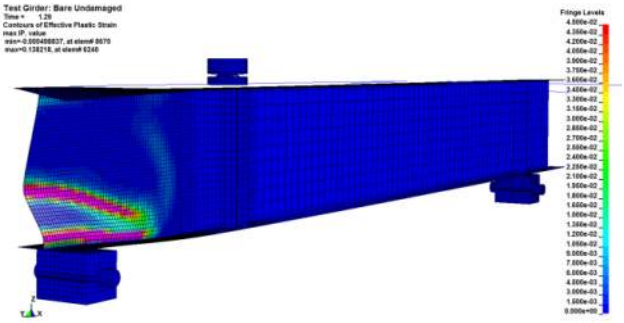

Figure D.1.25 Undamaged Plastic Strain: +0.25in

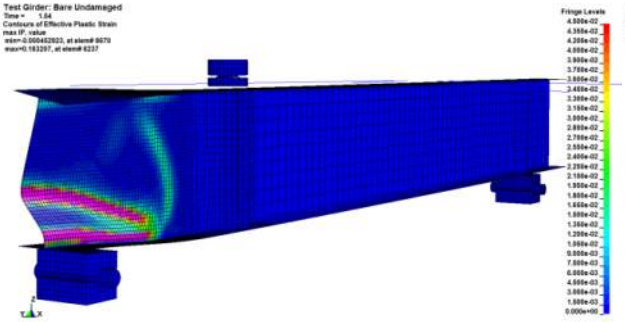

Figure D.1.26 Undamaged Plastic Strain: +0.50in

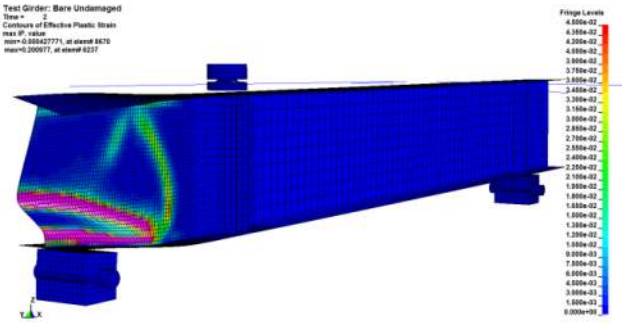

Figure D.1.27 Undamaged Plastic Strain: +0.75in

Figure D.1.28 Undamaged Plastic Strain: +1.25in

D.1.3 Undamaged - Triaxiality Factor ($^{\sigma e}/_{\sigma m}$) (-0.55 - 0.55)

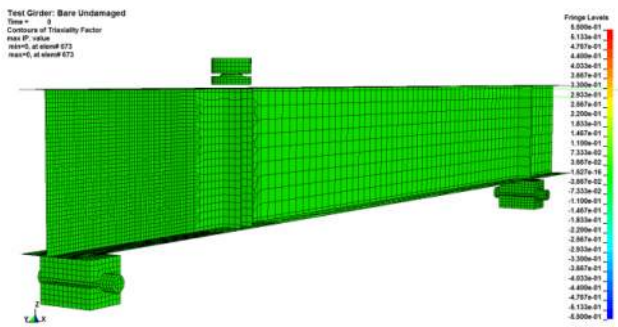

Figure D.1.29 Undamaged Triaxiality: 0 kip

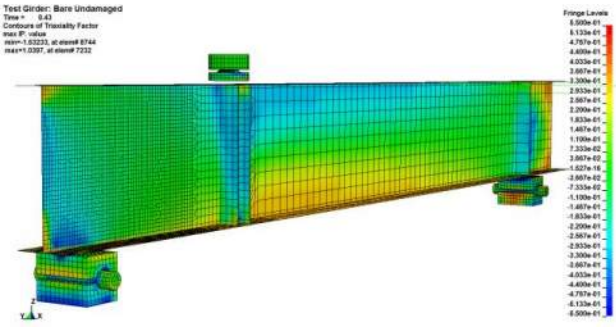

Figure D.1.30 Undamaged Triaxiality: 40 kip

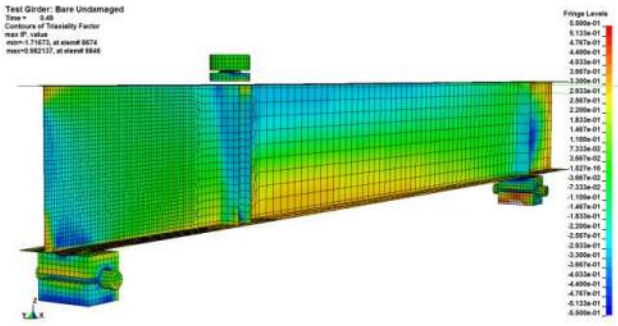

Figure D.1.31 Undamaged Triaxiality: 60 kip

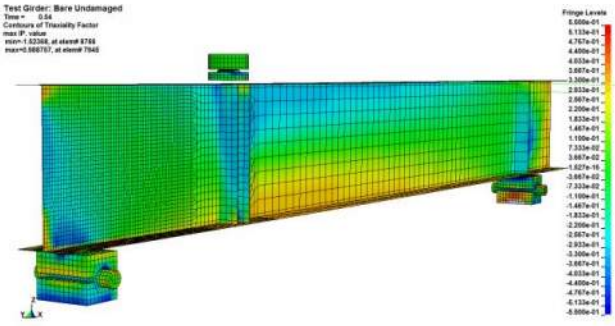

Figure D.1.32 Undamaged Triaxiality: 80 kip

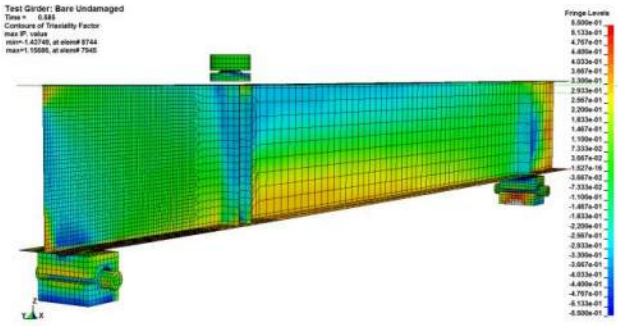

Figure D.1.33 Undamaged Triaxiality: 100 kip

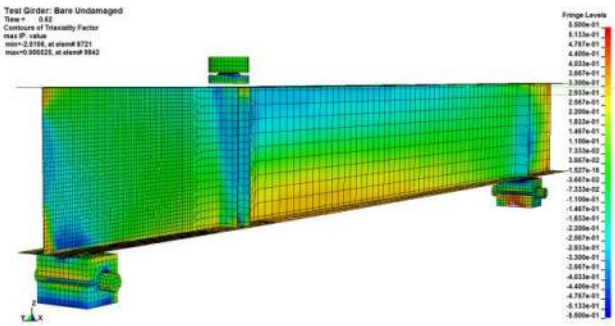

Figure D.1.34 Undamaged Triaxiality: 120 kip

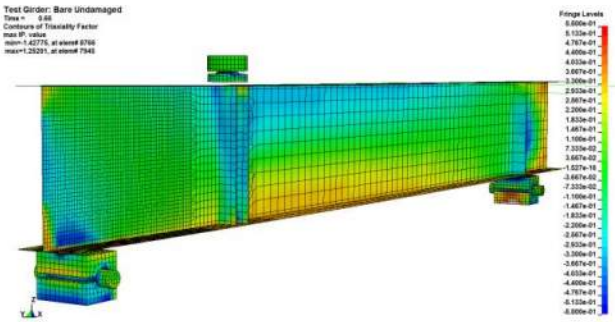

Figure D.1.35 Undamaged Triaxiality: 140 kip

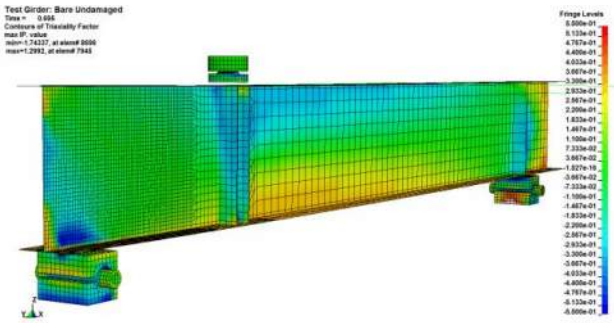

Figure D.1.36 Undamaged Triaxiality: 160 kip

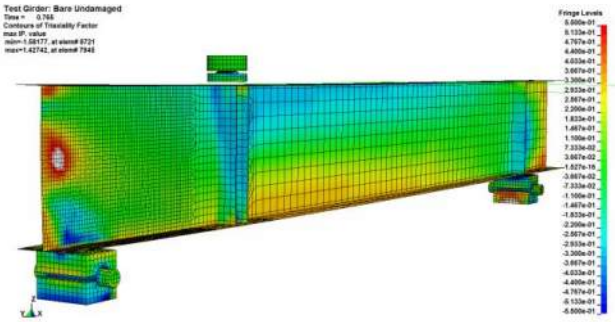

Figure D.1.37 Undamaged Triaxiality: 193 kip

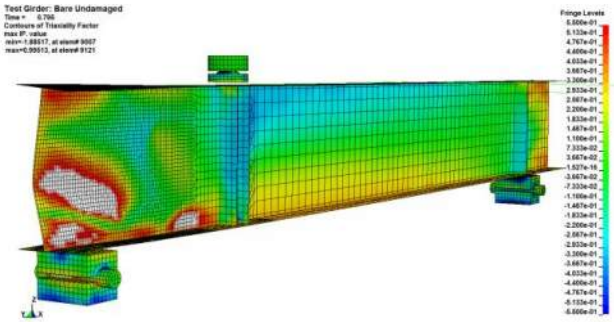

Figure D.1.38 Undamaged Triaxiality: Failure

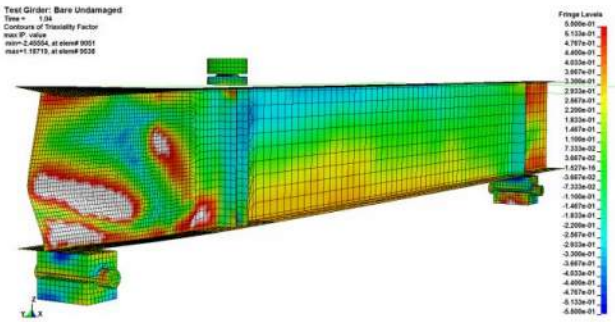

Figure D.1.39 Undamaged Triaxiality: +0.25 in

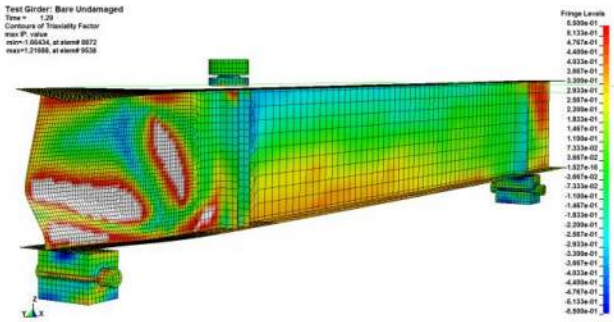

Figure D.1.40 Undamaged Triaxiality: +0.50 in

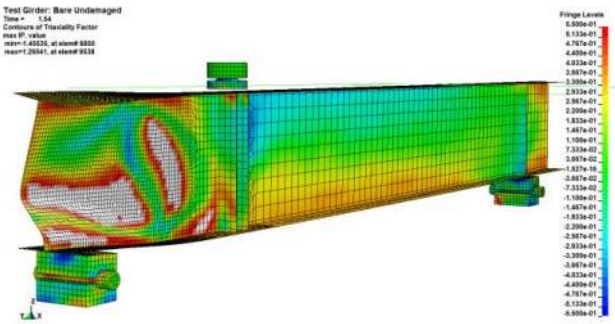

Figure D.1.41 Undamaged Triaxiality: +0.75 in

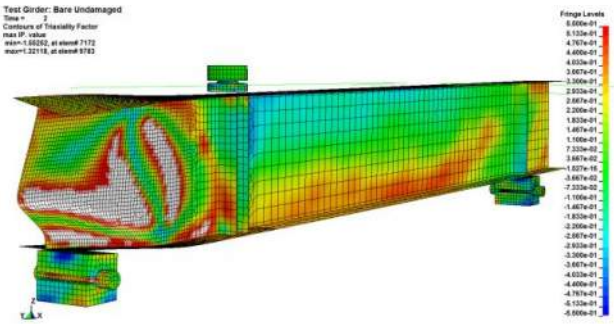

Figure D.1.42 Undamaged Triaxiality: +1.25 in

D.2 DAMAGED GIRDER

D.2.1 Damaged - Girder Von Mises Stress Distribution (0 - 70 ksi)

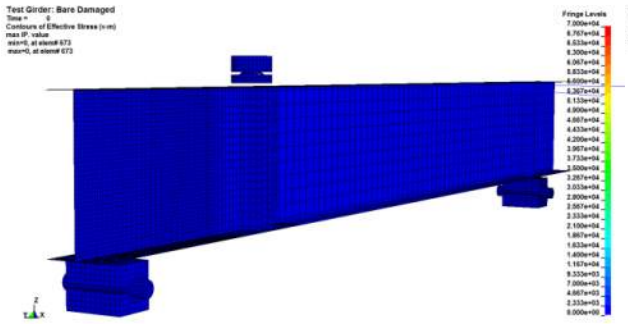

Figure D.2.1 Damaged Von Mises: 0 kip

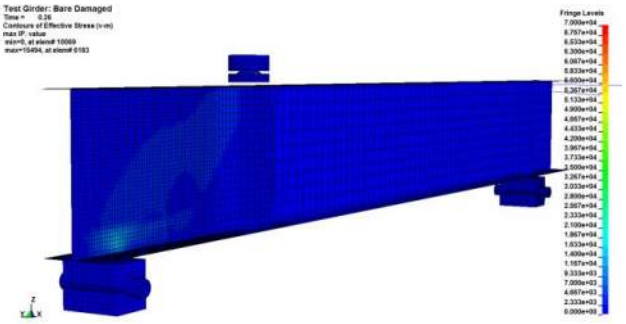

Figure D.2.2 Damaged Von Mises: 8 kip

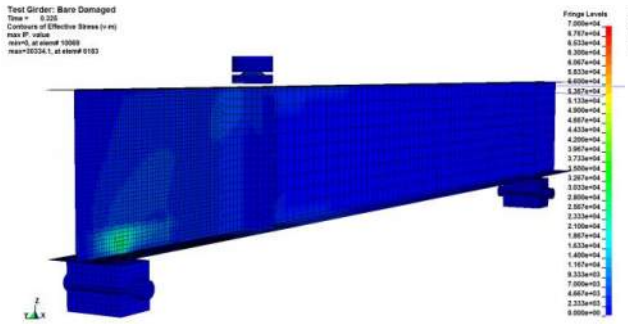

Figure D.2.3 Damaged Von Mises: 16 kip

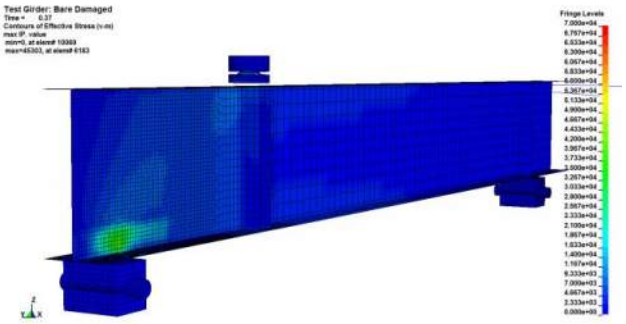

Figure D.2.4 Damaged Von Mises: 24 kip

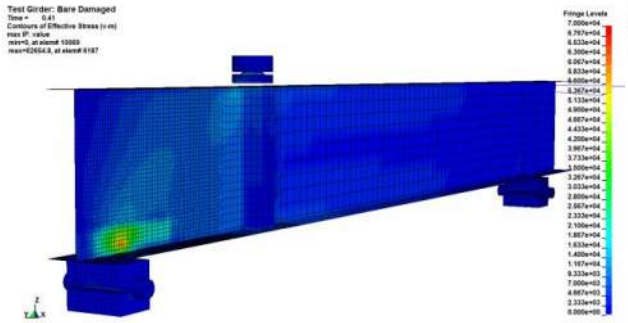

Figure D.2.5Damaged Von Mises: 32 kip

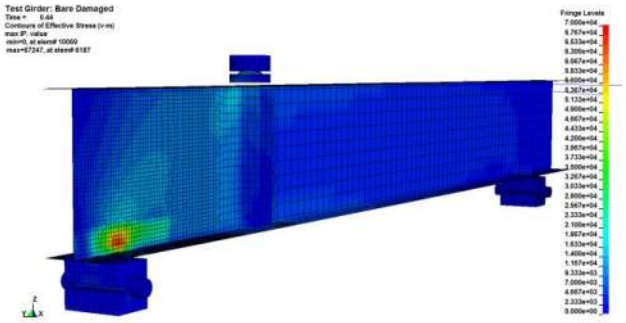

Figure D.2.6 Damaged Von Mises: 40 kip

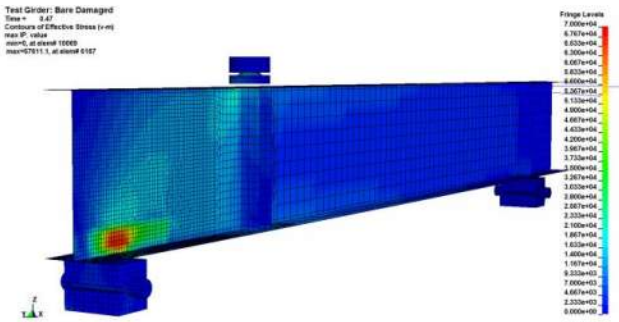

Figure D.2.7 Damaged Von Mises: 48 kip

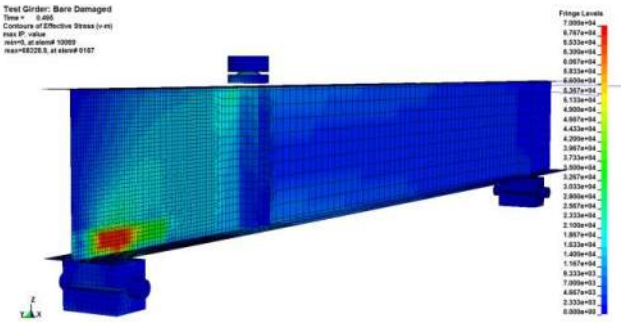

Figure D.2.8 Damaged Von Mises: 56 kip

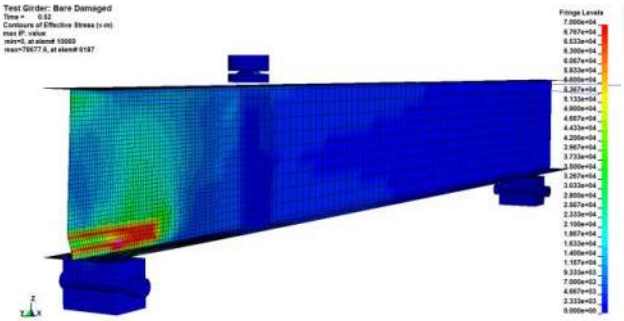

Figure D.2.9 Damaged Von Mises: Failure

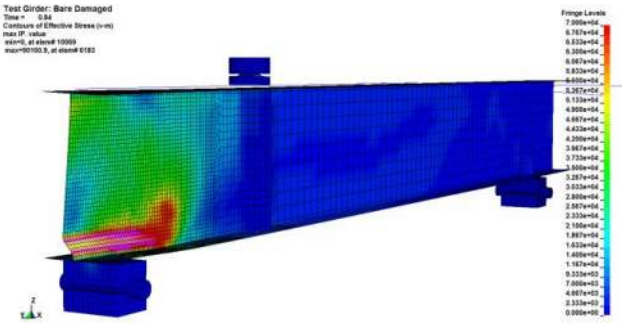

Figure D.2.10 Damaged Von Mises: +0.25 in

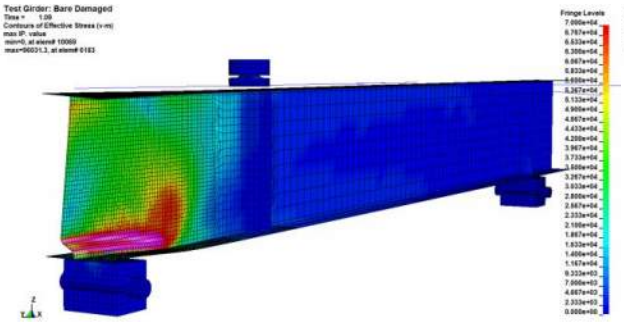

Figure D.2.11 Damaged Von Mises: +0.50 in

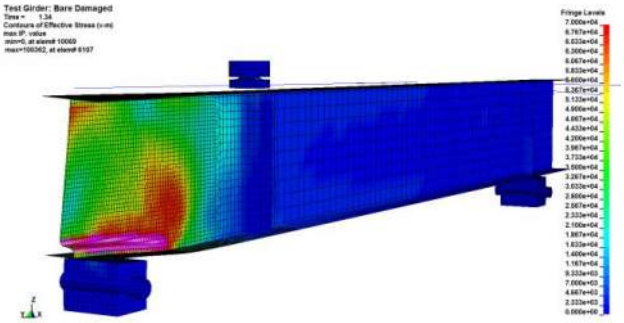

Figure D.2.12 Damaged Von Mises: +0.75 in

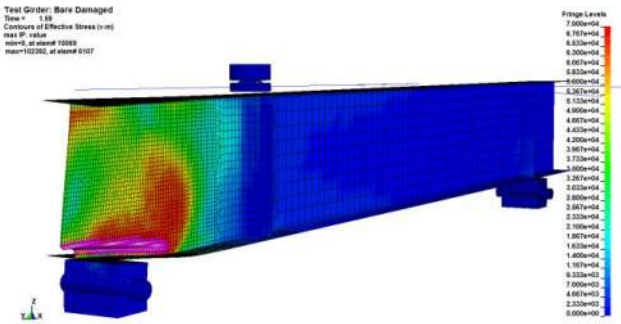

Figure D.2.13 Damaged Von Mises: +1.00 in

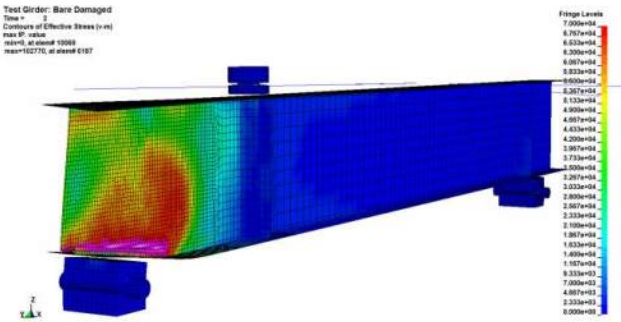

Figure D.2.14 Damaged Von Mises: +1.50 in

D.2.2 Damaged - Girder Plastic Strain Development (0 - 45,000 με)

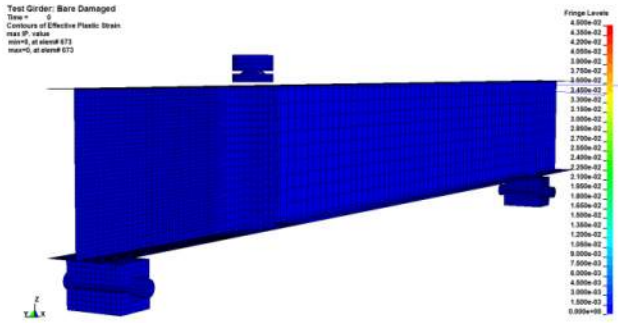

Figure D.2.15 Damaged Plastic Strain: 0 kip

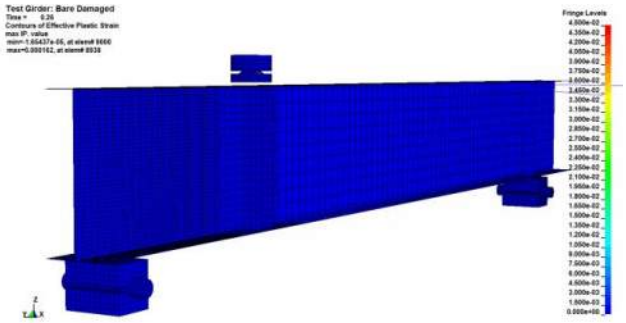

Figure D.2.16 Damaged Plastic Strain: 8 kip

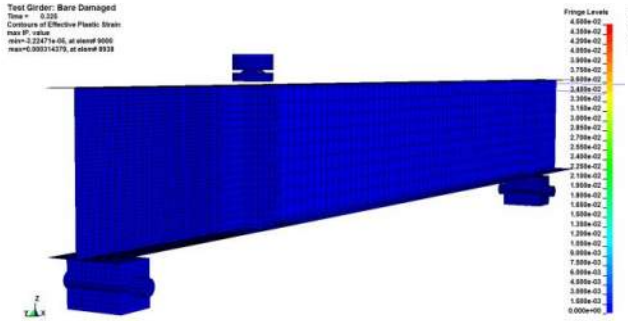

Figure D.2.17 Damaged Plastic Strain: 16 kip

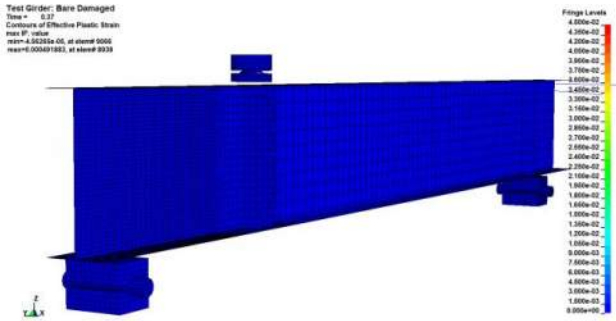

Figure D.2.18 Damaged Plastic Strain: 24 kip

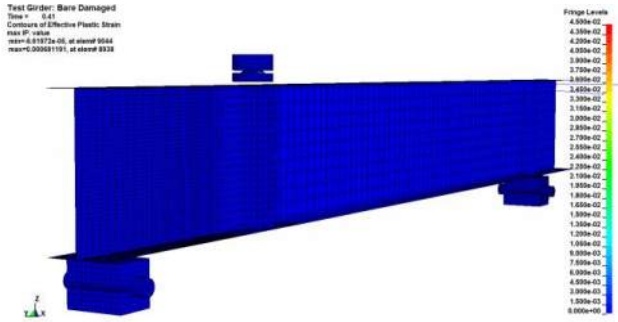

Figure D.2.19 Damaged Plastic Strain: 32 kip

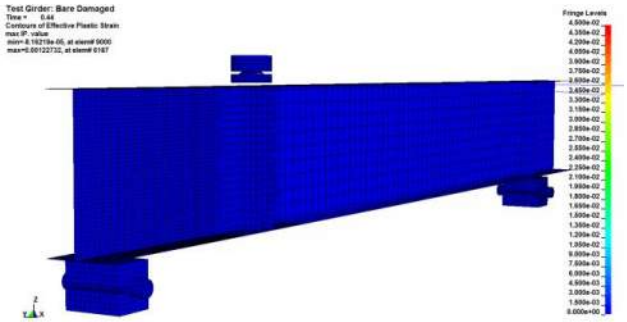

Figure D.2.20 Damaged Plastic Strain: 40 kip

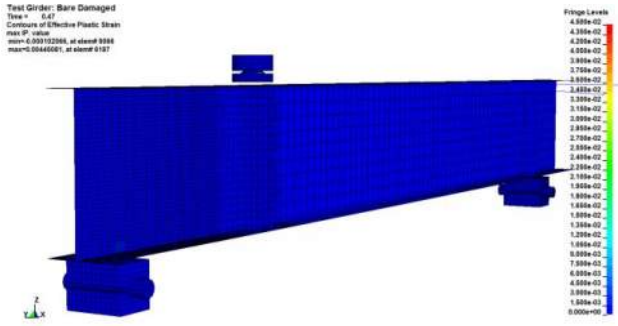

Figure D.2.21 Damaged Plastic Strain: 48 kip

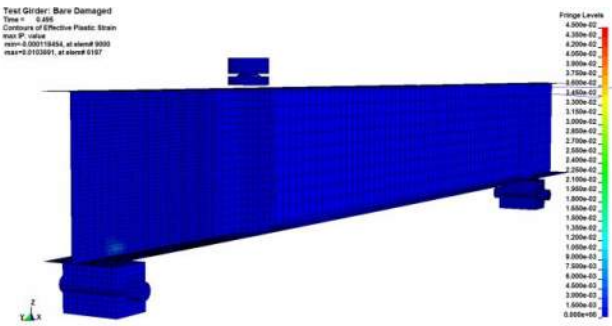

Figure D.2.22 Damaged Plastic Strain: 56 kip

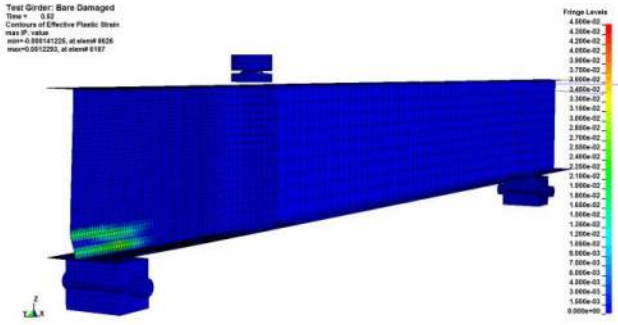

Figure D.2.23 Damaged Plastic Strain: Failure

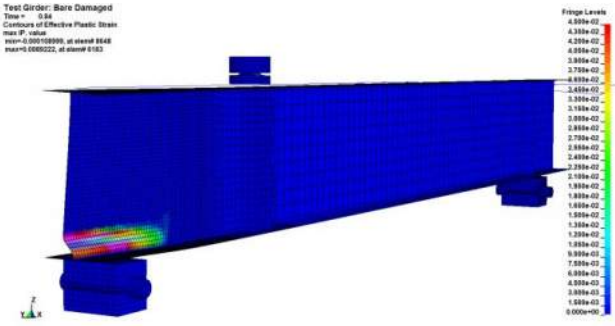

Figure D.2.24 Damaged Plastic Strain: +0.25 in

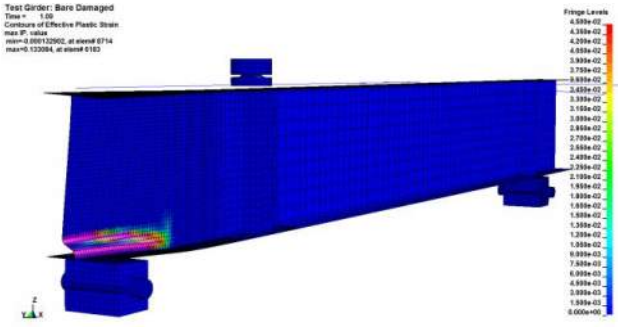

Figure D.2.25 Damaged Plastic Strain: +0.50 in

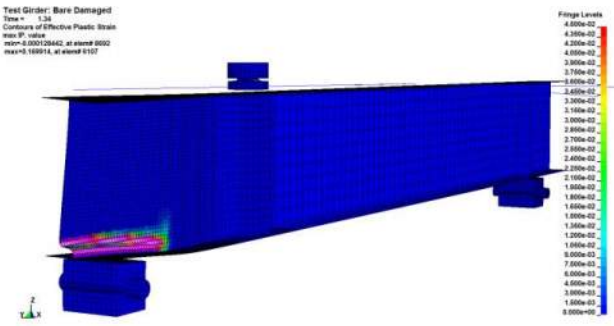

Figure D.2.26 Damaged Plastic Strain: +0.75 in

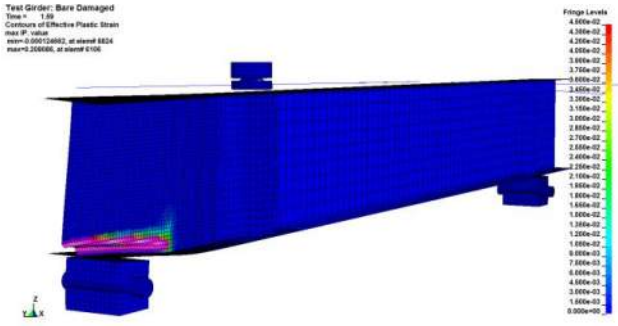

Figure D.2.27 Damaged Plastic Strain: +1.00 in

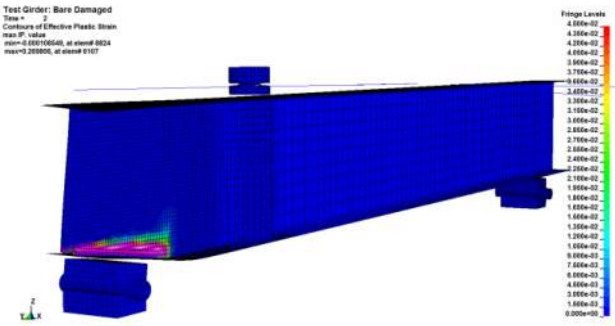

Figure D.2.28 Damaged Plastic Strain: +1.50 in

D.2.3 Damaged - Triaxiality Factor ($^{\sigma e}/_{\sigma m}$) (-0.55 - 0.55)

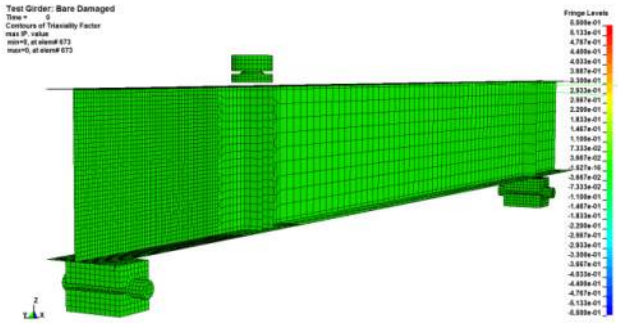

Figure D.2.29 Damaged Triaxiality: 0 kip

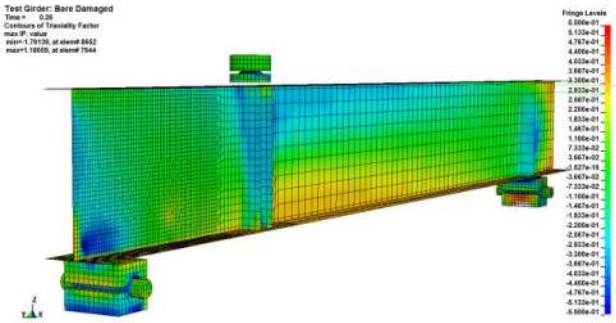

Figure D.2.30 Damaged Triaxiality: 8 kip

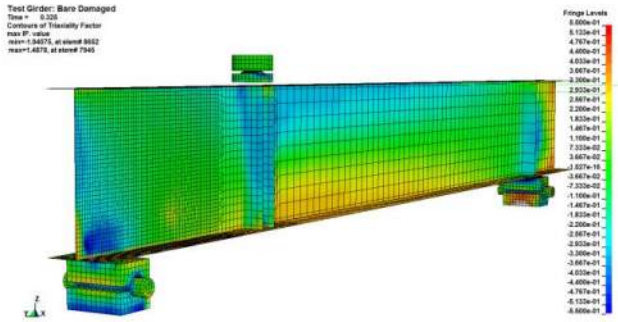

Figure D.2.31 Damaged Triaxiality: 16 kip

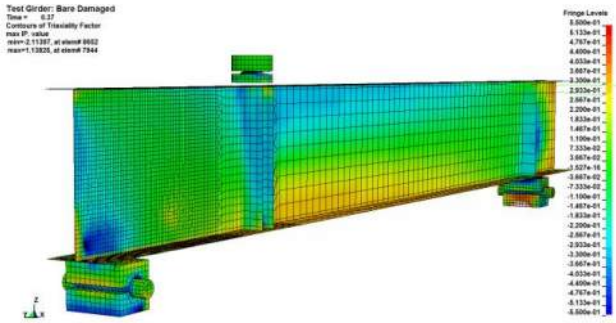

Figure D.2.32 Damaged Triaxiality: 24 kip

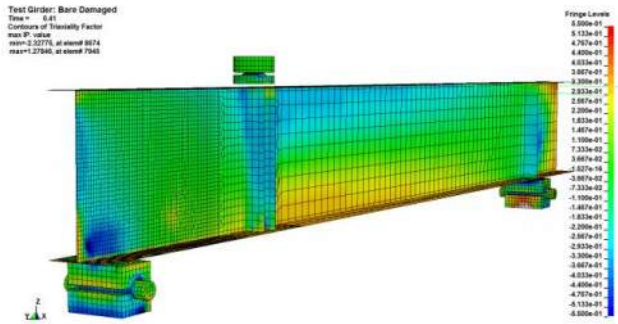

Figure D.2.33 Damaged Triaxiality: 32 kip

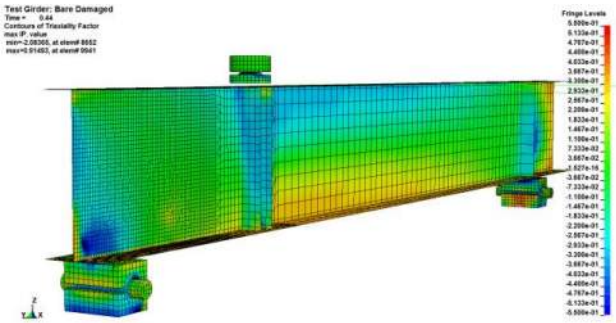

Figure D.2.34 Damaged Triaxiality: 40 kip

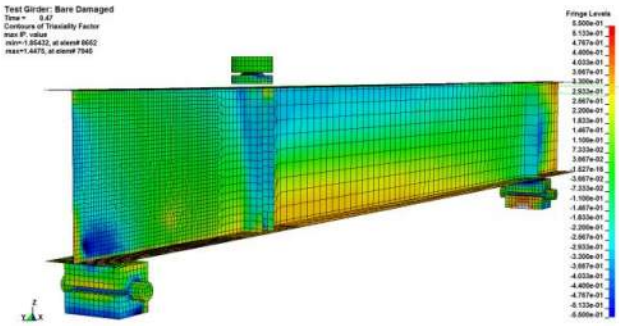

Figure D.2.35 Damaged Triaxiality: 48 kip

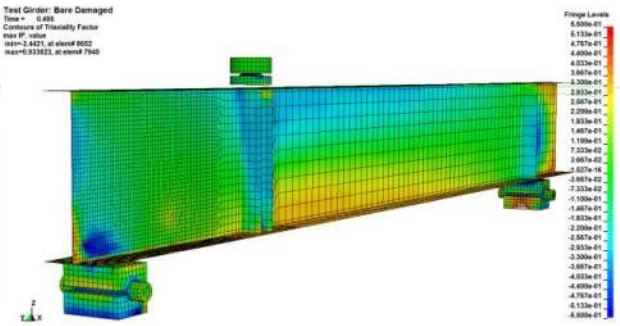

Figure D.2.36 Damaged Triaxiality: 56 kip

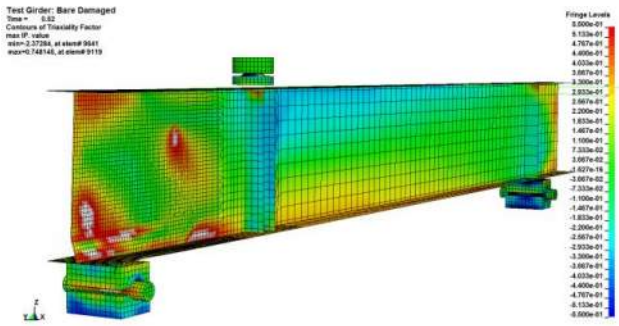

Figure D.2.37 Damaged Triaxiality: Failure

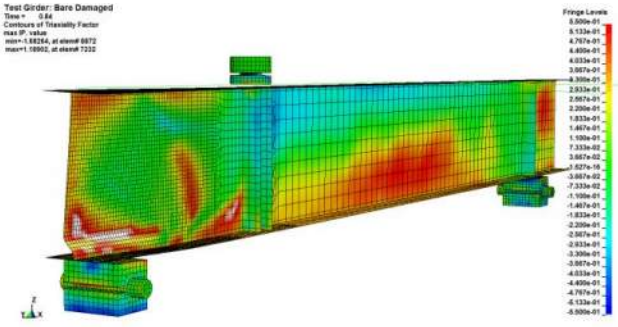

Figure D.2.38 Damaged Triaxiality: +0.25 in

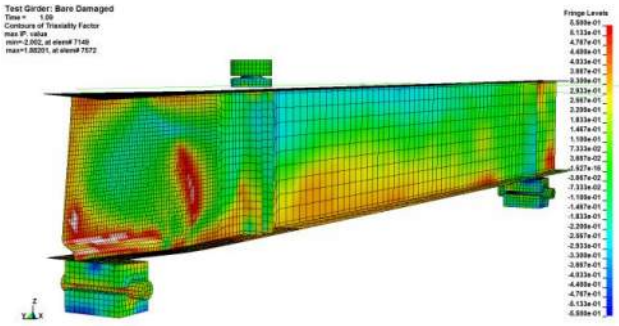

Figure D.2.39 Damaged Triaxiality: +0.50 in

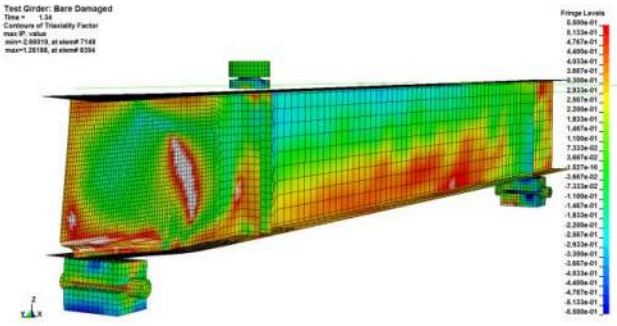

Figure D.2.40 Damaged Triaxiality: +0.75 in

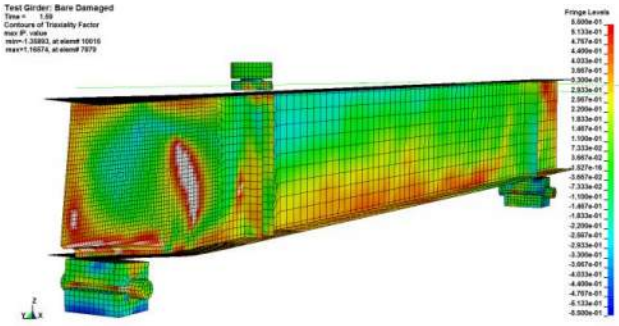

Figure D.2.41 Damaged Triaxiality: +1.00 in

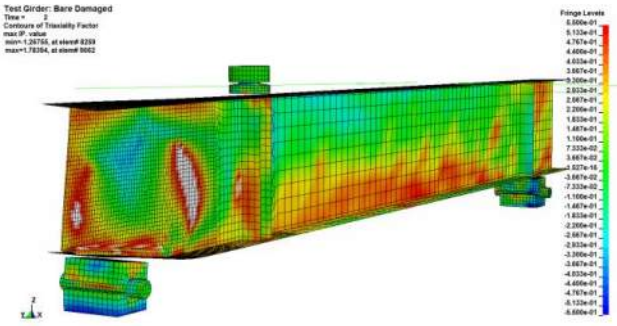

Figure D.2.42 Damaged Triaxiality: +1.50 in

D.3 REPAIRED GIRDER

D.3.1 Repaired - Girder Von Mises Stress Distribution (0 - 70 ksi)

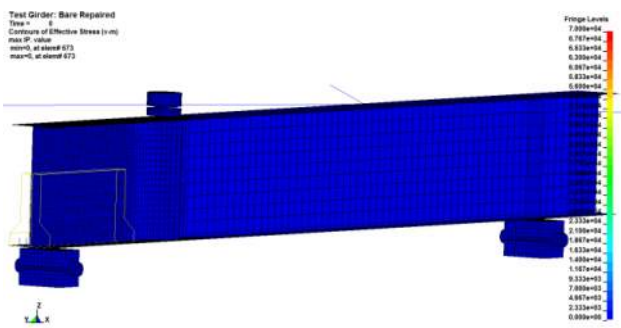

Figure D.3.1 Repaired Von Mises: 0 kip

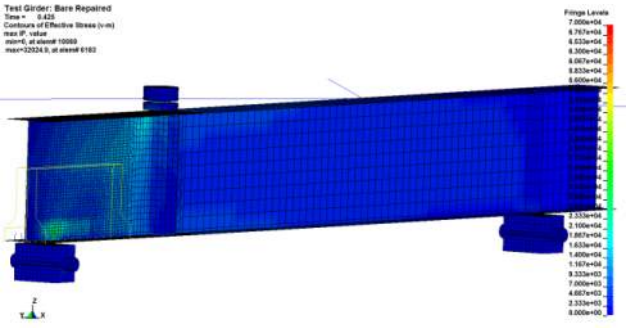

Figure D.3.2 Repaired Von Mises: 40 kip

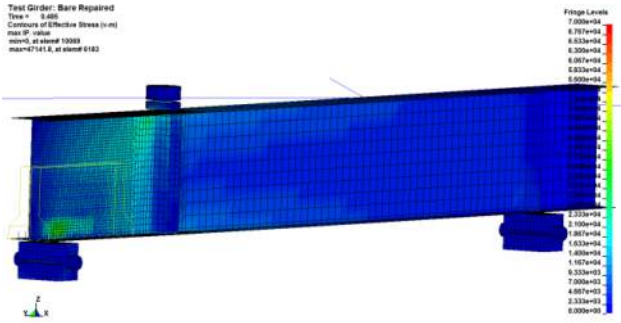

Figure D.3.3 Repaired Von Mises: 60 kip

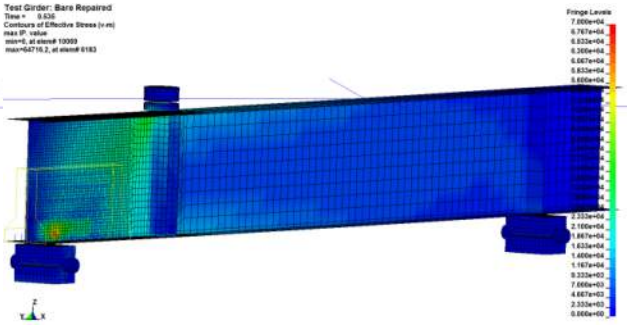

Figure D.3.4 Repaired Von Mises: 80 kip

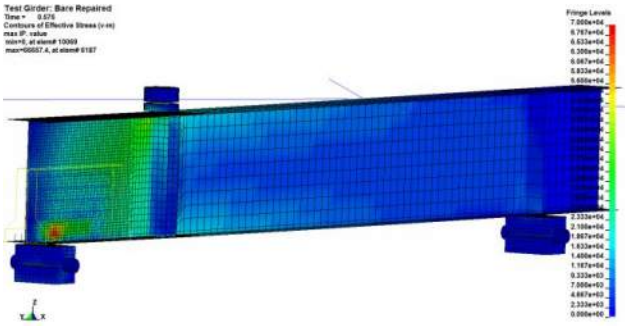

Figure D.3.5 Repaired Von Mises: 100 kip

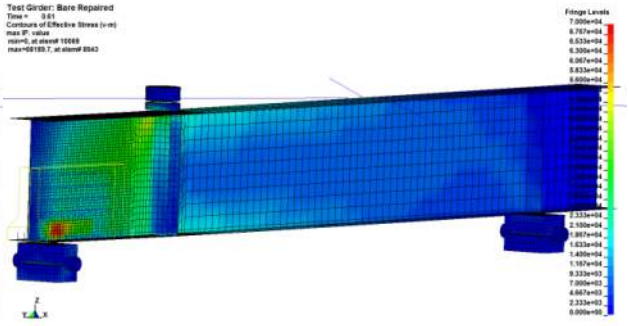

Figure D.3.6 Repaired Von Mises: 120 kip

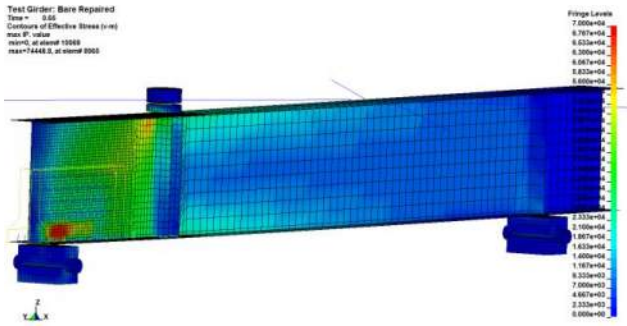

Figure D.3.7 Repaired Von Mises: 140 kip

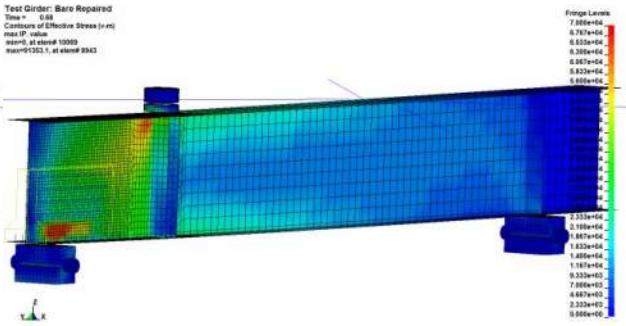

Figure D.3.8 Repaired Von Mises: 160 kip

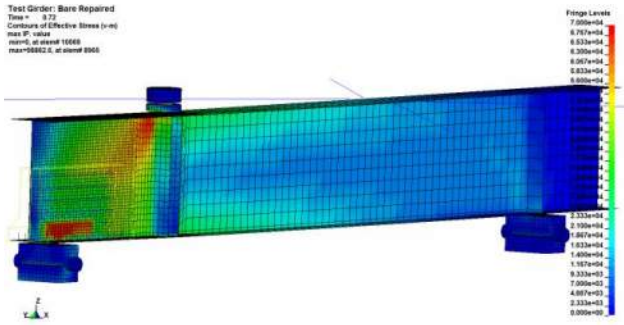

Figure D.3.9 Repaired Von Mises: 180 kip

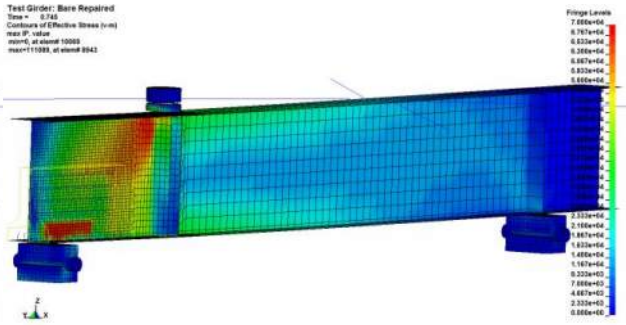

Figure D.3.10 Repaired Von Mises: 200 kip

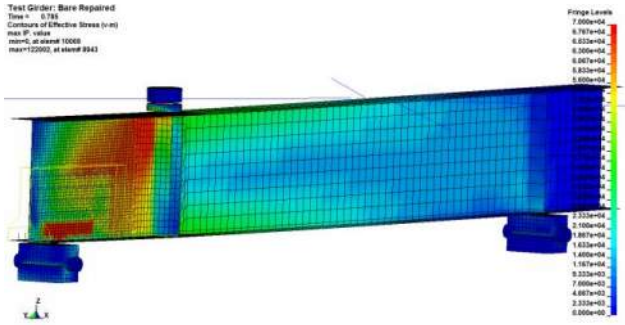

Figure D.3.11 Repaired Von Mises: 220 kip

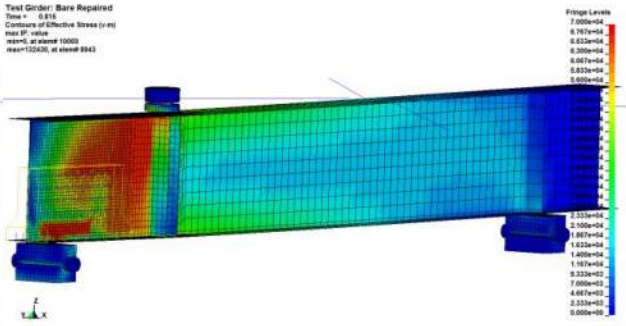

Figure D.3.12 Repaired Von Mises: 240 kip

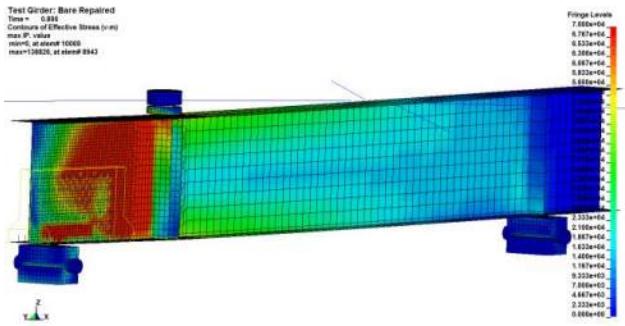

Figure D.3.13 Repaired Von Mises: 260 kip

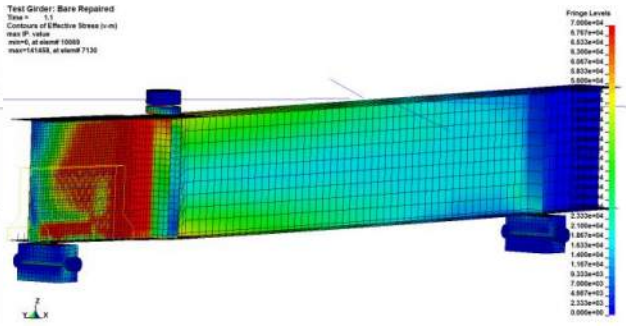

Figure D.3.14 Repaired Von Mises: 268 kip

D.3.2 Repaired - Girder Plastic Strain Development (0 - 45,000 με)

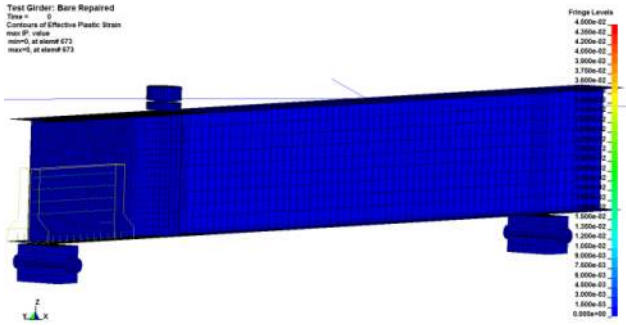

Figure D.3.15 Repaired Plastic Strain: 0 kip

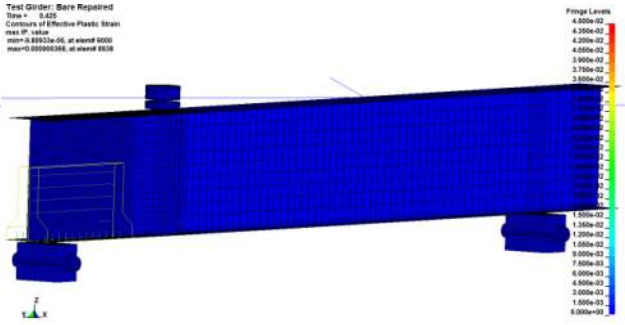

Figure D.3.16 Repaired Plastic Strain: 40 kip

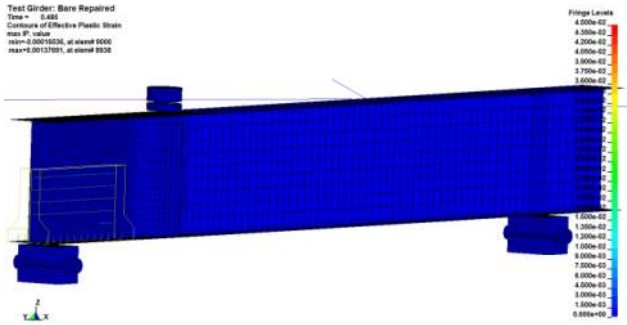

Figure D.3.17 Repaired Plastic Strain: 60 kip

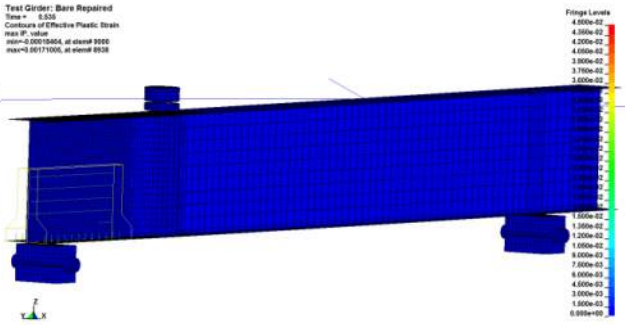

Figure D.3.18 Repaired Plastic Strain: 80 kip

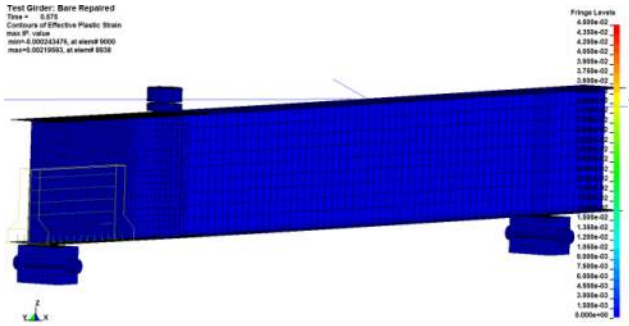

Figure D.3.19 Repaired Plastic Strain: 100 kip

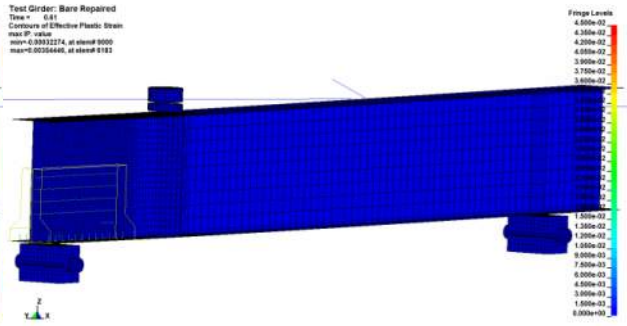

Figure D.3.20 Repaired Plastic Strain: 120 kip

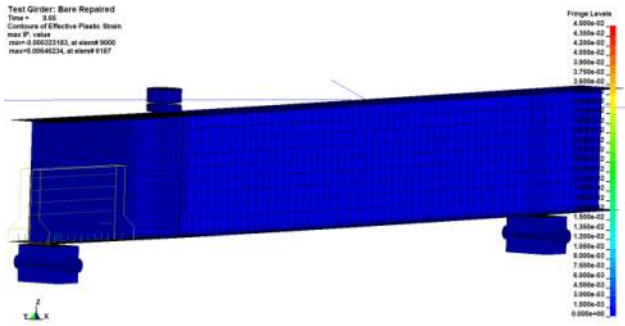

Figure D.3.21 Repaired Plastic Strain: 140 kip

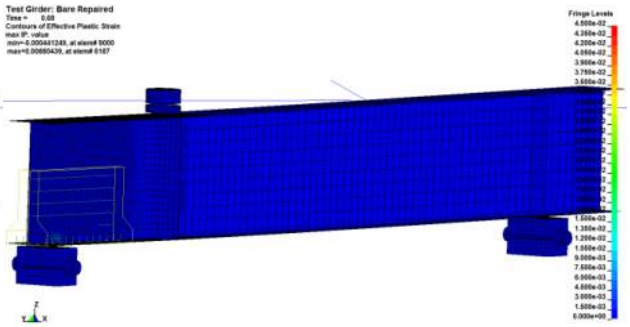

Figure D.3.22 Repaired Plastic Strain: 160 kip

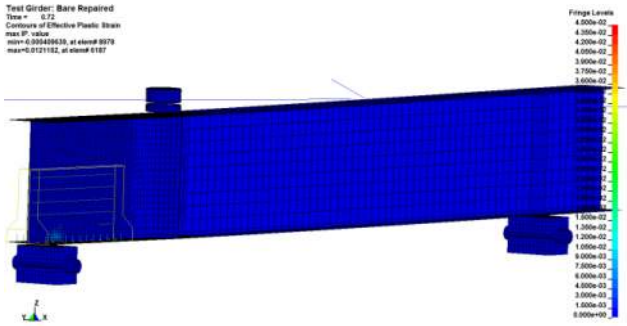

Figure D.3.23 Repaired Plastic Strain: 180 kip

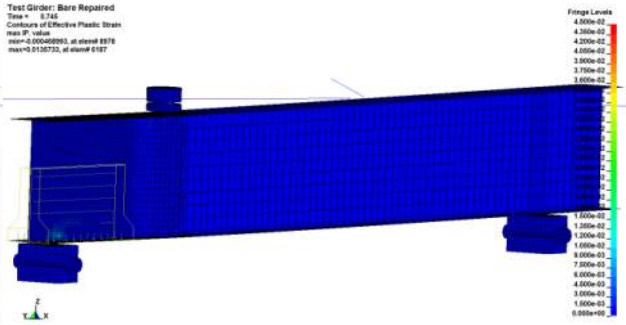

Figure D.3.24 Repaired Plastic Strain: 200 kip

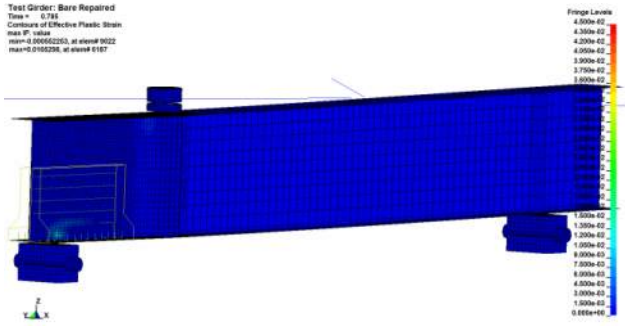

Figure D.3.25 Repaired Plastic Strain: 220 kip

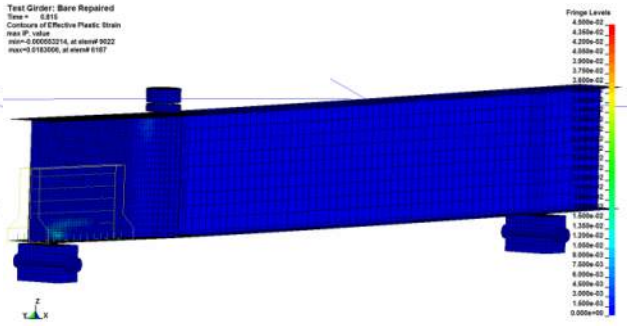

Figure D.3.26 Repaired Plastic Strain: 240 kip

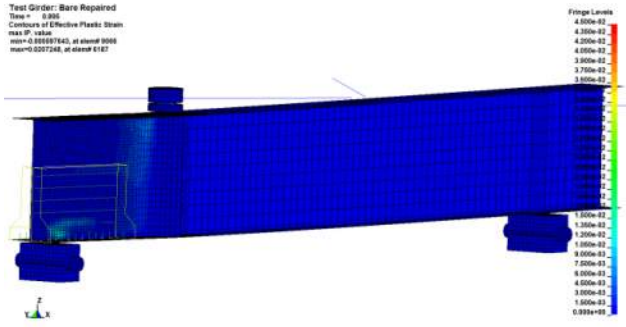

Figure D.3.27 Repaired Plastic Strain: 260 kip

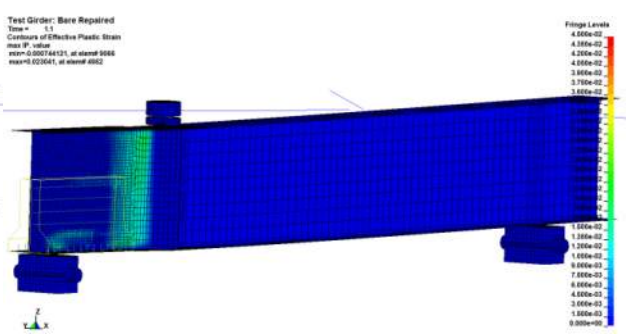

Figure D.3.28 Repaired Plastic Strain: 268 kip

D.3.3 Repaired - Triaxiality Factor ($^{\sigma e}/_{\sigma m}$) (-0.55 - 0.55)

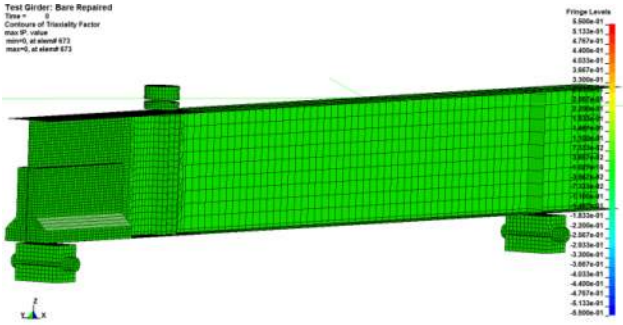

Figure D.3.29 Repaired Triaxiality: 0 kip

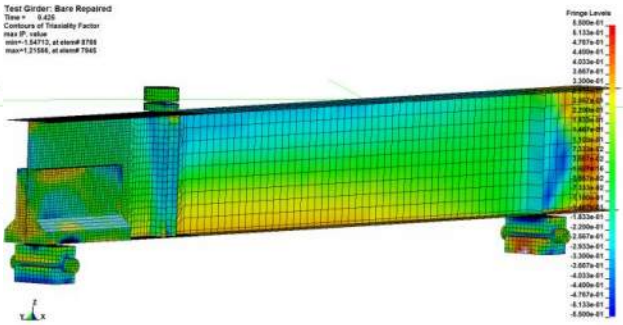

Figure D.3.30 Repaired Triaxiality: 40 kip

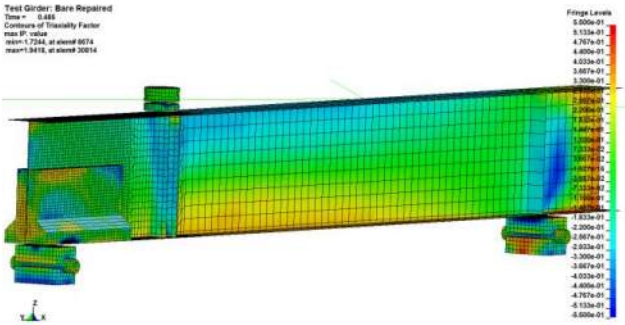

Figure D.3.31 Repaired Triaxiality: 60 kip

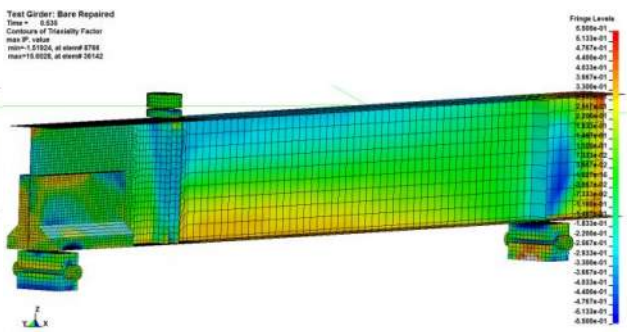

Figure D.3.32 Repaired Triaxiality: 80 kip

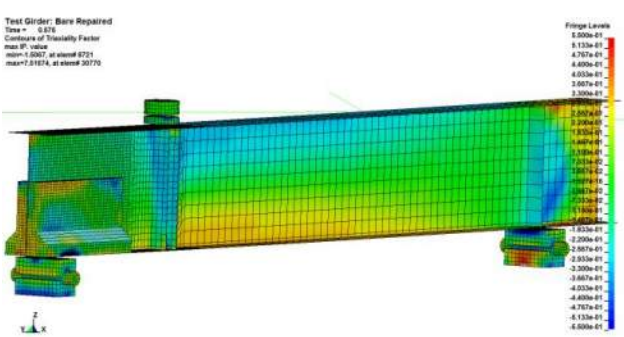

Figure D.3.33 Repaired Triaxiality: 100 kip

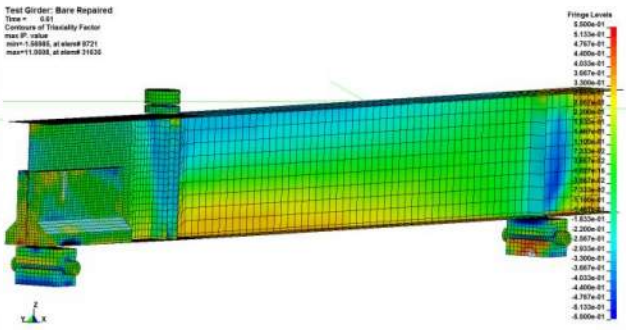

Figure D.3.34 Repaired Triaxiality: 120 kip

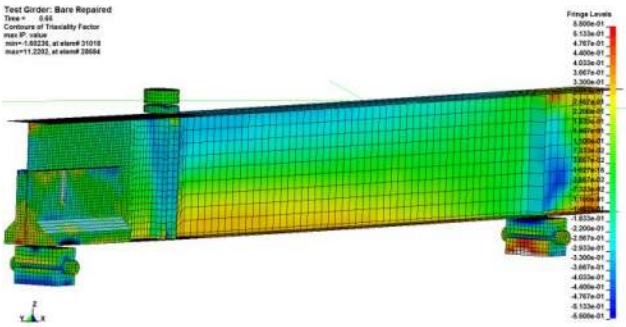

Figure D.3.35 Repaired Triaxiality: 140 kip

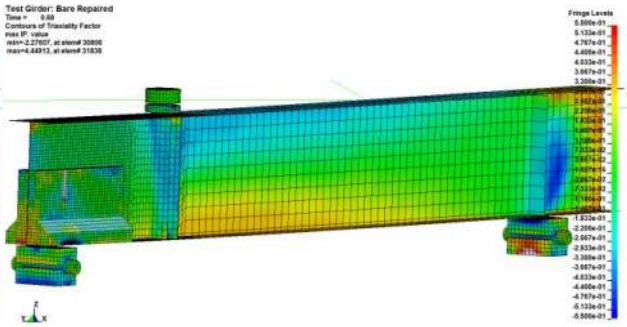

Figure D.3.36 Repaired Triaxiality: 160 kip

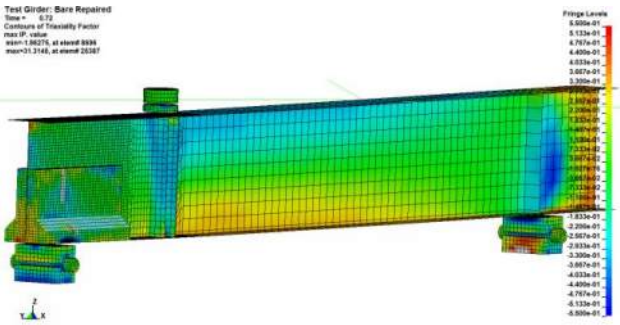

Figure D.3.37 Repaired Triaxiality: 180 kip

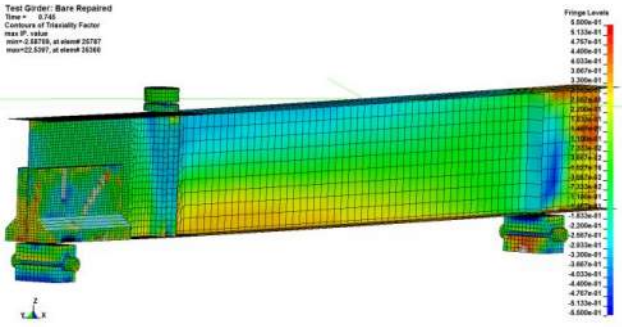

Figure D.3.38 Repaired Triaxiality: 200 kip

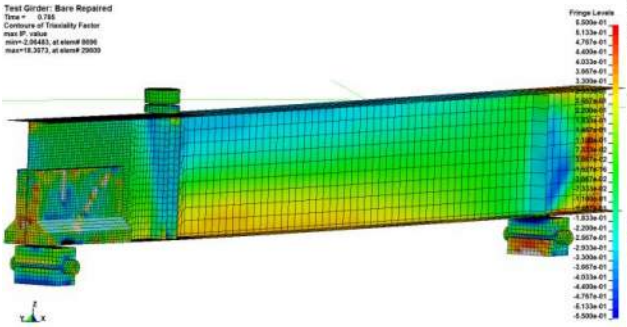

Figure D.3.39 Repaired Triaxiality: 220 kip

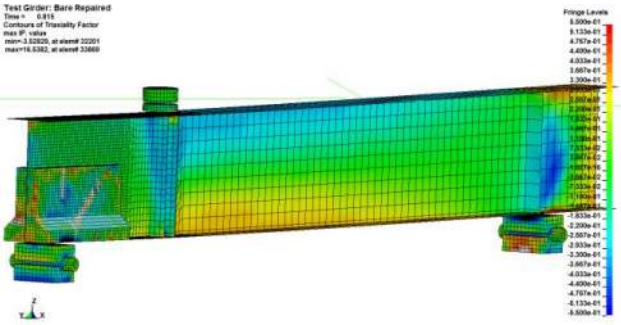

Figure D.3.40 Repaired Triaxiality: 240 kip

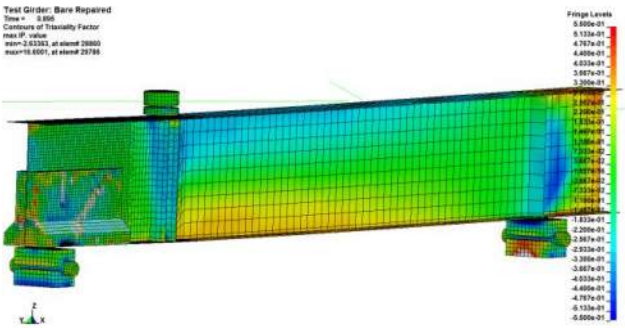

Figure D.3.41 Repaired Triaxiality: 260 kip

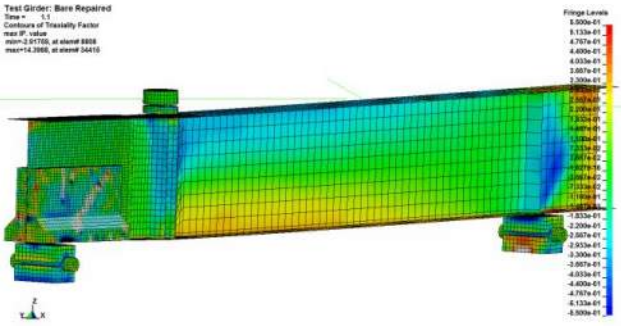

Figure D.3.42 Repaired Triaxiality: 268 kip

D.3.4 Repaired - Concrete Scaled Damage Measure (δ) (0 - 2)

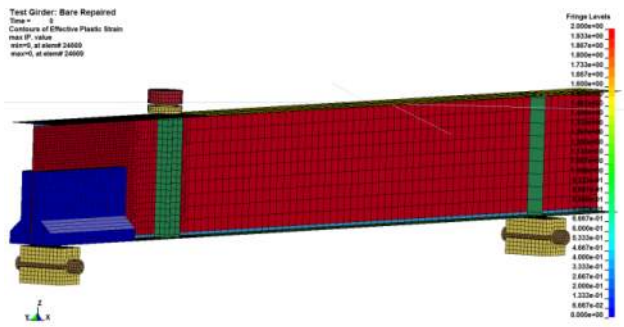

Figure D.3.43 Concrete Scaled Damage: 0 kip

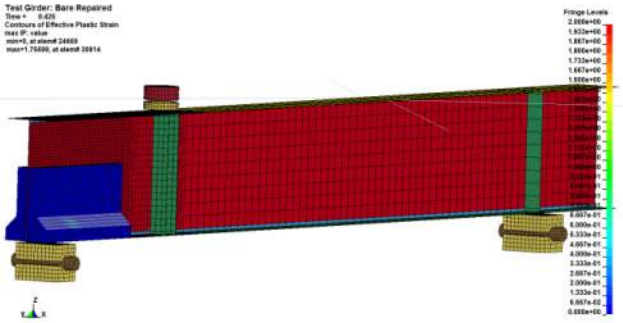

Figure D.3.44 Concrete Scaled Damage: 40 kip

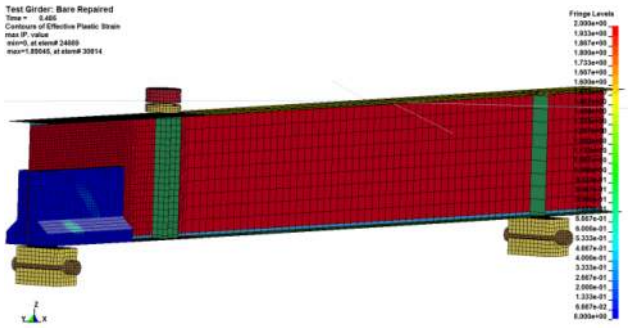

Figure D.3.45 Concrete Scaled Damage: 60 kip

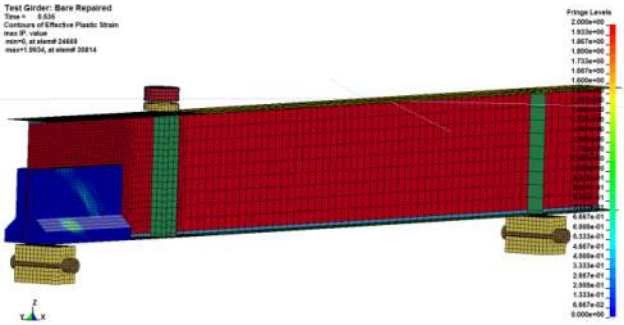

Figure D.3.46 Concrete Scaled Damage: 80 kip

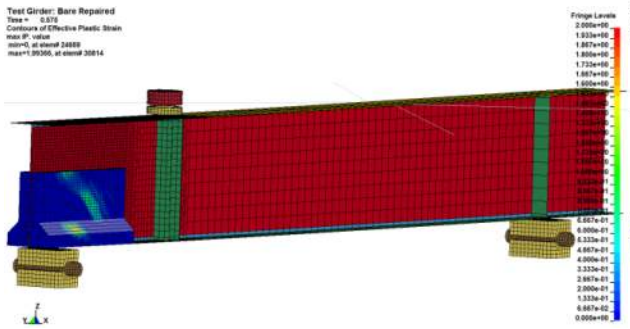

Figure D.3.47 Concrete Scaled Damage: 100 kip

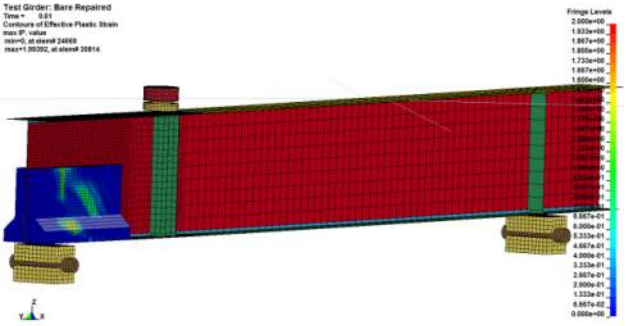

Figure D.3.48 Concrete Scaled Damage: 120 kip

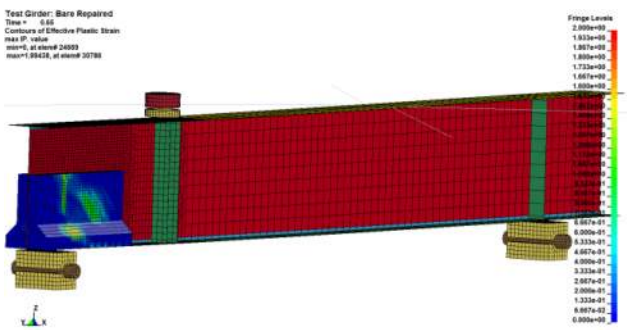

Figure D.3.49 Concrete Scaled Damage: 140 kip

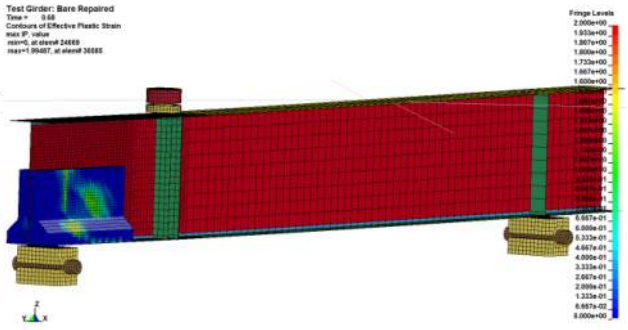

Figure D.3.50 Concrete Scaled Damage: 160 kip

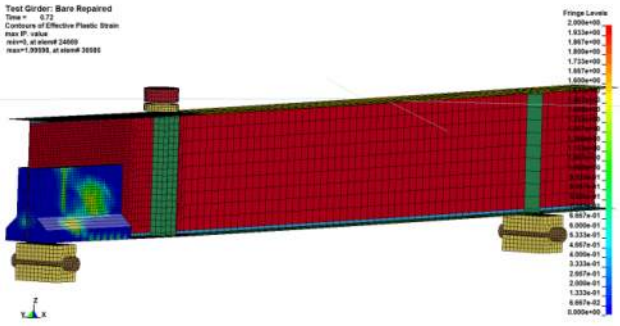

Figure D.3.51 Concrete Scaled Damage: 180 kip

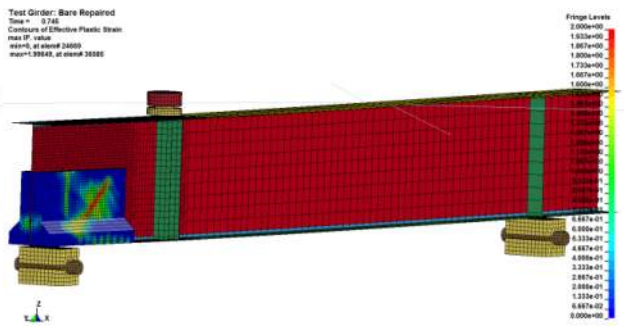

Figure D.3.52 Concrete Scaled Damage: 200 kip

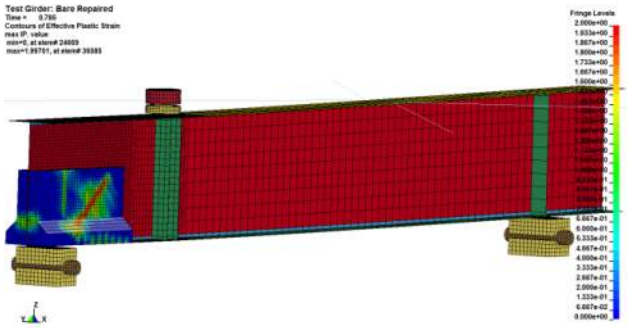

Figure D.3.53 Concrete Scaled Damage: 220 kip

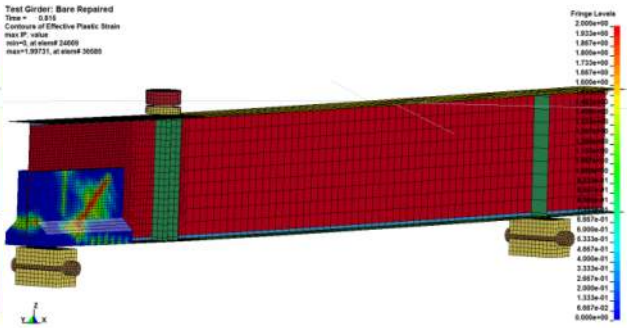

Figure D.3.54 Concrete Scaled Damage: 240 kip

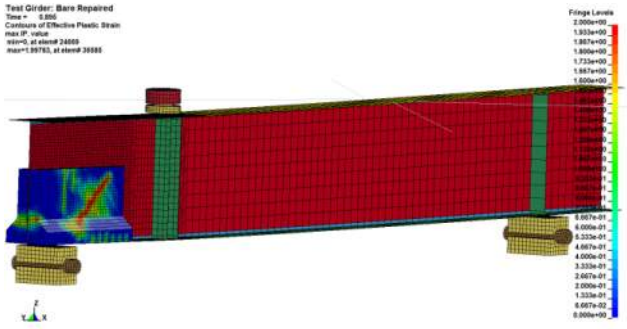

Figure D.3.55 Concrete Scaled Damage: 260 kip

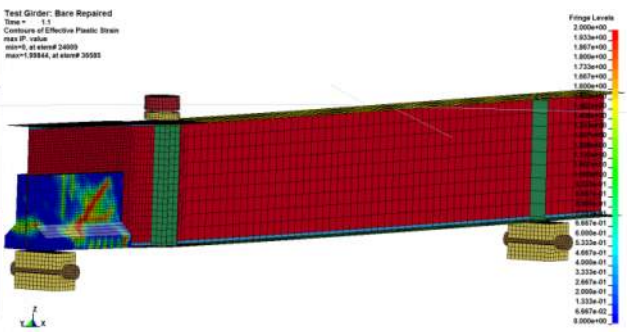

Figure D.3.56 Concrete Scaled Damage: 268 kip

Appendix E. Sample Matlab Codes

E.1 SHEAR BOX STRAIN CALCULATION

```
%MatLab Code to convert shear box potentiometer lengths to position and
    %convert those positions to strains

 %NOTE: points 3 and 4 reversed based on description in Section 3.5.3

% Define the initial lengths of potentiometers
VR10=20.5;
VR20=20.625;
HR10=16.0625;
HR20=16.0;
DR10=26;
VL10=20.5;
VL20=20.5;
HL10=16.25;
HL20=16;
DL10=26.125;
BR0=4.625;

%divines initial displacement readings for each potentiometer
INIT=[-0.126834 -0.217012   -0.063416   -0.079871   -0.083779   -0.463116
    -0.349082   -0.210417   -0.069622   -0.536419 -0.133039 0.807039];

%Define location of point in Q4 element to read strain (based off center)
X=0;
Y=0;

%load potentiometer and bearing displacement data
BOX=load('RepPot_05.txt');
ROT=load('RepRot_05.txt');



%Factor to correct for reversed displacement reading in the damaged and
    %repaired tests
m=-1;

%-------------------------------------------------------------------
%Perform initial calculations

RA=0;                                              %initial theta
```

```
AR1=acos((DR10^2+HR10^2-VR20^2)/(2*DR10*HR10));  %initial alpha right
AR2=acos((DR10^2+VR10^2-HR20^2)/(2*DR10*VR10));  %initial beta right
AL1=acos((DL10^2+HL10^2-VL20^2)/(2*DL10*HL10));  %initial alpha left
AL2=acos((DL10^2+VL10^2-HL20^2)/(2*DL10*VL10));  %initial beta left

%calculate initial x y locations
xr20=HR10*cos(RA);
yr20=-HR10*sin(RA);
xr30=VR10*sin(pi()/2+RA-AR1-AR2);
yr30=VR10*cos(pi()/2+RA-AR1-AR2);
xr40=DR10*cos(AR1-RA);
yr40=DR10*sin(AR1-RA);
xl20=HL10*cos(RA);
yl20=-HL10*sin(RA);
xl30=VL10*sin(pi()/2+RA-AL1-AL2);
yl30=VL10*cos(pi()/2+RA-AL1-AL2);
xl40=DL10*cos(AL1-RA);
yl40=DL10*sin(AL1-RA);

% define a b and the denominator value (4ab) for strain field
ar=(HR10+HR20)/4;
br=(VR10+VR20)/4;
al=(HL10+HL20)/4;
bl=(VL10+VL20)/4;
dr=1e6/(4*ar*br);  %1e6 for microstrain
dl=1e6/(4*al*bl);

STR=zeros(length(BOX),6);  %define output strain matrix

%increment through data
for i=1:length(BOX)

    %calc current length of each potentiometer based on initial length,
        %displacement reading, and initial values
    VR1=VR10+m*BOX(i,1)-m*INIT(1);
    VR2=VR20+m*BOX(i,2)-m*INIT(2);
    HR1=HR10+m*BOX(i,3)-m*INIT(3);
    HR2=HR20+m*BOX(i,4)-m*INIT(4);
    DR1=DR10+m*BOX(i,5)-m*INIT(5);
    VL1=VL10+m*BOX(i,6)-m*INIT(6);
    VL2=VL20+m*BOX(i,7)-m*INIT(7);
    HL1=HL10+m*BOX(i,8)-m*INIT(8);
    HL2=HL20+m*BOX(i,9)-m*INIT(9);
    DL1=DL10+m*BOX(i,10)-m*INIT(10);

    %calculate current angles based on potentiometer lengths
```

```
    RA=atan(((ROT(i,1)-INIT(11))-(ROT(i,2)-INIT(12)))/BR0);
    AR1=acos((DR1^2+HR1^2-VR2^2)/(2*DR1*HR1));
    AR2=acos((DR1^2+VR1^2-HR2^2)/(2*DR1*VR1));
    AL1=acos((DL1^2+HL1^2-VL2^2)/(2*DL1*HL1));
    AL2=acos((DL1^2+VL1^2-HL2^2)/(2*DL1*VL1));

    %calculate x and y locations based on angles and potentiometer lengths
    xr2=HR1*cos(RA);
    yr2=-HR1*sin(RA);
    xr3=VR1*sin(pi()/2+RA-AR1-AR2);
    yr3=VR1*cos(pi()/2+RA-AR1-AR2);
    xr4=DR1*cos(AR1-RA);
    yr4=DR1*sin(AR1-RA);
    xl2=HL1*cos(RA);
    yl2=-HL1*sin(RA);
    xl3=VL1*sin(pi()/2+RA-AL1-AL2);
    yl3=VL1*cos(pi()/2+RA-AL1-AL2);
    xl4=DL1*cos(AL1-RA);
    yl4=DL1*sin(AL1-RA);

    %calculate displacements based on current and initial positions

    ur2=xr2-xr20;
    vr2=yr2-yr20;
    ur3=xr3-xr30;
    vr3=yr3-yr30;
    ur4=xr4-xr40;
    vr4=yr4-yr40;
    ul2=xl2-xl20;
    vl2=yl2-yl20;
    ul3=xl3-xl30;
    vl3=yl3-yl30;
    ul4=xl4-xl40;
    vl4=yl4-yl40;

    %calculate strains based on displacements and shape function (Eq. 3.6)
    STR(i,1)=(ur2*(br-Y)-ur3*(br+Y)+ur4*(br+Y))*dr;  %Right Longitudinal
    STR(i,2)=(-vr2*(ar+X)+vr3*(ar-X)+vr4*(ar+X))*dr; %Right Vertical
    STR(i,3)=(vr2*(br-Y)-vr3*(br+Y)+vr4*(br+Y)-ur2*(ar+X)+ur3*(ar-
X)+ur4*(ar+X))*dr; %Right Shear
    STR(i,4)=(ul2*(bl-Y)-ul3*(bl+Y)+ul4*(bl+Y))*dl; %Left Longitudinal
    STR(i,5)=(-vl2*(al+X)+vl3*(al-X)+vl4*(al+X))*dl; %Left Vertical
    STR(i,6)=(vl2*(bl-Y)-vl3*(bl+Y)+vl4*(bl+Y)-ul2*(al+X)+ul3*(al-
X)+ul4*(al+X))*dl; %Left Shear
end
```

E.2 NI STRAIN DOWN SAMPLING

```
%MatLab File to down sample data from NI Strain Modules

%Load Raw Strain Data (800Hz) and valid time string (20Hz)
DAT=load('Undamaged_NI_Flange_01.txt');
TIM=load('Undamaged_Time_String_01.txt');

%Create output strain matrix
STR=zeros(length(TIM),9);

%Define data increment variable
j=1;

for i=1:length(TIM)

    %increment j until data file is just over time increment
    if TIM(i)<DAT(j,1)
        j=j+1;
    end

    %define interpolation value
    p=(DAT(j,1)-TIM(i))/(DAT(j,1)-DAT(j-1,1));

    %Insert current valid time
    STR(i,1)=TIM(i);

    %Fill Strain Matrix
    for k=2:9
        STR(i,k)=DAT(j-1,k)+p*(DAT(j,k)-DAT(j-1,k));
    end
end
```